



Johansen, Kristoffer (2018) *Stable-inertial cavitation*. PhD thesis.

<https://theses.gla.ac.uk/30796/>

Copyright and moral rights for this work are retained by the author

A copy can be downloaded for personal non-commercial research or study, without prior permission or charge

This work cannot be reproduced or quoted extensively from without first obtaining permission in writing from the author

The content must not be changed in any way or sold commercially in any format or medium without the formal permission of the author

When referring to this work, full bibliographic details including the author, title, awarding institution and date of the thesis must be given

Enlighten: Theses

<https://theses.gla.ac.uk/>
research-enlighten@glasgow.ac.uk

Stable-inertial Cavitation

Kristoffer Johansen

Submitted in fulfilment of the requirements for the
Degree of Doctor of Philosophy

School of Engineering
College of Science and Engineering
University of Glasgow



University
of Glasgow

September 2018

Abstract

Research and development of applications utilising acoustic cavitation, particularly medical therapy, is often based on the spectrum of the scattered emissions collected during the cavitation occurrence. There is, however, limited understanding as to how driven bubble behaviour is related to the myriad of non-linear features that can exist within the cavitation noise spectrum, including those commonly reported. Moreover, there is an enduring tendency to classify cavitation activity as either stable or inertial, with no clear delineation between the two categories in terms of associated emissions. The work described in this thesis is dedicated to reconciling bubble dynamics driven by focused ultrasound, and resolved with ultra-high speed shadowgraphic imaging, to the acoustic emissions simultaneously detected via a broadband calibrated needle hydrophone system. Specifically, the role of periodic bubble collapse shock waves are experimentally investigated, supported by bubble oscillation models and spectral analysis. First, hydrophone-deconvolution for restoring an approximation to physical pressure data is demonstrated, through laser-plasma mediated bubble detection. Subsequent application to precision measurements of an acoustically driven cavitation bubble, verifies a contribution from periodic shock waves to all features within the emission spectrum, including the sub-harmonics. Moreover, complete spectral peak suppression at the sub-harmonic is demonstrated for a specific two-bubble configuration. Finally, the design of a bespoke passive cavitation detector, optimised for shock wave detection is described, and its performance evaluated against a comparable, commercially available device. Implications for cavitation detection and detector characterisation are discussed, as is the conventional classification of activity as stable or inertial, with reference to the literature.

Contents

Abstract	i
Acknowledgements	xxi
Dissemination of Thesis	xxiii
Declaration	xxv
List of symbols	xxvi
List of abbreviations	xxx
Overview of thesis	1
1 An introduction to cavitation	10
1.1 The emergence of cavitation as a research topic	10
1.2 The resonant acoustic bubble	12
1.3 The collapsing bubble and shock waves	13
1.4 The acoustic cavitation emission signal and noise spectrum	15
1.4.1 Reporting protocols and detectors for cavitation measurements	19
1.4.2 Historical context for classification of cavitation as stable or transient	22
1.4.3 Stable-inertial cavitation	24
1.4.4 Proposed mechanisms for specific spectral features	30
1.5 Focused ultrasound surgery	36
1.5.1 Cavitation in medical therapy	38

1.5.2	Rapid control feedback loop	39
1.5.3	Microbubble dynamics and possible acoustic emission mechanisms	41
1.5.4	Cavitation therapy without contrast agent microbubbles	45
1.6	The legacy of cavitation research to date	47
2	The Sonoptic chamber	49
2.1	The HIFU source	50
2.2	The sonoptic chamber	50
2.3	Bubble regimes	52
2.3.1	Calibration of bubble nucleation	54
2.4	High-speed imaging	56
2.4.1	Dark pixel counting algorithm	57
2.5	Acoustic detectors	58
3	Deconvolution of acoustically detected bubble collapse shock waves	59
3.1	A brief introduction to shock waves	60
3.2	Materials and methods	62
3.2.1	Bubble regimes	62
3.2.2	Needle hydrophone	62
3.2.3	High-speed imaging and acoustic measurements	63
3.2.4	Assessment of needle hydrophone rise time	66
3.2.5	Deconvolution of hydrophone voltage data	68
3.2.6	Rayleigh-Plesset-like equations and shock wave generation model	70
3.3	Results	76
3.3.1	Single-frequency calibration	76
3.3.2	Magnitude-only deconvolution	79
3.3.3	Full waveform deconvolution	81
3.4	Discussion	84
3.5	Conclusion	87

4	An analysis of the acoustic cavitation noise spectrum: The role of periodic shock waves	88
4.1	Materials and methods	89
4.1.1	Spectral analysis model for periodic shock waves	89
4.1.2	High-speed imaging and acoustic measurements	90
4.1.3	Assessment of HIFU field perturbation	93
4.2	Results	95
4.2.1	High-speed imaging	95
4.2.2	Needle hydrophone data	98
4.2.3	Bubble collapse and shock wave generation	103
4.2.4	Synthetic cavitation signal and spectrum	104
4.2.5	Comparing cavitation noise spectra for $f_0/2$ and $f_0/3$	109
4.3	Discussion	110
4.4	Conclusion	114
5	Covert cavitation: Spectral peak suppression in the acoustic emissions from spatially configured nucleations	115
5.1	Materials and methods	116
5.2	Results	117
5.2.1	High-speed imaging	117
5.2.2	Hydrophone data	118
5.2.3	Simulation of bubble-bubble interaction	121
5.2.4	Spectral analysis model for dual bubbles	127
5.3	Discussion	129
5.4	Conclusion	130
6	Performance characterisation of a passive cavitation detector optimised for sub-harmonic periodic shock waves from acoustic cavitation in MHz and sub-MHz ultrasound	131
6.1	Design considerations for a PCD	133

6.2	Rationale for the swPCD and review of a bespoke PCD	134
6.3	Materials and Methods	138
6.3.1	Experimental setup	138
6.3.2	Finite element method model of swPCD	139
6.4	Results	145
6.4.1	Detection of a single laser plasma mediated bubble collapse shock wave	146
6.4.2	swPCD and Y-107 detection of acoustic cavitation	149
6.4.3	Spectral peak suppression from reflections	153
6.5	Discussion	155
6.6	Conclusion	156
7	Conclusions and Future Work	158
A	Blind deconvolution of a hydrophone with a bubble collapse shock wave	164
A.1	Materials and methods	165
A.2	Results	166
A.3	Conclusion	169
B	Validity of the Keller–Miksis equation for ‘non-stable’ cavitation and the emissions generated	170
B.1	$f_0/2$ regime	172
B.2	$f_0/3$ regime	174
B.3	Conclusion	177
C	Characterising focused ultrasound via high-speed shadowgraphic imaging at 10 million fps	178
C.1	Methods	179
C.2	Needle hydrophone–acoustic field interaction	180
C.3	Speed of sound estimation	181
C.4	Phase characterisation of needle hydrophone	183
C.5	Conclusion	186

D	Absolute sensitivity characterisation of all construction stages of swPCD	187
E	Selection of Matlab scripts	189
E.1	Gilmore equation and acoustic emissions	189
E.2	Keller-Miksis for single bubble and bubble pair	193
E.3	Deconvolution of needle hydrophone	197
E.4	Dark pixel counting algorithm	207

List of Tables

3.1	Shock wave properties from Fig. 3.8a, including rise time (RT), full width half maximum (FWHM) and peak positive pressure amplitude of the shock wave ($PPPA_{SW}$), for single-frequency calibration and simulated shock wave profile, at each of the propagation distances.	78
3.2	Shock wave properties from Fig. 3.9a, including full width half maximum (FWHM) and peak positive pressure amplitude of the shock wave ($PPPA_{SW}$), for magnitude-only and filtered simulated shock wave profile, at each of the propagation distances.	81
3.3	Shock wave properties from Fig. 3.10, including full width half maximum (FWHM) and peak positive pressure amplitude of the shock wave ($PPPA_{SW}$), for full waveform deconvolved and filtered simulated shock wave profile, at each of the propagation distances.	83
6.1	Material properties of backing layer investigated using finite element method. Attenuation and longitudinal speed of sound are measured at 1 MHz, taken from the PZFlex database.	142
6.2	Material properties of matching layer investigated using finite element method. Attenuation and longitudinal speed of sound are measured at 1 MHz, taken from the PZFlex database.	144
6.3	Material properties of final swPCD taken from PZFlex database	145
6.4	Summary of normalised amplitude, rise time (RT) and FWHM for both experimental and computational results for all build stages of the swPCD. All results are normalised to PVdF–film only	148

List of Figures

1	Basic cavitation detection experiment	2
2	Sample images of periodically collapsing acoustic cavitation cloud, driven by HIFU of $f_0 = 254$ kHz.	5
3	(a) Shadowgraphic high-speed images of laser-plasma mediated bubble collapsing from maximum radius at $32.97 \mu\text{s}$ after laser-pulse generation with the emission of a bubble collapse shock wave. (b) The bubble collapse shock wave time waveform, detected by the needle hydrophone used throughout this thesis.	6
4	(a) Acoustic emissions from single sub-harmonic ($f_0/2$) cavitation bubble driven by $f_0 = 692$ kHz. (b) The corresponding acoustic cavitation noise spectrum from the measurement in (a).	7
5	(a) Bubble collapse shock wave detected by swPCD and commercial device. (b) Spectra of detected acoustic emissions in (a).	8
1.1	(a) Time domain representation of collected sub-harmonic acoustic emissions over 300 cycles of ultrasound with $f_0 = 31$ kHz. (b) Frequency spectrum of acoustic emissions up to the fundamental driving frequency, $f_0 = 31\text{kHz}$, with a spectral features at the first sub-harmonic.	15
1.2	Spectrogram of acoustic emissions from sound irradiated water at $f_0 = 22.9$ kHz as driving voltage is increased.	17
1.3	<i>In vitro</i> acoustic emissions from microbubbles driven by 100-cycles of 500 kHz ultrasound, for which multiple spectral features were monitored.	21

1.4	(a) Schematic of experimental setup used to make some of the first acoustic cavitation measurements. (b) Three successive frames of HIFU-field interacting with aerated water	22
1.5	Classes of high and low energy cavitation regimes.	24
1.6	Computed radial dynamics and scattered pressure at 1 cm from a microbubble undergoing stable-inertial cavitation.	25
1.7	Phase-plane representation of stable cavitation index versus inertial cavitation index, for cavitation activity driven by $f_0 = 550$ kHz at a pressure amplitude of 6 bars.	27
1.8	Collected acoustic emissions from a microbubble suspension in human plasma driven by $f_0 = 1$ MHz ultrasound at 100, 200, 350 and 1 000 kPa peak-negative pressure.	29
1.9	Growth of a 4th order surface mode vibration for a bubble with equilibrium radius of 36 μm after 5 cycles of ultrasound.	31
1.10	(a) Acoustic emissions at $f_0/2$ and white noise from air-saturated water driven at $f_0 = 28$ kHz. (b) Acoustic emissions at $f_0/2$ and white noise for pure glycerol containing large bubbles of resonance frequency $f_r = f_0/2$ driven at $f_0 = 31$ kHz.	32
1.11	Bubble response at different driving pressure amplitudes, as a function of frequency.	34
1.12	Solutions of Rayleigh-Plesset equation in the phase-plane. $R_0 = 5 \times 10^{-4}$ m, $f_0 = 500$ kHz. The numbers on the curves refer to the ratio between PPA/P_0	35
1.13	(a) Radius-time curve of air-bubble in water. $R_0 = 10^{-6}$ m; $f_0 = 500$ kHz. The number of the curves refers to the ratio of driving pressure amplitude PPA , and the ambient pressure P_0 , PPA/P_0 . (b) Unstable cavitation driven at twice its resonance frequency, eventually transiently collapsing.	36
1.14	(a) Side-view diagram of the focused ultrasound system and patient positioning. (b) MR image obtained with the patient in position for treatment of fibroid.	37
1.15	(a) Experimental setup for blood-brain barrier disruption using microbubbles and HIFU. (b) Example of acoustic exposure where where $3f_0/2$ and $5f_0/2$ are detected when the pressure amplitude of the driving signal is increased.	40

1.16 (A) Schematic representation of the feedback loop which controlled the drug delivery system. (B) Illustration of the dual-aperture focused ultrasound setup with a PCD.	41
1.17 High speed images of surface wave oscillations from a microbubble driven by a 12-cycle ultrasound pulse of $f_0 = 1.7\text{MHz}$	43
1.18 Detected acoustic emissions at $f_0/2$, $4f_0$ and broadband noise from cavitation driven by 1.69 MHz ultrasound of intensity 786 W/cm^2 (1.77 MPa).	46
1.19 Graphical representation of stable and inertial cavitation. Taken from [1]	47
2.1 Free field mapping of fundamental frequency for the HIFU transducer used in this thesis, and simulation of the acoustic field using Field II.	51
2.2 Top view schematic representation of the sonoptic chamber, including high-speed camera, pulsed laser illumination configuration, nucleation laser with objective lens placed inside a sealed unit, and HIFU transducer.	52
2.3 Photographs of sonoptic chamber, including Shimadzu HPV-X2 high-speed camera, xyz manipulators used to position the laser nucleation optics relative to transducer focus, HIFU transducer and second xyz manipulator used to position needle hydrophone and PCD in rapid prototyped fixture relative to nucleation position.	53
3.1 (a) Blast wave pressure plotted against time. Taken from [2]. (b) Example of lithotripsy shock wave used in medical therapy. The shock wave is characterised by an abrupt rise in pressure ($\sim 40\text{ MPa}$), followed by a longer tensile phase ($\sim -8\text{ MPa}$). Taken from [3].	60
3.2 Phase and magnitude calibration of 1 mm PVdF needle hydrophone over a bandwidth of 125 kHz to 20 MHz.	63
3.3 High-speed shadographic imaging of laser-plasma mediated vapour bubble collapse with emissions of bubble collapse shock wave, and needle hydrophone voltage trace.	65

3.4	(a) Schematic diagram of nucleation laser lens generating a bubble which collapses with the emissions of a double fronted bubble collapse shock wave, and the location of the needle hydrophone. (b) Representative high-speed images of laser-plasma mediated vapour bubble collapse generating a double-fronted bubble collapse shock wave (arrowed), and splitting into two separate bubbles, recorded at 5×10^6 fps. The bubble had a $R_{\max} = 342 \mu\text{m}$, which is $\sim 6\%$ smaller than the bubbles considered for further analysis in §3.3. (c) Voltage-trace of double-fronted bubble collapse shock wave. Effects of the shock wave being double-fronted is arrowed. Note, the needle hydrophone is oriented with the tip toward the top-side of the image as seen in (a), 40 mm away from the bubble with a $\sim 26 \mu\text{s}$ propagation time delay from high-speed image capture to hydrophone detection.	67
3.5	Approximation of the needle hydrophone rise time using an optical break down shock wave: (a) Representative frames from a high-speed image sequence, taken at 1×10^6 fps, showing the formation of an laser-plasma mediated vapour bubble and an optical break down shock wave (arrowed), with the laser Q-switch taken as $t = 0 \mu\text{s}$. The laser-plasma mediated vapour bubble continues to expand up to its maximum radius, captured at $33 \mu\text{s}$, followed by collapse and emission of a bubble collapse shock wave (arrowed). The bubble had a $R_{\max} = 365 \mu\text{m}$. (b) The needle hydrophone trace detected, with the tip located ~ 50 mm from the laser-plasma mediated vapour bubble location. (c) Higher temporal resolution than in (b) of the optical break down shock wave and bubble collapse shock wave profiles (dotted blue). Hydrophone deconvolved shock waves are also presented (black with grey shading representing the uncertainty). The rise time of a device is defined as the time taken to rise from 10% to 90% of peak voltage amplitude, indicated by the arrows.	69
3.6	(a) Magnitude response of zero-phase bandpass filter, $H_{\text{bpf}}(f)$, with the -3 dB corner points, at 145 kHz and 19.9 MHz marked \times . (b) Impulse response to needle-hydrophone in the time domain.	71

-
- 3.7 The experimental radius-time curve (red star and grey shading representing uncertainty), which was acquired using the dark pixel counting algorithm described in §2.4.1, of the bubble collapse depicted in Fig. 3.3a (blue diamonds are the data points of the images presented). The dashed black line curve is the best fit solution of the Gilmore equation with the following parameters, for water; $c_0 = 1484\text{ms}^{-1}$, $p_0 = 101\text{ kPa}$, $R_0 = 61\ \mu\text{m}$; $R_{\text{max}} = 364\ \mu\text{m}$; $\rho_0 = 998\text{ kg m}^{-3}$, $\gamma = 4/3$, $\sigma = 0.072\text{ Nm}^{-1}$ and $\eta = 0.001\text{ Pa s}$ 74
- 3.8 (a) Single-frequency calibrated hydrophone signal (black with grey shaded uncertainty), with the calibration value at 10 MHz, for bubble collapse shock waves measured at propagation distances of 30, 40 and 50 mm, and the simulated shock wave profile prediction (black dash). The horizontal lines are the r^{-1} envelopes to the measured and computed shock waves for the different distances. (b) Frequency spectra of the single-frequency calibrated signal (black with grey shaded uncertainty) and simulated shock (black dash) at $r = 30\text{ mm}$, normalised to the experimental data. Also shown (grey dot) is the noise floor, sampled from the hydrophone data between the Q-switch and the optical break down shock wave, Fig. 3.3b. All three bubbles had a $R_{\text{max}} = 365 \pm 4\ \mu\text{m}$ 77
- 3.9 (a) Magnitude-only deconvolved hydrophone signal (black with grey shaded uncertainty), at propagation distances of 30, 40 and 50 mm, and filtered simulated shock wave profile (black dash). Sloped lines are the r^{-1} envelopes to the respective shock waves. All three bubbles had a $R_{\text{max}} = 365 \pm 4\ \mu\text{m}$. (b) Frequency spectra of the magnitude-only deconvolved signal (black with grey envelope) and simulated shock (black dash) at $r = 30\text{ mm}$, normalised to the experimental data. 80
- 3.10 Full waveform deconvolved hydrophone signal (black with grey shaded uncertainty), at propagation distances of 30, 40 and 50 mm, and filtered simulated shock wave profile (black dash). Sloped lines are the r^{-1} envelopes to the respective shock waves. All three bubbles had a $R_{\text{max}} = 365 \pm 4\ \mu\text{m}$ 82

3.11	Full waveform deconvolved double-fronted bubble collapse shock wave (grey shaded uncertainty) detected by needle hydrophone at a distance of 40 mm. The voltage-trace to this bubble collapse shock wave is shown in Fig. 3.4c. The bubble had a $R_{\max} = 342 \mu\text{m}$ and a FWHM of 50 ns.	83
4.1	Representation of the spectral analysis model for periodic shock waves, in the time domain.	89
4.2	Representation of the spectral analysis model for periodic shock waves, in the frequency domain, for 3 shock waves (red dash), and 5 shock waves (solid black).	91
4.3	Illustrates the specific configuration used to validate the spectral analysis model described: (a) cross-sectional side view, and (b) an axial scan of the HIFU focal region, with representations of the needle hydrophone outlined for 'emission collection' position (solid black).	92
4.4	(a) Representation of the hydrophone configuration used to assess the field perturbation, introduced by the needle hydrophone in the emission collection position (b) Image depicting the needle hydrophone and fibre-optic hydrophone tips during the measurements taken. Scale bar represents $250 \mu\text{m}$. (c) Frequency spectra of HIFU field used to drive cavitation in the $f_0/3$ regime, measured by the fibre-optic hydrophone both with and without the needle hydrophone in the emission collection position.	94
4.5	Images extracted from a high-speed sequence recorded at 5×10^6 fps, of cavitation activity in the $f_0/2$ regime. (a) The whole field of view, depicting the needle hydrophone tip position relative to the activity, with a shock wave (arrowed white) incident to it. (b) Selected images representing the cavitation oscillation dynamics, including three strong collapses, and coincident shock wave emission. (c) Radius-time curve based on a dark pixel counting algorithm, described in §2.4.1 and Matlab script in Appendix E.4, for the time interval under investigation. Diamond and squares indicate the specific images represented in (a) and (b), respectively. Scale bar represents $250 \mu\text{m}$	95

-
- 4.6 Images extracted from a high-speed sequence recorded at 5×10^6 fps, of cavitation activity in the $f_0/3$ regime. (a) The whole field of view, depicting the needle hydrophone tip position relative to the activity, with a shock wave (arrowed white) incident to it. (b) Selected images representing the cavitation oscillation dynamics, including the 3rd and 6th strong collapses, as presented in (c) radius-time curve based on a dark pixel count algorithm (§2.4.1), for the time interval under investigation. Diamond and squares indicate the specific images represented in (a) and (b), respectively. Scale bar represents $250 \mu\text{m}$ 97
- 4.7 (a) Raw needle hydrophone data recorded during the cavitation activity (blue solid) of Fig. 4.5, and control exposure for an equivalent HIFU burst (red dot), without cavitation nucleation. It is worth noting how the two events are close to completely overlaid, as shown in Fig. 4.8a. (b) Control subtracted and needle hydrophone-deconvolved data, revealing the signal emitted by the cavitation, $\tilde{x}_{\text{cav}}^{\text{p}}(t)$. (c) The cavitation spectrum $\tilde{X}_{\text{cav}}^{\text{p}}(f)$, obtained via Fourier Transform of (b). Rectangular box (cyan) in (a,b) represent the section of the signal that is considered for further analysis. 99
- 4.8 (a) Section of raw needle hydrophone data recorded during the cavitation activity of Fig. 4.5, (blue solid) and control exposure for an equivalent HIFU burst (red dot), without cavitation nucleation. The inset zoom around $19.0 \mu\text{s}$, reveals a detected shock wave in the raw data, also arrowed for the rest of the trace. (b) Control subtracted and needle hydrophone-deconvolved data, revealing the signal emitted by the cavitation, $\tilde{x}_{\text{cav}}^{\text{p}}(t)$, captured in the high-speed imaging of Fig. 4.5c. (c) The cavitation spectrum $\tilde{X}_{\text{cav}}^{\text{p}}(f)$, obtained via Fourier Transform of (b). 100
- 4.9 (a) Control subtracted and needle hydrophone-deconvolved data, revealing the signal emitted by the cavitation activity, $\tilde{x}_{\text{cav}}^{\text{p}}(t)$. (b) The cavitation spectrum $\tilde{X}_{\text{cav}}^{\text{p}}(f)$, obtained via Fourier Transform of (a). Rectangular box (cyan) in (a) represent the section of the signal that is considered for further analysis. 101

4.10 (a) Section of deconvolved needle hydrophone data used in analysis of the cavitation noise spectrum. (b) The cavitation spectrum $\tilde{X}_{\text{cav}}^{\text{P}}(f)$, obtained via Fourier Transform of (a).	102
4.11 Simulated radius-time curve (black dash) and bubble collapse shock wave (solid red) for a free bubble with the parameters, $R_0 = 4.4 \mu\text{m}$, $\dot{R}(0) = 0 \text{ ms}^{-1}$, $R_{\text{max}} = 50 \mu\text{m}$, $c_0 = 1484 \text{ ms}^{-1}$, $p_0 = 101 \text{ kPa}$, $\rho_0 = 998 \text{ kg m}^{-3}$, $m = 0$, $\sigma = 0.072 \text{ Nm}^{-1}$, $\eta = 0.001 \text{ Pa s}$, and $r = 3 \text{ mm}$	103
4.12 (a) The filtered simulated shock wave profiles, $s_{\text{sim}}^{\text{bpf}}(t)$, fitted to each of the shock waves detected experimentally, in the $f_0/2$ regime. The grey envelope represents the calibration uncertainty, incorporated via the deconvolution process. (b) the synthetic periodic shock wave signal (red dot), overlaid to the experimentally detected signal $\tilde{x}_{\text{cav}}^{\text{P}}(t)$, (solid black). (c) The synthetic periodic shock wave spectrum overlaid to the experimentally measured cavitation emission spectrum, $X_{\text{cav}}^{\text{P}}(f)$	105
4.13 (a) The synthetic cavitation signal (red dot) composed of filtered simulated shock wave profiles, $s_{\text{sim}}^{\text{bpf}}(t)$, and synthetic acoustic wave of f_0 and $2f_0$, overlaid to the experimentally detected signal $\tilde{x}_{\text{cav}}^{\text{P}}(t)$, (solid black). (b) The synthetic cavitation spectrum, overlaid to the measured cavitation emission spectrum, $\tilde{X}_{\text{cav}}^{\text{P}}(f)$	106
4.14 (a) The filtered simulated shock wave profiles, $s_{\text{sim}}^{\text{bpf}}(t)$, fitted to each of the shock waves detected experimentally, in the $f_0/3$ regime. The grey envelope represents the calibration uncertainty, incorporated via the deconvolution process. (b) the synthetic cavitation emission signal (dotted red), with acoustic emission components $\tilde{x}_{\text{AW}}^{\text{P}}(t)$ added, overlaid to the experimentally measured cavitation emission signal (solid black). (c) The synthetic periodic shock wave spectrum, overlaid to the experimentally measured cavitation emission spectrum, $\tilde{X}_{\text{cav}}^{\text{P}}(f)$	108
4.15 A comparison of the acoustic cavitation noise spectra from $f_0/2$ (black) and $f_0/3$ (red) data.	109

5.1	Illustration of experimental setup: (a) cross-sectional view of HIFU transducer-needle hydrophone configuration, and two long-working distance objective lenses facilitating dual-laser nucleation of cavitation bubbles. (b) An axial scan of the HIFU focal region, including the targeted laser-nucleation zones, to which the laser-nucleating foci were aligned.	116
5.2	(a) Schematic of dual-nucleated cavitation bubbles emitting periodic shock waves (arrowed) displaced $\approx \lambda_0$ apart such that the $nf_0/2$ spectral content in the shock waves is detected 90° out of phase for the respective bubbles. The bubbles are positioned approximately in-line with the needle hydrophone. (b) Selected high-speed shadowgraphic images, recorded at 5×10^6 fps of two cavitation-bubbles, with an inter-bubble spacing $\approx \lambda_0$. Bright and dark regions, indicated by dash box C and R, represent compressional and rarefactional phases of the HIFU driving. Periodic shock wave emission, arrowed (white) at $28.58 \mu\text{s}$ and $31.38 \mu\text{s}$ (but not $30.18 \mu\text{s}$, when an intervening compressive phase is incident) verifies that both bubbles are in the $f_0/2$ sub-harmonic regime.	118
5.3	(a) Raw needle hydrophone data recorded during the cavitation activity captured in Fig. 5.2 (blue solid) and control exposure for an equivalent HIFU burst (black dot). (b) Pressure-time waveforms of control-subtracted and deconvolved needle hydrophone data (solid grey). (c) The acoustic emission spectrum (solid grey) for the combination system. Rectangular box (cyan) in (a,b) represent the section of the signal that is considered for further analysis.	119
5.4	(a) Pressure-time waveforms of control-subtracted and deconvolved needle hydrophone data (solid grey) and synthetic periodic shock wave signal (red dot), with the blue-dash box reproduced in (b) corresponding directly to the selected images of Fig. 5.2. (c) The experimental needle hydrophone (solid grey) and periodic shock wave synthetic (red dot) spectra for the combination system, revealing no sub-harmonic content including at odd-numbered higher harmonics.	120

5.5	(a) Control-subtracted deconvolved needle hydrophone signal after bandpass filtering from 1.5 MHz to 20 MHz for the acoustic emissions in Fig. 5.4b. (b) 2nd and 3rd shock wave from Fig. 5.4b, which demonstrates the difference in FWHM from the top and bottom bubble (arrowed) caused by the positioning relative to the needle hydrophone, Fig. 5.2.	122
5.6	Normalised maximum radius defined as $R^* = (R_{\max} - R_0)/R_0$ for solutions of Keller-Miksis equation for single bubble (solid black) and bubble-pair (stapled green) as a function of separation distance. Computed radial dynamics and acoustic emissions for two separation distances (blue dots), are shown in Figs. 5.8 and 5.7. Parameters used are $\sigma = 0.072 \text{ N m}^{-1}$, $\mu = 0.001 \text{ Pa s}$, $p_0 = 101 \text{ kPa}$, $\rho = 998 \text{ kg m}^{-3}$, $\gamma = 4/3$, $R_0 = 3 \text{ }\mu\text{m}$, $f_0 = 692 \text{ kHz}$ and $PPA = 1.6 \text{ MPa}$. Where the initial conditions are $R(0) = R_0$ and $\dot{R}(0) = 0$	123
5.7	(a) Radius-time curves for single bubble (solid black) and bubble-pair (stapled green) for solutions of Keller-Miksis equation separation distances of 0.3 mm. (b) Predicted acoustic emissions affecting the neighbouring bubble. Parameters used are $\sigma = 0.072 \text{ N m}^{-1}$, $\mu = 0.001 \text{ Pa s}$, $p_0 = 101 \text{ kPa}$, $\rho = 998 \text{ kg m}^{-3}$, $\gamma = 4/3$, $c = 1500 \text{ m s}^{-1}$, $R_0 = 3 \text{ }\mu\text{m}$, $f_0 = 692 \text{ kHz}$ and $PPA = 1.6 \text{ MPa}$. Where the initial conditions are $R(0) = R_0$ and $\dot{R}(0) = 0$	125
5.8	(a) Radius-time curves for single bubble (solid black) and bubble-pair (stapled green) for solutions of Keller-Miksis equation separation distances of 2.3 mm. (b) Predicted acoustic emissions affecting the neighbouring bubble. Parameters used are $\sigma = 0.072 \text{ N m}^{-1}$, $\mu = 0.001 \text{ Pa s}$, $p_0 = 101 \text{ kPa}$, $\rho = 998 \text{ kg m}^{-3}$, $\gamma = 4/3$, $c = 1500 \text{ m s}^{-1}$, $R_0 = 3 \text{ }\mu\text{m}$, $f_0 = 692 \text{ kHz}$ and $PPA = 1.6 \text{ MPa}$. Where the initial conditions are $R(0) = R_0$ and $\dot{R}(0) = 0$	126
5.9	The magnitude of the synthetic $f_0/2$ periodic shock wave spectrum, $ X_{\text{PSW}}^{\text{b}}(f) $, expected from the bottom bubble only (red dot), the windowing function (solid blue) for both bubbles with ξ and τ deduced from the experimental needle hydrophone data, and the resulting needle hydrophone periodic shock wave spectrum, $ X_{\text{PSW}}^{\text{NH}}(f) $ (solid red), on application of the window.	128

6.1	Picture of Y-107 PCD from Sonic Concepts with stated bandwidth of 10 kHz to 15 MHz, and geometrically focused to 68 mm.	135
6.2	Cross-section of PCD described in O'Reilly <i>et al</i> using PVdF as active material where the film is clamped between two brass tubes that function as electrical connections to the electrodes. Taken from [4].	136
6.3	Area under Fourier Transform of acoustic emissions from microbubbles detected by PVdF receiver and ceramic receiver for increasing driving pressure amplitudes. Second harmonic (a,d), first sub-harmonic (b,e) and broadband emissions (c,f) are monitored. Taken from [4].	137
6.4	Experimental setup used for detection of laser plasma-mediated bubble collapse shock waves (no HIFU), and laser-nucleated acoustic cavitation (with HIFU). Three sensors are depicted, the needle hydrophone, swPCD, and Y-107. The needle hydrophone is used for determining the characteristics of the input function used in the finite element method simulation. Needle hydrophone and Y-107 are positioned with an xyz-manipulator. A nucleating laser pulse is focused through the microscope objective lens. swPCD is placed through a hole in a transducer with an O-ring retainer. All sensors are placed at a distance of 68 ± 1 mm from the nucleation site, equal to the geometric focus of the Y-107.	138
6.5	(a) Photograph of final stage swPCD, (b) schematic cross-section of the swPCD, and (c) schematic of finite element method geometry used in the guidance of swPCD construction.	139

6.6	(a) High-speed shadowgraphic images of a laser plasma-mediated bubble, including maximum radius, $t = 33\mu\text{s}$, and collapse with coincident emission of a bubble collapse shock wave at $t = 66\mu\text{s}$, imaged at 1×10^6 fps. The $PPPA_{\text{SW}}$ of the bubble collapse shock wave is intrinsically related to R_{max} (b) Full waveform deconvolved bubble collapse shock wave (solid black) measured by needle hydrophone from laser plasma-mediated bubble at a distance of 68 mm, and computed bubble collapse shock wave (stapled grey) bandpass filtered at 125 kHz – 20 MHz. (c) Spectra of experimentally detected and computed bubble collapse shock wave, where the computed bubble collapse shock wave spectra is normalised to the maximum of the experimentally detected bubble collapse shock wave.	140
6.7	(a) Finite element method simulation of bubble collapse shock wave detection using air backing (violet) and 25% Tungsten-Epoxy (grey) backing layers, as representatives of low and high acoustic impedance respectively. Results are normalised to PVdF-only (green) as no backing (or water backing). (b) Relative sensitivity for the backing configurations investigated in (a).	141
6.8	(a) Finite element method simulation of bubble collapse shock wave detection using epoxy materials Vantico HY956EN/CY208 (light blue) and Vantico HY956EN/CY221(red) as matching layers, representatives of close to desired acoustic impedance respectively. All results have a backing layer of 25% Tungsten-Epoxy (red) and normalised to PVdF-only (water backing), 6.7. (b) Relative sensitivity for the matching configurations investigated in (a). . . .	144
6.9	Raw data from experimentally detected acoustic emissions from laser-plasma mediated vapour bubbles for different construction stages of the swPCD. For PVdF-only (green),backed PVdF (grey), matched and backed (red). All measurements are performed at $\sim 68 \pm 1$ mm from nucleation site, where all laser plasma-mediated bubbles had a maximum radius of $365 \pm 4 \mu\text{m}$. All data is normalised to the bubble collapse shock wave detected by PVdF-only. See Fig. 6.10 for zoomed in bubble collapse shock wave profiles.	146

6.10	Comparison of experimentally detected (solid) and simulated bubble collapse shock wave (dashed) response for different construction stages of swPCD. For PVdF-only (green),backed PVdF (grey), matched and backed (red). All measurements are performed at $\sim 68 \pm 1$ mm from nucleation site, where all laser plasma-mediated bubbles had a maximum radius of 365 ± 4 μ m. (b) Spectra of shock waves detected by different build stages. Same color coding as in (a), with dotted spectra representing the noise floor for the different stages. All experimental and simulated results are normalised to PVdF-only.	147
6.11	Raw voltage-trace comparing final stage swPCD (solid red) and Y-107 (solid blue) for detection of a acoustic emissions from laser-plasma mediated vapour bubble.	148
6.12	(a) Voltage-trace comparing final stage swPCD (solid red) and Y-107 (solid blue) for detection of a bubble collapse shock wave. (b) Spectra of shock waves in (a), where stapled data represents the noise floor. Spectra are normalised to final stage swPCD.	149
6.13	(a) Raw voltage data from swPCD for cavitation event (black dots) and control exposure (green solid). (b) Control subtracted cavitation emission data for the swPCD. (c) Raw voltage data from Y-107 for cavitation event (black dots) and control exposure (green solid). (d) Control subtracted cavitation emission data for the Y-107. Rectangle in (b,d) contains the cavitation emissions which are considered for further analysis.	150
6.14	(a) High-speed shadowgraphic images of sub-harmonically collapsing cavitation cloud imaged at 1×10^6 fps. (b,c) Control subtracted cavitation emission data in the time-domain detected by (b) swPCD and (c) Y-107. (d,e) Spectra of data in (b,c), where swPCD (solid red) with noise-floor (stapled red), and Y-107 (solid blue) with noise-floor (stapled blue). All spectra are normalised to the maximum of swPCD, with $f_0 = 220$ kHz.	152

6.15	(a) High-speed image of multi-fronted periodic shock waves from asymmetric cavitation cloud collapse imaged at 1×10^6 fps. Cavitation emission data subtracted control during detection of multi-fronted periodic shock waves, detected by (b) Y-107 and (c) swPCD	153
6.16	(a) Voltage-trace of Y-107 (blue), synthetically reconstructed direct acoustic emission (stapled black), and synthetically reconstructed reflected acoustic emission (dotted magenta). (b) Spectra of all time domain signals in (a), and spectral window (solid black) imposed on the voltage-trace spectrum (blue) from the reflections (dotted magenta). For the spectral window the parameters are $\xi = 0.34$ and $\tau = 3.4\mu\text{s}$	154
A.1	(a,b) A full hydrophone voltage-trace, recorded at 50 ± 1 mm and 68 ± 1 mm, respectively, with key features described in the text. Both laser-plasma mediated vapour bubbles have a collapse time $T_c = 32.8 \mu\text{s}$, equalling an estimated maximum radius of $R_{\text{max}} = 358 \mu\text{m}$	165
A.2	(a) Convolved voltage-trace (black) and computed bubble collapse shock wave (red) at 50 ± 1 mm, (b) spectra of bubble collapse shock waves in (a), (c) convolved voltage-trace (black) and computed bubble collapse shock wave (stapled magenta) at 68 ± 1 mm, (d) spectra of bubble collapse shock waves in (c).The noise floor (dotted black) from the needle hydrophone is shown in both (b,d). Computed bubble collapse shock waves are bandpass filtered at 125 kHz – 20 MHz. Parameters used solving Eq. (A.1); $R_0 = 75 \mu\text{m}$, $\rho = 998 \text{kgm}^{-3}$, $\mu = 0.001 \text{Pa s}$, $\sigma = 0.072 \text{Nm}^{-1}$ $c = 1484 \text{ms}^{-1}$, $P_0 = 101 \text{kPa}$, $R(0) = 358 \mu\text{m}$, and $\dot{R}(0) = 0 \text{ms}^{-1}$	167
A.3	Calibrated magnitude response (black) of the needle hydrophone over a bandwidth of 125 kHz to 20 MHz in 25 kHz increments.The shadow represent the uncertainty of the calibration. Blindly deconvolved magnitude response at 50 ± 1 mm (solid red) and at 68 ± 1 mm (stapled magenta).	168

B.1	(a) High-speed images of a single $f_0/2$ cavitation event, 2.7 mm from needle hydrophone tip. (b) High-speed images of a single $f_0/3$ cavitation event, 2.5 mm from needle hydrophone tip.	172
B.2	(a)(left) Simulated radius-time curve from Keller-Miksis equation (red), with dashed rectangle representing the sub-harmonic oscillation imaged, and (right) normalised dark-pixel count (black scatter) from images in Fig. B.1(a). (b) Acoustic emissions from the driven bubble, measured by the needle hydrophone (black) and simulated (red), with periodic shock wave features arrowed from collapses in (b). The Keller-Miksis equation is solved with the following parameters: $R_0 = 3 \mu\text{m}$, $\rho = 998 \text{ kg m}^{-3}$, $\mu = 0.001 \text{ Pa s}$, $\sigma = 0.072 \text{ N m}^{-1}$ $c = 1484 \text{ ms}^{-1}$, $P_0 = 101 \text{ kPa}$, $PPA = 1.31 \text{ MPa}$, $R(0) = 3 \mu\text{m}$, and $\dot{R}(0) = 0 \text{ ms}^{-1}$	173
B.3	Spectra of acoustic emissions in Fig B.2 (b), where measured by needle hydrophone (black) and simulated (red).	175
B.4	(a) (left) Simulated radius-time curve from Keller-Miksis equation, with dashed rectangle representing the sub-harmonic oscillation imaged, and (right) normalised dark-pixel count (black scatter) from images in Fig. B.1 (b). (b) Acoustic emissions from the driven bubble, measured by the needle hydrophone (grey) and simulated (red), with periodic shock wave features arrowed from collapses in (b). The Keller-Miksis equation is solved with the following parameters: $R_0 = 6 \mu\text{m}$, $\rho = 998 \text{ kg m}^{-3}$, $\mu = 0.001 \text{ Pa s}$, $\sigma = 0.072 \text{ N m}^{-1}$ $c = 1484 \text{ ms}^{-1}$, $P_0 = 101 \text{ kPa}$, $PPA = 2.40 \text{ MPa}$, $R(0) = 6 \mu\text{m}$, and $\dot{R}(0) = 0 \text{ ms}^{-1}$	176
B.5	Spectra of acoustic emissions in Fig B.4 (b), where measured by needle hydrophone (black) and simulated (red).	177
C.1	Schematic of experimental setup, including high-speed camera, synchronised 10 ns laser pulses, Monozoom 7 lens, HIFU transducer, and needle hydrophone.	179

C.2	Optical and acoustic measurement of 3.4 MHz ultrasound field. In (a) and (b), shadowgraphic imaging of ultrasound field, where the two frames are separated by 100 ns. Rectangular boxes (magenta and red) indicate the region of interest for constructive and destructive interference. In (c), needle hydrophone measurement (blue), and pixel values obtained along line centred at needle hydrophone for (a) and (b), respectively (magenta) and (red).	181
C.3	In (a), high-speed shadowgraphic imaging of a 1.1 MHz ultrasound field at 10×10^6 fps, and acoustic measurement with needle hydrophone. Red line indicates pixels are sampled for speed of sound estimation and phase characterisation of needle hydrophone.	182
C.4	In red (solid) speed of sound estimate along the red line in Fig. C.3 from cross correlation of pixels that are separated by $\lambda/2$, where stapled red line is the average estimated speed of sound, and dotted blue is the theoretical prediction. The shaded region represent the standard deviation of the measurement.	183
C.5	Acoustical and optical measurement of ultrasonic field at 1.1 MHz. In (a), deconvolved needle hydrophone measurement (solid black), pixel sampled at midpoint (stapled green) of red line in Fig. C.3, and propagation time delayed pixel data (dotted red) relative to deconvolved needle. In (b), propagation time delayed (dotted red), and convolved needle hydrophone measurement (stapled black). All amplitudes are normalised to their respective maxima.	184
C.6	Phase characterisation of needle hydrophone along red line in Fig. 2 (a) using high-speed shadowgraphic imaging, where black cross is NPL calibrated phase with uncertainties, blue circle is averaged estimated phase, and green asterisks is average estimated phase in acoustic focus, Fig. C.3. Uncertainties are represented by the standard deviation of estimated phase for respective regions.	185

D.1 Characterised sensitivity for all construction stages of the swPCD, Y-107, and
needle hydrophone calibration. Where unbacked and unmatched (green), backed
(grey), backed and matched (red), Y-107 (blue), and needle hydrophone (black).
All uncertainties are represented by shading. 188

Acknowledgements

There are several people who deserves a special thanks, and I would like to mention a few by name: André Adelsten Søvik, thank you for taking time to discuss topics related to my PhD-thesis. Kenneth Kirkeng Andersen, thank you for constructive conversations regarding multiple technical challenges. Torbjørn Danielsen, thank you for showing interest in my work and motivating me to finish the thesis. Kristian Austreim, thank you for always reminding me that there is a future. Arthur Uno Rognmo, my conversations with you have been pure therapy and I will always be grateful for that you were willing, and able to listen to what I had on my mind.

Assel Ryspayeva, I can state with overwhelming certainty that the support you have given me over the last year has been invaluable, and I would not have been able to pull through without you there to ‘kick my ass’ when times were dark. Thank you.

I am entirely grateful for the support my family has given me in this process. Talania Johansen, Regine Johansen and Rebekka Johansen, thank you for all the uplifting conversations that we have had during my PhD. Moreover, I would like to thank my mom, Elisabeth Rasmussen and my father, Johannes Johansen.

I would like to thank my co-workers. Keith Johnston, thank you for introducing me to the experimental side of cavitation research. Your practical insight is infinite, and you always had a solution to every problem we encountered. Jae Hee Song, your analytical skills have inspired me, and I am grateful for having worked with such a talented person. You always push forward, and your brilliance has already made an impact on the field of cavitation.

Paul Prentice, thank you for securing funding and supervising me through my PhD. I am very grateful for all the help you have provided me during writing of the papers we have published together, and the writing-process involved with producing this thesis. Moreover, I would also like

to thank you for showing interest in the work ‘on the ground’, specifically always being available for discussions on how to improve an experiment. Thank you for introducing me to the exciting world of experimental cavitation research, and for helping me become a better scientist.

The research leading to these results has received funding from the European Research Council under the European Union’s Seventh Framework Programme (FP/2007 - 2013)/ERC Grant Agreement no. 336189 (TheraCav).

Dissemination of Thesis

Publications

Peer-reviewed journals

The publications are listed in order of publication, from first to last.

- **Kristoffer Johansen**, Jae Hee Song, Keith Johnston, and Paul Prentice. "*Deconvolution of acoustically detected bubble-collapse shock waves.*" *Ultrasonics* vol. 73, pp. 144-153, 2017.
- Jae Hee Song, **Kristoffer Johansen**, and Paul Prentice. "*An analysis of the acoustic cavitation noise spectrum: The role of periodic shock waves.*" *The Journal of the Acoustical Society of America* vol. 140, no. 4, pp. 2494-2505, 2016.
- Jae Hee Song, **Kristoffer Johansen**, and Paul Prentice. "*Covert cavitation: Spectral peak suppression in the acoustic emissions from spatially configured nucleations.*" *The Journal of the Acoustical Society of America* vol. 141, no. 3, pp. EL216-EL221, 2017.
- **Kristoffer Johansen**, Jae Hee Song, and Paul Prentice. "*Performance characterisation of a passive cavitation detector optimised for subharmonic periodic shock waves from acoustic cavitation in MHz and sub-MHz ultrasound.*" *Ultrasonics sonochemistry* vol. 43, pp. 146-155, 2018.

Conference proceedings

- **Kristoffer Johansen**, Jae Hee Song, and Paul Prentice. "*Characterising focused ultrasound via high speed shadowgraphic imaging at 10 million frames per second.*" In IEEE Ultrasonics Symposium, pp. 1-4, 2016.
- **Kristoffer Johansen**, Jae Hee Song, and Paul Prentice. "*Validity of the Keller-Miksis equation for "non-stable" cavitation and the acoustic emissions generated.*" In IEEE Ultrasonics Symposium, pp. 1-4, 2017.
- **Kristoffer Johansen**, Jae Hee Song, and Paul Prentice. "*Blind deconvolution of a hydrophone with a bubble-collapse shock wave.*" In Ultrasonics Symposium (IUS), 2017 IEEE International, pp. 1-4, 2017.

Conferences attended

- Acoustic bubbles in therapy: recent advances with medical microbubbles, clouds and harmonic antibubbles, Tours France, oral presentation entitled: '*A comparison of single-bubble and cloud models for non-stable cavitation and the emissions generated*', 2017. **(IEEE Student Paper Award Finalist)**
- IEEE International Ultrasonic Symposium, Washington D.C. USA, oral presentation entitled: '*Validity of the Keller-Miksis equation for "non-stable" cavitation and the acoustic emissions generated*', 2017.
- IEEE International Ultrasonic Symposium, Washington D.C. USA, oral presentation entitled: '*Blind deconvolution of a hydrophone with a bubble-collapse shock wave*', 2017.
- IEEE International Ultrasonic Symposium, Tours France, poster and oral presentation entitled: '*Characterising focused ultrasound via high speed shadowgraphic imaging at 10 million frames per second*', 2016.
- Anglo-French Physical Acoustics Conference (AFPAC), Selsdon Park, Surrey UK, oral presentation entitled '*Acoustic cavitation emissions from a strongly driven bubble cloud*', 2016.

Declaration

The work presented in Chapter 1 contains introductory material which was first published by other researchers, however, the production of the Chapter was carried out by the author. All work in this thesis was carried out by the author unless otherwise explicitly stated.

List of symbols

A_{f_0}	acoustic wave f_0 component
A_{2f_0}	acoustic wave $2f_0$ component
b	empirical constant
C	instantaneous speed of sound at bubble wall
C_t	impulse train (frequency domain)
c	speed of sound throughout liquid
c_t	impulse train (time domain)
c_0	speed of sound
D	duration of shock wave train
$D_{i,j}$	distance between bubble i and j
f	frequency
f_0	fundamental frequency
f_{PSW}	frequency of periodic shock waves
f_{M}	Minnaert resonance frequency
f_{c}	centre frequency
f_{n}	f_0 normalised to 1 MHz
f_{r}	large bubble resonance frequency
H	enthalpy at bubble wall
\dot{H}	time derivative of enthalpy at bubble wall
H_{bpf}	spectrum of bandpass filter
H_{NH}	spectrum of impulse response to detector

H_{swPCD}	spectrum of impulse response to swPCD
h_{NH}	impulse response to detector
k	wave number
L	smallest common multiple of m and n
m	van der Waals core parameter
p_0	ambient pressure in host medium
p_i	internal pressure
P_{rad}	acoustic emission
$PPPA_{\text{sw}}$	peak positive pressure amplitude shock wave
$PPPA_{\text{sw}}^{\text{b}}$	peak positive pressure amplitude shock wave bottom bubble
$PPPA_{\text{sw}}^{\text{t}}$	peak positive pressure amplitude shock wave top bubble
p_w	pressure at bubble wall
$p_{i,w}$	pressure at bubble wall i
R	instantaneous radius of bubble
R_0	equilibrium radius
R_i	instantaneous radius of bubble i
R_j	instantaneous radius of bubble j
R_{i0}	equilibrium radius of bubble i
R_{max}	maximum radius
\dot{R}	speed of bubble wall
\dot{R}_i	speed of bubble wall i
\dot{R}_j	speed of bubble wall j
\ddot{R}	acceleration of bubble wall
\ddot{R}_i	acceleration of bubble wall i
\ddot{R}_j	acceleration of bubble wall j
r	distance from centre of cavity
T_c	collapse time
T_{PSW}	period of shock wave emission
t	time

S	shock wave function (frequency domain)
S_{sim}	simulated shock wave function (frequency domain)
s	shock wave function (time domain)
s_{sim}	simulated shock wave function (time domain)
$s_{\text{sim}}^{\text{bpf}}$	bandpass filtered simulated shock wave function (time domain)
U_{NH}	spectrum of needle hydrophone voltage-trace
U_{swPCD}	spectrum of swPCD voltage-trace
v	radial velocity
W_{D}	rectangular windowing function (frequency domain)
w_{D}	rectangular windowing function (time domain)
X_{Dir}	spectrum of direct periodic shock waves
X_{PSW}	spectrum of synthetic periodic shock waves
$X_{\text{PSW}}^{\text{b}}$	spectrum of periodic shock waves bottom bubble
$X_{\text{PSW}}^{\text{t}}$	spectrum of periodic shock waves top bubble
$X_{\text{PSW}}^{\text{NH}}$	spectrum of periodic shock waves detected by needle hydrophone
$X_{\text{Y-107}}$	spectrum of combined direct and reflected periodic shock waves
$\tilde{X}_{\text{cav}}^{\text{p}}$	deconvolved spectrum
$\tilde{X}_{\text{cav}}^{\text{v}}$	convolved spectrum
$\tilde{x}_{\text{AW}}^{\text{p}}$	acoustic wave component (pressure)
x_{Dir}	direct periodic shock waves
x_{PSW}	periodic shock waves (time domain)
$x_{\text{PSW}}^{\text{t}}$	periodic shock waves top bubble (time domain)
$x_{\text{PSW}}^{\text{b}}$	periodic shock waves bottom bubble (time domain)
x_{Ref}	reflected periodic shock waves
$x_{\text{cav}}^{\text{p}}$	acoustic emissions (pressure)
$x_{\text{cav}}^{\text{v}}$	acoustic emissions (voltage)
z	position along propagation axis
δ	Dirac delta function
ρ	instantaneous density of host medium

ρ_0	ambient density of host medium
Γ	empirical constant
γ	polytropic exponent
λ_0	wavelength of fundamental frequency
σ	surface tension
ω	angular frequency
ϕ	phase
ϕ_{NH}	phase of needle hydrophone
ϕ_{prop}	phase due to propagation
ϕ_{tot}	total phase difference
ϕ_{f_0}	phase of f_0 acoustic wave component
ϕ_{2f_0}	phase of $2f_0$ acoustic wave component
Φ	velocity potential
τ	propagation time difference
μ	shear viscosity
ξ	ratio of $PPPA_{\text{sw}}$ for top and bottom bubble

List of abbreviations

- Extra corporal shockwave lithotripsy (ESWL)
- Frames per second (fps)
- Food and Drug Administration (FDA)
- Focused ultrasound surgery (FUS)
- Full width half maximum (FWHM)
- High intensity focused ultrasound (HIFU)
- Inertial cavitation dose (ICD)
- Inertial cavitation index (IC)
- Lead zirconate titanate (PZT)
- Magnetic resonance imaging (MRI)
- Mechanical index (MI)
- National Physical Laboratory (NPL)
- Passive cavitation detector (PCD)
- Peak negative pressure (PNP)
- Polyvinylidene Flouride (PVdF)
- Peak-positive amplitude (PPA)
- Stable cavitation dose (SCD)
- Shock wave PCD (swPCD)
- Signal to noise ratio (SNR)
- Stable cavitation index (SC)

Overview of Thesis

"It is in conformity with the essence of the physical method that we should begin by reducing such acoustical complexes to much simpler elementary phenomena."

— Marcel Minnaert, On musical air-bubbles and the sounds of running water, 1933

Acoustic cavitation, that is bubbles driven by an ultrasound field of higher intensities, has found applications in a wide range of fields, such as sonochemistry, acoustic cleaning, and in medical therapy.

When utilising cavitation and particularly in any medical application, monitoring acoustic emissions is often undertaken for correlation to the cavitation-mediated effect. In the cavitation literature there is some tendency to classify the activity as either *stable* or *inertial*, according to detected components within the signal emitted by that activity, as discussed for multiple papers reviewed throughout Chapter 1. In recent literature a third regime of cavitation is being recognised, primarily describing the transition from *stable* to *inertial*, commonly known as *Stable-inertial Cavitation* or *high energy stable cavitation*. This regime is characterised by repeating high energy collapses and subsequent shock wave emissions, as discussed in §1.4.3. All observations of acoustic cavitation presented in this thesis are representative examples of this cavitation regime.

Figure 1 is a representation of the basics involved in a cavitation detection experiment, for the case in which cavitation is generated by focusing ultrasound into a host medium. Ultrasound from the concave transducer propagates to the focus of the acoustic field, constructively interfering to form a region of the required intensity. Cavitation bubbles will thereby be nucleated in a stochastic process, with bubbles forming from dissolved gas at impurities and discontinuities in the host medium far below the practical tensile strength, of water for example, as referenced

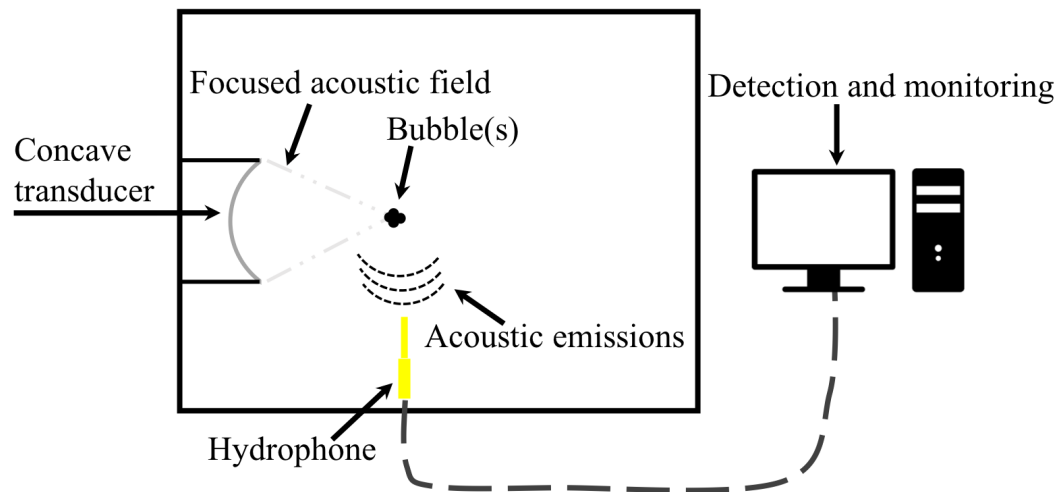


Figure 1: Basic cavitation detection experiment with a focused ultrasound transducer that nucleates cavitation activity in the focus. The bubbles are forced to oscillate and generate acoustic emissions. The acoustic emissions are measured by a hydrophone, and some detection and monitoring protocol is used to classify and quantify the cavitation activity.

in [5]¹. Once formed the bubbles interact very strongly with the ensuing ultrasound, as the gas contained within the bubble is several orders more compressible than the host medium. Any one of the oscillating bubbles will therefore act as a secondary acoustic source, which generally and in this thesis will be referred to as *acoustic cavitation emissions*, with the current understanding reviewed in detail in §1.4.4. These emissions are generally detected by a hydrophone (sometimes referred to in this role as a passive cavitation detector (PCD)), and the hydrophone voltage-data is then available for subsequent analysis.

However, complications that may ultimately distort the data and the interpretation of the analysis, can arise at every step, even for this seemingly simple experiment. In the reverse order of the procedure detailed in Fig. 1, a number of possible complications may be listed as:

- **Reporting of cavitation data:** Features within the acoustic cavitation noise spectrum of the emitted signal have a tendency to be used to infer stable or inertial cavitation. However, the features selected can vary significantly from paper to paper. A representative cross-section of cavitation reporting protocols across medical and industrial applications of cavitation is reviewed in §1.4.1

¹Cavitation nucleation is poorly understood with possible nuclei ranging from nano-bubbles [6] to cosmic rays [7] implicated for initiating bubble activity. The unpredictability of the location and the moment of nucleation are some of the reasons why it has been such a challenge to study cavitation.

- **Hydrophone convolution artefacts:** In selecting a hydrophone or detector the researcher has a wide range of options available, as discussed in Chapter 6. One of the most obvious options is the piezoelectric material selected; that is the active material in the detector which converts the acoustic emission into voltage-data. The distorting effect of a hydrophone, based on a commonly used piezoelectric material, on the shock wave emitted by a collapsing bubble and how to correct for that distortion, is the subject of Chapter 3. Indeed, *deconvolution of the detector response* from hydrophone data of acoustic cavitation emission signals, for physical pressure data restoration is underpinning the majority of the data in this thesis.
- **Bubble based mechanisms for the acoustic emissions:** Possibly the most significant deficit in understanding within the procedure depicted by Fig. 1, is reconciliation of the detected acoustic emissions (and specifically, spectral components within these emissions), to the source bubble dynamics. Development of any cavitation mediated application will benefit from insights into this relationship. The literature addressing this topic is reviewed in detail, in §1.4.4. Notably, the key papers still regularly cited by current reports developing cavitation applications, date from the 1950's to the 1980's.
- **Acoustic driving conditions:** Ultrasound of the intensities required to generate cavitation, will typically be non-linear, meaning it will develop frequency content at harmonics of the fundamental driving frequency. As bubbles are responsive to ultrasonic driving conditions the oscillations (and acoustic emissions) will be affected by the harmonic content. Indeed, many of the spectral features used to categorise cavitation activity are harmonics of the fundamental frequency, and so the source of any harmonic content in the detected emissions should be carefully identified. Moreover, any reflections of the ultrasound, from imaging objectives lenses placed in proximity to the cavitation activity to acquire high resolution high-speed imaging, for instance can distort both the driving acoustic field and the detected acoustic emissions.

This thesis is primarily an account of research undertaken to reconcile the acoustic emissions to the source bubble dynamics, also addressing the issues that may arise from convolution

artefacts imposed by the hydrophone.

A core technology employed throughout is a high-speed camera capable of imaging up to 10 million frames per second (fps). A further novel feature for the imaging is the use of synchronous 10 ns pulsed laser illumination defining the ‘effective’ temporal resolution. Moreover, the 10 ns illumination facilitates direct visualisation of pressure fluctuations, as a consequence of frame-by-frame changes in the refractive index of the host medium as the wave propagates, commonly known as shadowgraphic imaging. This has been critical to realising and investigating the previously under appreciated role of *periodic shock waves* within the signals emitted by acoustic cavitation described in §4.2.

The research presented in this thesis was carried out in CavLab at University of Glasgow, which is a dedicated cavitation laboratory studying laser-induced cavitation, acoustic cavitation and microbubbles. Previously in CavLab, high-speed imaging of acoustic cavitation had been undertaken with a predecessor of the experimental setup used in this thesis. A key technique distinguishing this experiment from others using high-speed imaging to observe cavitation, was the use of a single (low energy) laser pulse focused into a propagating acoustic field for nucleating a single cavitation cloud, at a predetermined position [8], as described in Chapter 4. This enables the use of a high-speed camera with high spatial and temporal resolution, to meaningfully interrogate acoustic cavitation dynamics in response to a well characterised ultrasound exposure.

Sample observations from the work at that time [9], driven by focused ultrasound at fundamental driving frequency $f_0 = 254$ kHz is given in Fig. 2. At this driving frequency, a cloud of bubbles rapidly forms from the laser nucleation. The subsequent behaviour of the cavitation cloud, can be described as undergoing f_0 oscillations with sub-harmonic collapses at f_0/n , where n is an integer number increasing in value as pressure amplitude of the driving is increased. Component bubbles within the cavitation cloud oscillate approximately in phase, however slight differences in the collapse times cause the clouds to have multi-fronted shock waves, as seen in Fig. 2. For these early observations acoustic detection of the cloud was undertaken with an uncharacterised lead zirconate titanate (PZT) element acting as the PCD. A crude filtering protocol was applied to the detected acoustic emissions, which indicated that periodic shock waves mediated the sub-harmonic signal. PZT materials, however are characterised by a high sensitivity over a

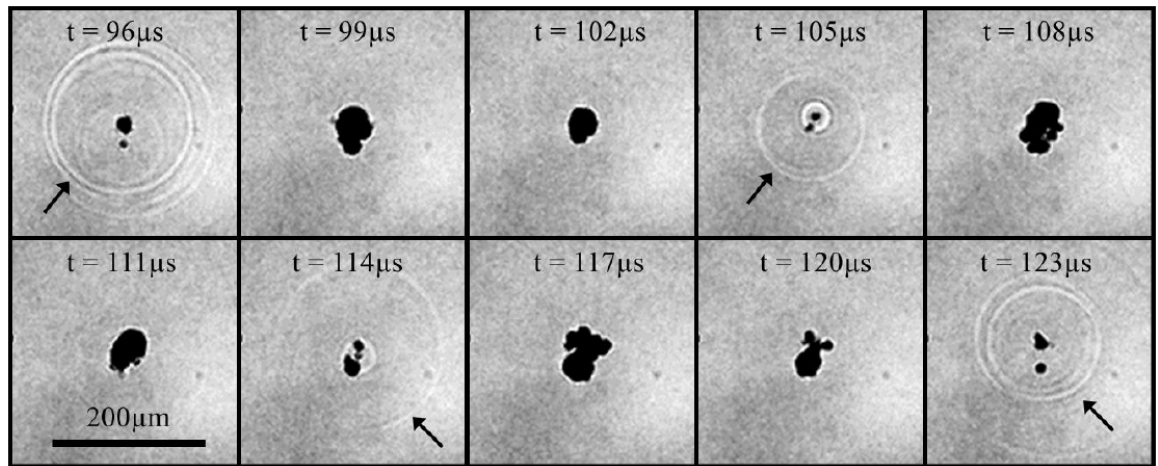


Figure 2: Sample images of periodically collapsing acoustic cavitation cloud, driven by a 254 kHz focused acoustic field, and imaged at 1×10^6 fps. Shock wave emissions, arrowed, from periodic bubble cloud collapses, are at $f_0/2$, half the acoustic driving frequency. Taken from [1]

narrow bandwidth, and are therefore unsuited to resolving multi-fronted periodic shock waves, such as those shown in Fig. 2. Detailed analysis for the role of periodic shock waves in the acoustic cavitation emission signal was therefore not possible at that time². Consequently, the experimental configuration had to be refined to facilitate full reconciliation of acoustic emissions and source bubble dynamics.

In this thesis acoustic detection is primarily undertaken with a commercially available polyvinylidene fluoride (PVdF) needle hydrophone system. Shock waves are particularly susceptible to the distortions introduced by this device, during the conversion from physical pressure signal to detected voltage-data. To study how the needle hydrophone distorts the measurement of shock waves, a single (high energy) laser pulse was focused into the host medium creating a laser-plasma mediated vapour bubble (also known as laser induced cavitation), described in §2.3. This technique has been extensively used to study single-bubble dynamics because the moment and location of bubble formation is predetermined by the laser pulse. It is well known that the process is characterised by the emission of two shock waves, the first generated on the absorption of the laser pulse (during supersonic plasma expansion), and the second from the inertial collapse of the resulting vapour bubble, Fig. 3a. In contrast to the periodic shock waves generated by acoustic cavitation, Fig. 2, the bubble collapse shock wave from a laser-plasma mediated vapour

²Phase synchronisation of multi-bubble systems is experimentally shown to take place in certain acoustic driving conditions. For such bubble behaviour, the measured acoustic emissions are to first approximation representative of constituent bubbles [10–12].

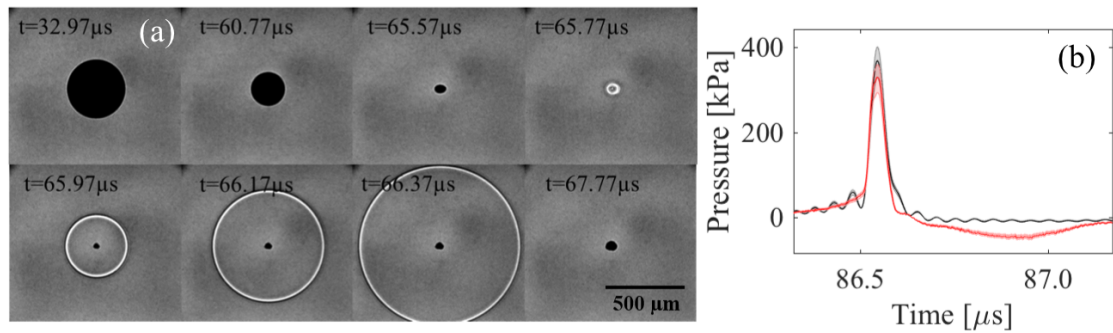


Figure 3: (a) Shadowgraphic high-speed images of laser-plasma mediated bubble collapsing from maximum radius at $32.97\mu\text{s}$ after laser-pulse generation with the emission of a bubble collapse shock wave and rebound oscillations, recorded at 5×10^6 fps. (b) The bubble collapse shock wave time waveform, detected by the needle hydrophone used throughout this thesis, showing both voltage data converted by a single-frequency calibration (red) and restored pressure data (black) over the calibration bandwidth after removal of convolution artefacts. The shading represents the uncertainty.

bubble is highly reproducible in terms of pressure amplitude and spatial-temporal waveform, Fig. 3b. This technique was used to verify hydrophone deconvolution with the broadband complex calibration (magnitude and phase response) obtained from the National Physical Laboratory, 2016, for the hydrophone system. This data was published as below, and features in Chapter 3

Deconvolution of acoustically detected bubble-collapse shock waves.

Ultrasonics, 73, 144-153

Kristoffer Johansen, Jae Hee Song, Keith Johnston, Paul Prentice

A further refinement in the experimental configuration used to generate the observations in Fig. 2 was the use of a focused ultrasound transducer at a higher frequency ($f_0 = 692\text{ kHz}$) and a much higher f-number³. Effectively this generates clouds of smaller bubbles that are more closely packed reducing the likelihood of multi-fronted shock wave emission during cloud collapse. Figure 4a is acoustic data collected from such cavitation activity by the needle hydrophone. It can be seen that single-fronted sub-harmonic shock wave emission was achieved. Deconvolution of the needle hydrophone-system for restoration of the physical-pressure data allowed for full and quantitative analysis of the role of periodic shock waves in the cavitation noise spectrum,

³The f-number is the ratio of the focal length to the diameter of a curved ultrasound transducer.

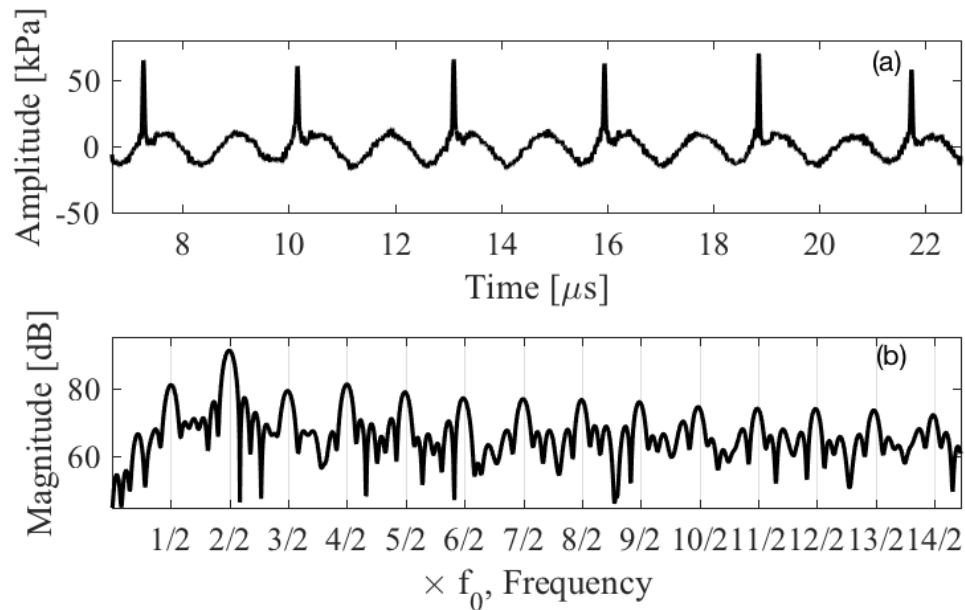


Figure 4: (a) The experimentally detected acoustic emissions from a single cavitation bubble after subtracting a control exposure where no bubble was nucleated. The cavitation bubble was driven by a focused ultrasound field of $f_0 = 692$ kHz in the $f_0/2$ regime with the pressure amplitude $PPA = 1.94 \pm 0.13$ MPa. (b) The corresponding acoustic cavitation noise spectrum from the measurement in (a).

Fig. 4b. This could be considered the main result of this thesis, featuring in Chapter 4, and was published as below.

An analysis of the acoustic cavitation noise spectrum:

The role of periodic shock waves.

The Journal of the Acoustical Society of America, 140(4), 2494-2505

Jae Hee Song, Kristoffer Johansen, Paul Prentice

The experiment was further adapted to facilitate the investigation of spatially configured cavitation detected by a single element hydrophone, or PCD. Specifically, it was found that two cavitation clouds, responding in the $f_0/2$ regime, spaced approximately one wavelength apart (~ 2.3 mm for $f_0 = 692$ kHz) with respect to the hydrophone, significantly suppresses spectral features associated with that regime. Moreover, an analytical expression which describes *spectral windowing* that may be anticipated from any distributed cavitation system, is derived. This data was published as below, and features in Chapter 5

Covert cavitation: Spectral peak suppression in the acoustic emissions from spatially configured nucleations.

The Journal of the Acoustical Society of America, 141(3), EL216-EL221

*Jae Hee Song, **Kristoffer Johansen**, Paul Prentice*

The final body of work presented in this thesis is a PCD designed for detecting low frequency components of periodic shock waves with high sensitivity, hereafter known as the shock wave PCD (swPCD). Design considerations were guided by the observation that most of the power in the bubble collapse shock wave spectrum is contained across the low frequencies, Fig. 5b. A finite element model was used in the selection of matching and backing layers, and the performance was evaluated against a commercially available device (Y-107, Sonic Concepts Inc., USA), Fig. 5.

Furthermore, the importance of evaluating the experimental configuration for reflections, and the spectral windowing effect this can have on the magnitude of features in the spectrum was highlighted. This data was published as below, and features in Chapter 6

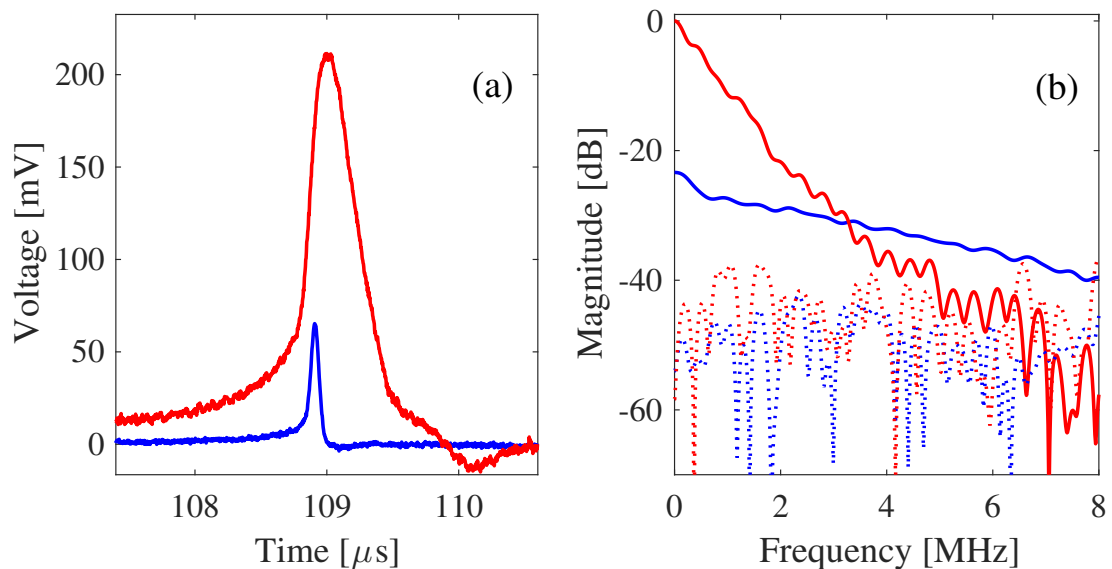


Figure 5: (a) Voltage-data comparing final stage swPCD (solid red) and the commercial device (solid blue) for detection of a bubble collapse shock wave. (b) Spectra of shock waves in (a), where dotted data represents the noise floor for respective detectors measured before the arrival of acoustic emissions. Spectra are normalized to final stage swPCD.

Performance characterisation of a passive cavitation detector optimised for subharmonic periodic shock waves from acoustic cavitation in MHz and sub-MHz ultrasound.

Ultrasonics Sonochemistry, 43, 146-155

Kristoffer Johansen, Jae Hee Song, Paul Prentice

Chapter 1

An introduction to cavitation

Cavitation (*noun Physics*): *ˌkavəˈtɑːʃən*

"The formation of an empty space within a solid object or body; the formation of bubbles in a liquid, typically by the movement of a propeller through it."

— Oxford English Dictionary

1.1 The emergence of cavitation as a research topic

The first mention of cavitation in academia was by Leonhard Euler in 1754, in his work on the theory of turbines [13]. However, the industrial revolution marked a requirement for increased understanding of cavitation in both industry and academia. For example the practical implications of cavitation manifested in the construction and testing of the British torpedo boat destroyer *HMS Daring*. This vessel was designed to achieve a maximum speed of 27 knots, but could only reach 24 knots. It was discovered during the trials that the propeller shaft was rotating more rapidly than expected from normal power absorption relationships. The engineer, Barnaby, proposed that as the surrounding liquid has a specific tensile strength, the propeller inflow may breakdown due to the medium rupturing under the tension imposed by the rotating propeller. Shortly afterwards, Sir Charles Parsons encountered similar effects during the trials of his experimental steam turbine ship *Turbina*. This led him to develop the forerunner to cavitation tunnels in 1895, for which great advances in understanding of hydrodynamic cavitation ¹ are owed. Typically, modern

¹Hydrodynamic cavitation refers to bubbles generated due to specific flow conditions and changes in ambient pressure. It is commonly encountered around in valves, propellers and impellers. Hydrodynamic bubbles invariably cause a reduction in efficiency, and ultimately erosion damage to such systems.

cavitation tunnels are depressurised to allow the observation of cavitation flows at speeds down to 1500 RPM, instead of normal operation around 12000 RPM. The lower rotation speed makes it easier to perform detailed photographic observation of propeller cavitation, which was first achieved in 1911. This meant that from early 20th century photographic observations of cavitation were possible, however, a theoretical description of bubble dynamics was lacking.

An equation describing the temporal dynamics of a bubble was first published by Lord Rayleigh in 1917 [14]. The equation describes how the surrounding liquid does work on a single spherical bubble of compressible gas during compression, and vice versa during expansion. Furthermore, from the equation published by Rayleigh, the collapse time, T_c , for a freely collapsing bubble, was derived. This can be defined as the time it takes to collapse from maximum radius, R_{\max} , to minimum radius. The collapse time is expressed the following way [15]:

$$T_c \approx 0.915R_{\max}(\rho_0/p_0)^{1/2}, \quad (1.1)$$

where ρ_0 is the density of the host medium, and p_0 is the ambient pressure. Experimental verification has been realised for multiple bubble sizes, and it is remarkably accurate considering the relatively simple physical considerations that were made [5].

Noltingk *et al.* notes in 1950 that practical applications of ultrasonic techniques depending on the production of cavitation are increasing [16]. However, at that time "*no thorough examination has yet been made of what exactly occurs during ultrasonically induced cavitation.*" The theory published by Lord Rayleigh was primarily concerned with the freely collapsing bubble, for which there is no change in the surrounding pressure, making it inappropriate to describe acoustic cavitation. However, the theory was expanded on by Plesset in 1949 to include an acoustical driving term, forming the basis for the commonly known Rayleigh-Plesset equation [17]. This equation was used by Plesset to explain cavitation observations ² undertaken with high-speed imaging in 1948 by Knapp and Hollander [18].

In §3.2.6 Rayleigh-Plesset-like equations, and particularly the Gilmore equation, which is used to simulate the radial dynamics of a collapsing bubble [19], are explored. Furthermore,

²Although computational facilities at the time of publication and the following decades were limited or non-existent, so researchers were restricted to quasi-linear analytical solutions of the equation.

in §3.4 issues related to modelling of a collapsing cavitation bubble, such as determining the equilibrium radius, the assumption of an incompressible core during energetic collapses, and accounting for the compressibility of the host medium, are discussed.

1.2 The resonant acoustic bubble

A paper authored by Marcel Minnaert, entitled "*On musical air-bubbles and the sounds of running water*" addressed the sound produced by oscillating bubbles [20]. From the theoretical considerations that are made, the first approximation to the *resonance frequency*, f_r ³, of a gas bubble is presented. The resonance frequency is found to be strongly dependent on the equilibrium radius R_0 , in combination with the ambient pressure, p_0 and material properties such as, ambient density of the host medium, ρ_0 , and the polytropic exponent of the gas within the bubble, γ . For large bubbles where surface tension, σ , can be neglected, the resonance frequency, f_r , can be approximated by:

$$f_r \approx 3/R_0 \quad (1.2)$$

Thus, if a bubble is brought into small amplitude oscillations compared to R_0 , it will ring back down to its equilibrium radius, at the resonance frequency dictated by its size. In the reciprocal sense, *Acoustic Cavitation* can generally be defined as bubbles generated and driven by an acoustic field, for which the bubbles produced are of a size governed by Eq. (1.2), determined by frequency of insonation. However, for frequencies of approximately a few hundred kHz, such as used in this thesis, the bubbles spawned by the acoustic field are of sizes, $R_0 < 10 \mu\text{m}$, for which surface tension becomes relevant. This increases the resonance frequency, and renders the approximation in Eq. (1.2) insufficient. In this case, the full Minnaert resonance frequency, f_M , should be used, as presented below [21]⁴:

³The resonance frequency of the bubble f_r is distinguished from the fundamental driving frequency f_0 of the acoustic driving.

⁴This is not the expression that Minnaert derived in his historic paper [20], as he did not consider the effects of surface tension, however, it is convention in the literature to define the resonance frequency for bubbles without the dampening effects of a stabilising shell as the Minnaert resonance frequency.

$$f_M = \frac{1}{2\pi} \sqrt{\frac{1}{\rho_0 R_0^2} \left[3\gamma p_0 + \frac{2(3\gamma - 1)\sigma}{R_0} \right]} \quad (1.3)$$

In §1.1 the first photographic imaging of cavitation is described. However, to do any meaningful observation using this technique, an objective lens is necessary to form an image which resolves the bubble activity. As the bubbles generated by the acoustic fields in this thesis are relatively small, a strong objective lens is required. However, strong objective lenses are characterised by (i) a small field of view due to the increased magnification, which makes it likely to miss stochastically generated cavitation event produced by the acoustic field. (ii) Reduced depth of field, which has similar effect as (i). (iii) Short working distance, which requires the lens to be placed close to the cavitation activity. This disturbs the acoustic field, which is a challenge as development of applications of cavitation are often concerned with understanding how bubbles respond to particular ultrasound exposure conditions. (iv) With enhanced magnification, the requirement for high intensity illumination increases, which demands that a light source is also placed close to the location of cavitation activity, further disturbing the acoustic field. Moreover, acoustic measurements of the bubble activity are also influenced as a consequence of the microscope objective lens and light source, because they limit (or prevent) the freedom for ideal positioning of a hydrophone relative to the desired location of the bubble activity. This is why the spatial and temporal precision afforded by the laser nucleation technique described in §2.3, has been pivotal for achieving unprecedented acoustic cavitation observations.

1.3 The collapsing bubble and shock waves

A bubble which has expanded to a size much larger than the equilibrium radius is associated with significant potential energy. This potential energy is converted to kinetic energy when the bubble starts to contract, with bubble wall speeds well in excess of 100 ms^{-1} as the collapse is approached [22]. Indeed, the deflating bubble may be characterised as an increasingly non-linear system as it reaches minimum radius. Moreover, during violent collapses extreme conditions with temperatures greater than 10 000 K and pressures in excess of 100's of atmospheres have been reported [23, 24], together with the remarkable phenomena of sonoluminescence; emission

of pico-second flashes of light during the repeated collapses of an acoustically driven bubble [25]. The conditions associated with collapsing bubbles underpin many of the applications that utilise acoustic cavitation, notably sonochemistry [26] and acoustic cleaning [27].

It was even speculated that the high energy densities in a collapsing bubble might induce nuclear fusion. In 1982, Flynn was issued a patent for a "*Method of generating energy by acoustically induced cavitation fusion and reactor therefor*" [28], and since then multiple papers have been published that treat cavitation induced fusion as plausible [29, 30]. For example, Taleyarkhan *et al.* [29] devised a setup with a neutron source radiating into cavitation activity, to initiate deuterium-deuterium fusion. Evidence for cavitation induced fusion was supported by measuring simultaneous sonoluminescence and increased neutron emission near 2.5 MeV, which is the energy that would be expected for deuterium-deuterium fusion. Cavitation induced fusion remains a topic of scientific inquiry.

Furthermore, the collapse of a bubble is also known to be synonymous with the emission of a bubble collapse shock wave, an example of which is captured shadowgraphically in Fig. 3a and acoustically Fig. 3b. The bubble collapse shock wave is typically only supersonic for a brief and limited time after its generation before it retards down to the speed of sound for the host medium. This process is associated with significant loss of energy from the bubble collapse shock wave [22]. The shock wave can be characterised as a broadband acoustic impulse, described by a short rise-time and full width half maximum (FWHM), Fig. 3b. (These are technically defined in §3.2.4.) This is a notably different bubble emission to the single-frequency note described by Minnaert for a low amplitude bubble oscillation [20].

In the next section, the acoustic emissions and associated spectral features in the cavitation noise spectrum from bubbles driven at increasingly higher acoustic pressures, are detailed. Moreover, it may be expected that bubble collapse shock waves should have a major influence on the collection and interpretation of measured acoustic emissions, discussed in §1.4.4.

1.4 The acoustic cavitation emission signal and noise spectrum

Figure 1 of *Overview of Thesis* is a generalised representation of the use of a single element hydrophone, or PCD, to collect the signal emitted by acoustic cavitation. Cavitation literature is dominated by reports investigating a given cavitation-mediated effect, whilst simultaneously collecting the signal emitted [31, 32]. Typically, such reports will subsequently compare the degree to which the effect was correlated to the emission signal, nominally for the purpose of monitoring the process [31, 33].

This is particularly the case for the development of medical therapy applications as discussed in §1.5.1, whereby some degree of cavitation-induced ‘damage’ is required to deliver drugs to biological cells (*in-vitro*) [34], or tissue (*in-vivo*) [33], but the degree of damage should be limited to avoid long term adverse effects, such as extensive cell lysis [35], or inflammation following blood-brain barrier disruption [36, 37].

Acoustic cavitation emission data is seldom presented in the time-domain, however one rare example from an early report on sub-harmonic emissions [38], is provided in Fig. 1.1a⁵. This is likely because the emission signal will be collected over the duration of the exposure, or at least a significant part of it, which will be many cycles of driving (in the case of Fig. 1.1a

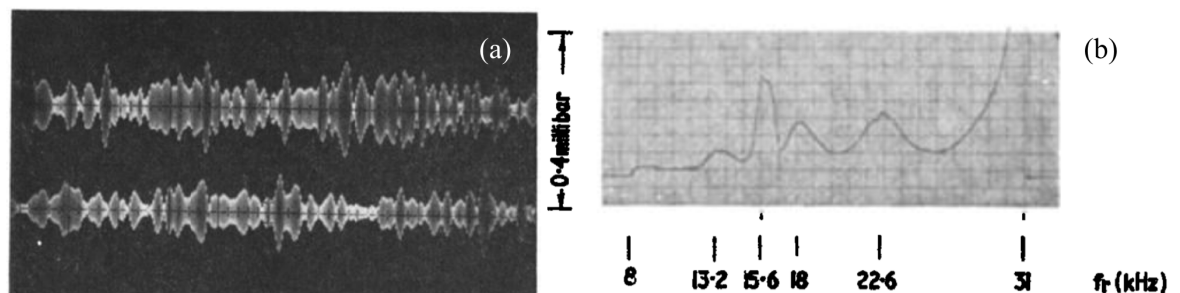


Figure 1.1: (a) Picture of oscilloscope screen during collection of acoustic emission from sub-harmonic ($f_0/2$) cavitation activity driven at $f_0 = 31$ kHz. Note that there is no time axis on the oscilloscope, however the collected emissions signal is equal to 300 cycles of driving. (b) Frequency spectrum of acoustic emissions up to the fundamental driving frequency, $f_0 = 31$ kHz, with a spectral features at the first sub-harmonic. Taken from [38]

⁵Another example from recent cavitation literature which features time-domain representations of acoustic emissions from cavitating liquids is found in [39].

300 cycles of ultrasound driving is displayed), through which little insight is gained about the source bubble dynamics or emission signal. Moreover, cavitation in ‘real-world’ applications will typically involve many bubbles and bubble clouds, sometimes geometrically distributed throughout a significant volume of the acoustic field. Presenting such a signal in the time-domain would therefore be both unwieldy and uninformative, as it is difficult to distinguish how the detected collective behaviour of multiple bubbles is representing what is expected from an individual bubble. In contrast, the cavitation noise spectrum, generated via application of a Fourier-transform, provides a convenient and concise representation of the emission signal, in the frequency domain, in terms of both the presence and pressure amplitude of different frequency components. Fig. 1.1b, is the spectrum of the time-domain data of Fig. 1.1a, which clearly reveals the $f_0/2$ sub-harmonic at 15.6 kHz ($f_0 = 31$ kHz), at an amplitude (magnitude) far below the f_0 spectral feature. The overwhelming difference in amplitude renders it challenging to identify any $f_0/2$ sub-harmonic signal in the time-domain data, that the spectrum reveals clearly, Fig. 1.1b.

The acoustic emission data shown in Fig. 1.1 is significantly different from that displayed in Fig. 4. This is expected as these two experiments are not directly comparable. In Fig. 1.1 the collected acoustic emissions are generated by a cavitation field which is spontaneously spawned by the acoustic exposure, for the purpose of investigating the cavitation threshold and spectral features below the driving frequency. In contrast, the data shown in Fig. 4 is from a single cavitation bubble, which was nucleated using a laser-nucleation technique that permitted the bubble to be placed in-line with a broadband calibrated needle hydrophone, for the purpose of reconciling detected acoustic emissions to observed source bubble dynamics.

In §1.2 a weakly oscillating bubble emitting a single note was discussed, and in §1.3 high energy inertial collapse with the emission of a broadband bubble collapse shock wave, was introduced. These two emissions would be represented as a single peak at f_0 and a broadband contribution to the cavitation noise spectrum, respectively. Moreover, in acoustically driven cavitation, bubble collapse shock waves are generally held to be responsible for raising the ‘noise floor’, or the broadband noise in the detected acoustic emissions [41], as discussed in §1.4.4. The typical cavitation noise spectrum, however, is also rich in spectral features such as those seen in Fig. 4.12b and Fig. 1.2, many more than can be accounted for by single frequency emissions

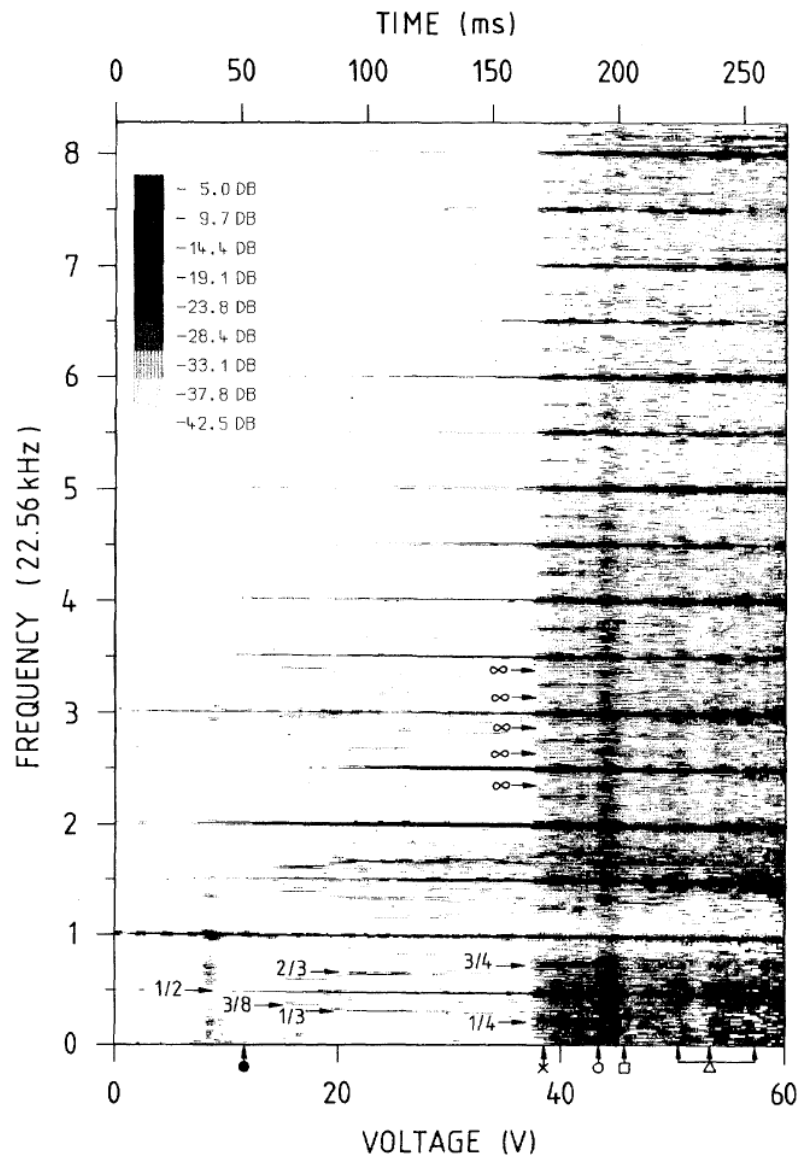


Figure 1.2: Spectrogram of acoustic emissions from sound irradiated water at $f_0 = 22.9$ kHz as driving voltage is increased. Taken from [40].

associated with low amplitude driving, and broadband noise associated with high amplitude driving, as described below.

This section outlines the current empirical⁶ understanding of the acoustic cavitation noise spectrum, in terms of the relative pressure amplitude of the acoustic driving based on the seminal work for the topic; W. Lauterborn and E. Cramer, "Subharmonic Route to Chaos Observed in Acoustics", *Phys. Rev. Lett.* 47 1445, 1981. The experiment consists of a cylinder-type

⁶'empirical' in the sense that the representative cavitation noise spectra of Fig. 1.2 are well known to result from cavitation driven by an acoustic exposure of the relative amplitudes indicated. The bubble-based origin of any frequency component, however, has hitherto been largely based on simulation and speculation. Specific influential papers on this topic are reviewed in some detail in §1.4.4.

transducer driven at $f_0 = 22.56$ kHz, generating a line-focus along the geometrical axis. Acoustic detection was undertaken with an in-house constructed microphone, based on a ‘thin disk’ of PZT-4, presumably located at an open end of the transducer. The collected acoustic emissions are displayed in Fig. 1.2 which contains ~ 1000 spectra collected over increments as the drive voltage is increased from 0 - 60 volts, during a total exposure time of 250 ms. This temporal representation of multiple consecutive spectra is known as a spectrogram. Such a graphical portrayal is highly beneficial when assessing the evolution of spectral features as a function of some control parameter, which in this case is the driving amplitude.

At low amplitude driving (< 5 V), spectral features at f_0 , $2f_0$ and $3f_0$ are apparent. It is not clear if the non-linearity of the acoustic field was assessed, at representative voltage amplitudes. In any case, harmonic emissions at nf_0 from bubbles driven at low amplitude, are generally accepted as an indicator for stable cavitation (see §1.4.2). The next spectral feature to manifest, on increasing the driving voltage to an amplitude of ~ 12 V is the first-order sub-harmonic at $f_0/2$, simultaneously with its over-harmonics at $nf_0/2$ (above f_0 , certainly $3f_0/2$ and $7f_0/2$ are visible). This was attributed to a period-doubling bifurcation phenomenon, a property which multiple other non-linear dynamic systems exhibit⁷. The next bifurcation, to $nf_0/4$, is not observed until ~ 38 V, and is accompanied by a marked increase in broadband noise. At intervening driving voltages other (non-bifurcation) sub-harmonic emissions are detected, such as $f_0/3$ and $2f_0/3$ and their over-harmonics, and higher order-harmonics of $f_0/8$, and over-harmonics. Acoustic chaos (or turbulence), which is typically associated with high-levels of broadband noise, was identified to occur between 43 - 46 V (arrowed with ∞), with reverse bifurcations, whereby the system returned to $f_0/2$ emission with reduced broadband noise, at ~ 52 V.

Note, papers that explore acoustic cavitation when it emerged as a research topic, typically have employed low f_0 driving (~ 20 kHz), though the general trend is thought to hold, independently of f_0 including for relatively high frequency therapeutic applications (*i.e.* nf_0 harmonics at lower driving amplitudes, $nf_0/2$ emerging for intermediate, higher order sub-harmonics and broadband noise at higher amplitudes). The relatively low frequencies in the preliminary studies,

⁷The discovery of universal properties in period-doubling bifurcations could be confirmed for the Lorenz model and a five-variable model of the Navier-Stokes equation. The search for additional universal features of non-linear dynamical systems is on going [40].

may be related to the fact that the *cavitation threshold*, which depends on the overall thermodynamic state of the host medium, is at a lower pressure amplitude, as discussed by Apfel and Holland [42]. Thus the low frequencies used allow for ultrasound transducers which are driven by less powerful amplifiers to generate sufficient pressures for cavitation to occur. Optical observations are also made easier, as the size of the bubbles increases with lower frequency, as discussed in §1.2.

In the following section, the different spectral features used in reported cavitation measurements, are discussed. This is achieved by reviewing a collection of papers investigating a wide selection of cavitation applications, and fundamental cavitation research. Generally, the literature can be summarised as categorising detected emissions in terms of four spectral features, detailed below.

1.4.1 Reporting protocols and detectors for cavitation measurements

Reporting of cavitation is one of the multiple complications which are highlighted in the description of the basic cavitation experiment discussed in Fig. 1. The protocols used to represent acoustic measurements of recorded cavitation activity are many, with both single or some combination of spectral features, being taken as representative of the source bubble dynamics. The hydrophone, or PCD that is used, typically exploit the non-linearity in source bubble dynamics, such that measurements are undertaken at spectral features exclusive to cavitation, such as sub-harmonics, ultra-harmonics (defined below) and broadband noise. However, some choose to measure multiples of the fundamental frequency of the acoustic driving, which may contain non-linear components due to propagating-effect [41, 43]. Following below, a selection of literature surveyed, is categorised in terms of how they are using the four spectral features for detection of cavitation;

- **Sub-harmonics** (f_0/m , where m is an integer value) [4, 9, 40, 41, 43–51],
- **Ultra-harmonics** (nf_0/m , where n is also an integer value, $\neq m$) [4, 31, 32, 40, 44–48, 51–54],
- **Over-harmonics** (nf_0) [4, 40, 41, 43–56]

- **Broadband noise**, sampled from between spectral peaks [4, 32, 40, 44–48, 50, 51, 53, 55, 57–59].

Another metric used for detection, instead of measuring single or combinations of individual features, is the *cavitation index* which quantifies the arithmetic mean power over a certain bandwidth of the spectrum, after the electrical noise has been subtracted [45, 60].

The primary performance characteristic used to select a hydrophone, or PCD is the sensitivity to the target monitored spectral feature(s), described above. In this thesis, the majority of acoustic emissions are detected by a broadband PVdF needle hydrophone (1.0 mm diameter, 28 μm thick active element, supplied with pre-amplifier, Precision Acoustics Ltd., UK), calibrated for both magnitude and phase over a bandwidth of 125 kHz–20 MHz (National Physical Laboratory, 2016). This hydrophone is used to detect broadband bubble collapse shock waves, both from laser-plasma mediated vapour bubbles in Chapter 3 and acoustic cavitation in Chapter 4 and 5. PZT is also used as the active material in many hydrophones and PCD designs, potentially providing higher sensitivity over a narrow bandwidth compared to PVdF. The superior bandwidth of PVdF made it the preferred choice for investigating the role of broadband bubble collapse shock waves in the acoustic cavitation noise spectrum. Multiple papers detecting cavitation are reviewed in more detail throughout the remaining sections of this chapter, in the case that PCD characteristics have been stated, they are included, such as information of the active element, sensitivity, bandwidth and geometry. This is to demonstrate that detection of cavitation is undertaken with multiple types of detector designs, and that this will directly affect the measurements taken [4, 31, 33].

Wu *et al.* published a paper titled "*Transcranial cavitation detection in primates during blood-brain barrier opening - a performance assessment study*", which detected cavitation using multiple spectral features [53]. In this paper microbubbles⁸ were driven by a focused ultrasound field of fundamental frequency $f_0 = 500$ kHz and acoustic emissions were detected by a commercially available focused PCD (Y-107, Sonic Concepts Inc., USA)⁹, which uses

⁸Microbubble suspensions were originally developed as a contrast agent for diagnostic ultrasound imaging. A microbubble typically consists of a 1-2 μm low diffusivity gas core, and a biocompatible stabilising shell material. Commercially available and FDA-approved (SonoVue[®], Bracco; Sonazoid[®], GE Healthcare, for example), contrast agents are reconstituted and injected in advance, or during, an ultrasound examination.

⁹The is the same PCD as the final stage swPCD is compared against, using both laser-plasma mediated vapour bubbles and acoustic cavitation in Chapter 6.

PVdF as the active material. To monitor the acoustic emissions from the microbubble activity, the paper defines the *stable cavitation dose* (SCD) as a metric to represent the extent of stable cavitation, which is defined "as the cumulative of harmonic or ultraharmonic emission", Fig 1.3a,b. Furthermore, the *inertial cavitation dose* (ICD) is introduced as a metric to represent the extent of inertial cavitation, which is defined "as the cumulative broadband acoustic emission", Fig 1.3c. The paper further defines the cavitation signal to noise ratio (SNR) as the cavitation dose (based on SCD and ICD) pre- and post-microbubble administration, for which it is claimed that safe opening of the blood-brain barrier can be achieved by surpassing the detection limit by 1 dB. Undoubtedly, the PCD design becomes relevant for safe applications of cavitation if the threshold for blood-brain barrier opening only needs to be exceeded by 1 dB. In Chapter 6 design and performance characterisation for an in-house built PCD is presented. The chapter features a comparison between the in-house built PCD and the commercial PCD used in the study described above.

Cavitation has generally been classified in two types: *transient* or *stable* cavitation. Today, the more specific terminology is typically used; "non-inertial" and "inertial", and these two regimes are described in §1.4.2 below.

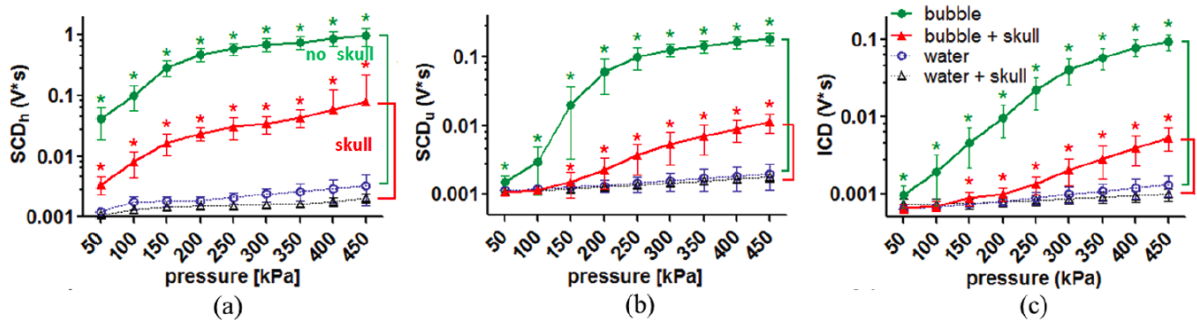


Figure 1.3: *In vitro* acoustic emissions quantified for the macaque skull experiments using 100-cycle pulses of fundamental frequency $f_0 = 500$ kHz; (a) Stable cavitation dose defined as the cumulative of over-harmonic emissions (b) Stable cavitation dose defined as the cumulative of ultra-harmonic emissions (c) Inertial cavitation dose defined as the cumulative broadband acoustic emission. Taken from [53].

1.4.2 Historical context for classification of cavitation as stable or transient

The classification of cavitation into two separate regimes traces back to the first experimental observations made of acoustic cavitation [61, 62], as seen in Fig. 1.4a. Willard describes in his paper "*Ultrasonically Induced Cavitation in Water: A Step-by-Step Process*" [62], how feather-shaped cavitation is generated by bursts of ultrasound, which abruptly expands to a catastrophic plume portion. It was believed at the time that the plume was formed by a myriad of micro-cavities, too small and close to be individually observed. This was identified as the two first steps of the cavitation process, identically produced in both degassed and aerated water. The first two steps took place over a few milliseconds, however for aerated water a third bubble step was identified. "*In aerated water, non-collapsing gas bubbles are generated by and concurrent with, the catastrophic step. These bubbles remain after collapse of the burst, to be blown down stream by the sonically induced liquid streaming.*" [62]

This led Flynn in "*Physics of acoustic cavitation in liquids*" [63]¹⁰ to introduce the terminol-

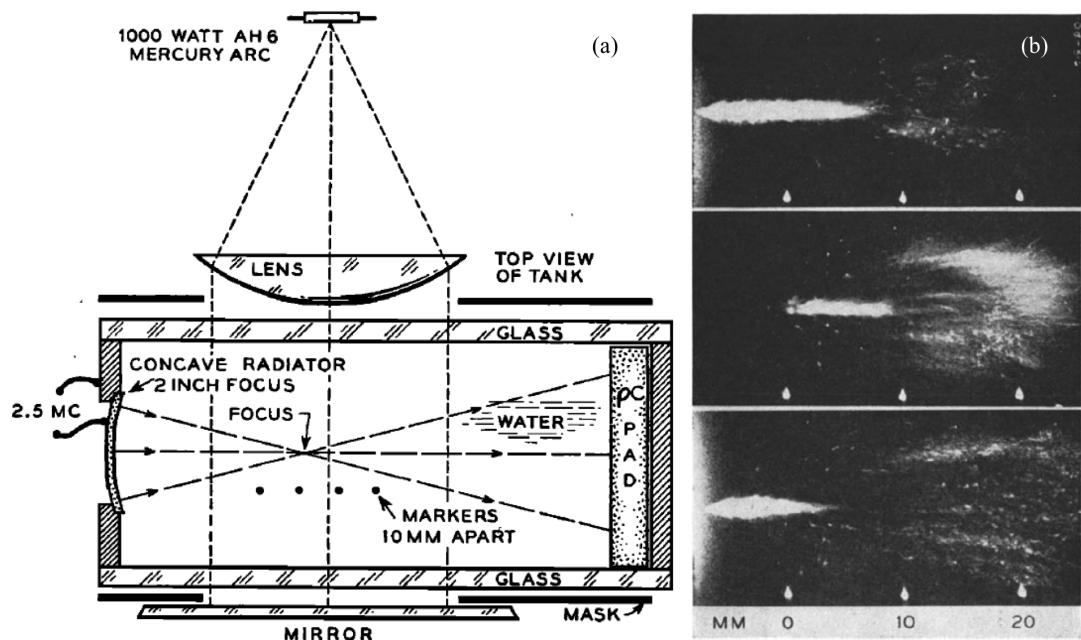


Figure 1.4: (a) Schematic of experimental setup used to make some of the first acoustic cavitation measurements. Observations are made from above. (b) Three successive frames of HIFU-field interacting with aerated water. Taken from [62].

¹⁰This publication has 631 citations, and several of the citing papers are iconic to the field, 9th of September 2018.

ogy in order to describe these observations (as discussed by [64]). Transient was attributed to vapour or gas bubbles that expanded to large sizes during the negative part of the pressure cycle, after which they began to collapse. Because of the large radius attained during the expansion, their collapse was very rapid and violent, often resulting in the fragmentation of bubbles. Moreover, it is stated that, a bubble can be represented by a transient cavity "*if, on contraction from some maximum size, its initial motion approximates that of a Rayleigh cavity...*", so similar to a cavity collapsing freely due to the inertia of the surrounding liquid, as discussed by Rayleigh in 1917 and in §1.1. The source bubble dynamics is characterised as stable cavitation by Flynn: "*if it oscillates nonlinearly about its equilibrium radius.*" Later Flynn refined his definition using the expansion ratio, R_{\max}/R_0 , where R_{\max} is the maximum radius attained during a given acoustic cycle and R_0 is the equilibrium radius [64,65]. A threshold was defined, and bubbles pulsating with R_{\max}/R_0 above this threshold normally developed into transient cavities, whereas bubbles below this threshold developed into stable cavities. In the case where stable cavitation is reached, the bubble may continue to grow due to rectified diffusion, and if the threshold for transient cavitation is not surpassed during the ultrasound exposure, the bubble can separate under gravity. This process is known as de-gassing, a well known effect of stable cavitation, which is being utilised in several industrial applications, such as de-gassing metal melts, optical glass, resins and photographic emulsions [39,66–68].

Definitions of the above type are useful in an academic discussion, however, in ‘real world’ applications it is more desirable to be able to make a statement about the *effects* expected from some cavitation activity, such as if the collapses are violent enough to produce extreme conditions (e.g. attain sufficiently high temperature [69], generate free radicals [70], radiate strong bubble collapse shock waves [22], etc.) or not. This challenge is recognized in recently published literature [31,33,71,72].

However, as research into cavitation has advanced, there is an emerging realisation that cavitation activity often exhibits both stable and inertial characteristics, variously referred to as stable-inertial or repetitive transient cavitation, as discussed in the section below [71,73,74].

1.4.3 Stable-inertial cavitation

Leighton discussed the different regimes of cavitation throughout multiple chapters in *"The Acoustic Bubble"*, for which he argues: *"the terms 'stable' and 'transient' are perhaps unfortunate, since they suggest a temporal differentiation, when in fact they are most useful in describing the energy and effects of the collapse."* [71] This is notably different to an enduring tendency to classify the cavitation activity itself, as stable or inertial, which persists even through much of modern cavitation literature.

Ashokkumar is another researcher, who has realised that the binary classification of cavitation is not satisfactory. In the paper titled *"The characterization of acoustic cavitation bubbles - an overview"* [74], this issue is explored, for which the discussion is largely based on what Leighton published in *"The Acoustic Bubble"*. Ashokkumar emphasises the unfortunate misunderstanding caused by the binary classification suggested by Flynn, when describing a single bubble that is periodically emitting light via sonoluminescence in a "stable" fashion, whilst at the same time the acceleration of the bubble wall is dominated by the inertia of the surrounding liquid during the collapse, which is distinctive for inertial cavitation.

Leighton proposed an alternative system of classification based on high energy and low energy cavitation, which could be a meaningful step towards a better understanding, as displayed in Fig. 1.5. For example, high-energy collapse (transient cavitation) is divided into 'Fragmentary transient

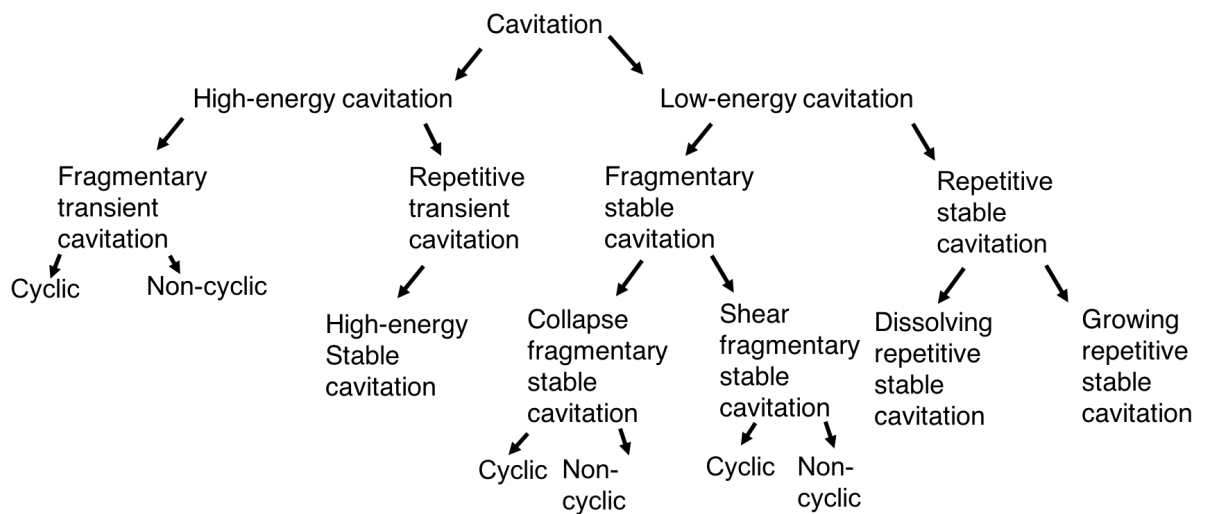


Figure 1.5: Classes of high and low energy cavitation regimes. Adopted and modified from [71].

cavitation’ and ‘Repetitive transient cavitation’, which may also be described as ‘High-energy stable cavitation’.

‘Low-energy cavitation’ is also branched into multiple subcategories with distinguishing features, such as ‘Fragmentary stable cavitation’ and ‘Repetitive stable cavitation’, with their respective subcategories, Fig. 1.5.

The discussion of stable-inertial cavitation is not limited to unseeded cavitation generated stochastically by the acoustic field. For example, Church presented an analysis suggesting that for clinically relevant pressures and diagnostic frequencies, coated microbubbles can undergo *stable-inertial* cavitation [73]. The discussion presented in the paper is a reinterpretation of microbubble observations presented by Shi *et al.* [75], for which a single bubble (Sonazoid[®]) drifted into the optical field of view, and was exposed to a 2.5 MHz tone burst of 2-16 cycles. The bubble behaviour was monitored by a 25 MHz pulse-echo system. In Fig.1.6 the Gilmore equation is solved for the radial dynamics (stapled line) of a microbubble with equilibrium radius of 1.5 μm , driven by 4-cycle 2.5 MHz acoustic field of 0.5 MPa, which demonstrates

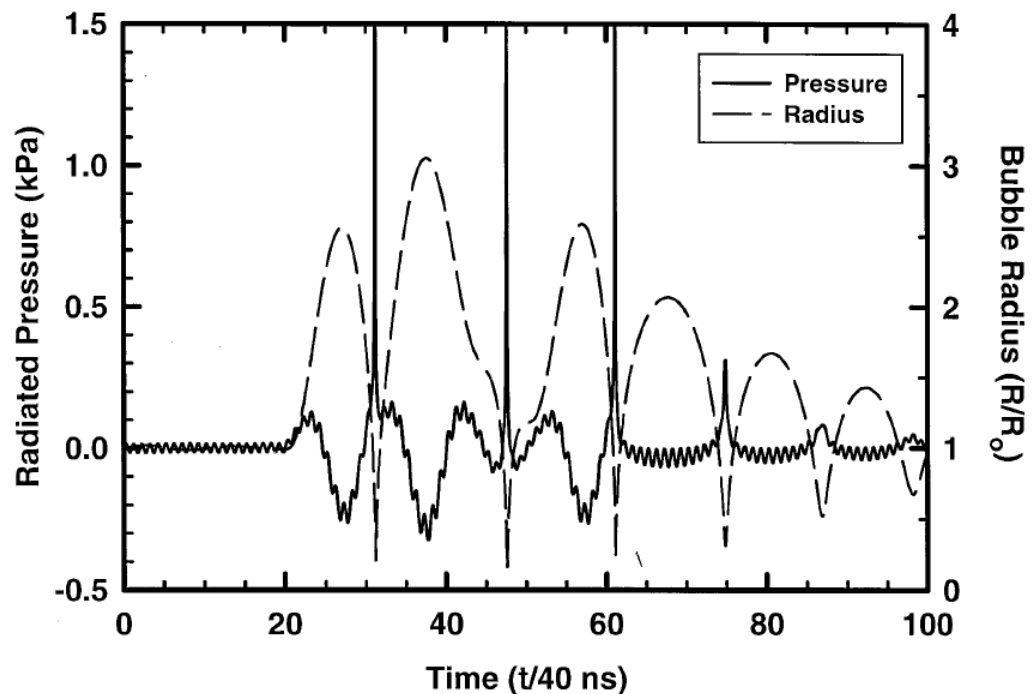


Figure 1.6: Computed radial dynamics and scattered pressure at 1 cm from a microbubble of $R_0 = 1.5 \mu\text{m}$ driven by a 4-cycle-long 2.5 MHz acoustic field of pressure amplitude 0.5 MPa, and probed by a 128-cycle-long 0.1 MPa 25 MHz tone burst. The time is normalised by 40 ns such that the x-axis is defined from 0 - 100 in normalised time. Taken from [73].

behaviour where the maximum radius during expansion exceeds twice the equilibrium radius. Indeed, achieving an expansion ratio above two, which was suggested by Flynn as an indicator for a subsequent inertially dominated collapse over a wide range of parameters [65]. Also shown is the acoustic emissions (solid line), which are computed by a method described by Akulichev [76]¹¹. The computed emissions are characterised by pressure spikes, which are typically associated with inertial cavitation. However, in the experimental data recorded by Shi *et al.*, which have comparable parameters to the simulation in Fig. 1.6, there is an absence of pressure spikes. Church suggests that this is likely due the bandpass filter imposed by the probe used to detect the cavitation activity, which would replace such pressure spikes by short duration, high amplitude acoustic signals at the resonance frequency of the probe. This clearly demonstrates that the characteristics of the detector used can have major influence on the interpretation of the measurement. Issues related to convolution artefacts arising from the detector characteristics and how they are effecting the measurements, are discussed in Chapter 3.

Based on the previous observation of cavitation presented in *Overview of Thesis*, Fig. 2, the author proposes that the onset of stable-inertial cavitation is characterised by: The non-linear acoustic emissions (sub-harmonics, ultra-harmonics and over-harmonics) are shock wave mediated, and depending on the variation in the periodicity to consecutive shock waves, spectral features exclusive to the cavitation regime are more or less well defined. Moreover, a higher variation in the periodicity to the periodic shock waves is associated with less stable cavitation activity, and therefore a higher level of broadband noise. This is discussed in Chapter 4.

Below two papers that detect cavitation, and classify the measurements in terms of spectral features in the acoustic emission, are reviewed. Both papers acknowledge that cavitation is neither exclusively stable nor inertial, in most cases.

Cornu *et al.* attempts to classify cavitation regimes from an unseeded bubble cloud during pulsed sonication [72]. The experimental setup consisted of a focused ultrasound transducer operating at $f_0 = 550$ kHz and a ceramic-based needle hydrophone (Onda, HNC C1500) for collection of acoustic emissions. The cavitation activity was driven by 50 ms pulses of ultrasound

¹¹The approximation relies on the method of characteristics, which is also used to derive the Gilmore equation [19].

at a predetermined pressure amplitude, followed by 250 μs of no sound, repeating over a duration of 60 seconds. For each sonication interval the cavitation activity is classified the following way; stable cavitation is connected to the sub-harmonic emission, and inertial cavitation is linked to the broadband noise by taking the arithmetic mean of all signal components within a bandwidth of 0.1 - 5 MHz. To understand how stable cavitation and inertial cavitation emissions coexist, and if the sub-harmonic emission is primarily linked to intense bubble collapse activity, the stable cavitation/inertial cavitation phase space was investigated, Fig. 1.7. The dashed red line represents the threshold for which the sub-harmonic emission emerges from the broadband noise. For an acoustic pressure of 6 bars, the classification applied puts all events into two zones. The first zone is identified by the low level of broadband noise, while the second represents cavitation activity where both acoustic emission from stable and inertial cavitation coexist at a significant

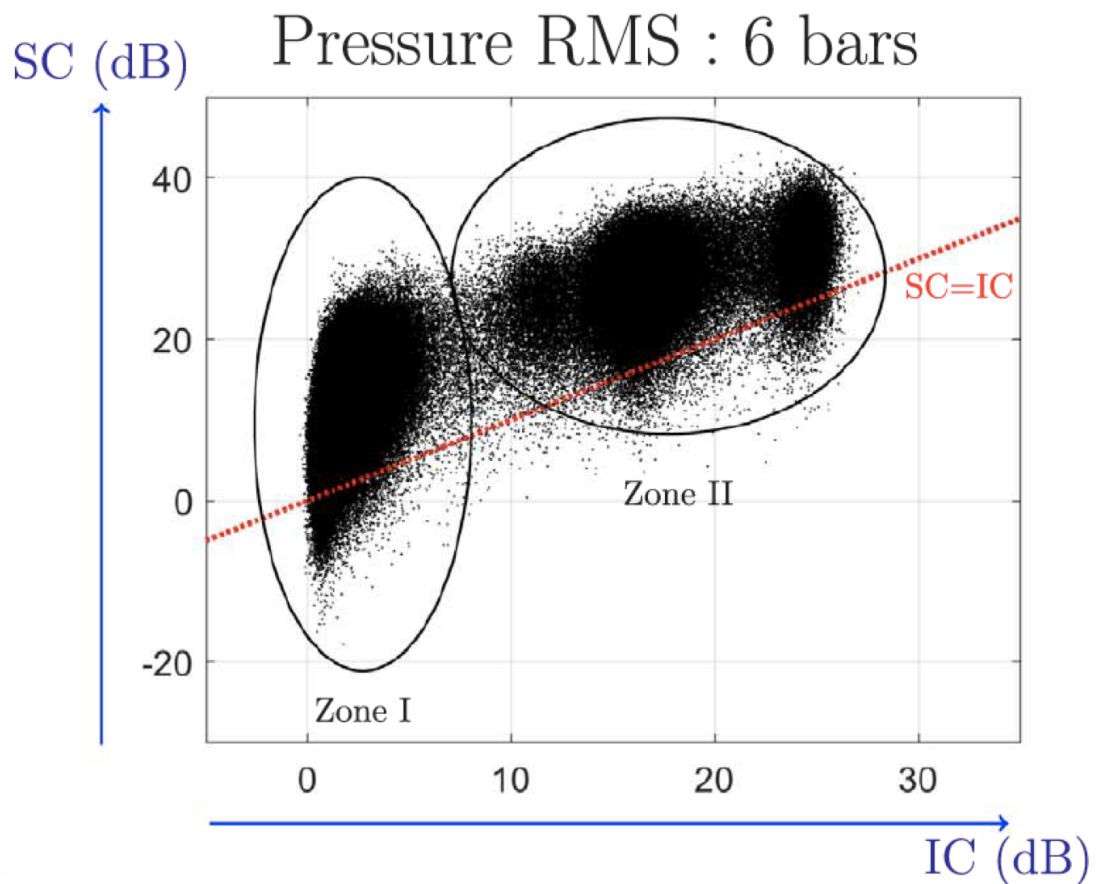


Figure 1.7: Stable cavitation (SC) index versus inertial cavitation (IC) index for the acoustic pressures of 6 bars. The dashed line $SC=IC$ shows the threshold when the sub-harmonic emerges from the broadband noise. Adopted and modified from [72].

amplitude (according to the classification used)¹². The paper goes on to implement a control feedback loop based on the suggested classification, for which it claims; "*stable cavitation activity is ensured and maintained within a single acoustic pulse, while inertial cavitation activity is monitored in parallel through broadband noise quantification.*" Yet, the paper notes that at sufficiently high acoustic pressures, the coexistence of both cavitation regimes is making the full discrimination of ultrasound-induced bioeffects difficult, as discussed in §1.5.1.

Sonothrombolysis is an application where microbubble-mediated cavitation is becoming relevant, as discussed by Petit *et al.* [32]. This paper contains an extended discussion on the role of stable and inertial cavitation to clot lysis, for which the classification of cavitation regimes is justified by citing "*Acoustic Cavitation*" by Neppiras [15], reviewed below in §1.4.4. The methodology for evaluating the collected acoustic emissions, relies on the commonly accepted definition, where the stable cavitation threshold corresponds to the onset of the ultra-harmonic response, and the inertial cavitation threshold, to the sharp increase in acoustic broadband noise. In this experiment, microbubbles were infused into human plasma which was exposed to ultrasound of fundamental frequency $f_0 = 1$ MHz at 100, 200, 350 and 1,000 kPa peak-negative pressure. Acoustic emissions were detected by a commercially available focused single element PVdF-based PCD (Y-107, Sonic Concepts Inc., USA)¹³.

A sample of the results from the acoustic emission spectra are displayed in Fig. 1.8 at four different acoustic pressure amplitudes. The bandwidths of the first ultra-harmonic ($3f_0/2$) and broadband noise which are collected and evaluated for classification purposes, is highlighted in the figure. It is worth noting that as the pressure amplitude is increased from 100 kPa to 200 kPa, the first sub-harmonic ($f_0/2$) and the first ultra-harmonic ($3f_0/2$) is detectable, however, it remains unclear as why one spectral feature is chosen over the other in terms of monitoring the microbubble activity. Increasing the pressure amplitude of the driving ultrasound to 350 kPa, the measured broadband noise increased by ~ 15 dB, and the ultra-harmonic feature increased by ~ 10 dB. Applying the definition, and methodology proposed by Petit *et al.*, it is tempting to conclude that both the stable cavitation activity and the inertial cavitation activity has increased.

¹²However, little insight into the expected effects from the cavitation activity is gained, as the acoustic measurements are not complemented by, for instance, photographic observations.

¹³Features as the commercially available PCD, against which the swPCD is tested.

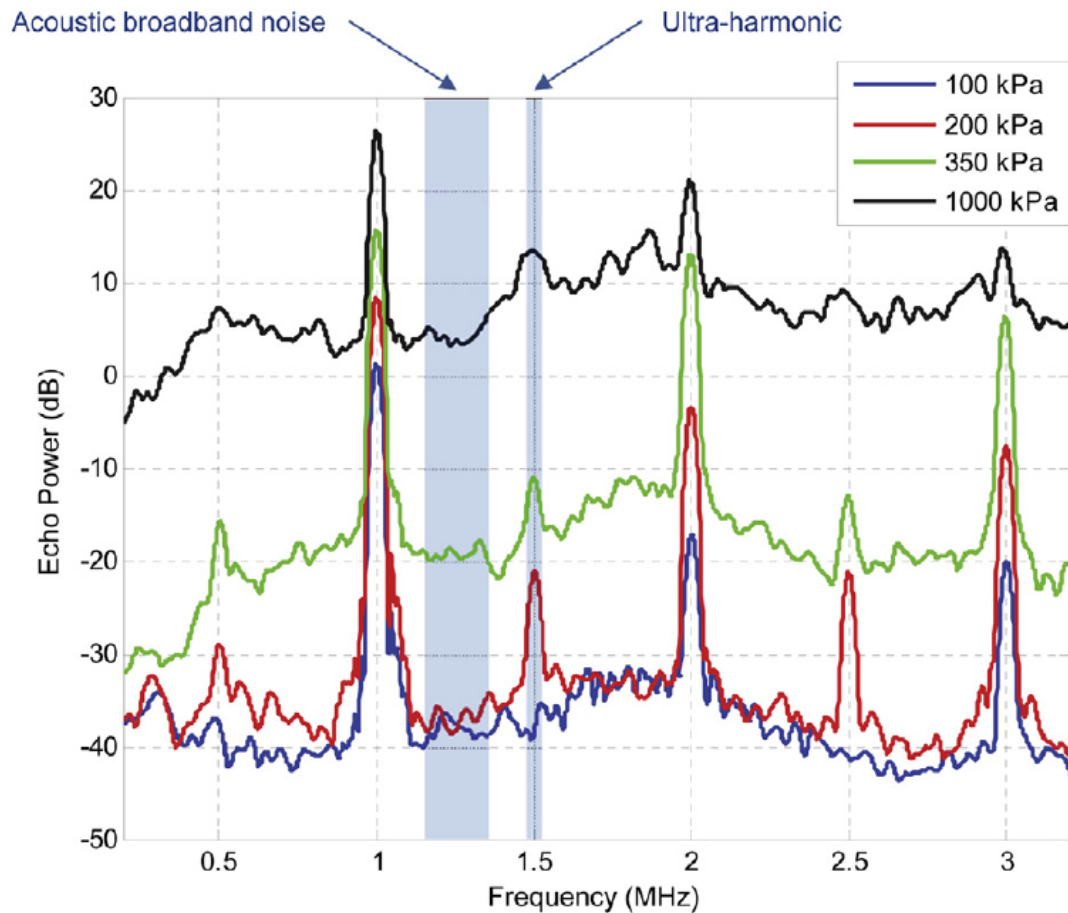


Figure 1.8: Representative acoustic emissions (called echo power in the paper) spectra of a suspension of microbubbles in human plasma exposed to 1.0 MHz ultrasound at 100, 200, 350 and 1000 kPa peak-negative pressure. This is done to determine the stable and inertial cavitation threshold. For all driving pressure amplitudes, the ultra-harmonic and broadband noise levels are calculated for the highlighted bandwidths (blue). Taken from [32].

This report could be taken as evidence for the existence of individual bubbles that are responding inertially and collapsing with the emission of shock waves, as suggested from theories published in previous decades, discussed in §1.4.4. While at the same time, a sub-set of bubbles, are responding in a stable fashion, emitting the ultra-harmonic signature separately. An alternative explanation would be, that the majority of the bubbles are responding, to first approximation *synchronously*, and serving as a source for all three spectral features (sub-harmonic, ultra-harmonic and broadband noise) [11, 47]¹⁴. The paper notes in the discussion of results; "*...at 350 kPa, stable cavitation is more efficient than inertial cavitation for inducing clot lysis.*", and the authors propose the following hypothesis; "*...that at the point of highest acoustic pressure*

¹⁴The preliminary cavitation cloud data in Fig. 2, also suggests that this effect might be of importance when analysing collective acoustic emissions.

(position 0 mm), a large proportion of microbubbles present underwent inertial cavitation, which may induce more shear stress than stable cavitation, but for a much shorter period, leading to lower efficacy."

The following section, §1.4.4, explores the current understanding underpinning interpretation of acoustic emissions from cavitation. In combination the papers reviewed have had a notable influence on the discussion and interpretation of acoustic cavitation emissions, including in recently published papers, as discussed in §1.6. Topics discussed in the section below span across all acoustic emissions, such as the origin of over-harmonics, sub-harmonics, ultra-harmonics, and broadband noise. This includes how sub-harmonic emissions may be related to the ultra-harmonic emissions and broadband noise.

1.4.4 Proposed mechanisms for specific spectral features

Below, three influential papers, that sought to relate source bubble dynamics to specific spectral features, thus associating those features with stable or inertial cavitation, are reviewed.

E. Neppiras, Subharmonic and other low-frequency emission from bubbles in sound-irradiated liquids, *The Journal of the Acoustical Society of America* 46 (3B) (1969) 587-601

In 1969, Neppiras published on the acoustic emissions from cavitation, including the sub-harmonic and other spectral components below f_0 [38]. The paper starts out by stating that bubbles are sources of spectral features at the driving frequency (linear scattering), and its over-harmonics. The over-harmonics derive from non-linear bubble oscillations undergoing *stable* cavitation. The first sub-harmonic ($f_0/2$), appears as the pressure amplitude of the driving ultrasound is increased, and "*usually*", this is also the sub-harmonic of the highest amplitude¹⁵. Additionally, Neppiras remarks that at high driving pressure amplitudes, the level of white (broadband) noise increases significantly, and is presumed to be related to transient cavitation events and associated shock waves.

¹⁵However, no explanation is provided as to why the first sub-harmonic is *usually* the spectral feature of the highest amplitude below the excitation frequency, nor why it is specifically written that it is only *usually* of highest amplitude. These are indications that the sub-harmonic was somewhat mysterious.

Whilst the over-harmonics and white noise arise from the *stable* and *transient* cavitation, respectively, the sub-harmonics and its over harmonics remained undetermined in terms of source bubble dynamics generating them. Neppiras forwarded four hypothesis to resolve this issue;

- **Shock waves from collapsing bubbles:** It was recognised that shock waves from transiently collapsing cavitation, are a source of broadband emissions containing frequencies below f_0 , which could represent a source for spectral features in the emission spectrum below f_0 . This theory is at the time discouraged as no equation of motion for the bubble was thought to support this, and shock waves generated via other methods (non-linear ultrasound propagation), did not contain sub-harmonic spectral features ¹⁶.
- **Surface waves:** The source of the sub-harmonic is surface waves (Faraday waves), such as depicted in the high-speed images shown in Fig. 1.9. Generally, surface waves are excited at frequencies different than f_0 , including $f_0/2$ [77–79]. However, according to Neppiras it has been shown that surface waves only contribute to small volume changes, and are therefore a poor candidate to explain the strong sub-harmonic emission. This insight is also supported by literature reviewing microbubble dynamics in §1.5.3. However, surface waves are discussed in the modern cavitation literature both in relation to contrast enhanced imaging and therapy.
- **Parametric amplification:** That the sub-harmonic is generated by parametric amplification of small amplitude components already present at this frequency. It was shown theoretically that if the compliance of the host medium was suitably non-linear, the first sub-harmonic could exist. Experimentally, this was not satisfactorily supported, as the

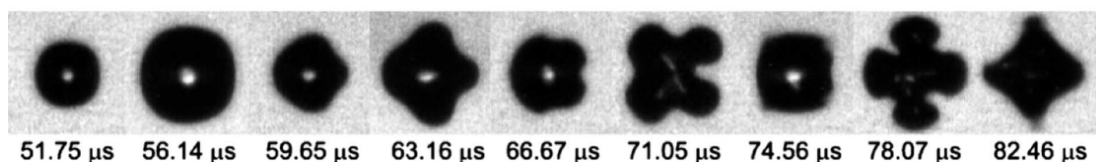


Figure 1.9: Growth of a 4th order surface mode vibration for a bubble with equilibrium radius of $36\ \mu\text{m}$ after 5 cycles of ultrasound. Taken from [77].

¹⁶This is thought to be related to lack of computational facilities, as the Rayleigh–Plesset equation and also the later Gilmore equation was already published, and both support such bubble motion, however it is computationally demanding to study such solutions.

sub-harmonic signal measured was too strong, compared to what the theory suggested, and only detectable when bubbles were present. Moreover, this suggested explanation could only address the first sub-harmonic, and no other spectral features below the fundamental frequency, further weakening it as a viable candidate.

- **Large bubble:** Large bubbles excited by harmonics of their radial resonance frequency respond sub-harmonically [63,80]. It is assumed that these sub-harmonic oscillations might build up in a liquid containing bubbles, and collectively contribute to a strong sub-harmonic component. It is further speculated that this kind of bubble behaviour could develop into high amplitude oscillation, more than twice R_0 , and transition into a transiently collapsing cavity.

One of the aims of this paper, was to study whether the sub-harmonic could be used as an indicator for the cavitation threshold. From the experimental results presented, it was concluded, that in an unprepared liquid, with no pre-existing bubbles the sub-harmonic and transient cavitation threshold coincides, as seen in Fig. 1.10a. For a liquid pre-seeded with bubbles larger than the excitation frequency, a weak sub-harmonic appears well below the transient cavitation threshold, as presented in Fig. 1.10b. If the amplitude of the fundamental frequency of the driving

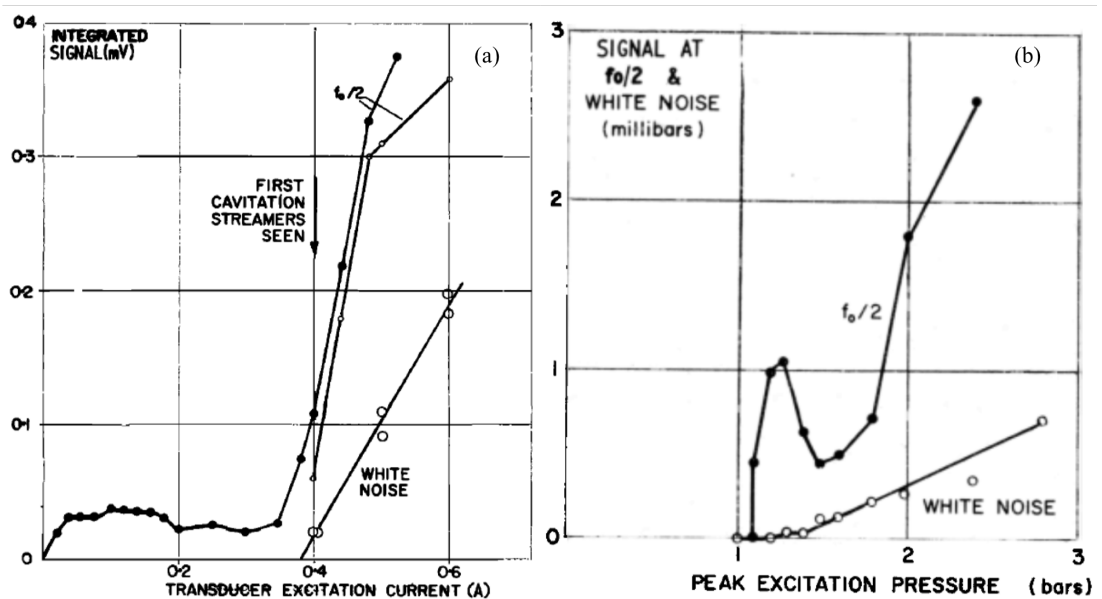


Figure 1.10: (a) Acoustic emissions at $f_0/2$ and white noise from air-saturated water driven at $f_0 = 28$ kHz. (b) Acoustic emissions at $f_0/2$ and white noise for pure glycerol containing large bubbles of resonance frequency $f_r = f_0/2$ driven at $f_0 = 31$ kHz. Taken from [38].

acoustic field is increased, the stable-type sub-harmonic emission breaks up into short bursts, and the average signal is decreased, as the transient threshold is approached. Further increasing the excitation amplitude, the sub-harmonic reappears, and grows usually to a much higher level, Fig. 1.10b. Regarding the content between f_0 and $f_0/2$, it is suggested that this could be generated by other large bubbles that have initially coalesced. Neppiras notes, as one of the final remarks, that the nature of the sub-harmonic is still uncertain, however, experimental data seemed to suggest that large bubbles were primarily responsible ¹⁷.

W. Lauterborn, Numerical investigation of nonlinear oscillations of gas bubbles in liquids, Journal of the Acoustical Society of America 59 (2) (1976), 283 - 293

Almost a decade later, Lauterborn had acquired some computer facilities to aid his research efforts into the complex behaviour exhibited by cavitation bubbles [81]. In this report, the Rayleigh–Plesset equation was numerically solved for different bubble responses as a function of f_0 , R_0 and the acoustic pressure, PPA , Fig 1.11. This was used to initiate a discussion on harmonic, ultra-harmonic and sub-harmonic oscillations and acoustic emissions. The sub-harmonic was also discussed as a threshold for transient cavitation. The numerical results suggested similar trends as observed experimentally, for instance, the onset of the sub-harmonic has a certain threshold, depending on the f_0 , R_0 , and PPA . Moreover, the relationship between ultra-harmonics and sub-harmonics was discussed. The first proposed explanation was based on large bubbles oscillating sub-harmonically [82], though this assumption relies on the liquid containing bubbles, driven at twice their resonance frequency. This was not supported by high-speed imaging observations at that time, which failed to identify bubbles of the required size [81].

From the numerical results presented, it was suggested that the ultra-harmonics, might be connected to the sub-harmonic bubble motion, that was not dependent on the large bubble assumption. This was supported by experimental results (as discussed by [81]), suggesting that ultra-harmonic bubble oscillations may be the source of the first sub-harmonic acoustic emission, as the spectral features at $3f_0/2$ of the driving fundamental frequency and $5f_0/2$ appear at lower

¹⁷Strangely, the door is also still kept open to the surface wave theory, for no apparent physical reason. This is something that might suggest that Neppiras and other cavitation researchers were uncertain about the conclusions they were drawing, from relatively rudimentary experiments.

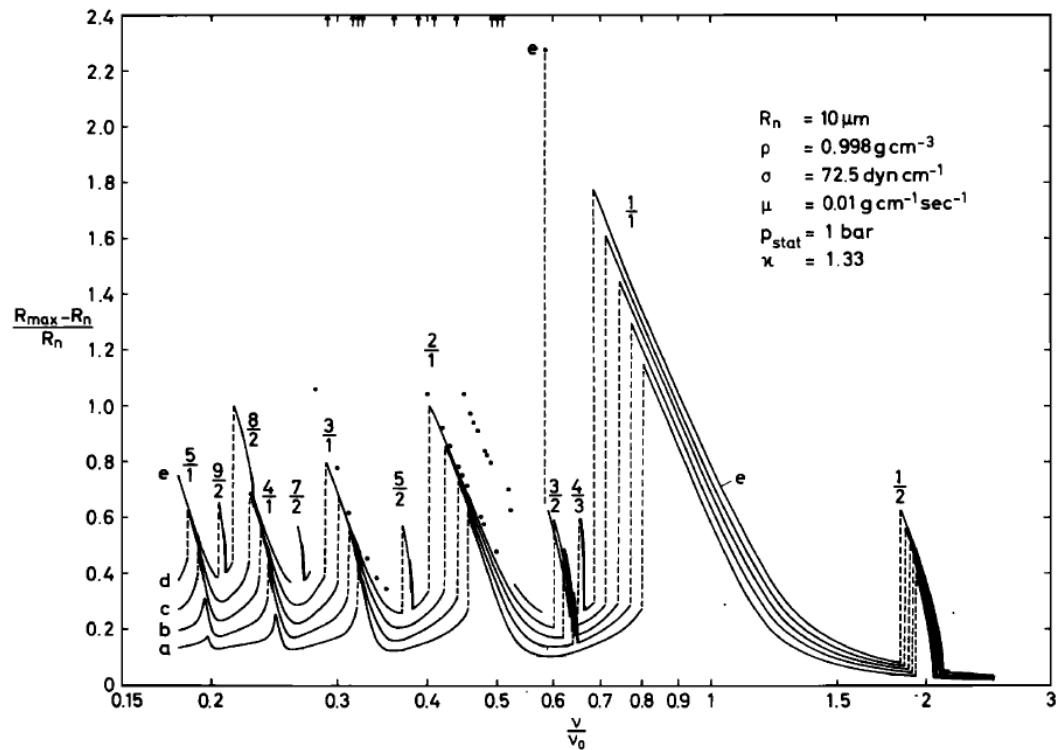


Figure 1.11: Bubble response at different driving pressure amplitudes, as a function of frequency. Taken from [81].

pressure amplitudes than the sub-harmonic spectral feature at $f_0/2$, for a previously attempted experimental configuration [81]. The paper concedes that: "*This complicated situation shows that despite of its experimental suitability as a measure of some sort of cavitation threshold the first sub-harmonic in the spectrum of the cavitation noise is not easily related to bubble dynamics. Experiments are under way to gain more insight into the relationship by sophisticated spectral measurements.*"

E. Neppiras, Acoustic cavitation, Physics Reports 61 (3) (1980) 159 -251

In 1980, Neppiras published his seminal work "*Acoustic Cavitation*"¹⁸, presenting a detailed discussion of both stable and transient cavitation, as well as the transition between the two regimes. Moreover, it defines that a bubble is stable if the radial dynamics displayed in the phase-plane, with dR/dt as a function of R , is forming closed curves, and transient oscillations form discontinuities going to infinity in some direction, as seen in Fig. 1.12. However, this

¹⁸Today this paper is cited 799 times (9th September 2018), including by reports on recent developments of therapeutic applications of cavitation.

definition is not helpful when attempting to determine if a measurement of acoustic emissions from cavitation are generated by stable or transient cavitation. Acoustic emissions at both low and high driving intensities are discussed, and it reiterates what has been published over the last few decades. Briefly, harmonics, sub-harmonics and ultra-harmonics can be generated by stable cavitation. The sub-harmonic in stable cavitation is relatively much weaker than what is expected from transient cavitation, and at high driving amplitudes the amplitude of the measured white noise increases significantly. Neppiras goes on to state that there are two potential sources of the sub-harmonic from transient collapsing cavitation:

- **Incomplete bubble oscillations:** Due to the inertia of the surrounding liquid, the bubble does not have time to collapse before the end of a single acoustic cycle, and may complete their transient collapse on the second, or subsequent pressure maxima. Under this assumption, with the bubble transiently collapsing at the sub-harmonic frequency, it could be a potential strong source of this spectral feature, Fig. 1.13a. It was also suggested that the linear acoustic emission and the total non-linear acoustic emissions would be of comparable amplitudes.

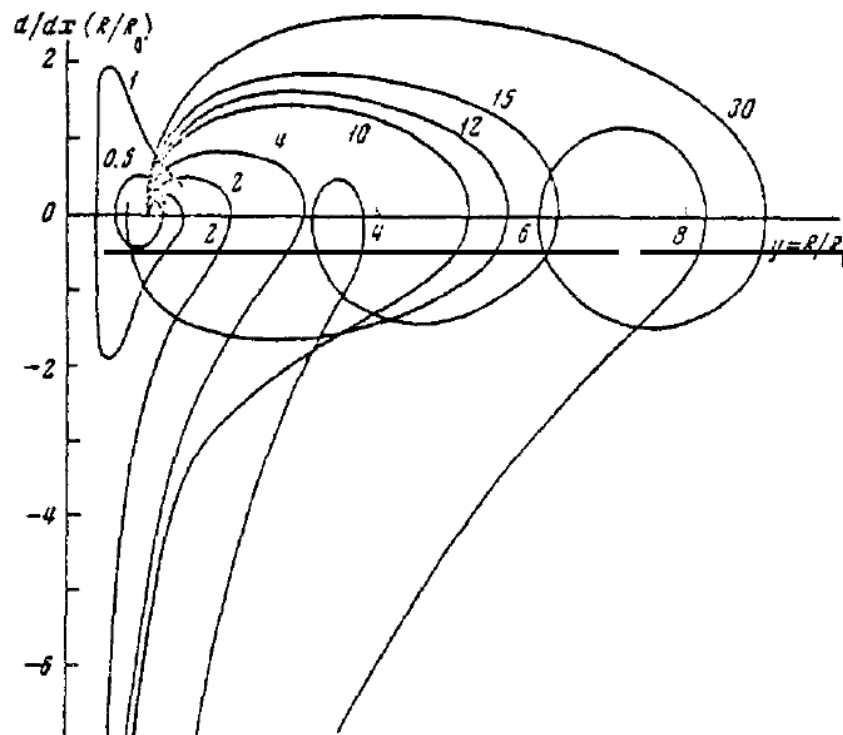


Figure 1.12: Solutions of Rayleigh-Plesset equation in the phase-plane. $R_0 = 5 \times 10^{-4}$ m, $f_0 = 500$ kHz. The numbers on the curves refer to the ratio between PPA/P_0 . Taken from [15].

- **A development of large bubble theory:** A reiteration of the large bubble theory excited at twice the resonance frequency, where the oscillations start as small sub-harmonic oscillations, and develop into a transient sub-harmonic bubble motion. Neppiras hypothesised the emission of shock waves from this type of collapsing cavity, which would spectrally be displayed as an infinite series of harmonic components, repeating sub-harmonically and decreasing in amplitude proportional to f_0^{-2} , Fig. 1.13b.

1.5 Focused ultrasound surgery

As mentioned in *Overview of Thesis*, the acoustic cavitation observations presented in this thesis have been undertaken in focused ultrasound of fundamental driving frequency, $f_0 = 220$ kHz and $f_0 = 692$ kHz. This frequency range is highly relevant for applications currently under development in medical therapy, as discussed below.

Focused ultrasound surgery (FUS), or high intensity focused ultrasound (HIFU), is an attractive method to address diseased tissue [83–85]. The technique is minimally invasive, targeted and uses a low energy density non-ionising form of radiation (compared to conventional external beam radiotherapy, which typically employs X-rays and electrons), and can be conducted under ultrasound or MRI-guidance [83, 86, 87].

Clinical FUS is currently mediated via thermal effects, whereby viscous absorption in the

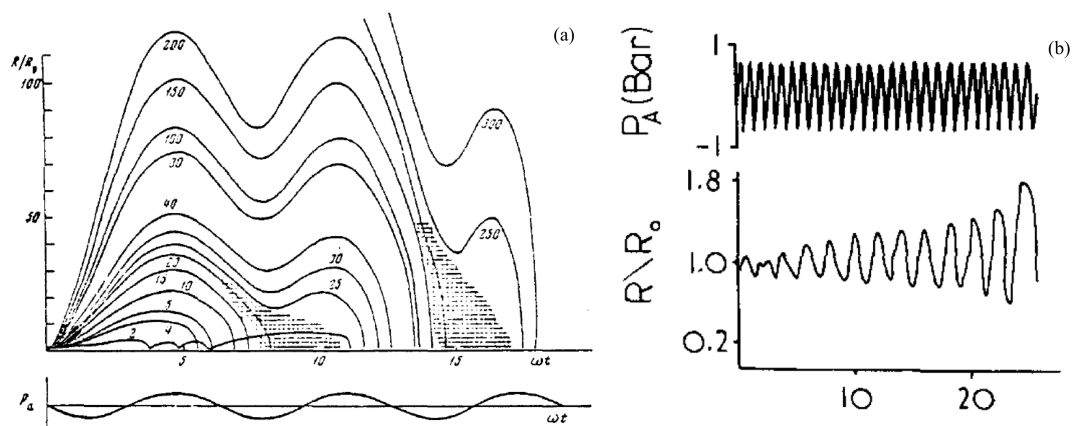


Figure 1.13: (a) Radius-time curve of air-bubble in water. $R_0 = 10^{-6}$ m; $f_0 = 500$ kHz. The number assigned to the curves refers to the ratio of driving pressure amplitude to the ambient pressure p_0 . (b) Unstable cavitation driven at twice its resonance frequency, eventually transiently collapsing. Taken from [15].

tissue transforms acoustic energy to heat, leading to lesion formation which is associated with protein denaturation, irreversible cell damage, and coagulative necrosis. Heating of tissue through this process is notoriously inefficient, which, compounded by a need to protect tissue in the near- and far- field, leads to lengthy procedure times.

The frequency used for any particular FUS application is largely guided by anatomical considerations for the pathology it is intended to treat, and the attenuation coefficient for tissue, which generally increases with frequency [88, 89]. For example, trans-rectal FUS of the prostate can be performed at a relatively high frequency (> 3 MHz) as the transducer is located in close proximity to the target gland [90]. For the treatment of deeper-seated tissue, however, lower frequencies are required for sufficient penetration, with acceptable attenuation¹⁹. For example, in Fig. 1.14a a diagram of a focused ultrasound system of fundamental frequency 1 – 1.5 MHz designed to treat uterine leiomyomas (fibroids), is seen. The fibroids can be positioned within and around the uterus, and the penetration depth required for this procedure is significantly greater than for trans-rectal prostate applications, Fig. 1.14b, thus the frequencies chosen are proportionally lower. Transcranial treatment of the brain represents the lower limit for therapeutic

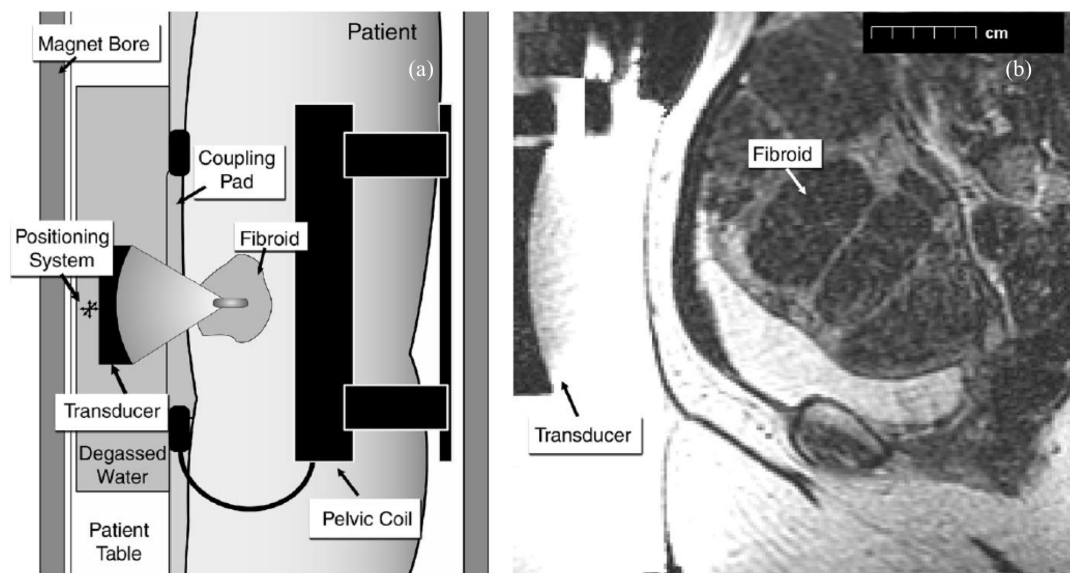


Figure 1.14: (a) Side-view diagram of the focused ultrasound system and patient positioning. (b) MR image obtained with the patient in position for treatment of fibroid. Taken from [83].

¹⁹An analogous compromise applies for diagnostic ultrasound. Higher resolution imaging may of course be achieved with higher frequencies, but absorption in tissue limits practical implementation. Lower frequencies (several MHz) must be used for deeper imaging, with higher frequencies (> 10 MHz) favoured for superficial examinations.

FUS frequencies, with focused ultrasound of several hundred kHz sufficiently transmitted across the skull. A recent (thermally-mediated) clinical trial for the treatment of Essential Tremor, under MR-guidance employed a frequency of 690 kHz [91].

1.5.1 Cavitation in medical therapy

It is generally held that cavitation can have adverse biological effects, and for that reason the *mechanical index*, MI , was introduced to gauge the likelihood of cavitation from diagnostic ultrasound [42]. Though, the MI is not related to what cavitation mediated effects can be expected from some bubble activity. The MI is defined as;

$$MI = \frac{PNP}{\sqrt{f_n}}, \quad (1.4)$$

where PNP is the peak negative pressure amplitude normalised to 1 MPa, and f_n is f_0 normalised to 1 MHz. For higher MI the likelihood of cavitation increases, however the safety threshold for which adverse mechanical bioeffects becomes pronounced, remains an open topic²⁰.

Recently, there has been a surge in interest for utilising the mechanical effects incurred by focusing ultrasound into tissue, for therapy. In this role, contrast agent microbubbles may be used to significantly promote cavitation (or equivalent, such as sub-micron vapourisation droplets [93,94]), via intravascular infusion. Cavitation-mediated effects are being investigated for applications, such as transient blood-brain barrier disruption [31,95,96], and sonothrombolysis [32,97], for example.

Furthermore, in medical applications of cavitation it is common to correlate detection of certain spectral features to make statements and inferences about drug delivery or avoidance of collateral damage, such as inflammation [36,37].

Following below, two papers employing rapid control feedback loop systems, between detector and source focused ultrasound transducer, are reviewed. This is similar to the experimental setup

²⁰Current research suggests that a MI of 0.4 has the potential to introduce some mechanical bioeffects, and for $MI = 0.7$ there is a significant probability for the occurrence of cavitation [92]. Interestingly, the Food and Drug Administration (FDA) limit is much higher, at $MI = 1.9$. However, this limit assumes precautions are taken, such as short scans and avoidance of lungs, to limit negative effects of ultrasound. It is worth to note that these guidelines are based on ultrasound knowledge and device specifications from 1976.

used by Cornu *et al.*, discussed in §1.4.2, but with contrast agent microbubbles. Rapid control feedback loops facilitate the modulation of the exposure according to the spectrum of the acoustic emissions detected from the cavitating microbubbles. This is emerging as a key technology for safe clinical realisation for preclinical development of blood-brain barrier disruption.

1.5.2 Rapid control feedback loop

O'Reilly *et al.* published a paper titled "*Blood-Brain Barrier: Real-time Feedback-controlled Focused Ultrasound Disruption by Using an Acoustic Emissions-based Controller*" [31]. In this paper, a rapid control feedback loop system is implemented, for which a diagram of the experimental setup is seen in Fig. 1.15a. Briefly, it consists of a focused ultrasound transducer of fundamental frequency $f_0 = 550$ kHz, and an in-house built 4.8 mm in diameter broadband PVdF-based PCD to detect acoustic emissions²¹. The feedback loop was designed to monitor the amplitude of the $3f_0/2$ and $5f_0/2$ spectral feature as the pressure amplitude of the driving ultrasound was increased, as seen in Fig. 1.15b. After ultra-harmonics are detected, the pressure amplitude of the driving ultrasound is decreased to a predetermined level. In this controller design, both spectral features used are taken as indicators of stable cavitation, and the definition of stable cavitation is justified by citing "*Acoustic Cavitation*" by Neppiras [15]. No spectral feature was measured to monitor the emergence of inertial cavitation.

Sun *et al.* recently published a paper titled "*Closed-loop control of targeted ultrasound drug delivery across the blood-brain/tumor barriers in a rat glioma model*" [33]. The experimental setup consisted of a dual-aperture HIFU arrangement of fundamental frequency $f_0 = 274.3$ kHz, Fig. 1.16. The combined focus of the two transducers significantly improved beam focusing in the axial direction due to the enlarged effective aperture size [98]²². An in-house built PCD of centre frequency $f_c = 650$ kHz was used to collect the acoustic emissions from microbubbles

²¹The PCD is similar to that described in [4].

²²The paper notes that, "*Two coherent wave sources inevitably yields an interference pattern, which would result in inhomogeneous blood-brain barrier disruption. To combat this, and redistribute the acoustic energy at focus and produce spatially homogenous blood-brain barrier disruption, each transducer was driven with a slight offset ($\delta f = 31$ Hz), modulating the interference pattern over the course of each burst. This design enabled a fully constrained and homogenous treatment profile in the rat brain at a clinically relevant frequency range.*" [33]

infused into the blood stream together with the liposomal drug²³. No construction details are provided about the PCD. The microbubble activity was monitored by measuring the level of broadband noise as an inertial cavitation marker (transient bubble collapse), and the level of

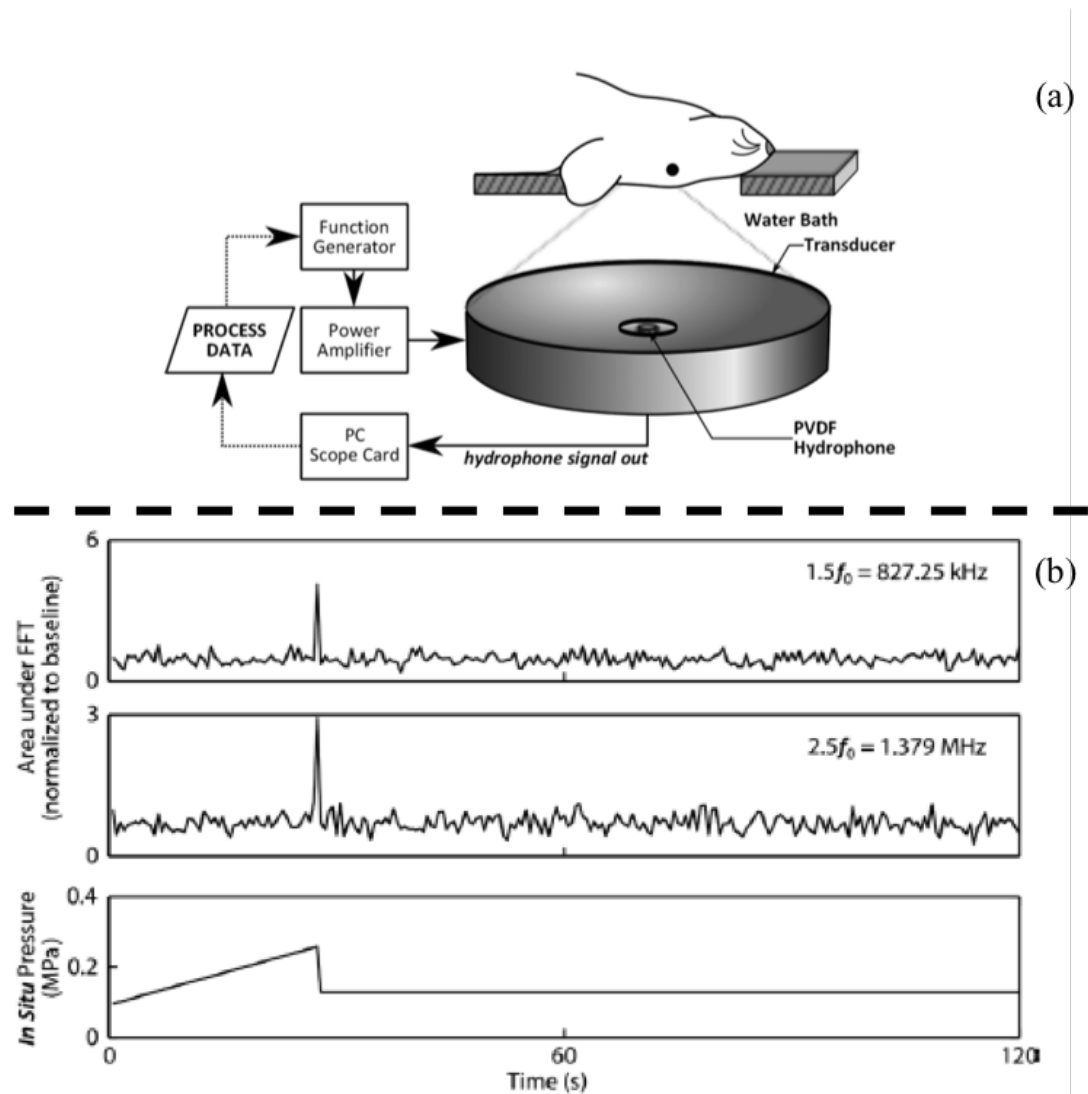


Figure 1.15: (a) Experimental setup for blood-brain barrier disruption using microbubbles and HIFU. Acoustic emissions are detected by an in-house built PVdF-based PCD revised in detail in Chapter 6, which is connected to a control feedback loop to adjust the exposure parameters in such a way that stable cavitation is not exceeded. (b) Example of acoustic exposure where $3f_0/2$ and $5f_0/2$ are detected when the pressure amplitude of the driving signal is increased. After the two spectral features are detected, the driving pressure amplitude is lowered to a pre-configured value before it is increased up to detection of the respective spectral features again. Taken from [31].

²³The drug was encapsulated in a liposome, which is a spherical vesicle having at least one lipid bilayer. The lipid bilayer may be disrupted during sonication, allowing the encapsulated therapeutic agent to react with surrounding cells.

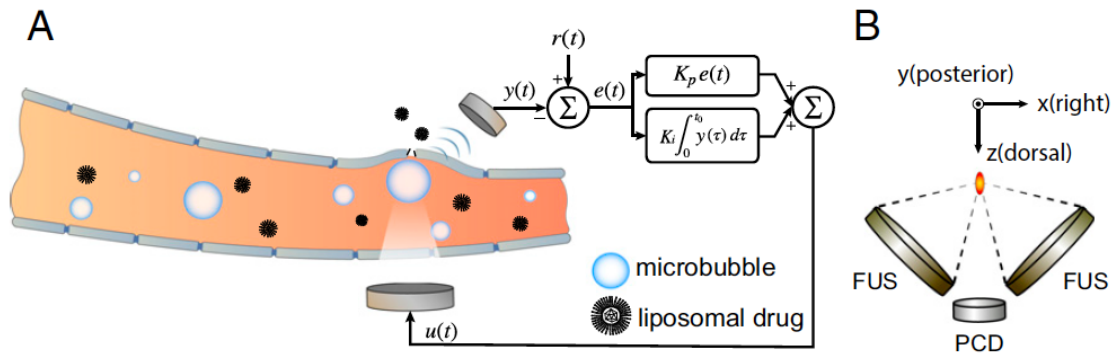


Figure 1.16: (A) Schematic representation of the feedback loop which controlled the drug delivery system. (B) Illustration of the dual-aperture focused ultrasound setup with a PCD. Taken from [33].

harmonic emissions nf_0 ²⁴ as an indicator of stable cavitation ("sustained low amplitude bubble oscillations"). It is proposed that measuring both spectral features facilitates more effective enhancement and suppression of stable and inertial cavitation, respectively. The paper further claims that: "Here a closed-loop, real-time control paradigm is shown capable of sustaining stable microbubble oscillations at a preset level while minimizing microbubble behavior that may result in vascular damage."

In the next section, the current understanding of microbubble dynamics is reviewed. This is done to both show how the research presented in this thesis is of broader interest, and to justify that the understanding of microbubble dynamics may be representative to what is generally accepted for free gas bubbles.

1.5.3 Microbubble dynamics and possible acoustic emission mechanisms

In this chapter, several studies that have used contrast agent microbubbles, and collected acoustic emissions analysed to make inferences regarding what regime of source bubble dynamics is responsible for the observed cavitation-mediated bioeffects, are reviewed. For this reason, a brief introduction to current understanding of microbubble dynamics, is presented below, to complement what has been previously discussed with regards to free (unencapsulated) acoustic cavitation.

Kooiman *et al.* published a thorough review of microbubble behaviour in acoustic fields, with

²⁴Stable cavitation is, according to this paper, correlated to harmonic emissions, sub-harmonic emissions and ultra-harmonic emissions, however, in the control feedback loop only the harmonic emissions are used.

particular attention to how the different regimes of microbubble dynamics can have implications for drug delivery [99]. The paper presents the generally held notion, that microbubbles with a coating exhibit various oscillation regimes, depending on the pressure amplitude of the acoustic field, shell properties, equilibrium radius, as well as vasculature environment for *in-vivo*. In order of increasing volumetric oscillation amplitude, they may be listed as: (1) no oscillation; (2) linear spherical oscillations; (3) non-linear spherical oscillations; (4) non-spherical oscillations; (5) violent inertial collapses; and (6) bubble fragmentation/ coalescence. Following below regime (3), (4) and (5), are expanded on as they are the most relevant in terms of generating acoustic emissions which are correlated to cavitation-mediated effects.

Non-linear spherical microbubble oscillations are primarily used for contrast enhanced imaging with clinical scanners. This bubble regime is typically present for pressure amplitudes of $\sim 30 - 120$ kPa at 1.7 MHz, which is lower than what is typically used for drug delivery applications [100]. Examples of non-linear effects include the generation of higher order harmonics of the driving frequency [71, 101], and period doubling which has been investigated for purposes of sub-harmonic imaging [102]. Thin shelled microbubbles with a phospholipid-coating, can also show ‘compression-only’ behaviour, in which the compressional half-cycle has much larger amplitude than the expansion half-cycle [103]. Bubbles that undergo compression-only behaviour respond significantly more non-linearly, than same equilibrium size bubbles with a ‘symmetric’ response, at the same driving amplitude. This behaviour is related to buckling of the shell material during compression (*i.e.* it will not happen with a free bubble), which was first described theoretically by Marmottant *et al.* [104]. It has also been shown experimentally that the elastic properties of the shell material, due to buckling can influence the threshold for sub-harmonic behaviour at twice the resonance frequency [102].

For higher driving amplitudes, it has been shown that microbubbles undergo non-spherical shape oscillations [105]. Multiple causes are linked to this type of behaviour; (1) Parametric instabilities of the surface can occur. These need multiple cycles of tone bursts to build up, as seen in Fig. 1.17. (2) Placing a microbubble close to a wall can also cause non-spherical shapes oriented perpendicular to the wall [106].

Dollet *et al.* was first to perform a systematic study of non-spherical oscillations, or surface

modes, of ultrasound contrast agent microbubbles with high-speed imaging, Fig. 1.17 [105]. Moreover, this regime of microbubble behaviour is linked to the sub-harmonic spectral features, discussed in §1.4.4, as the expansion and contraction of the different modes are sub-harmonic. An example demonstrating the sub-harmonic nature of a 4th order shape oscillation, is shown in Fig. 1.17 [105]. However, the maximum observed deformation was lower than 3%, and in terms of acoustic emissions: "*...the subharmonic character of nonspherical oscillations may be interesting in the context of nonlinear imaging, but the outcome in terms of sound emission remains unclear at this stage.*"

However, recently a paper building on the control feedback loop work by O'Reilly *et al.* described in §1.5.1, subscribes a significant role to non-spherical shape oscillations [107]. In this paper, different concentrations of contrast agent microbubbles were investigated for opening

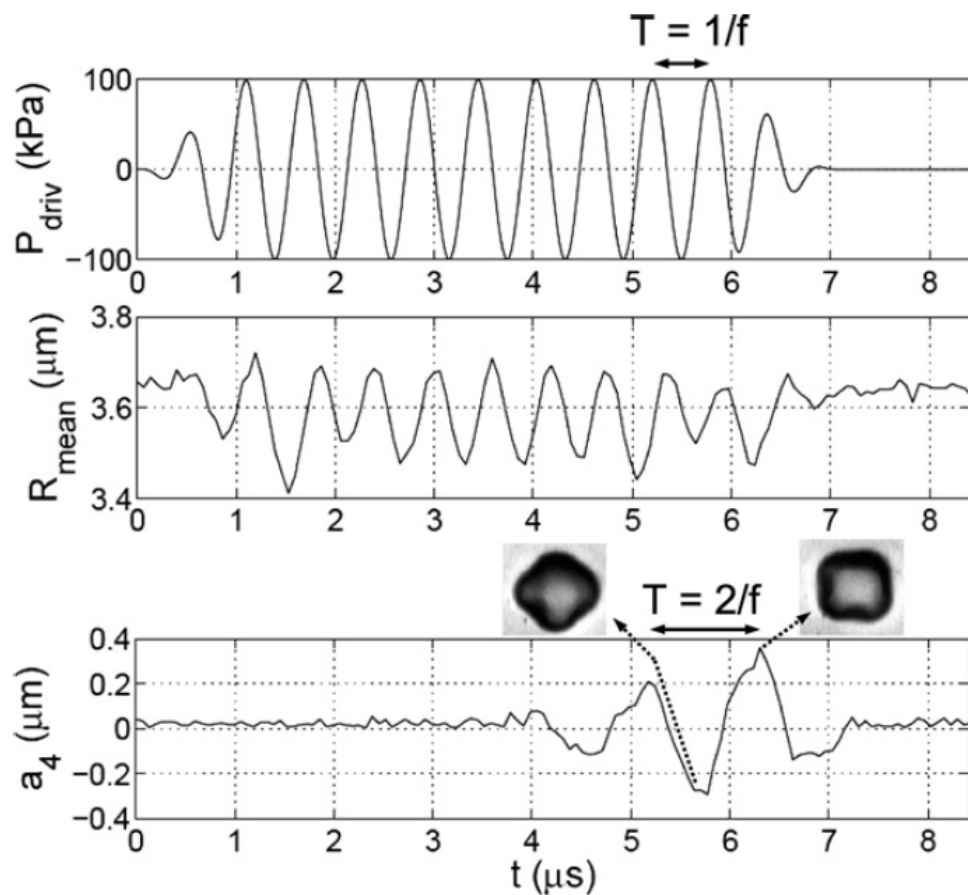


Figure 1.17: Surface wave oscillations from a microbubble of equilibrium radius $R_0 = 3.6 \mu\text{m}$. (a) Excitation pulse with 12-cycle burst of $PPA = 100 \text{ kPa}$ and fundamental frequency $f_0 = 1.7 \text{ MHz}$. (b) Radius-time curve reconstructed from 128 images at frame rate $15 \times 10^6 \text{ fps}$. (c) Evolution of mode 4 surface oscillation. Taken from [105].

of blood-brain barrier, using two different sonication regimes. The acoustic emissions from the microbubbles, which are used in the feedback loop, are understood the following way: "*As the PNP [peak-negative pressure] of sonication increases, there is a point at which a significant portion of MBs [microbubbles] shift from oscillating with spherical symmetry to having non-spherical oscillations. This shift in MB behaviour presents as a peak in acoustic emissions at sub- and ultraharmonic frequencies.*"

No reference is provided for this statement, however, in the absence of other bubble-based mechanistic sources, non-spherical shape oscillations persist as a proposed detectable mechanism mediating the sub-harmonic and ultra-harmonic acoustic emissions²⁵. Moreover, it is reasonable to assume that future advances in rapid control feedback implementations, and other applications, will benefit from an increased understanding of the relationship between source bubble dynamics and detected acoustic emissions. This is because detected acoustic emissions, and corresponding spectral features are used to classify the cavitation activity in terms of stable (usually wanted) and inertial (unwanted) cavitation.

As for non-spherical oscillations contribution to drug delivery, Vos *et al.* estimated that the value of the shear stress due to acoustic streaming at the oscillation frequency may reach up to 75 kPa for bubbles which are not splitting due to the non-spherical oscillations [108]. Although, the flow around the microbubble enhances mixing of fluids in its proximity, which may increase drug delivery efficacy; a direct relation between fluid motion and drug delivery has yet to be experimentally verified [99]. However, this remains a topic of investigation [109].

When the volumetric oscillation amplitude becomes large relative to the equilibrium volume, violent collapses of microbubbles can occur. Such violent collapses leads to the emission of shock waves, as described in §1.3. As for acoustic cavitation generally, shock waves are associated with broadband emissions, which can be detected experimentally [58, 110–112]. However, shock waves from microbubbles are typically not related to any other spectral features. For drug delivery, this regime of microbubble behaviour is associated with effects ranging from membrane opening to haemorrhage.

²⁵According to Neppiras in "Acoustic Cavitation", surface waves have been measured by placing a bubble close to a hydrophone, however, the detected acoustic emissions were of low amplitude [15].

1.5.4 Cavitation therapy without contrast agent microbubbles

It should be noted that applications of cavitation in medical therapy are not limited to the frequency range described above, or indeed reliant on contrast agent microbubbles.

Cavitation mediated drug delivery across the gastrointestinal wall was recently demonstrated, in a porcine model, with a 20 kHz unfocused trans-rectal probe [43]. The relatively low frequency of the ultrasound was chosen to maximise the cavitation activity, as the pressure required to spontaneously nucleate cavitation is lower, for lower frequencies (with a high MI see Eq. (1.4)) [42]. However, conventional FUS which relies on thermal effects, would typically have applied frequencies in the MHz range, as discussed above in §1.5. Acoustic emissions were detected by an omnidirectional PZT-based hydrophone (Teledyne Reson TC4013, 1Hz to 170kHz bandwidth), and the monitoring was undertaken at two spectral features; $f_0/2$ and $2f_0$. The sub-harmonic acoustic emission was correlated to inertial cavitation, and the conclusions of the paper suggested this category of cavitation as predominantly responsible for enhanced molecular transportation.

Effects of unseeded cavitation and boiling, are also investigated at higher frequencies, for instance McLaughlan *et al.* published a report employing multiple detection modalities to monitor cavitation and boiling in *ex vivo* tissue [50]. The experimental setup used, consisted of a focused ultrasound transducer of fundamental frequency $f_0 = 1.69$ MHz, which was used to initiate and drive the cavitation activity, and passive acoustic detection was undertaken via two focused PZT-based detectors (Olympus NDT Inc, Waltham, MA, USA): 1 MHz receiver (1.5 cm diameter, focal length 4 cm, bandwidth 0.1 to 2 MHz) and a 10 MHz sensor (3.0 cm diameter, focal length 4.5 cm, bandwidth 5 to 12 MHz). The passive cavitation detection was performed at $f_0/2$, $4f_0$ and broadband noise, as seen in Fig. 1.18. Some contribution from non-linear propagation was noted, however, the $4f_0$ was identified as having good temporal coincidence with increased levels of broadband emissions and was sensitive to the occurrence of boiling. Furthermore, the experiment encompassed two additional methods for detecting cavitation and boiling; a Z.One diagnostic scanner (Zonare, Mountain View, CA, USA) with an L10.5 linear array probe (centre frequency 8 MHz, 6-cm maximum imaging depth, frame rate 14 Hz) used for active cavitation detection, and audio microphone (bandwidth 2 - 8 kHz). Active cavitation detection

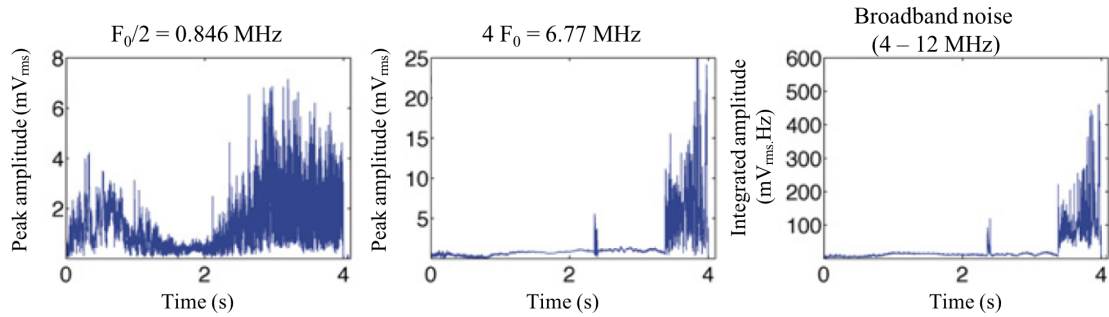


Figure 1.18: Detected acoustic emissions at $f_0/2$, $4f_0$ and broadband noise from cavitation driven by 1.69 MHz ultrasound of intensity 786 W/cm^2 (1.77 MPa). Taken from [50].

uses pulse-echo ultrasound to detect bubbles, however, it can be difficult to differentiate between areas of B-mode hyperechogenicity generated during HIFU exposure *in vivo* by acoustic bubbles from those caused by boiling bubbles, even when a PCD is present [113]. In the discussion, it is noted that for degassed water; "...*inertial cavitation was definitely present, noninertial cavitation may also have been occurring at the same time in a lower-pressure region of the bubble cloud at the periphery of the focus. Thus, both types of activity may have been occurring within the two confocally aligned PCD foci.*" This suggests a non-binary nature of cavitation is recognised, however, source bubble dynamics was still distinguished into two separate regimes.

Histotripsy is another therapeutic technique that harnesses cavitation to mechanically disrupt tissue. This method is described by a short-duration, very high-amplitude pulse of ultrasound which is focused at a region of interest where localised cavitation activity is generated [114]. This technique is being investigated for applications within non-invasive thrombolysis [115].

In the next section, the legacy of the papers reviewed in §1.4.4, is explored. The pioneering work performed in previous decades is influencing the current literature. This is for instance demonstrated by several of the papers reviewed throughout this chapter citing "Acoustic Cavitation" by Neppiras [15].

1.6 The legacy of cavitation research to date

The cavitation spectrum has been a topic of investigation for multiple decades, and is used presently by studies seeking to develop cavitation-mediated applications. The main theories and experiments were developed in the 1950's to early 1980's, and since then little experimental and theoretical corroboration has been realised, as discussed in §1.4.4. Of the diverse, and somewhat bewildering array of proposed mechanisms, it is quite striking how the majority are not supported by direct experimental observations, particularly around the relationship between source bubble dynamics and detected acoustic emissions, as well as classification and interpretation of measurements, as demonstrated by papers reviewed throughout this chapter.

The complex nature of energetic and highly nonlinear cavitation, combined with the difficulty of making precise direct cavitation observations, as discussed in §1.2, may have contributed to an enduring tendency for 'binary classification' of stable and inertial cavitation, often conceptualised as Fig. 1.19, or some variation. The binary classification may be justified in applications where the regime or level of cavitation is not critical for the overall process, however that is rarely the case for applications involving cavitation.

In §1.4.3 Leighton, Ashokkumar and Church as "fundamental cavitation researchers" have

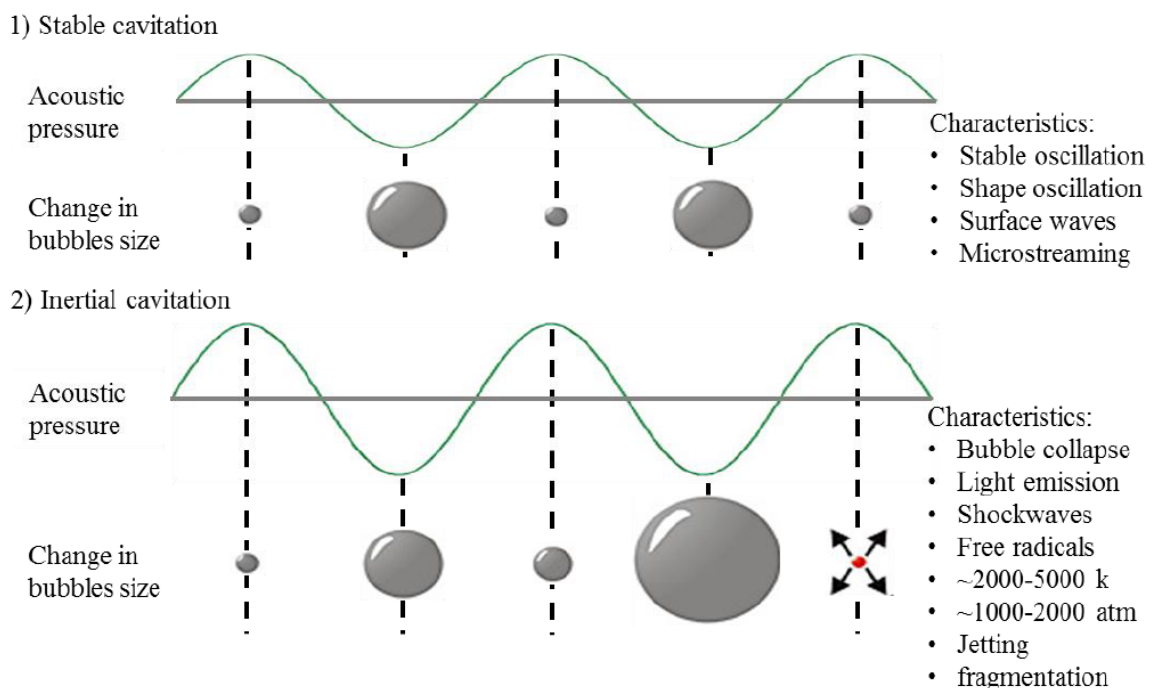


Figure 1.19: Graphical representation of stable and inertial cavitation. Taken from [1]

suggested that classifying cavitation as stable or inertial, is at best inadequate, at worst unhelpful, but no systematic study has been undertaken to translate circumstantial speculation into unequivocal confirmation.

It would seem fair to suggest that a more sophisticated and detailed categorisation would assist the development of applications. This may create a basis that allows for statements about specific effects that would be expected from certain acoustic emissions. However, if this is to be achieved, it is obvious that the first step is to reconcile the acoustic emissions to source bubble dynamics, which is the topic of Chapter 4.

Discussing the role of different regimes of cavitation, is important for safe and effective realisation of future applications - therapy in particular. As described by previous literature, this is not a settled topic of investigation and more fundamental research is required. This thesis and the underpinning published papers go some way to addressing this epistemic deficit.

Chapter 2

The Sonoptic chamber

In this chapter, the chamber in which shadowgraphic high-speed imaging and acoustic measurements of cavitation was undertaken, is described. The chamber is named "*The Sonoptic Chamber*", which indicates that this experimental setup facilitates both acoustic and optical observations of bubble activity.

The rationale for the design considerations made during the construction of the sonoptic chamber may be listed as: (1) The cavitation activity should be driven by a characterised propagating acoustic field, as discussed in §1.2. This is to ensure control over the ultrasound parameters used, such as focal width, axial focal length, pressure amplitude, and appropriate duration of excitation pulses, to limit reflections. Satisfying these conditions makes it possible to relate observed cavitation activity as in response to a well defined ultrasound exposure. (2) Optical equipment both for nucleation of cavitation and high-speed imaging requires positioning such that disturbance of the acoustic field is minimised, and sufficient imaging resolution and magnification is obtained. (3) The chamber should be constructed such that a range of hydrophones and PCDs may be incorporated and appropriately positioned for collection of acoustic emissions, whilst at the same time limiting the perturbation of the acoustic field, and preventing damage caused by strong bubble activity, often in close proximity.

This chapter is structured as follows: In §2.1 the HIFU source used to drive acoustic cavitation, is described. In §2.2 the sonoptic chamber including the nucleation laser, are discussed. In §2.3 the two bubble regimes used in this thesis, along with a description of high-speed imaging configuration in §2.4, and the acoustic detectors in §2.5, are described.

2.1 The HIFU source

In this thesis, all acoustic cavitation observations are driven by a spherically focused transducer (H-149 Sonic Concepts, Bothell USA), which has an outer diameter of 110 mm, and is a geometrically focused at a focal length of 68 mm, with an acoustic field of fundamental frequency $f_0 = 220$ kHz (used in Chapter 6) and third harmonic $f_0 = 692$ kHz (used in Chapter 4 and 5). Moreover, it has a 20 mm through opening in the centre of the device, into which the needle hydrophone, Y-107 Sonic Concepts PCD, and swPCD can be inserted. The transducer is driven using an arbitrary waveform generator (DG4102, Rigol Technologies, Beijing China) and a power amplifier (2100L, Electronic and innovation, NY, USA), via matching networks (Sonic Concepts) for each frequency.

Free field mapping was performed via a 1 mm needle hydrophone for the fundamental frequency to the HIFU transducer, which measured the -6 dB focal width, as 4.9 mm and axial focal length, 22.4 mm, Fig. 2.1. The focal dimensions at the third harmonic are even smaller, with a focal width of 1.8 mm and axial focal length of 8.5 mm, due to the higher frequency. Free field mapping of the third harmonic is presented in Chapter 4 and 5 in §4.1.2 and §5.1, respectively.

2.2 The sonoptic chamber

To fulfil the design requirements outlined above, an open-architecture custom chamber was built¹, for which a schematic representation is seen in Fig. 2.2. The chamber measures $420 \times 438 \times 220$ mm³, and was filled with > 30 L of deionised water, which was degassed via boiling and cooling in sealed containers, to achieve a dissolved O₂ level below 4 mgL⁻¹, during all experiments. The water was degassed to prevent random nucleation of cavitation bubbles in the HIFU field. This was combined with the use of a nucleation laser (described below), to precisely determine the moment and location of a cavitation bubble. Two of the walls are recessed (described as tunnels), allowing imaging optics to be placed in proximity to the intended location of the bubble activity, as seen in the zoomed inset featuring in Fig. 2.2.

¹The author acknowledges Graeme Casey and Miraim Jiménez García for constructing the sonoptic chamber used in this thesis.

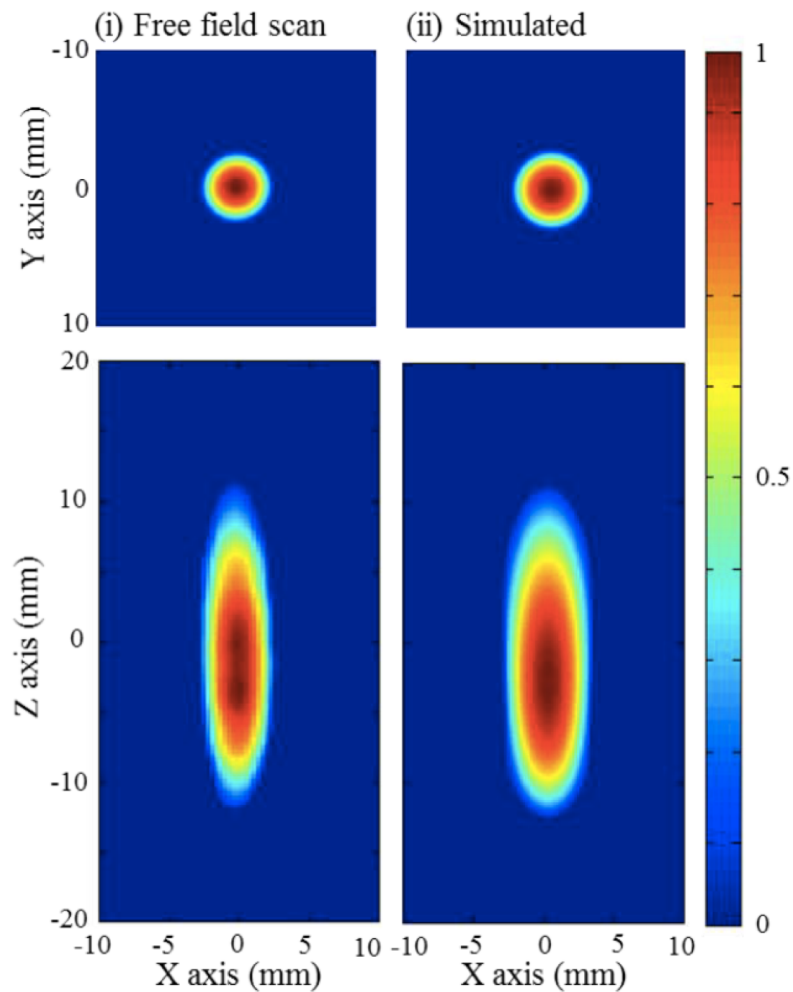


Figure 2.1: Free field mapping of fundamental frequency for the transducer described in §2.1, carried out via needle hydrophone measurements and simulation of acoustic field using Field II simulator [116]. The focal width at -6 dB measures, 4.9 mm and axial focal length, 22.4 mm. Taken from [1].

The HIFU source is placed on a rapid prototyped base such that the ultrasound can propagate upwards without being perturbed by the tunnels (arrowed), Fig. 2.2. The measured focal width (for both frequencies) is small compared to the distance between the two tunnels ~ 66 mm, which suggests that the disturbance of the acoustic field would be negligible, Fig. 2.2, confirmed by ‘*in situ*’ scanning.

Bubble activity is initiated via a single 6 – 8 ns 532 nm laser pulse (Nano S 130-10 frequency doubled Q-switched Nd:YAG, Litron Lasers, Rugby, UK), focused through a long working distance objective lens ($50\times$ 0.42 NA Mitutoyo, Japan) submerged in a sealed unit mounted on an xyz manipulator (Velmex Motor, Bloomfield, NY, USA), Fig. 2.2 and Fig. 2.3.

2.3 Bubble regimes

Two distinct regimes of cavitation activity are reported here, primarily distinguished by the energy of the laser pulse described above; (i) single laser-plasma mediated vapour bubbles and (ii) laser-nucleated acoustic cavitation, which also requires a burst of HIFU simultaneously incident to the combination focal region [8, 117]. For the former regime, laser pulses of > 4 mJ (determined to be the breakdown threshold for the medium, and the laser focusing optic) generate a plasma and an optical breakdown shock wave, Fig. 3.5a. The plasma rapidly expands to form a comparatively large bubble, of maximum diameter determined by the pulse energy. The inertia of the host medium then deflates and collapses the bubble such that a second shock wave, the bubble collapse shock wave, is emitted, Fig. 3 (in *Overview of Thesis*). The peak positive pressure amplitude of the bubble collapse shock wave is, in turn, determined by the maximal

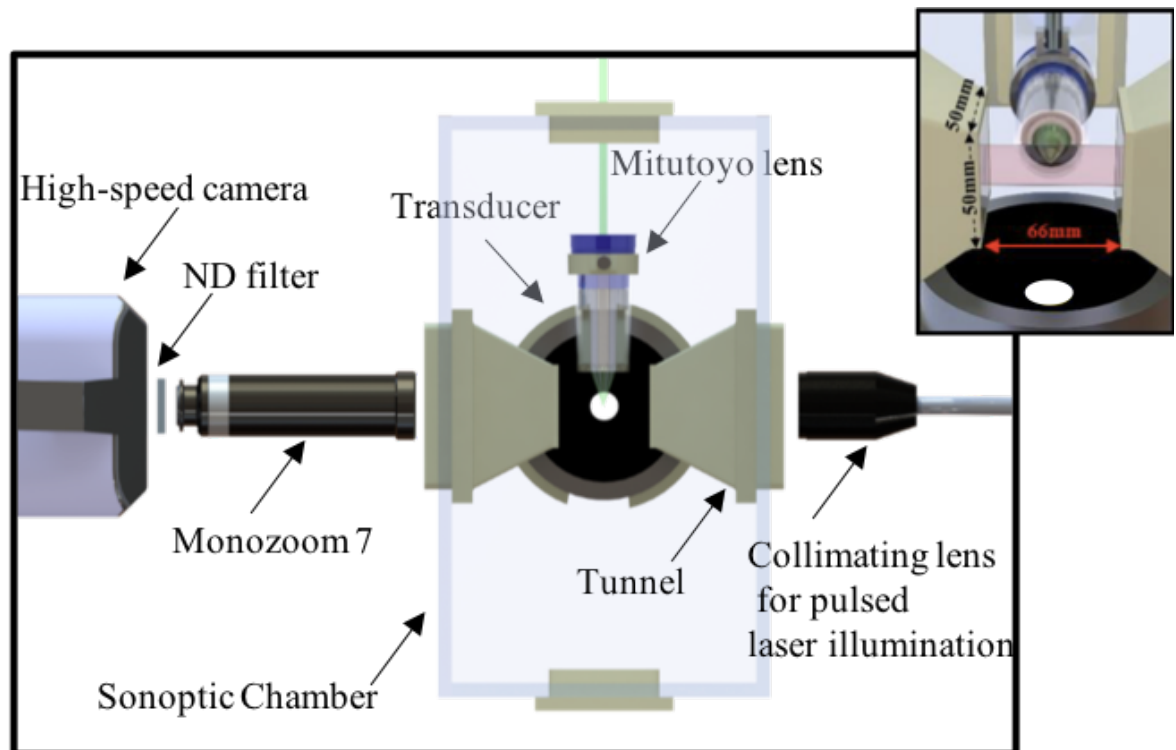


Figure 2.2: Top view schematic representation of the sonoptic chamber, including high-speed camera and pulsed laser illumination configuration. Inset top right shows the HIFU transducer and the hole within which needle hydrophone or PCDs can be located, as well as nucleation objective lens positioned inside a sealed unit. The approximate distance between the two tunnels (arrowed) is ~ 66 mm, which is large compared to the 4.9 mm measured focal width during free field mapping of the acoustic field with a needle hydrophone (Precision Acoustics). The neutral density (ND) filter is used to adjust the brightness of the image by reducing transmission of the pulsed laser illumination. Adopted and modified from [1].

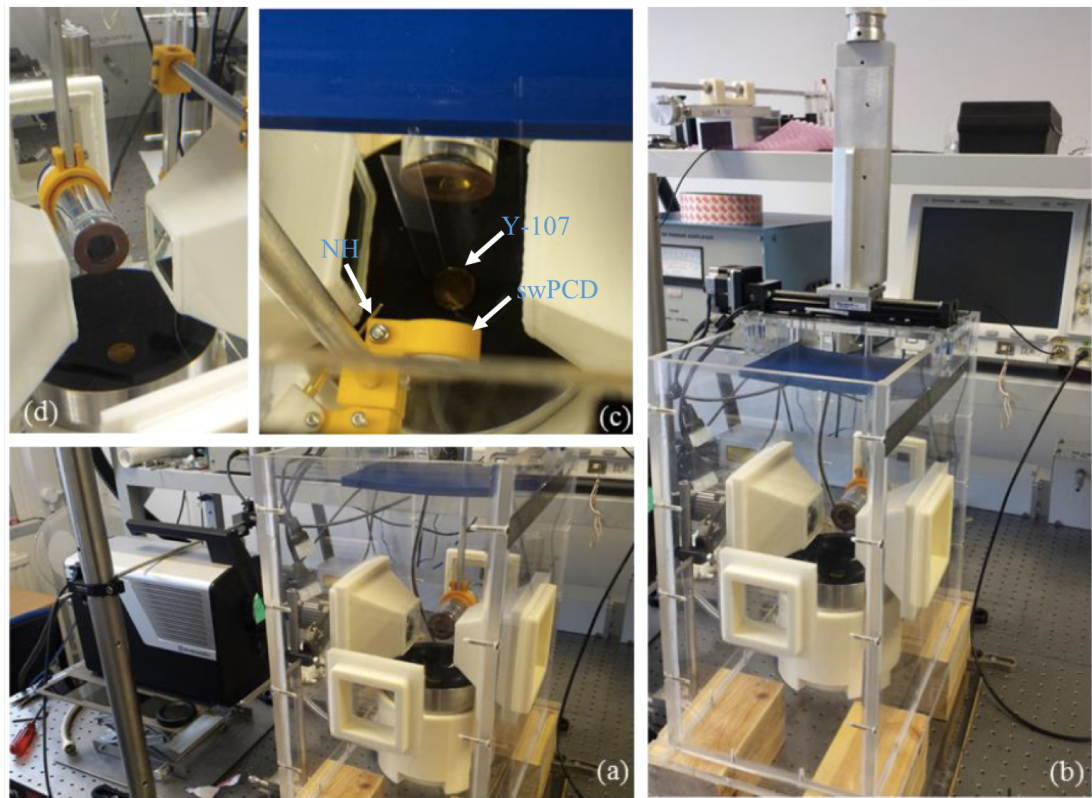


Figure 2.3: Photographs of sonoptic chamber (a) Shimadzu HPV-X2 high-speed camera and sonoptic chamber. (b) Displayed top centre of the photo, is the xyz manipulator that was used to micro position the laser nucleation optics relative to the transducer focus. Also shown on the first shelf is the power amplifier, oscilloscope, and on the second shelf, (top left) a secondary xyz manipulator for adjustment of the needle hydrophone/PCD. (c) needle hydrophone and swPCD (arrowed) secured to a xyz manipulator via a rapid prototyped fixture. Sonic Concepts Y-107 PCD (gold circle, arrowed, also seen in Fig. 6.1) is positioned inside the through opening of the HIFU transducer. In the top of the chamber, acoustic absorber is placed to minimise reflections, as shown in (c,d) Laser nucleation objective, placed in a sealed unit to prevent water damage and the Sonic Concepts HIFU transducer, described in §2.1, positioned such that the focal region is centred between two tunnels. Taken from [1]

size of the bubble, which is verifiable through high-speed imaging (described below). In this way, reproducible bubble collapse shock waves from bubbles of similar maximum radius, may be generated. This regime of bubble activity is used in Chapter 3 to assess the convolution artefacts imposed by the impulse response to the needle hydrophone during bubble collapse shock wave detection. In Chapter 6 it is used to conduct performance evaluation of different swPCD designs with regards to choice of backing layer and matching layer, as well as for comparing the final stage swPCD design to the commercial Y-107 Sonic Concepts PCD. Further details regarding this cavitation regime, and considerations made during collection of data, are featuring in Chapter 3 and 6.

For the latter regime, laser-nucleation of acoustic cavitation, a laser pulse of energy below the breakdown threshold (thereby insufficient to generate a plasma), is co-incident to the combined focal region with a burst of 50-90 cycles HIFU (depending on the driving frequency), and serves to nucleate a single cloud of acoustic cavitation in Chapter 4 and 6. A second independently positioned cavitation cloud is nucleated in Chapter 5 by splitting the laser beam and focusing it via a second long working distance objective lens (also $50\times$ 0.42 NA Mitutoyo, Japan) mounted on a second xyz manipulator (Velmex Motor, Bloomfield, NY, USA), described in detail in §5.1.

2.3.1 Calibration of bubble nucleation

As mentioned in *Overview of Thesis*, previously CavLab has reported cavitation observations where the activity consisted of a cloud of bubbles approximately oscillating in-phase and collapsing sub-harmonically. This resulted in multi-fronted shock waves, which were deemed as a complicating element when attempting to reconcile detected acoustic emissions to source bubble dynamics. Therefore, in this thesis acoustic emissions from cavitation bubbles, which primarily consisted of single fronted shock waves, were analysed. This also facilitated the use of accepted bubble models, such as the Gilmore equation [19] and the Keller-Miksis equation [118], which both assume a spherically symmetric bubble. From the solutions of the bubble models, expected acoustic emissions were computed and compared to measurements.

Laser-plasma mediated vapour bubbles

As described in §2.3, the energy of the nucleation laser was increased to surpass the optical break down threshold of the host medium, such that a plasma was formed at the focus of the objective lens to the nucleation laser. To focus the image at the location where the laser-plasma mediated vapour bubble was nucleated, a needle was attached to the end of a steel rod and positioned using the xyz manipulator approximately midway between the tunnels, Fig. 2.2. The nucleation laser was focused at the tip of the needle, which was subsequently removed and switched with the needle hydrophone positioned at the detection distance. The laser was adjusted such that a single spherical bubble was nucleated at the focus, however, due to variations in the energy of the nucleation laser, the maximum radius of bubbles varied. Only bubbles which were of a

maximum radius equal to $R_{\max} = 365 \pm 4 \mu\text{m}$, collapsing symmetrically with the emission of a single fronted shock wave, and a spherical rebound were considered for analysis. More than 5 laser-plasma mediated vapour bubbles were nucleated at each propagation distance, from which one measurement was selected with similar maximum radius at each propagation distance: 30 mm, 40 mm and 50 mm. This was confirmed using high-speed imaging, Fig. 3.3a, and facilitated propagation effects to be assessed. Due to the elliptical focus of the nucleation laser objective lens, some of the bubbles became elliptical during the collapse emitting a double fronted shock wave, followed by splitting of the bubble, Fig. 3.4. This was considered as a complicating element, which was not well described by the bubble theory used to compute the collapse dynamics as well as acoustic emissions, and it was therefore not analysed any further. The frame rate of the high-speed imaging observations shown in the proceeding chapters, is stated in the respective captions.

Laser-nucleated acoustic cavitation

For the second regime of cavitation studied in this thesis, the experimental procedure was as follows: The nucleation laser energy was adjusted such that a single bubble was generated at the focus of the driving HIFU field. In the case when the energy of the nucleation laser was too high, multiple bubbles were nucleated along the focus of the nucleation laser. Such data were not considered any further in Chapter 4 as the purpose was to analyse the cavitation noise spectrum from a single bubble, and relate the spectral features to the source bubble dynamics. In Chapter 5, a two bubble system is studied to understand effects of spectral peak suppression caused by spatially configured cavitation bubbles. The two bubbles are positioned in the HIFU field using a second objective lens, as described above. The amplitude of the driving HIFU field is adjusted such that the nucleated cavitation bubble responds in the desired sub-harmonic regime. This is achieved by gradually increasing the amplitude of the driving field, and always nucleating the bubble activity approximately in the same location. The nucleation process was deemed sufficiently optimised when the bubble was responding consistently in the same sub-harmonic regime for at least 6 consecutive collapses. Measuring acoustic emissions for this duration was sufficient to acquire adequate resolution in the analysed cavitation noise spectra, as discussed

in §4.1.1. The overall characteristics of the measurements are repeatable, such as sub-harmonic collapses result in periodic shock waves, however the number of repeating sub-harmonic spherical collapses emitting single fronted shock waves may vary. The frame rate of the high-speed imaging observations shown in the proceeding chapters, is stated in the respective captions.

For this nucleation technique, the equilibrium radius of the resulting bubble is difficult to assess directly as it is in part nucleated by presence of the acoustic field which is driving it continuously during the high-speed imaging observation. After the acoustic exposure, the bubble quickly dissolves back in to the host medium such that a meaningful measurement of the equilibrium radius cannot be done using high-speed imaging. However, the cavitation observations analysed in Chapter 4, are studied using the Keller-Miksis equation in Appendix B, which suggests that the nucleated bubbles have an equilibrium radius approximately equal to the resonance size of the acoustic field ($4.4 \mu\text{m}$), as discussed in §1.2. This nucleation technique does not facilitate precise adjustment of the equilibrium radius, but rather nucleating bubbles of approximately resonance size. Therefore, bubbles at twice the resonance frequency cannot be selectively studied. Such bubbles sizes are of interest as the large bubble theory remains a prevalent mechanism thought to be responsible for the sub-harmonic spectral features, as discussed in §1.4.4. Selective nucleation of large bubbles combined with precision high-speed imaging observations and acoustic measurements, require a re-design of the experimental setup and is outside the scope of this work. It is worth to note that Lauterborn indicated that previous high-speed imaging observations failed to identify bubbles at twice the resonance frequency in unprepared liquids, which is in agreement with the observations presented in this thesis [81].

2.4 High-speed imaging

High-speed shadowgraphic imaging is undertaken at up to 10×10^6 fps (400×250 pixels) with 256 images per sequence (HPV-X2, Shimadzu, Japan), and each frame is illuminated by synchronous 10 ns laser pulses (632 nm, red) (CAVILUX Smart, Cavitar, Finland) determining the effective temporal resolution, Fig. 2.2. The short duration of the illumination pulse also enables the imaging system to capture changes in the refractive index, as a result of the propagating

acoustic field ², and acoustic emissions from cavitation, Fig. 2 [9, 119]. This is commonly known as shadowgraphic imaging.

In terms of objective lenses, a Monozoom 7 lens system (Bausch & Lomb, Rochester, NY) was used to resolve the bubble activity when higher magnification and resolution was required. To facilitate a larger field of view, such that HIFU propagation as well as shock wave emission from the bubble activity could be visualised, a macro-objective lens (Zeiss 100mm f2 Makro-Planar Milvus ZF.2, Oberkochen, Germany), was used. The specific objective lens configuration applied to the different cavitation observations, is stated in the respective chapters. A delay generator (DG535, Stanford Research Systems, USA) provides electronic triggering to synchronise each of the instruments.

2.4.1 Dark pixel counting algorithm

To analyse high-speed imaging data, a dark pixel counting algorithm was created in MATLAB[®] 2016a (The Mathworks, Inc., Natick, MA, USA) ³. The script used in this thesis was inspired by a previous version published in [120], and the working principle may be listed by the following bullet points:

- Read all 256 images.
- Show image in the middle of sequence where bubble is visible.
- Select section of image to be analysed further containing the bubble.
- The bubble appears as black in the images, and the background is grey, Fig. 2. Apply black and white filter, for which the threshold is adjusted to get an accurate representation of the bubble radius. If the threshold is too low, the bubble becomes artificially large, and if the threshold is too high the bubble is not detected by the algorithm. This is particularly true

²In Appendix C shadowgraphic high-speed imaging is used to characterise aspects of the acoustic field for another transducer, the medium of propagation, and phase characterization of a needle hydrophone. This work originally featured as a conference proceeding; *K. Johansen, J. H. Song, P. Prentice. "Characterising focused ultrasound via high speed shadowgraphic imaging at 10 million frames per second". In IEEE Ultrasonics Symposium, pp. 1-4. 2016.*

³The dark pixel counting algorithm script is found in Appendix E.4

when the bubble approaches and rebounds from the collapse, because the boundary of the bubble becomes blurred.

- After thresholding, all dark pixels are counted in each image, so that the area of the bubble in each image is known.
- The images are calibrated to an object of known size, for instance the needle hydrophone.
- By approximating the bubble as a circle the radius is estimated for each frame.

The frame rate determines the Nyquist frequency, which may be expressed as $f_{\text{nyq}} = \text{fps}/2$. This is the limit frequency that the high-speed imaging can resolve in the bubble dynamics. For instance, in Chapter 4 the driving frequency is $f_0 = 692$ kHz and the cavitation activity is imaged at 5×10^6 fps. This allows for radial dynamics up to 2.5 MHz to be sufficiently sampled, and meaningfully compared over an extended bandwidth to a numerical simulation, which is done in Appendix B.

2.5 Acoustic detectors

Three different detectors are used through this thesis; The needle hydrophone (fully described in §3.2.2), Y-107 Sonic Concepts PCD (described in §6.2, Fig. 6.1), and swPCD (described in §6.2, Fig. 6.5a). Acoustic emissions were collected by either using a second xyz manipulator to position detector(s) relative to the nucleation site, or within the central hole through the HIFU source as described in §2.1. An example showing how the different detectors (arrowed) are fixed relative to the nucleation site, is shown in Fig. 2.3c. The specific detector(s) used, and the positioning, is described in the individual chapters. The detectors are connected to an oscilloscope (MS07104A, Agilent Technologies, USA), and data collected at 4 GSs^{-1} .

Chapter 3

Deconvolution of acoustically detected bubble collapse shock waves

As described in *Overview of Thesis*, a 2014 paper from our research group reported that periodic shock waves emitted by acoustic cavitation is a mechanistic source of the sub-harmonic signal [9]. A sample of high-speed images from these experiments is shown in Fig. 2, however, detection of acoustic emissions were at a preliminary stage. This motivated the current work on how to treat detected bubble collapse shock waves, such that their contribution to the acoustic cavitation emission may be quantitatively analysed, in particular for hydrophones with a non-flat frequency response ¹.

¹The results presented in this chapter features in **K. Johansen, J. H. Song, K. Johnston, P. Prentice, Deconvolution of acoustically detected bubble-collapse shock waves, *Ultrasonics*, 73, 144-153, 2017.** However, the materials and methods section is different from the published article to limit repeating sections in the proceeding chapters.

3.1 A brief introduction to shock waves

A shock wave is an acoustic disturbance which propagates (at least initially) faster than the local speed of sound in the host medium, and is characterised by a sudden, almost discontinuous change in pressure, temperature and density [2]. The phenomenon can broadly be categorised as; (1) *Moving shocks*, which are shock waves propagating in a stationary medium, generated by two bodies of gas at different pressure, such as a balloon bursting. (2) *Bow shocks* (detached shocks), which are curved shocks forming a small distance in front of a moving body, for instance a bullet. (3) *Attached shocks*, which are shock waves that appear to be attached to the tip of a sharp supersonic object. (4) *Detonation wave* (blast wave), which are different from shock waves caused by supersonic objects, as the propagation of the shock wave is driven by a trailing exothermic reaction behind the shock front, for example caused by a trinitrotoluene (TNT) explosion. Figure 3.1a shows a typical detonation wave with the sharp change in pressure from A to B, followed by a negative phase. The negative phase is caused by an over-expansion of the shocked host medium, generating a partial vacuum such that air is sucked in, which is commonly known as the ‘blast wind’ and it may cause windows to shatter outwards [121].

Shock waves are currently being used in medical therapy by extra corporal shockwave lithotripsy (ESWL) to treat urinary and kidney stones by physically disintegrating them. A typical treatment consists of 1500 – 3000 shock waves focused towards the target region, with shock waves characterised by an abrupt rise (~ 10 's of ns) in pressure (~ 40 MPa), which only lasts for

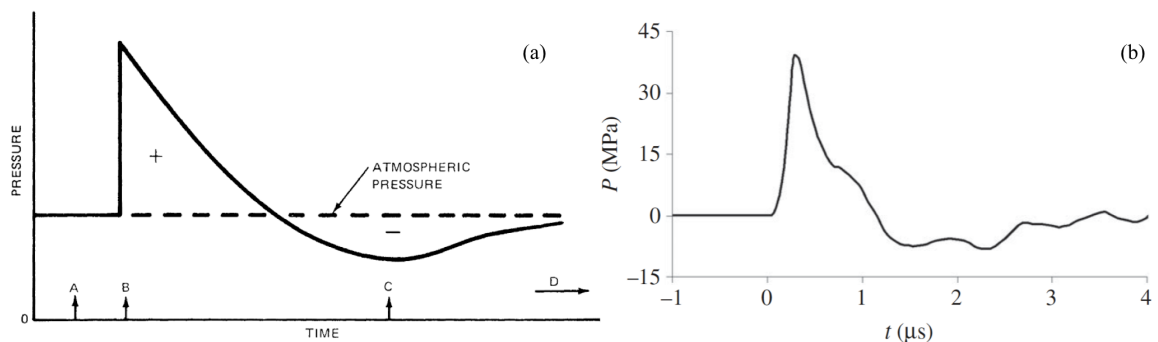


Figure 3.1: (a) Blast wave pressure plotted against time. Taken from [2]. (b) Example of lithotripsy shock wave used in medical therapy. The shock wave is characterised by an abrupt rise in pressure (~ 40 MPa), followed by a longer tensile phase (~ -8 MPa). Taken from [3].

short durations ($\sim 1 \mu\text{s}$), followed by a longer ($\sim 3 \mu\text{s}$) trailing negative phase ($\sim -8 \text{ MPa}$), Fig. 3.1b.

The trailing negative phase is well documented for the shock waves generated during lithotripsy, and it is accepted that this represents a tensile phase which is caused by medium response to a strong compressive pulse, although diffraction at the lithotripter aperture also provides a contribution to the tensile phase [122]. In some cases, the negative phase from lithotripsy shock waves can even nucleate bubbles in the host medium, which are then forced in to a regime of high amplitude oscillations with intervening collapses, during subsequent shock wave excitations [3]. Enhanced utilisation of cavitation mediated effects may facilitate controlled fragmentation of stones and minimise potential tissue damage [123]. Other mechanisms thought to be responsible for breaking up stones include spallation, shear stress and squeezing. Indeed features of lithotripsy are similar to histotripsy, discussed in §1.5.4, where high amplitude acoustic pulses are used to nucleate cavitation, which is the primary mechanism responsible for tissue destruction. Lithotripsy treatment plans are developed by precisely measuring the characteristics of shock waves produced by the Litotripter using a hydrophone. Measurements include rise time, which is the time it takes to go from 10% to 90% of PPA, full width half maximum (FWHM), which is the time it takes to rise and fall to 50% of PPA, peak positive pressure, and peak negative pressure.

In many reports, acoustic detection of the bubble collapse shock waves is undertaken with a PVdF needle-type hydrophone [22, 124–130], and an apparent negative phase indicated within the profile [126–132], trailing the positive compressive pulse that characterise shock waves generally. The negative phase is not often discussed in any detail, but could be interpreted as the detection of a tensile pressure phase, generated via medium response to the propagation of a compressive pulse.

3.2 Materials and methods

3.2.1 Bubble regimes

In this Chapter, laser-plasma mediated vapour bubbles were generated by focusing a sufficiently energetic laser-pulse which exceeded the optical break down threshold of the host medium, 4.0 ± 0.2 mJ, where the error is attributed to instrumental fluctuations in the pulse energies generated, as described in §2.3. This allowed for repeatable generation of reproducible bubble collapse shock waves, unlike those generated from an acoustically driven cavitation cloud, Fig. 2. Hence, this nucleation technique is used as a more reliable source of bubble collapse shock waves during assessment of detector deconvolution for the commercial PVdF needle hydrophone used throughout this thesis.

3.2.2 Needle hydrophone

A PVdF needle hydrophone (1.0 mm diameter, 28 μm thick active element, supplied with pre-amplifier, Precision Acoustics Ltd, UK), with end-of-cable calibration for both magnitude and phase over a bandwidth of 125 kHz - 20 MHz in 25 kHz increments, Fig. 3.2 (National Physical Laboratory (NPL), 2016), mounted on an xyz manipulator, is positioned vertically over the bubble site to minimise reflections from the front face of the laser focusing lens unit, Fig. 2.2. The fluctuations in both magnitude and phase illustrate the non-flat response of the hydrophone, and the need for detector deconvolution when measuring a broadband signal. Precision Acoustics Ltd define the magnitude response of the needle hydrophone to be flat when the variation is less than ± 2 dB². As such, the magnitude response to the hydrophone in the frequency range 4 - 12 MHz, may be considered flat, with the fluctuations occurring at < 4 MHz and > 12 MHz, Fig. 3.2. Precision Acoustics Ltd does not benchmark the flatness of the phase response, and no claim is made with regards to its characteristics. However, it is seen from the calibration that in the frequency range where the magnitude response is to be considered flat, the phase response is limited to $\sim 10^\circ$ variation. Below 4 MHz, there is a $\sim 50^\circ$ variation in the phase response,

²On the website to Precision Acoustics Ltd they write frequency response, and not magnitude response, however it is likely that this is just an example of mixed terminology as all the information provided about the hydrophone is concerned with its magnitude response (sensitivity), and the variation in phase response is typically not given in dB.

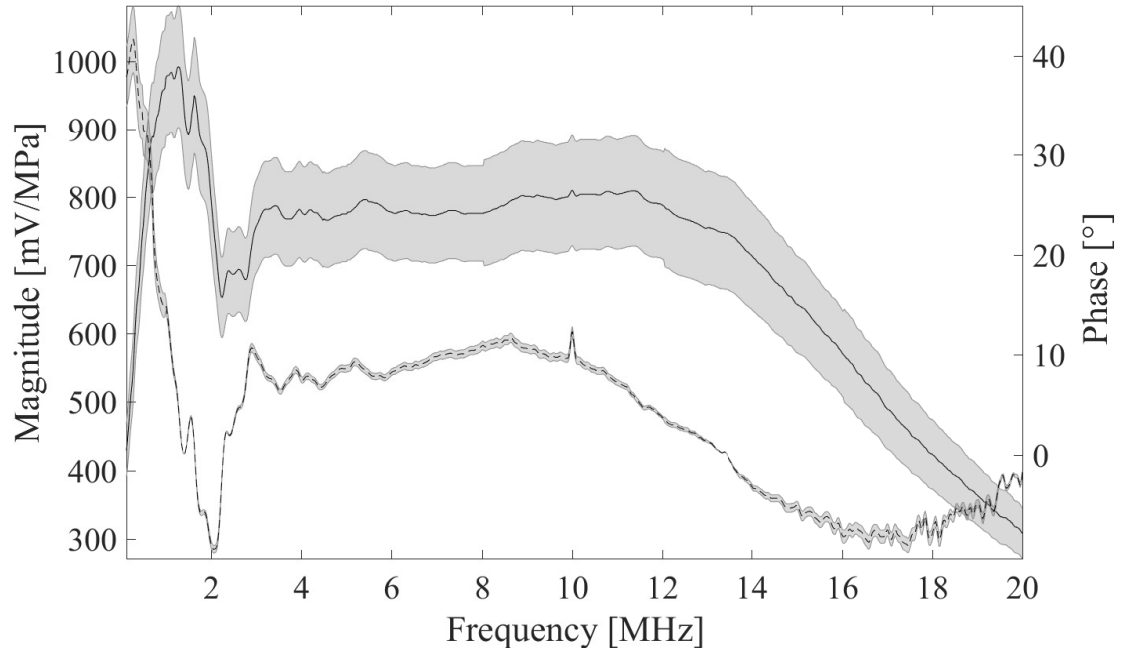


Figure 3.2: End-of-cable magnitude (solid) and phase (dash) response for the needle hydrophone and pre-amplifier, over a bandwidth of 125 kHz to 20 MHz in 25 kHz increments. Uncertainties are represented by the grey shading at 9 – 12 % for the sensitivity and 4 – 8 % for the phase, as provided by National Physical Laboratory (NPL). Taken from [117].

and this will distort the detected temporal profile of a shock wave containing these frequency components.

3.2.3 High-speed imaging and acoustic measurements

For high-speed imaging the Monozoom 7 lens system (Bausch & Lomb, Rochester, NY), facilitating spatial resolution at $7.6 \pm 0.1 \mu\text{m}$ per pixel, was used³. This allowed the HPV-X2 camera, which offers 256 frames per image sequence, to sufficiently sample the dynamics of a single collapsing bubble for modelling purposes, as described in §3.2.6. Much of the literature on this type of experiment relies on the amalgamation of frames from a number of different high-speed sequences of different bubbles, under the assumption that each bubble reaches an equivalent maximum radius and undergoes an equivalent collapse [22, 133].

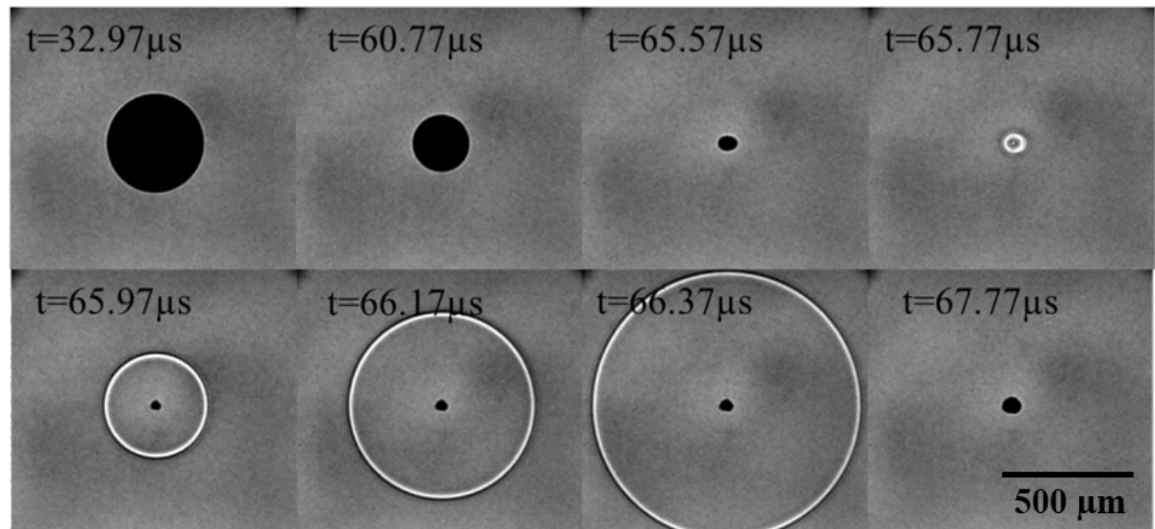
Acoustic bubble collapse shock wave measurements are undertaken at distances of 30, 40

³Many thanks to Dr Keith Johnston for help with collecting experimental measurements, and Dr Jae Hee Song with implementing the NPL calibration for deconvolution. The author contributed with the Gilmore model, computation of bubble collapse shock waves and all analysis of experimental data and corresponding discussion, particularly the negative phase of a bubble collapse shock wave.

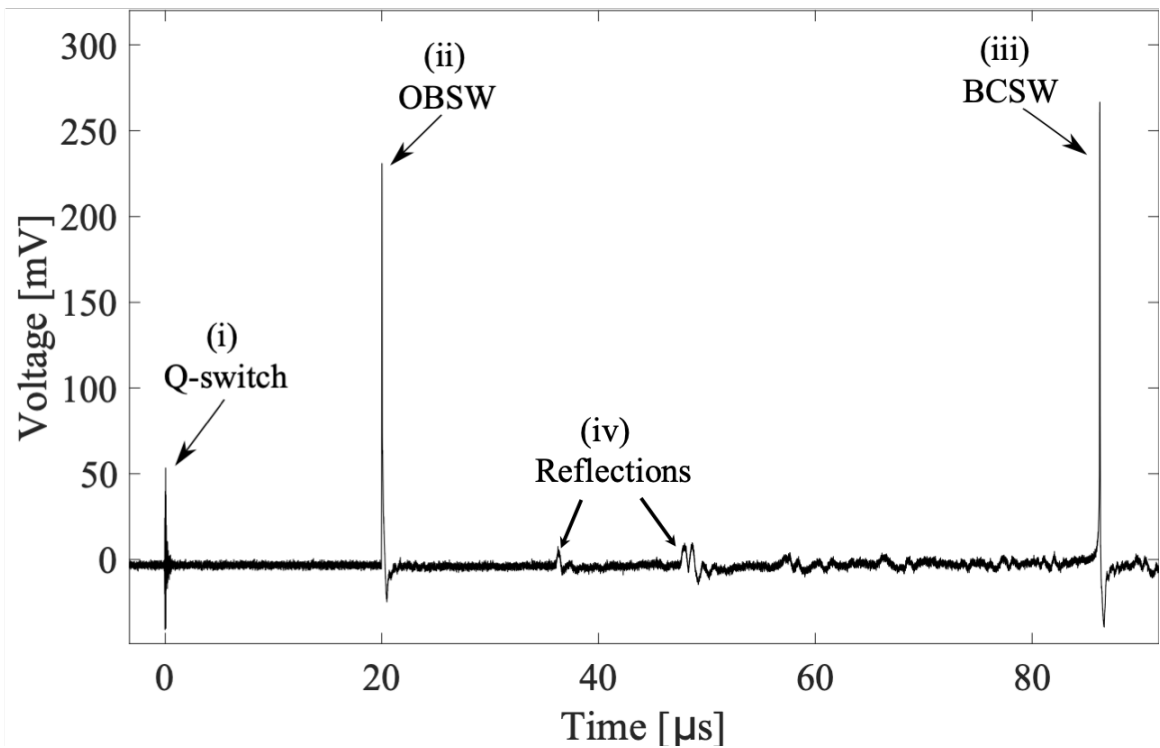
and 50 (± 0.5) mm. At these distances the angle subtended by the 1 mm active area of the needle hydrophone is $< 1^\circ$, and the shock wave may be assumed planar to a first approximation. At shorter distances, the curvature of the shock wave would have a pronounced effect on the measured characteristics, including the FWHM, through geometric spreading across the active area.

Fig. 3.3a are representative frames extracted from a single high-speed image sequence, captured at 5×10^6 fps, with each frame exposed for 10 ns (effective temporal resolution). The criteria for a laser-plasma mediated vapour bubble collapse and bubble collapse shock wave to be included in the dataset from which profiles are considered, are (i) an $R_{\max} = 365 \pm 4 \mu\text{m}$, Fig. 3.3a at 32.97 μs , (ii) single fronted bubble collapse shock wave generation, 3.3a from 65.97 - 66.37 μs , and (iii) a spherical post-collapse rebound, 3.3a at 67.77 μs . The stated inclusion criteria was arrived at for the following reasons: (i) This was the bubble size that had the smallest variation in maximum radius, at the different propagation distances. (ii,iii) The solution to the Gilmore equation, which is used to model the collapsing bubble, assumes a spherical symmetric bubble, and computes a spherically symmetric acoustic emission, §3.2.6. Validation of the deconvolution process for the needle hydrophone, described in §3.2.5, is achieved using the computed acoustic emissions. Complicating elements, such as double fronted shock waves are not considered for comparison to the computed acoustic emissions in Chapter 3, as the theory used does not describe these events. It is well known that the size of a bubble is critical in determining the amplitude of the bubble collapse shock wave generated when it collapses [128]. To make meaningful comparisons between bubble collapse shock wave profiles at different propagation distances, equivalent R_{\max} 's are therefore critical, (i). It is also well reported that due to spherical aberration, there is an extended elliptical focal region for a laser-pulse passed through an objective lens. The plasma generated, and the laser-plasma mediated vapour bubble that forms, will therefore be slightly elliptical [133], which is seen at 65.57 μs , Fig. 3.3a.

Fig. 3.3b is the voltage trace recorded by the needle hydrophone during the laser-plasma mediated vapour bubble collapse of Fig. 3.3a. Notable features are arrowed, including (i) the Q-switch of the laser, indicating laser-pulse emission, which is taken as $t = 0 \mu\text{s}$ for all data presented, (ii) the optical breakdown shock wave, indicating laser absorption and plasma formation, and (iii)



(a)



(b)

Figure 3.3: (a) Representative high-speed images of an laser-plasma mediated vapour bubble collapse, bubble collapse shock wave generation and rebound, recorded at 5×10^6 fps. $R_{\max} = 364 \mu\text{m}$ for this bubble collapse. (b) A full hydrophone voltage trace, recorded at 30 mm, with key features described in the text, arrowed. Note, there is $\sim 20 \mu\text{s}$ propagation time for the shock waves between the high-speed imaging capture and hydrophone detection. The ripples between the two shock waves are reflections from the surrounding.

the bubble collapse shock wave, detection of which is the topic of this work.

A common observation made during the collection of this data was that in the event that the plasma generated on laser-pulse absorption is too extended, the collapse could occur at two separate locations, generating a double-fronted shock wave. Moreover for such cases, the rebounded bubble will have fragmented, and such data was not considered for comparison to a computed bubble collapse shock wave, as the Rayleigh-Plesset-like equations (discussed in §3.2.6) do not describe the dynamics of a splitting bubble in a satisfactory manner. An example of a split collapse is seen in Fig. 3.4. The high-speed images demonstrate how the bubble is elliptically shaped 200 ns before the collapse, and rebounds after splitting with the emission of a double-fronted shock wave (arrowed in the images). The final image shows the two fragments having expanded, and separated from each other. As the needle hydrophone is oriented with the tip towards the top-side of the image, and the elongated focus of the nucleation laser is orthogonal to that, the effect of the bubble collapse shock wave being double-fronted is reduced, compared to placing the needle hydrophone on axis with the focus of the nucleation laser (right side of high-speed images). In the voltage-trace, the double-fronted shock wave is manifested as a ‘bump’ on the back of the shock wave, before the apparent negative phase. The two fronts are not resolved in the voltage-traces, which is indicating that they are closely spaced.

3.2.4 Assessment of needle hydrophone rise time

An important characteristic of any detector used to measure a shock wave is the rise time, which may be defined as the time taken to rise from 10% of the maximum signal amplitude, to 90%, in response to a step function with zero-rise time⁴. If the rise time of a particular detector is not shorter than the physical rise time of the shock wave it is measuring, then a good estimate of the peak positive pressure amplitude of the shock wave, $PPPA_{SW}$, may not be taken. It is difficult to implement a step function experimentally, however, a good approximation can be realised using laser-plasma mediated vapour bubbles, and specifically the optical break down shock wave,

⁴The original version of this section featured as an Appendix in Song *et al* [48], however, for purposes of presenting the materials in a thesis format, the appendix has been modified to eliminate repeating paragraphs, and introduced in Chapter 3 which is primarily concerned with the detection of bubble collapse shock waves from laser-plasma mediated vapour bubbles.

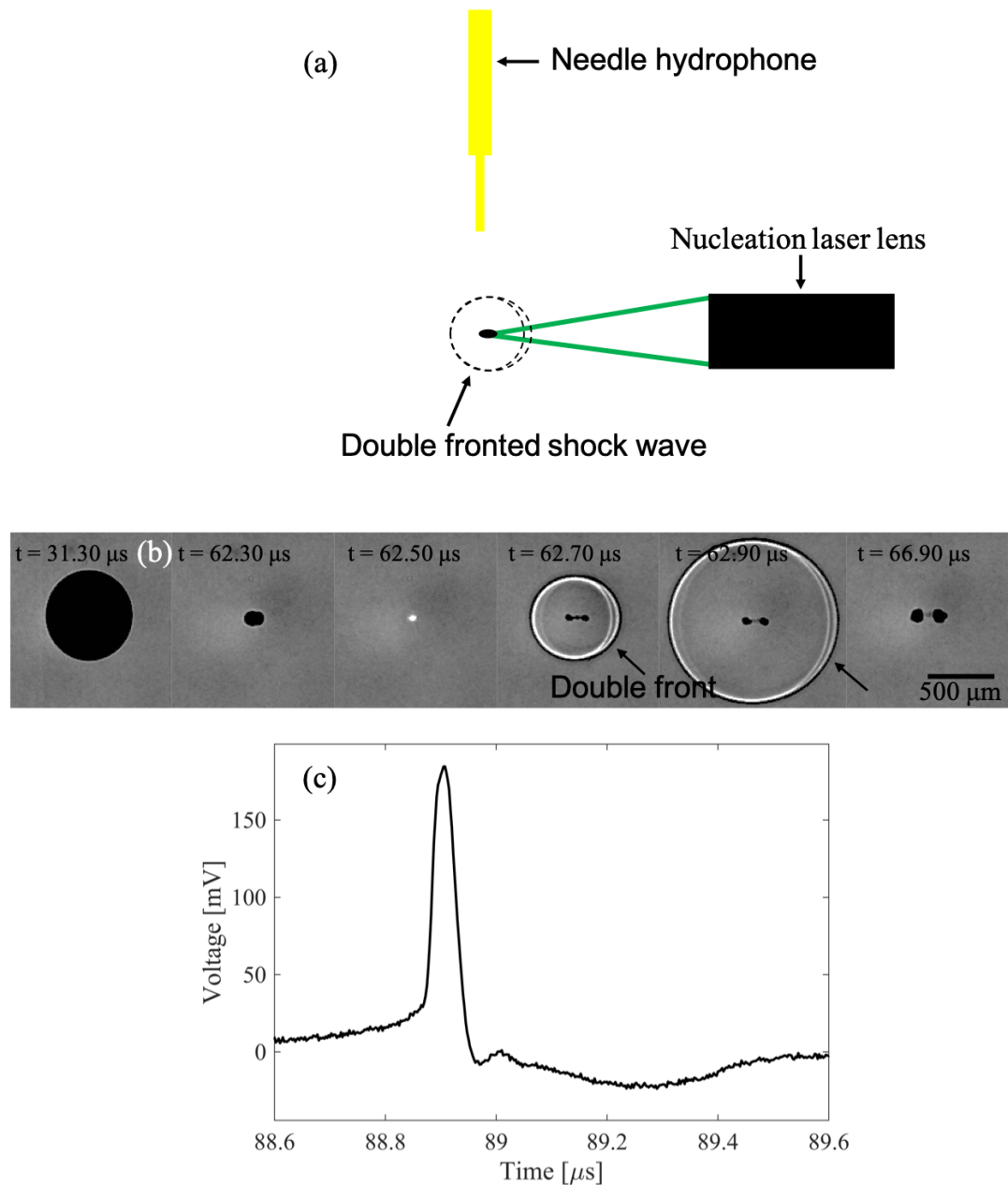


Figure 3.4: (a) Schematic diagram of nucleation laser lens generating a bubble which collapses with the emissions of a double fronted bubble collapse shock wave, and the location of the needle hydrophone. (b) Representative high-speed images of laser-plasma mediated vapour bubble collapse generating a double-fronted bubble collapse shock wave (arrowed), and splitting into two separate bubbles, recorded at 5×10^6 fps. The bubble had a $R_{\text{max}} = 342 \mu\text{m}$, which is $\sim 6\%$ smaller than the bubbles considered for further analysis in §3.3. (c) Voltage-trace of double-fronted bubble collapse shock wave. Effects of the shock wave being double-fronted is arrowed. Note, the needle hydrophone is oriented with the tip toward the top-side of the image as seen in (a), 40 mm away from the bubble with a $\sim 26 \mu\text{s}$ propagation time delay from high-speed image capture to hydrophone detection.

described in §3.2.3.

Thus, optical break down shock waves are used to assess the rise time of the needle hydrophone, and therefore its suitability for measuring rise time, FWHM and $PPPA_{SW}$ of bubble collapse shock waves from laser-plasma mediated vapour bubbles, and periodic shock waves from acoustic cavitation in the proceeding Chapters.

Through calculation and experiment with a pulsed laser similar to the experiments reported on in this Chapter (and Chapter 6), Vogel *et al.* [22] indicate an optical break down shock wave with a RT of ~ 6 ns and an initial $PPPA_{SW}$ in the order of a GPa, may be expected. To avoid damage to the hydrophone through exposure to such a high amplitude, the tip is located ~ 50 mm from the laser-plasma mediated vapour bubble location, during the acquisition of the data presented, Fig. 3.5b.

Fig. 3.5c depicts the optical break down shock wave and bubble collapse shock wave profiles. Clearly, the rise from ambient pressure for the optical break down shock wave is much sharper than that of the bubble collapse shock wave, as an approximation to a step function, with an $RT \approx 22.5$ ns measured from the detected profile between the red arrows (10 and 90% of peak voltage amplitude). As the physical optical break down shock wave itself has a non-zero RT, 22.5 ns can thus be taken as an upper bound for the actual RT of the needle hydrophone. The RT of the measured bubble collapse shock wave profile, Fig. 3.5b is ~ 73 ns, due to the gradual rise integral to the shock wave generated by a bubble collapse profile. The $PPPA_{SW}$ of the bubble collapse shock wave is therefore reasonably estimated, as opposed to that of the optical break down shock wave⁵.

3.2.5 Deconvolution of hydrophone voltage data

The voltage data recorded by the needle hydrophone, including the cavitation emission signal, will be convolved with the impulse response of the hydrophone, such that the raw voltage-time signal will be distorted. Shock waves, as broadband signals, are particularly susceptible to

⁵By extension, the $PPPA_{SW}$'s of the periodic bubble collapse shock waves (within the acoustic cavitation emission signal) in Chapter 4 and 5 are also reasonably estimated, within the limit of the calibration bandwidth of the needle hydrophone.

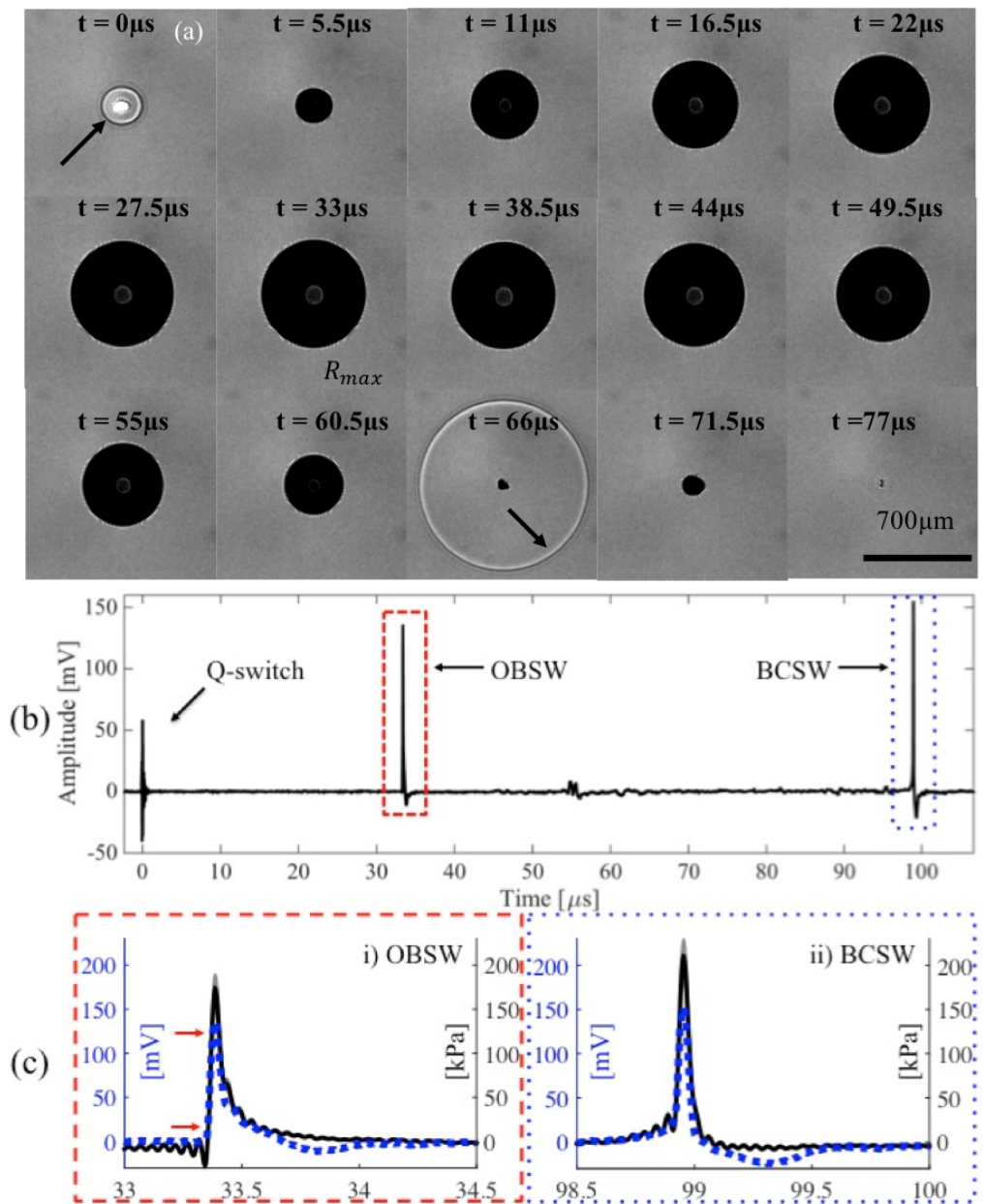


Figure 3.5: Approximation of the needle hydrophone rise time using an optical break down shock wave: (a) Representative frames from a high-speed image sequence, taken at 1×10^6 fps, showing the formation of a laser-plasma mediated vapour bubble and an optical break down shock wave (arrowed), with the laser Q-switch taken as $t = 0 \mu\text{s}$. The laser-plasma mediated vapour bubble continues to expand up to its maximum radius, captured at $33 \mu\text{s}$, followed by collapse and emission of a bubble collapse shock wave (arrowed). The bubble had a $R_{max} = 365 \mu\text{m}$. (b) The needle hydrophone trace detected, with the tip located ~ 50 mm from the laser-plasma mediated vapour bubble location. (c) Higher temporal resolution than in (b) of the optical break down shock wave and bubble collapse shock wave profiles (dotted blue). Hydrophone deconvolved shock waves are also presented (black with grey shading representing the uncertainty). The rise time of a device is defined as the time taken to rise from 10% to 90% of peak voltage amplitude, indicated by the arrows.

convolution artefacts, and require deconvolution to be adequately assessed, as discussed in §1.3 ⁶.

To distinguish between various data types, superscript notation is introduced, where ^v indicates a raw data voltage trace and ^p indicates the physical pressure signal. The usefulness of this notation is appreciated in Chapter 4 and 5, particularly. As such, the cavitation emission signal, $x_{\text{cav}}^v(t)$, detected by the NH in the voltage-time domain, is the convolution of the physical pressure signal, $x_{\text{cav}}^p(t)$, and the detector response, $h_{\text{NH}}(t)$.

$$x_{\text{cav}}^v(t) = x_{\text{cav}}^p(t) * h_{\text{NH}}(t) \quad (3.1)$$

Full waveform deconvolution is applied, according to,

$$\tilde{X}_{\text{cav}}^p(f) = \tilde{X}_{\text{cav}}^v(f) / H_{\text{NH}}(f) \times H_{\text{bpf}}(f), \quad (3.2)$$

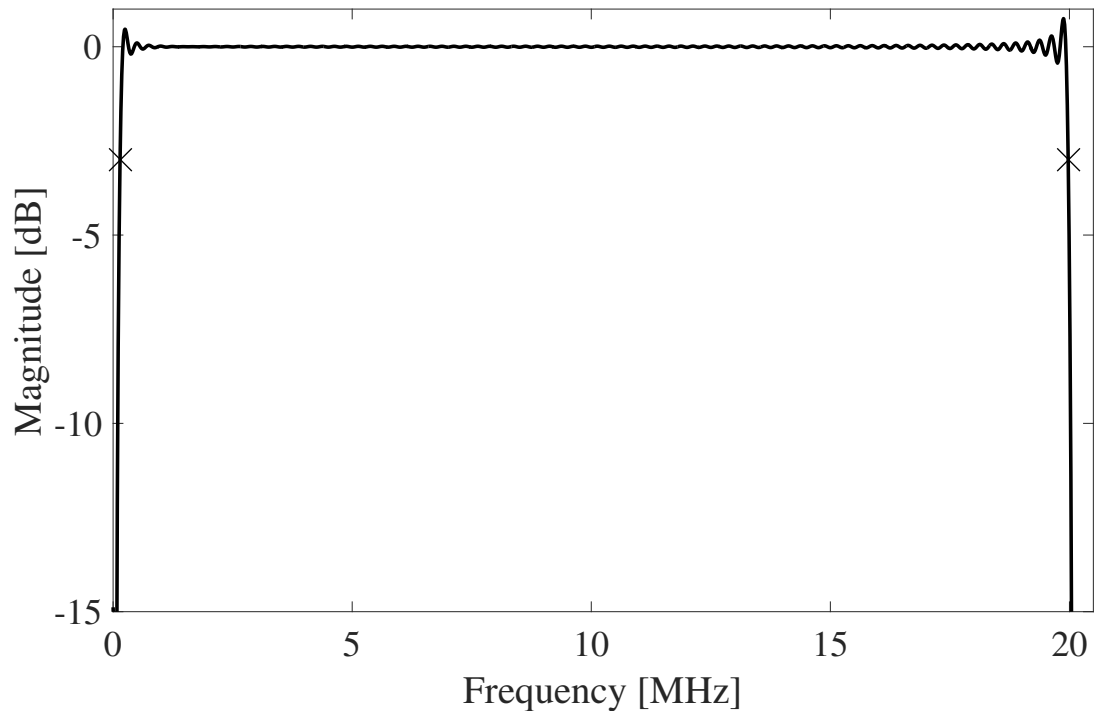
where $\tilde{X}_{\text{cav}}^p(f)$ is the estimated spectrum after deconvolution within the calibration bandwidth, $X_{\text{cav}}^p(f) = \text{FT}\{x_{\text{cav}}^p\}$ and $H_{\text{NH}}(f) = \text{FT}\{h_{\text{NH}}\}$, the complex (magnitude and phase) sensitivity, known for 125 kHz – 20 MHz. $H_{\text{bpf}}(f)$ is a bandpass filter of the same bandwidth as the needle hydrophone calibration, Fig. 3.6a. The estimated deconvolved pressure time waveform, within the calibration bandwidth can then be obtained as $\tilde{x}_{\text{cav}}^p(f) = \text{FT}^{-1}\{\tilde{X}_{\text{cav}}^p\}$ ⁷. Magnitude-only deconvolution follows an equivalent process, assuming the phase, $\phi = 0^\circ$, for all frequencies of $H_{\text{NH}}(f)$. Estimated uncertainties for the time-waveform and spectral content to the deconvolved bubble collapse shock waves, are computed by using the uncertainties associated with the calibration in Fig. 3.2.

3.2.6 Rayleigh-Plesset-like equations and shock wave generation model

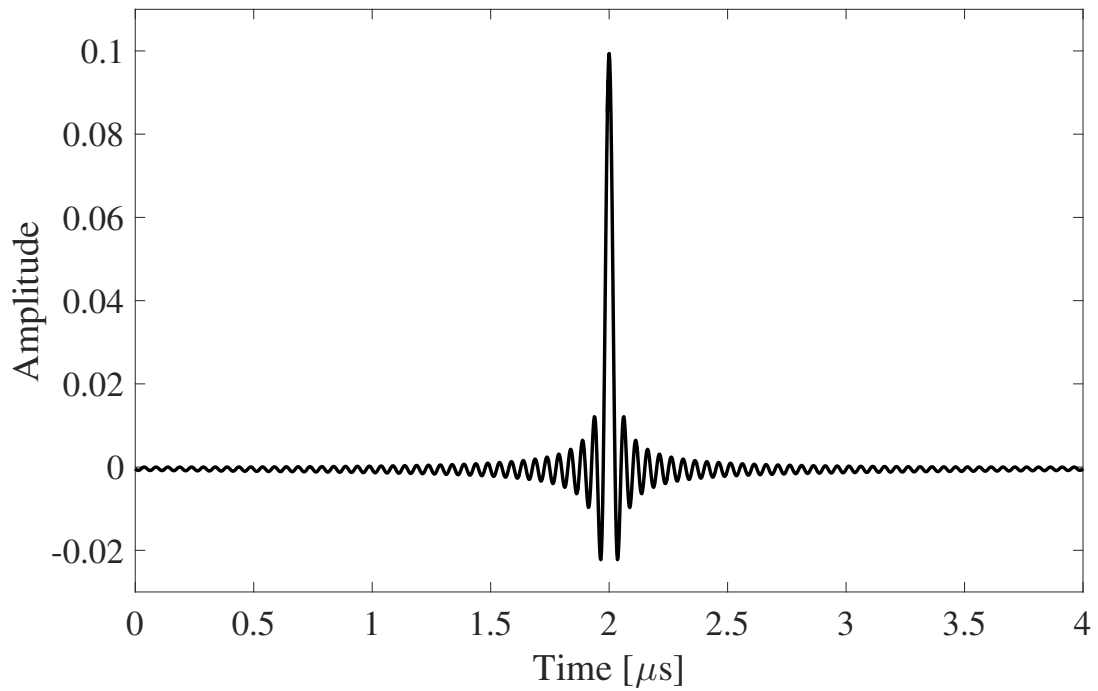
There are multiple Rayleigh-Plesset-like equations in the literature that account for liquid compressibility [19, 118, 134–136]. These equations become relevant when the Mach number \dot{R}/c_0 becomes ‘small’ during expansion [137], where, c_0 is the speed of sound far from the bubble,

⁶In Appendix A preliminary results for a method that uses bubble collapse shock waves to characterise the sensitivity of the needle hydrophone, is presented. This work featured as a conference proceeding; *K. Johansen, J. H. Song, P. Prentice. Blind deconvolution of a hydrophone with a bubble-collapse shock wave. International Ultrasonics Symposium (IUS) IEEE, pp. 1-4, 2017*

⁷Matlab script is found in Appendix E.3.



(a)



(b)

Figure 3.6: (a) Magnitude response of zero-phase bandpass filter, $H_{\text{bpf}}(f)$, with the -3 dB corner points, at 145 kHz and 19.9 MHz marked \times . (b) Impulse response to needle-hydrophone in the time domain.

and \dot{R} is the bubble wall velocity. Examples of first-order formulations of liquid compressibility are the Keller-Miksis [118] and Herring-Trilling [138] equations, whereas the Gilmore equation contains additional second order terms [19]. As the Gilmore equation depends on the liquid enthalpy at the bubble wall, it is well suited to studying inertial collapses [137]. Hence, the Gilmore equation is used in the work presented in the main chapters⁸. The formulation presented is taken from Kreider *et al.* with some modifications [135].

The Gilmore equation can be represented the following way:

$$\left(1 - \frac{\dot{R}}{C}\right) R\ddot{R} + \frac{3}{2} \left(1 - \frac{\dot{R}}{3C}\right) \dot{R}^2 = \left(1 + \frac{\dot{R}}{C}\right) H + \left(1 - \frac{\dot{R}}{C}\right) \frac{R}{C} \dot{H}, \quad (3.3)$$

where the overdot represents the time derivative, where R is the instantaneous radius, C and H are the instantaneous speed of sound and enthalpy evaluated at the bubble wall, respectively. A modified form of the Tait equation for the liquid state is used to express C and H explicitly [139]

$$p = p_0 + \frac{1}{b\Gamma} \left[\left(\frac{\rho}{\rho_0} \right)^\Gamma - 1 \right], \quad (3.4)$$

where p_0 is the ambient pressure, b and Γ are empirically determined constants, ρ and ρ_0 are the instantaneous and ambient densities of the liquid, respectively. $\Gamma = 6.5$ was chosen from data for water [139], and b is defined the following way $b = (\rho_0 c_0^2)^{-1}$.

The enthalpy h and the speed of sound c throughout the liquid can be defined as:

$$h = \int_{p_\infty}^p \frac{dp}{\rho} = \frac{c^2 - c_\infty^2}{\Gamma - 1}, \quad (3.5)$$

$$c^2 = \frac{dp}{d\rho} = \frac{\Gamma(p+B)}{\rho}, \quad (3.6)$$

where c_∞ is the speed of sound far from the bubble and $B \equiv ((b\Gamma) - p_0)^{-1}$. Evaluating h and c at the bubble wall, knowing that the pressure at the bubble wall p_w can be expressed as

$$p_w = p_i - \frac{4\mu\dot{R}}{R} - \frac{2\sigma}{R}, \quad (3.7)$$

⁸The Keller-Miksis equation is used for work presented in Appendix A and Appendix B, which demonstrates the validity of two different Rayleigh-Plesset-like equations, commonly used in the literature.

where p_i is the internal pressure in the bubble, μ is the shear viscosity of the surrounding liquid and σ is the surface tension at the gas-liquid interface. Assuming that the internal pressure is uniform, it can be represented as

$$p_i = \left(p_0 + \frac{2\sigma}{R_0} \right) \left(\frac{R_0^3 - mR_0^3}{R^3 - mR_0^3} \right)^\gamma, \quad (3.8)$$

where R_0 is the equilibrium radius of the bubble, m is the van der Waals core parameter, chosen as $m = 0.11$, and γ is the polytropic exponent. Now, the speed of sound and the enthalpy at the bubble wall can be explicitly expressed:

$$H = \frac{(b\Gamma)^{\frac{-1}{\Gamma}}}{\rho_0} \frac{\Gamma}{\Gamma - 1} \left[(p_w + B)^{\frac{(\Gamma-1)}{\Gamma}} - (p_0 + B)^{\frac{(\Gamma-1)}{\Gamma}} \right], \quad (3.9)$$

and

$$C^2 = c_0^2 + (\Gamma - 1)H. \quad (3.10)$$

This has been shown to be an adequate assumption, even for inertial collapses [140]. A recent finite volume investigation of the collapse of a laser bubble, demonstrated that there are differences in both the internal pressure of the bubble, and the maximum rebound radius, compared to that predicted by the Gilmore equation [141]. Evaporation, condensation, gas diffusion through the bubble wall, and heat conduction are neglected. The Gilmore equation was solved using ode45 Runge-Kutta algorithm in MATLAB[®] 2016a (The Mathworks, Inc., Natick, MA, USA)⁹.

The circle scatter plot of Fig. 3.7 is the radius measured from each frame of the high-speed sequence of the single laser-plasma mediated bubble collapse, represented in Fig. 3.3a. Other laser-plasma mediated bubble radius-time curves reported have been at higher frame rates, but the authors rely on compiling the curve from multiple sequences of different laser-plasma mediated bubbles, assuming identical bubble behaviour [22, 133]. An error is also assigned to the radius of the bubble, depicted as the shaded region of the star scatter plot, based on bubble boundary pixel ambiguity within each image. It is further noted that the minimum radius value, at $65.77 \mu\text{s}$

⁹The Matlab script is found in Appendix E.1

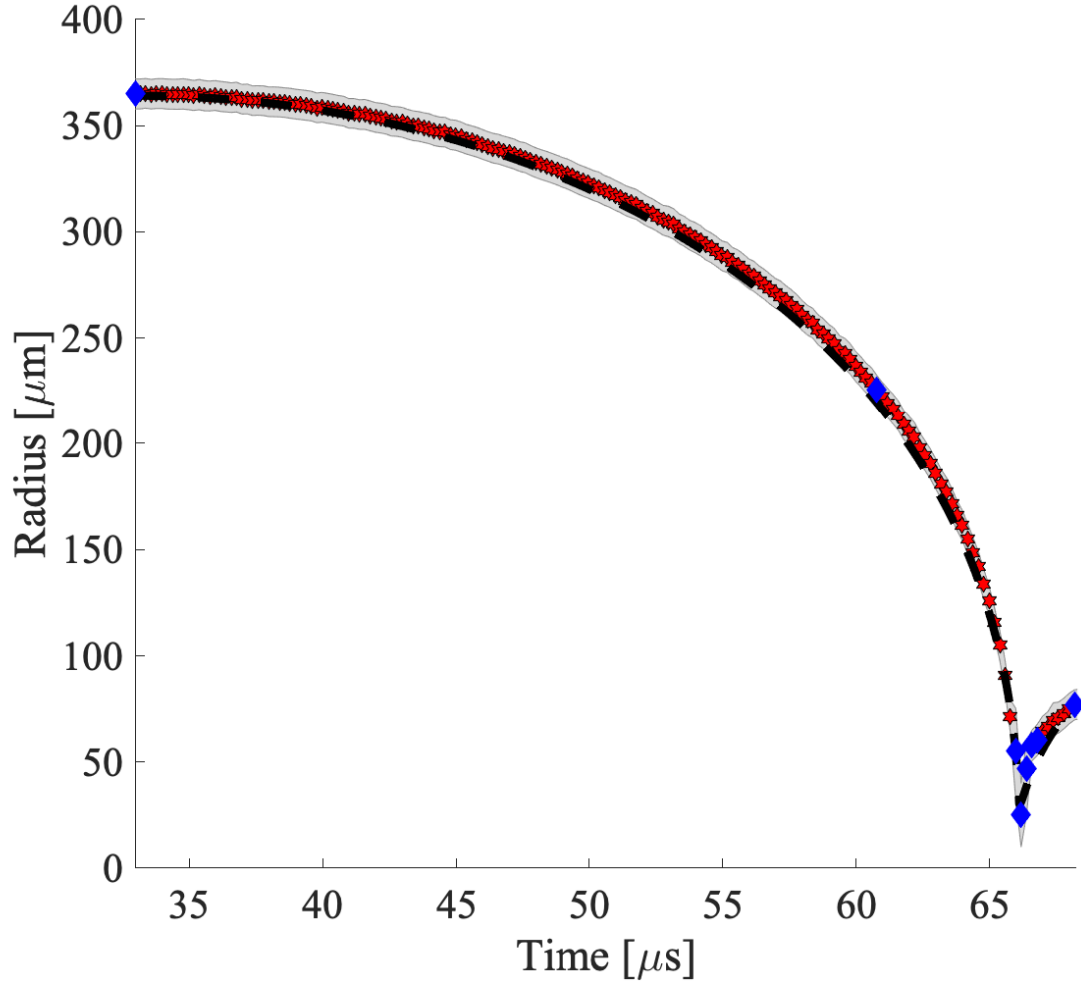


Figure 3.7: The experimental radius-time curve (red star and grey shading representing uncertainty), which was acquired using the dark pixel counting algorithm described in §2.4.1, of the bubble collapse depicted in Fig. 3.3a (blue diamonds are the data points of the images presented). The dashed black line curve is the best fit solution of the Gilmore equation with the following parameters, for water; $c_0 = 1484\text{ms}^{-1}$, $p_0 = 101\text{ kPa}$, $R_0 = 61\text{ }\mu\text{m}$; $R_{\text{max}} = 364\text{ }\mu\text{m}$; $\rho_0 = 998\text{ kg m}^{-3}$, $\gamma = 4/3$, $\sigma = 0.072\text{ Nm}^{-1}$ and $\eta = 0.001\text{ Pa s}$.

for the laser-plasma mediated vapour bubble of Fig. 3.3a, is likely underestimated as the bubble collapse shock wave generation and initial propagation obscures the bubble image. Regarding the spatial resolution ($7.6 \pm 0.1\text{ }\mu\text{m}$ per pixel) stated in §3.2.3, this is considered sufficient for modelling purposes, as the bubble never completely disappears during the collapse. Moreover, for the 200 ns period before and after the collapse, the measured radius is much greater ($\sim 50\text{ }\mu\text{m}$) than the minimum resolution.

Solving Eq. (3.3) for the bubble deflation, collapse and rebound, dashed curve of Fig. 3.7, allows the dynamics around the simulated collapse to be probed in more detail. As no mass

exchange is assumed between the gas-water interface, the radial velocity $v(r, t)$ in the surrounding fluid at a distance r from the centre of the bubble may be expressed as [71]:

$$v(r, t) = \frac{R^2 \dot{R}}{r^2}, \quad (3.11)$$

where r is the distance from the centre of the cavity, and since $v(r, t)$ is a conservative field, the following relationship holds;

$$\nabla \times v = \nabla \times \nabla \Phi = 0, \quad (3.12)$$

where Φ is the velocity potential of the surrounding fluid:

$$\Phi = -\frac{R^2 \dot{R}}{r}. \quad (3.13)$$

The velocity potential can be related to the the acoustic emission of a spherical wave, P_{rad} , the following way [131]:

$$P_{\text{rad}} = -\rho_0 \dot{\Phi} = \rho_0 \frac{R^2 \ddot{R} + 2R\dot{R}^2}{r}, \quad (3.14)$$

This approach is used to generate the simulated shock wave profiles, presented in dashed line, Figs. 3.8 – 3.10. Simulated shock wave profiles at all propagation distances are computed with a bandwidth of 100 MHz¹⁰. This method is also used to generate ‘synthetic shock waves trains’ to investigate the source of spectral features from acoustic cavitation in Chapter 4 and 5.

¹⁰The bandwidth of computed acoustic emissions is usually not given in most published cavitation literature, however, it should be disclosed to simplify comparison between different studies as the bandwidth/cut-off frequency influences the computed $PPPA_{\text{SW}}$, RT and FWHM. In contrast, experimental cavitation observations from different research groups are generally harder to directly compare because of the differences in experimental configuration.

3.3 Results

For the results reported below, bubble collapse shock waves are measured by the needle hydrophone, with the tip located at three propagation distances, $r = 30, 40$ and $50 (\pm 0.5)$ mm from the laser focus and the laser-plasma mediated vapour bubbles that form. A bubble collapse shock wave dataset was collected from comparable laser-plasma mediated vapour bubbles, in terms of R_{\max} , with single-fronted shock wave generation and spherical rebound phase, verified via high-speed imaging, as discussed previously. Accordingly, the bubble collapse shock waves presented may be considered as representative of the propagation of a single shock wave, such that propagation effects may also be assessed. Close to the bubble location, it may be expected that the bubble collapse shock wave speed is supersonic, during which the $PPPA_{\text{SW}}$ decays as $\sim r^{-2}$, [22]. At the measurement distances of 30 – 50 mm, however, it is expected that the pressure amplitude decays as $\sim r^{-1}$ [22, 128]. As such, the assessment includes broken r^{-1} envelopes across the peak pressures in each shock wave representation, including for the simulated data, according to Eq. (3.14).

The data presented below are for bubbles of $R_{\max} = 365 \pm 4 \mu\text{m}$, however, the results are independent of maximum bubble size, as the Gilmore equation (and similar models) has before been used to study both smaller and larger bubbles [5, 22, 142]. Furthermore, the discussion and conclusion presented below are not dependent on the maximum pressure amplitude of the bubble collapse shock wave.

Consistent with previous reports [126–132], the raw hydrophone data indicate an apparent negative phase in the voltage output of the detected bubble collapse shock wave profile, at all propagation distances over which measurements are taken.

3.3.1 Single-frequency calibration

The shock profiles of Fig. 3.8a, solid black line, are single-frequency calibrated bubble collapse shock waves, converted from voltage to pressure using the magnitude sensitivity at 10.0 MHz, which is $810.0 \pm 8.1 \text{ mV/MPa}$, Fig. 3.2. This frequency was selected as representative of how bubble shock wave literature is often reported, and also as it is within the flat bandwidth of the

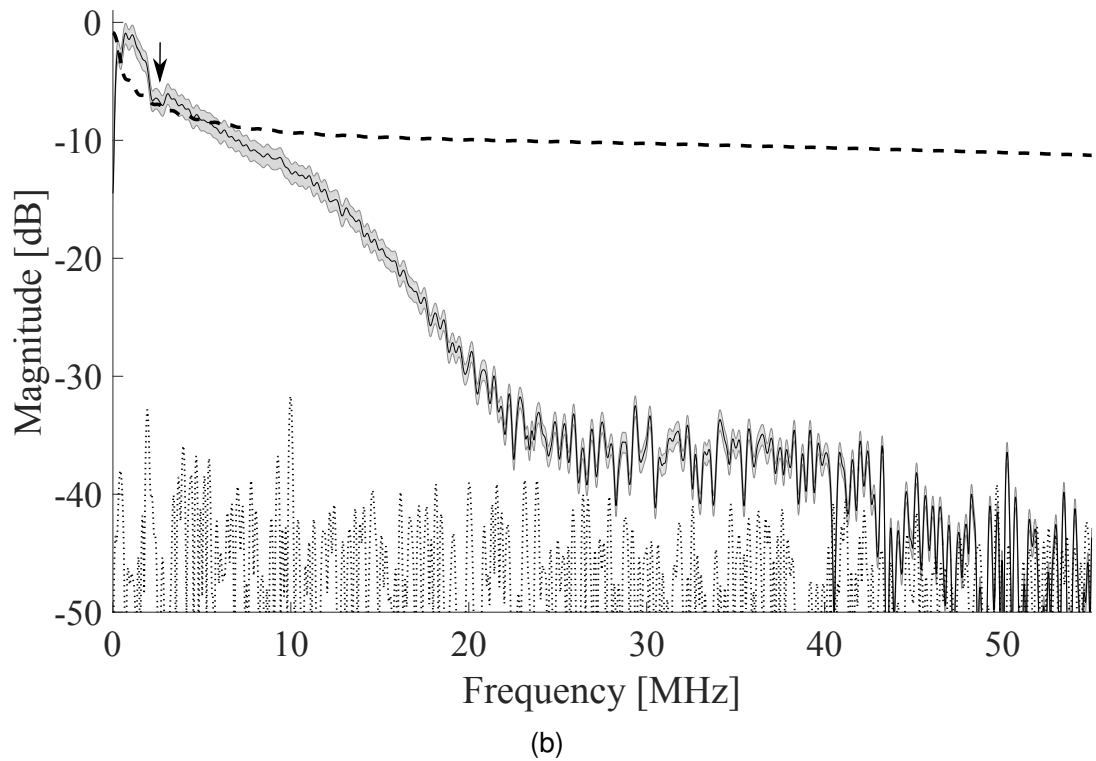
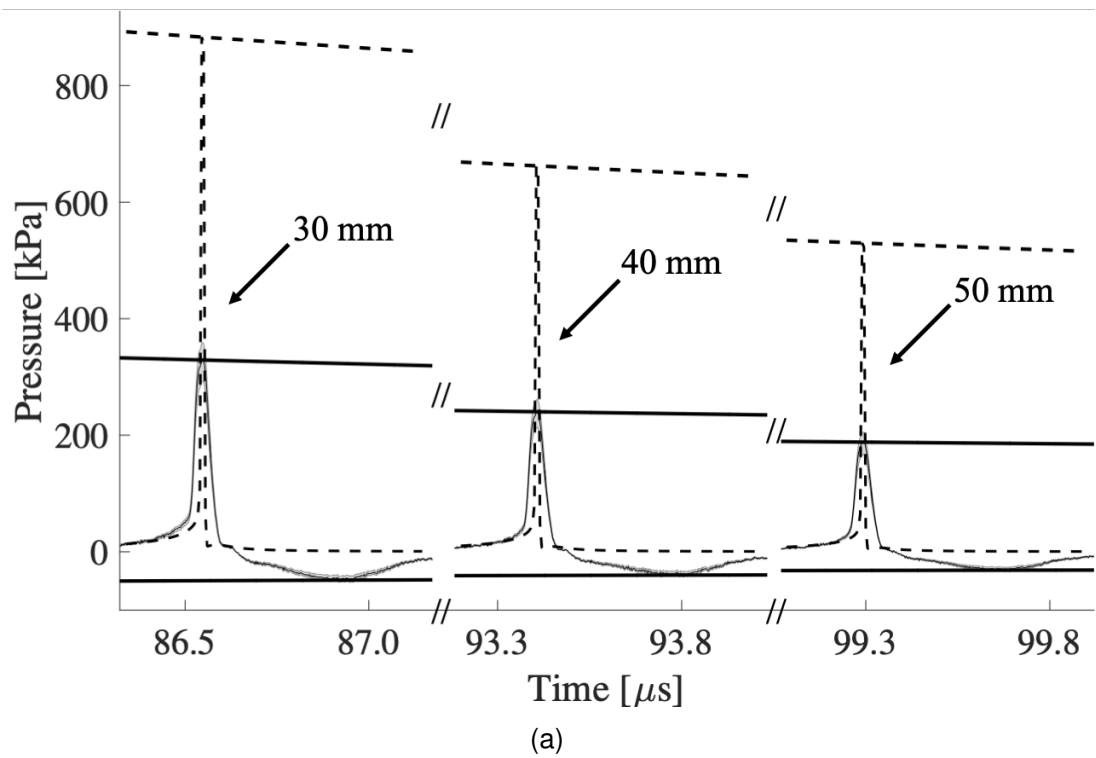


Figure 3.8: (a) Single-frequency calibrated hydrophone signal (black with grey shaded uncertainty), with the calibration value at 10 MHz, for bubble collapse shock waves measured at propagation distances of 30, 40 and 50 mm, and the simulated shock wave profile prediction (black dash). The horizontal lines are the r^{-1} envelopes to the measured and computed shock waves for the different distances. (b) Frequency spectra of the single-frequency calibrated signal (black with grey shaded uncertainty) and simulated shock (black dash) at $r = 30$ mm, normalised to the experimental data. Also shown (grey dot) is the noise floor, sampled from the hydrophone data between the Q-switch and the optical break down shock wave, Fig. 3.3b. All three bubbles had a $R_{\text{max}} = 365 \pm 4 \mu\text{m}$.

Prop. distance (mm)	Single frequency calibration			Simulated shock profile		
	RT (ns)	FWHM (ns)	$PPPA_{SW}$ (kPa)	RT (ns)	FWHM (ns)	$PPPA_{SW}$ (kPa)
30	71	46	326 ± 36	5	10	883
40	53	47	240 ± 26	5	10	662
50	57	48	188 ± 21	5	10	529

Table 3.1: Shock wave properties from Fig. 3.8a, including rise time (RT), full width half maximum (FWHM) and peak positive pressure amplitude of the shock wave ($PPPA_{SW}$), for single-frequency calibration and simulated shock wave profile, at each of the propagation distances.

needle hydrophone, thereby making it a suitable choice for demonstrating the assumption and implications of a flat frequency response. The time waveform shape of the profile is otherwise identical to the voltage signal detected by the needle hydrophone. The black-dash profiles of Fig. 3.8a are the bubble collapse shock waves predicted by the acoustic emissions computed by Eq. (3.14), from the solution of the Gilmore equation, with notable differences to those measured. In particular, the pressure amplitudes of the model profiles are around 2.5 times greater than the measured values, and the FWHM less than 25 % of those measured, Table 3.1. Furthermore, the experimental profiles all exhibit an apparent negative phase, lasting $\sim 0.5 \mu\text{s}$ and propagation independent, trailing the compressive phase of the shock wave. The amplitude of the apparent negative phase also follows the r^{-1} decay, exhibited by its positive pressure counterpart (broken envelopes, Fig. 3.8a), consistent with it representing a physical propagating pressure signal.

Fig. 3.8b are the frequency spectra of the experimental and simulated bubble collapse shock wave, at $r = 30$ mm. The shape of the spectrum, convolved with the needle hydrophone response, is best considered relative to the calibration data of Fig. 3.2. The steeper fall-off in the magnitude of frequency components > 12 MHz corresponds to the marked decrease in magnitude sensitivity exhibited > 12 MHz. Moreover, the dip (arrowed, Fig. 3.8b) in the magnitude of the experimental bubble collapse shock wave spectrum, from 2–3 MHz, is likely due to the structure in the end-of-cable magnitude calibration data over the same frequency range, Fig. 3.2. The unfiltered simulated shock wave has a spectrum indicating greater magnitude at higher frequencies compared to the measured shock wave, which predictably leads to a narrower FWHM in the time domain, Fig. 3.8a.

By sampling the hydrophone output between the Q-switch and the optical break down shock

wave, a noise floor for the hydrophone system is identified at -45 dB, grey dot, Fig. 3.8b. The spectrum of the detected shock wave falls to this value at ~ 45 MHz, indicating the needle hydrophone has sensitivity over a bandwidth beyond the calibration range of 125 kHz – 20 MHz, as expected from the assessment of the rise time of the device, discussed in §3.2.4. However, it should be noted that if the bandwidth of the calibration is extended beyond where the measured signal is above the noise floor (~ 45 MHz for Fig. 3.8b), then deconvolution would only amplify high frequency noise [143].

Approximately 98 % of the power above the noise floor, in the voltage trace of the measured shock wave is within the calibrated range, which gives some confidence that the calibration bandwidth for the needle hydrophone is sufficient for deconvolution of bubble collapse shock wave, and an assessment of the shock wave characteristics. For subsequent comparisons between simulated and experimental measurements, the bandpass filter $H_{\text{bpf}}(f)$ is applied, Fig. 3.6a, to the simulated shock wave profiles and spectra, such that the bandwidths considered are equivalent. The spectra are therefore subsequently presented from $0 - 20$ MHz.

3.3.2 Magnitude-only deconvolution

The experimental bubble collapse shock wave profiles of Fig. 3.9a are magnitude-only deconvolved according to Eq. (3.2), with $\phi = 0^\circ$ for $H_{\text{NH}}(f)$. Direct comparison with the single-frequency calibrated data, Table 3.1, indicates that magnitude-only deconvolution, Table 3.2, has increased the $PPPA_{\text{SW}}$ by ~ 9 %. At rapid pressure variations within the bubble collapse shock wave profile, a rippling artefact is introduced due to the bandpass filter $H_{\text{bpf}}(f)$ suppressing frequency content outside the calibration bandwidth, also apparent in Fig. 3.9b. This is known as the Gibbs' effect, which is a ringing artefact caused by the rippling in the impulse response to $H_{\text{bpf}}(f)$, Fig. 3.6b. This rippling prevents meaningful measurement of the RT of the experimentally measured filtered shock waves. An equivalent filter is applied to the simulated shock wave profiles of Fig. 3.9a, black-dash, for comparison to magnitude-only deconvolved hydrophone data, which also generates the Gibbs' effect. The filtering also reduces the pressure amplitude of the simulated shock wave profiles.

Note, however, that the apparent negative phase has been preserved through the magnitude-

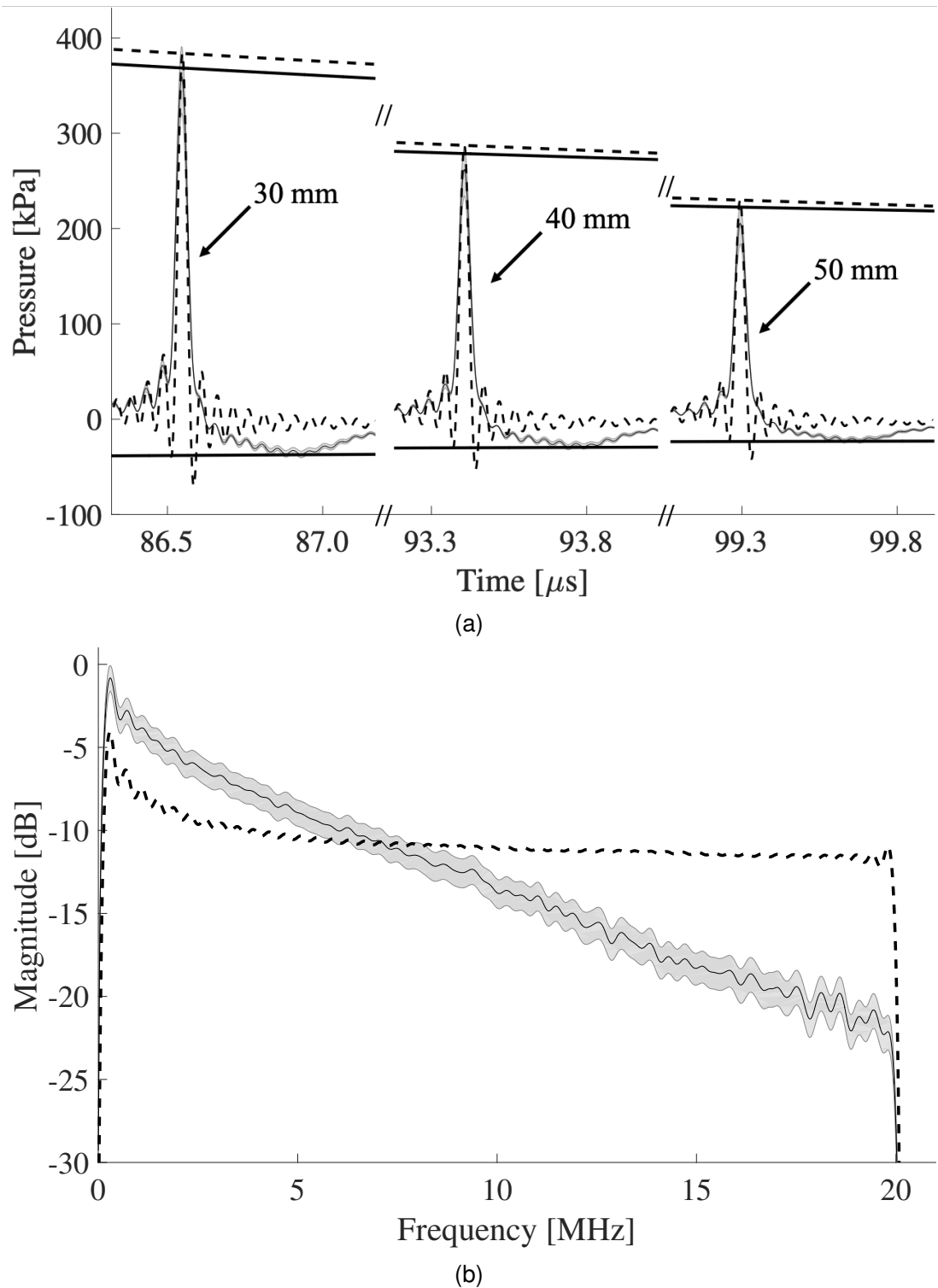


Figure 3.9: (a) Magnitude-only deconvolved hydrophone signal (black with grey shaded uncertainty), at propagation distances of 30, 40 and 50 mm, and filtered simulated shock wave profile (black dash). Sloped lines are the r^{-1} envelopes to the respective shock waves. All three bubbles had a $R_{\text{max}} = 365 \pm 4 \mu\text{m}$. (b) Frequency spectra of the magnitude-only deconvolved signal (black with grey envelope) and simulated shock (black dash) at $r = 30$ mm, normalised to the experimental data.

Prop. distance (mm)	Magnitude-only deconvolution		Simulated shock profile	
	FWHM (ns)	$PPPA_{SW}$ (kPa)	FWHM (ns)	$PPPA_{SW}$ (kPa)
30	44	359 ± 38	31	383
40	44	261 ± 27	31	287
50	45	205 ± 21	31	230

Table 3.2: Shock wave properties from Fig. 3.9a, including full width half maximum (FWHM) and peak positive pressure amplitude of the shock wave ($PPPA_{SW}$), for magnitude-only and filtered simulated shock wave profile, at each of the propagation distances.

only deconvolution, in accordance with assuming $\phi = 0^\circ$ for all frequencies, Fig. 3.9a.

Fig. 3.9b are the spectra of experimental and simulated shocks at 30 mm, with the effect of $H_{bpf}(f)$ clearly evident. As expected for a shock wave generally, the experimental spectrum now decays with a better approximation to linearity in the dB scale, at increasing frequency. For all frequencies with a sensitivity lower than that at 10 MHz, Fig. 3.2, the magnitude at the respective frequency components are increased according the Eq. (3.2), most notably > 12 MHz. Also, the dip (arrowed Fig. 3.8b) in the spectrum of the single-frequency calibration bubble collapse shock wave has been removed by magnitude-only deconvolution. Comparison to Fig. 3.9b indicates that the pressure amplitudes for the different frequency components are therefore better estimated in the frequency domain, compared to the single frequency calibration, as the whole bandwidth of calibration is utilised correcting for the non-flat magnitude response.

The Gibbs' effect is manifested in the spectrum of the simulated shock wave, Fig. 3.9b, at the limits of the bandpass filter, and is also apparent toward the low frequency limit of the filter in the experimental spectrum.

3.3.3 Full waveform deconvolution

Fig. 3.10 depicts the full waveform deconvolution of the bubble collapse shock wave hydrophone data, incorporating the phase calibration data. It is observed that the apparent negative phases of the experimental bubble collapse shock wave profiles have been removed when the phase response to the hydrophone system is corrected for.

The $PPPA_{SW}$ of the full waveform deconvolved profile is $\sim 3\%$ higher at each propagation

distance, than those of the magnitude-only deconvolved profiles. The peak pressure amplitudes of the filtered simulated profiles are now within the calibration error provided by NPL, of the full waveform deconvolved bubble collapse shock wave amplitudes, in the time domain.

The frequency spectrum of the full waveform deconvolution is equivalent to that of the magnitude-only deconvolution, Fig. 3.9b, as the magnitude in the frequency domain does not depend on the phase.

The FWHM for the experimental profiles, Table 3.3, are $\sim 30\%$ longer than those of the filtered simulated profiles. This is due to the filtered simulated profiles having higher magnitude than the experimental profiles from ~ 10 MHz, and lower magnitude for frequencies below, Fig. 3.9b.

To demonstrate the importance of high-speed imaging simultaneous to acoustic detection, the double-fronted bubble collapse shock wave in Fig. 3.4c has undergone full waveform deconvolution, displayed in Fig. 3.11. It shows that the deconvolved double-fronted bubble collapse shock wave is similar in appearance to the single-fronted bubble collapse shock waves,

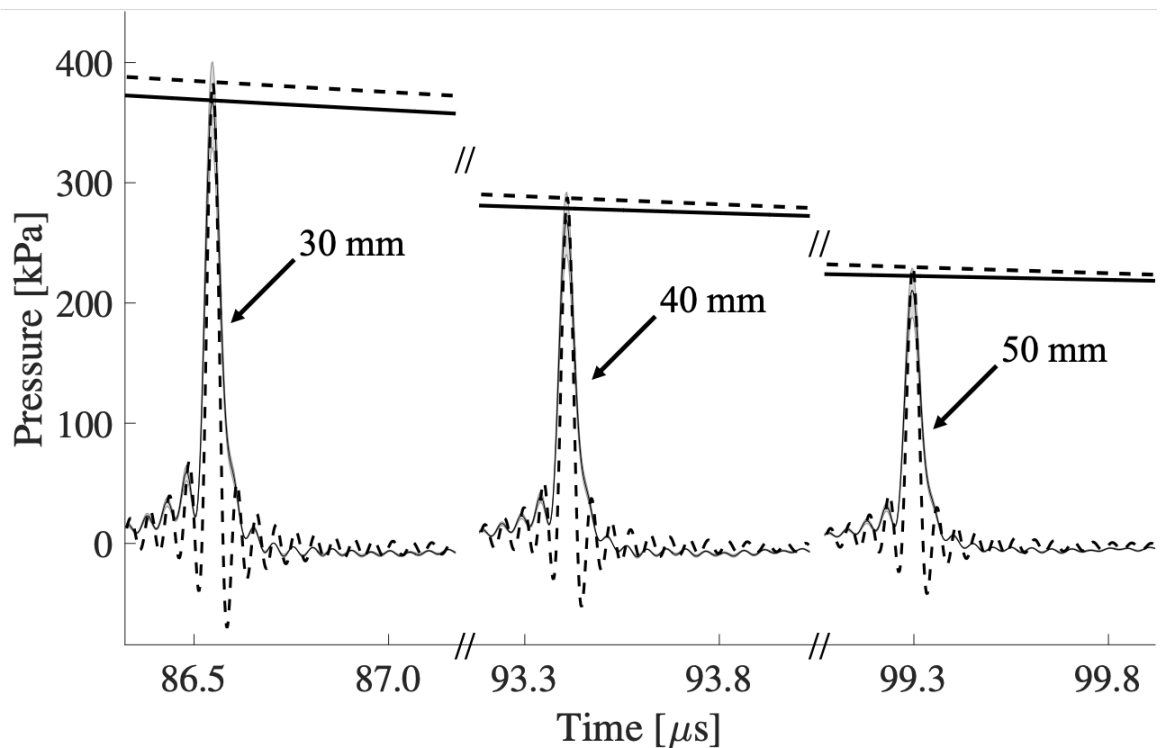


Figure 3.10: Full waveform deconvolved hydrophone signal (black with grey shaded uncertainty), at propagation distances of 30, 40 and 50 mm, and filtered simulated shock wave profile (black dash). Sloped lines are the r^{-1} envelopes to the respective shock waves. All three bubbles had a $R_{\max} = 365 \pm 4 \mu\text{m}$.

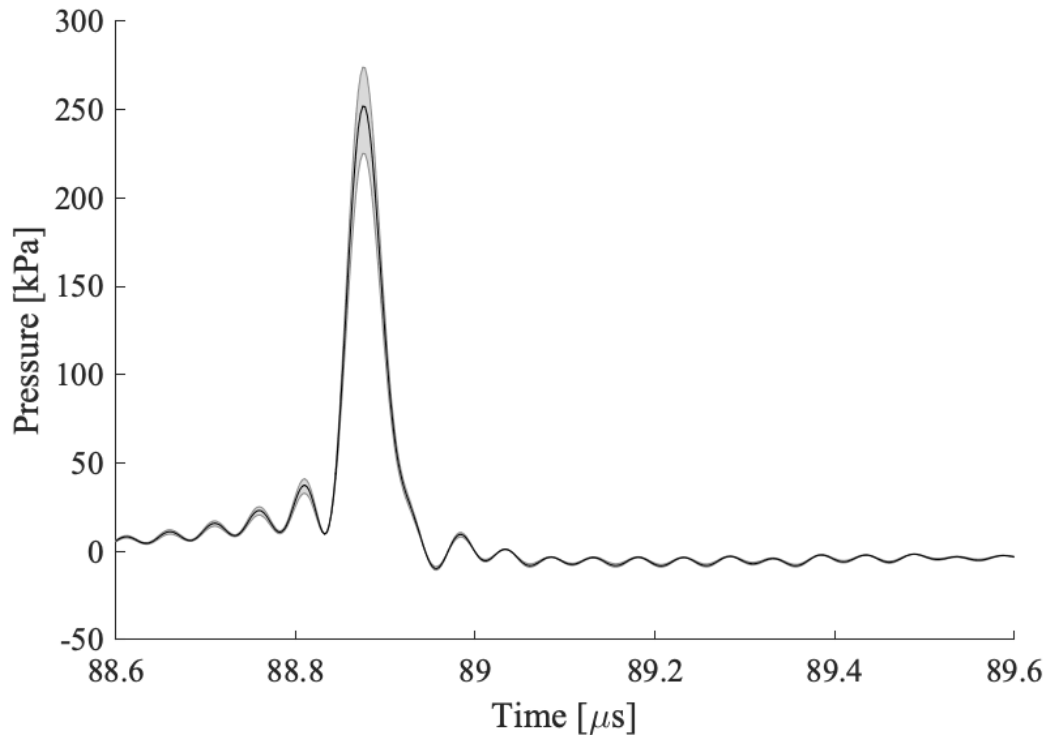


Figure 3.11: Full waveform deconvolved double-fronted bubble collapse shock wave (grey shaded uncertainty) detected by needle hydrophone at a distance of 40 mm. The voltage-trace to this bubble collapse shock wave is shown in Fig. 3.4c. The bubble had a $R_{\max} = 342 \mu\text{m}$ and a FWHM of 50 ns.

of Fig. 3.10, which suggests that high-speed imaging of the collapsing bubble is valuable during data analysis. Furthermore, it is worth noting that despite the acoustic emission originating from a slightly smaller bubble ($R_{\max} = 342 \mu\text{m}$ compared to $R_{\max} = 365 \pm 4 \mu\text{m}$ for the other data considered), the FWHM is $\sim 10\%$ longer than for a single-fronted bubble collapse shock wave at the same distance, 50 ns and 46 ns respectively. This would cause further discrepancy between the computed bubble collapse shock wave and the experimentally detected acoustic emission,

Prop. distance (mm)	Full waveform deconvolution		Simulated shock profile	
	FWHM (ns)	$PPPA_{\text{SW}}$ (kPa)	FWHM (ns)	$PPPA_{\text{SW}}$ (kPa)
30	45	368 ± 38	31	383
40	46	268 ± 28	31	287
50	47	210 ± 23	31	230

Table 3.3: Shock wave properties from Fig. 3.10, including full width half maximum (FWHM) and peak positive pressure amplitude of the shock wave ($PPPA_{\text{SW}}$), for full waveform deconvolved and filtered simulated shock wave profile, at each of the propagation distances.

which is expected as the Gilmore equation (discussed in §3.2.6) does not describe the radial dynamics of a splitting bubble.

3.4 Discussion

All bubble collapse shock wave generation models in the literature predict purely compressive shock wave profiles [22, 126, 131, 141], also confirmed experimentally using optical techniques [144]. Bubble collapse shock wave propagation, however, is not so well studied and many reports present measurements, taken with a range of detecting devices, which include an apparent trailing negative phase. Shock waves generally, such as those resulting from a detonation [145] or used for lithotripsy [122], are known to develop a tensile phase following the initial impulsive compression, attributed at least in part to medium response to the propagating compression. The results presented in this Chapter indicate that this is not the case, at least for bubble collapse shock waves from a collapsing laser-plasma mediated vapour bubble formed in water, and that the reported apparent negative phases are detector convolution artefacts, such as those in Figs. 3.8a and 3.9a, and this is confirmed by the computed bubble collapse shock waves. Such convolution artefacts become more noticeable for detectors with a non-flat frequency response, as suggested by both theory (§3.2.5) and experiments [143].

It is observed in Fig. 3.8a and Table 3.1 that the simulated profiles have FWHM $\sim 25\%$ of those measured with the needle hydrophone. The simulated profiles were computed with a bandwidth of 100 MHz, in addition it is seen in Fig. 3.8b that all frequency content > 6 MHz is overestimated, and so it would be expected to have FWHM shorter than those measured. However, both types of deconvolution, which are compared to filtered simulated profiles, also exhibit FWHM $\sim 70\%$ of the measured values, Tables 3.2 and 3.3. A spherically propagating shock wave incident to a detector with a finite active area will introduce a geometrical spreading effect to the measurement. Consideration of the experimental setup described, and assuming an impulse shock wave, propagating at the speed of sound at the distances measurements were taken, indicates a spreading of ~ 3 ns. Of course, the physical shock wave will have some finite width, and so the effect will be larger than for an impulse. One consequence of this effect will be that

the measurements of both RT and FWHM will be overestimated.

In Fig. 3.9b it is seen that the frequency content > 10 MHz is overestimated by the simulation, although this difference should reduce if experimental attenuation is taken into account. Continuous waves of 10 MHz and 20 MHz would be expected to be attenuated by ~ 0.07 dB and ~ 0.14 dB after 30 mm of propagation¹¹, respectively, although this effect may be expected to be stronger during early supersonic propagation of the bubble collapse shock wave from the bubble. This would shift the shape of the simulated bubble collapse shock wave spectrum closer to that of the measured one, particularly for frequencies above 10 MHz.

The spectrum of the magnitude-only, and consequently the full waveform deconvolved bubble collapse shock wave hydrophone data, Fig. 3.9b, indicate that the intensity decreases linearly with increasing frequency. Indeed, it is clear that the majority of the bubble collapse shock wave intensity is contained in the lower frequency region of the spectrum, with the magnitude falling below -10 dB at 5 MHz, Fig. 3.9b. This suggests that designing detectors for maximum sensitivity at lower frequencies should be considered, if detecting periodic shock waves and sub-harmonic signals from acoustic cavitation, is desired. This observation motivated the work to develop the swPCD, described in Chapter 6.

Possible improvements to this work include a more rigorous simulation of the bubble collapse, accounting for factors such as gas content, heat and mass transfer in the bubble oscillation model which would influence the collapse dynamic, and subsequently the predicted shock wave. More advanced computational efforts could also facilitate insights regarding the conditions required for splitting bubbles to occur, and their double-fronted shock waves, Fig. 3.4 [146, 147]. Moreover there are advanced shock wave generation models [124, 132, 141, 148], such as the Kirkwood-Bethe hypothesis accounting for the compressibility of the medium through which the shock wave is propagating, for example. Implementing a more refined bubble collapse shock wave simulation may deliver better matching spectra to those measured experimentally, with a wider calibration bandwidth. However, for the purposes of investigating the effects of deconvolution on cavitation bubble shock waves, and providing insight into how they may be treated with the appropriate hydrophone calibration, the results presented suggest the approaches adopted are adequate. In

¹¹This is computed using Field II [116].

this work end-of-cable sensitivity is used, where the complex sensitivity is a convolution of the needle and the pre-amplifier associated with the system. Obtaining the complex sensitivity to the pre-amplifier would allow for further deconvolution of the end-of-cable sensitivity such that the non-flat structure of the frequency response could be better understood.

Generally, studies that seek to develop cavitation applications will present the spectrum of the emissions collected, and typically link a feature within the spectrum to the cavitation-mediated effect under investigation, as discussed for papers reviewed in Chapter 1. The magnitude of that feature is often taken as an indicator of the level of cavitation that occurred, commonly as a result of increased pressure amplitude of the acoustic driving, as discussed in §1.5.1. The sub-harmonic or ultra-harmonics are often used, as these signals have long been considered exclusive to stable or inertial acoustic cavitation activity [71]. The results reported above confirm that magnitude-only deconvolution has an influence on the spectrum of a single bubble collapse shock wave for a hydrophone with non-flat magnitude response. To perform quantitative analysis on the sub-harmonic and ultra-harmonic peaks, from cavitation spectra with shock wave content, it is therefore necessary to use a detecting device that is calibrated for magnitude response, over an appropriate bandwidth with respect to the spectral features that are being monitored. This includes bespoke PCDs, particularly broadband PVdF-based detectors, where shock wave detection may be expected to constitute a significant proportion of the signal collected. If the purpose of the measurement is to reconstruct the shock wave in the time domain, for the whole bandwidth of the shock wave with a precise estimate of $PPPA_{SW}$, then certainly a spot-poled membrane hydrophone would be recommended rather than a 1 mm PVdF needle-type hydrophone, with a comparatively limited bandwidth [143, 149]. However, magnitude-only deconvolution would go some way to facilitating direct comparison of the cavitation spectra presented during different studies [43, 58] from different research groups provided the same bandwidth is compared, which is an issue in current literature. Moreover, quantitative analysis of inertial cavitation emissions that contains shock wave components, in the time domain, can only be meaningfully implemented with full waveform deconvolution for detectors with a non-flat frequency response, with magnitude and phase calibration data, as implemented for Chapter 4 and 5.

3.5 Conclusion

Single-frequency calibration of experimentally detected bubble collapse shock waves delivers profiles with notable differences to simulation predictions, generated via a bubble collapse and simple acoustic emission model. Magnitude-only deconvolution, in comparison to appropriately filtered simulation profiles, improves the $PPPA_{SW}$ estimate of the experimental measurement, but the waveform in the time domain retains phase distortion. Full waveform deconvolution provides the best match between the experimentally measured and filtered simulation data, removing the non-flat detector response within the calibration bandwidth; most notably the apparent negative phase.

Chapter 4

An analysis of the acoustic cavitation noise spectrum: The role of periodic shock waves

The previous chapter describes how single bubble collapse shock wave characteristics can be reasonably restored from detector-convolution artefacts introduced during the measurement. In this chapter, a further experimental refinement to the early work of Johnston *et al.* is described [9], as key to fully assessing the contribution of periodic shock waves to the cavitation emission signal, and spectrum. Specifically, a single laser-nucleated acoustic cavity is achieved, that emitted single-fronted $f_0/2$ sub-harmonic shock waves ¹. Comprehensive analysis is undertaken via simulated BCSWs similar to those described in Chapter 3, but adapted to the experimental parameters, and a novel *synthetic spectrum* approach ².

¹The clarity that achieving the simplest cavitating system possible inspired the Minnaert quote at the start of the thesis.

²The results presented in this Chapter were first published in; J. H. Song, **K. Johansen**, P. Prentice. "An analysis of the acoustic cavitation noise spectrum: The role of periodic shock waves". *The Journal of the Acoustical Society of America*, 140(4), 2494-2505, 2016.

4.1 Materials and methods

4.1.1 Spectral analysis model for periodic shock waves

To fully assess the role of periodic shock waves on the cavitation spectrum a simple generic model is developed. Five periodic shock waves are considered, $x_{PSW}(t)$, Fig. 4.1a, in an idealised case for which the period of emission, T_{PSW} , and the peak-positive pressure amplitude, $PPPA_{SW}$, of each component shock wave is constant.

An impulse train, $c_T(t)$, is multiplied and convolved with a rectangular window function, $w_D(t)$, where D represents the duration of the shock wave train and $s(t)$, a shock wave function, Fig. 4.1b;

$$x_{PSW}(t) = c_T(t) \times w_D(t) * s(t) \tag{4.1}$$

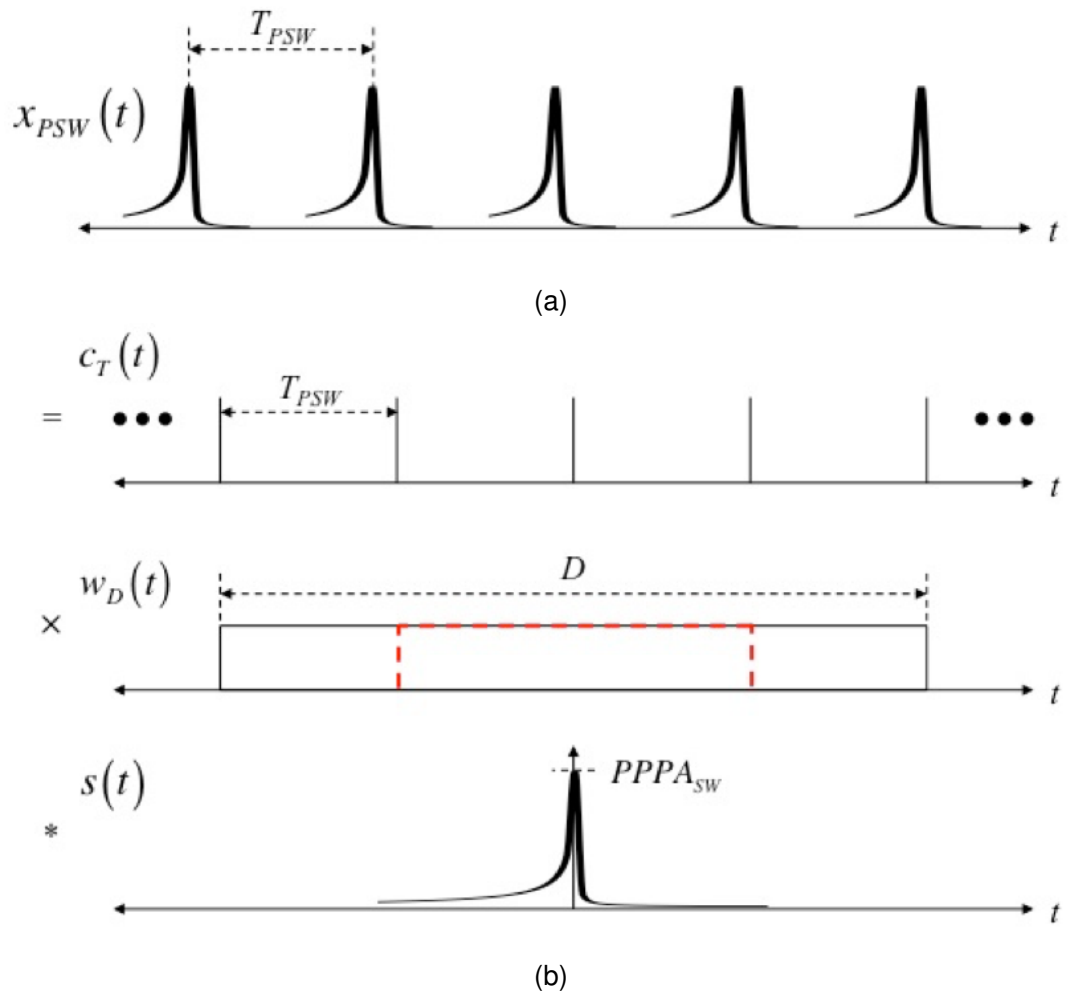


Figure 4.1: Representation of the spectral analysis model for periodic shock waves, in the time domain.

such that $c_T(t) = \sum_{k=-\infty}^{\infty} \delta\left(t - \frac{k}{T_{\text{PSW}}}\right)$, ($k \in \mathbb{N}$), where δ is the Dirac delta function and $w_D(t) = \Pi\left(\frac{t}{D}\right)$.

The Fourier Transform of Eq. (4.1), $X_{\text{PSW}}(f)$, can be represented as

$$X_{\text{PSW}}(f) = C_T(f) * W_D(f) \times S(f) \quad (4.2)$$

such that $C_T(f) = 1/T_{\text{PSW}} \sum_{k=-\infty}^{\infty} \delta(t - 2\pi f_{\text{PSW}}k)$, where $f_{\text{PSW}} = 1/T_{\text{PSW}}$, and $S(f)$ is the spectrum of a single shock wave, and $W_D(f) = D \text{sinc}(fD)$.

Figure 4.2a, the spectrum of Fig. 4.1a, indicates that periodic shock waves are manifested as a series of peaks at $n f_{\text{PSW}}$, $C_T(f)$, the Fourier Transform of $c_T(t)$ is itself an impulse train. The width of each spectral peak is determined by $W_D(f)$, the Fourier Transform of $w_D(t)$. The magnitude of the spectral peaks decrease at the same rate as the spectral content of the shock wave, $S(f)$, Fig. 4.2b. The spectral peaks for the three shock wave representation are wider, compared to those for the five shock wave train, due to the shorter duration of the window function, Fig. 4.1b.

Therefore, for a cavitation cloud driven by ultrasound at a fundamental frequency f_0 , in a regime where strong cloud collapses and shock wave emission occur at the half-harmonic, such that $f_{\text{PSW}} = f_0/2$, periodic shock waves may be expected to contribute to all spectral features at $n f_0/2$, including $n f_0$ (*i.e.* the fundamental and its higher harmonics)³.

As demonstrated by Johnston *et al.* [9] (and discussed in *Overview of Thesis*, Fig. 2), increasing the pressure amplitude of the acoustic driving generates cloud collapses occurring at higher-order sub-multiples, $n f_0/m$, for $m > 2$. For such regimes, periodic shock waves may be expected to contribute to all features at $n f_0/m$.

4.1.2 High-speed imaging and acoustic measurements

The experimental cavitation observations were undertaken in the sonoptic chamber, and the experimental arrangement depicted in Fig. 4.3a is showing the relative configuration of the HIFU source, needle hydrophone, and the nucleation laser optic. This configuration is used to study

³Many thanks to Dr Jae Hee Song for the development of the signal analysis model, collection of experimental data, and preparation of figures. The author contributed with the Gilmore model for computation of a BCSW, including analysis and discussion of experimental results for publication.

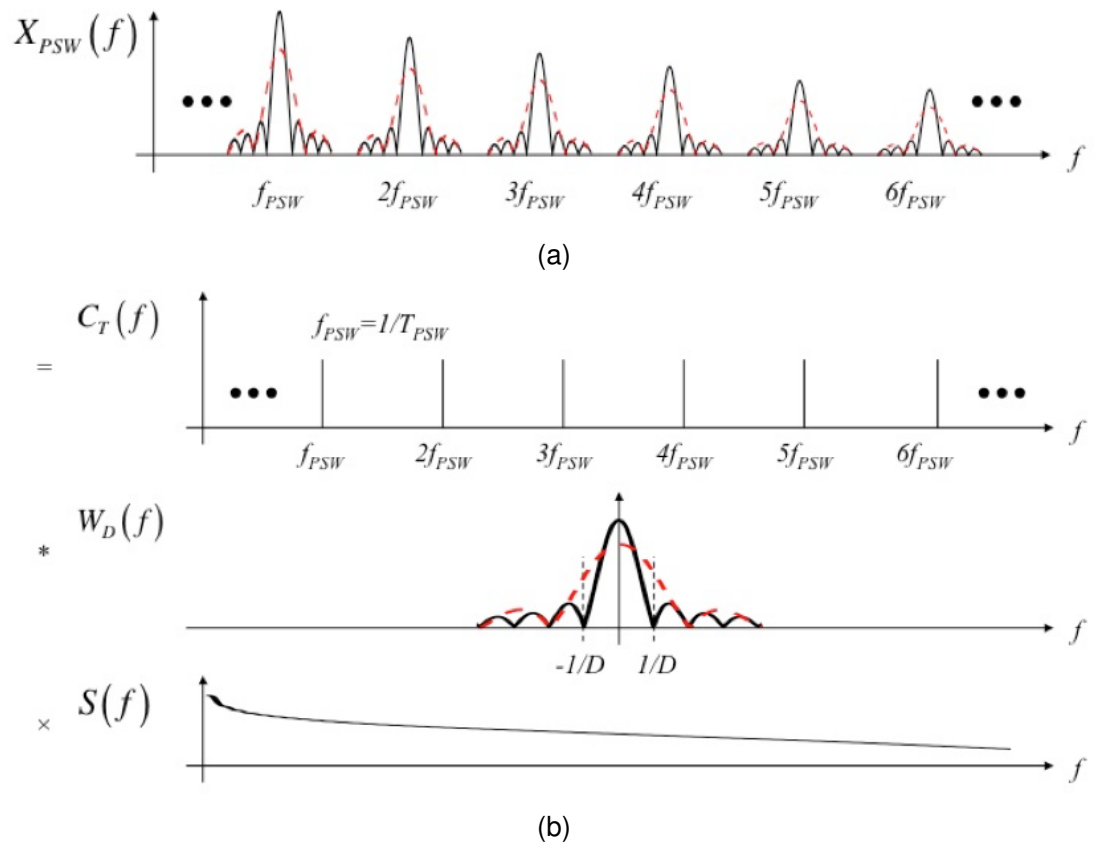


Figure 4.2: Representation of the spectral analysis model for periodic shock waves, in the frequency domain, for 3 shock waves (red dash), and 5 shock waves (solid black).

cavitation in unprecedented detail, both optically and acoustically. For the results presented below, the transducer is driven at the third harmonic, such that $f_0 = 692$ kHz.

As previously stated, this driving frequency is chosen to have more ‘controllable’ bubble activity, and ensure that acoustic cavitation emissions are well within the calibration bandwidth of the needle hydrophone (§3.2.2). For all the results presented in this Chapter, the needle hydrophone is mounted in the 20 mm central hole, through the body of the transducer, aligned vertically along the HIFU axis, Fig. 4.3a, with the tip located around the pre-focus -6 dB contour, ~ 3 mm from the focal point. This orientation is referred to as the ‘emission collection’ position, Fig. 4.3b. The needle hydrophone is connected to an oscilloscope (MS07104A, Agilent Technologies, USA), and data collected at 4 GS^{-1} . In this location, it is recognised, that the presence of the needle hydrophone will cause some perturbation of the field, for which a number of steps has been taken to assess the effect in terms of *PPA*, described in §4.1.3.

To precisely initiate cavitation activity relative to the needle hydrophone tip, and in the HIFU

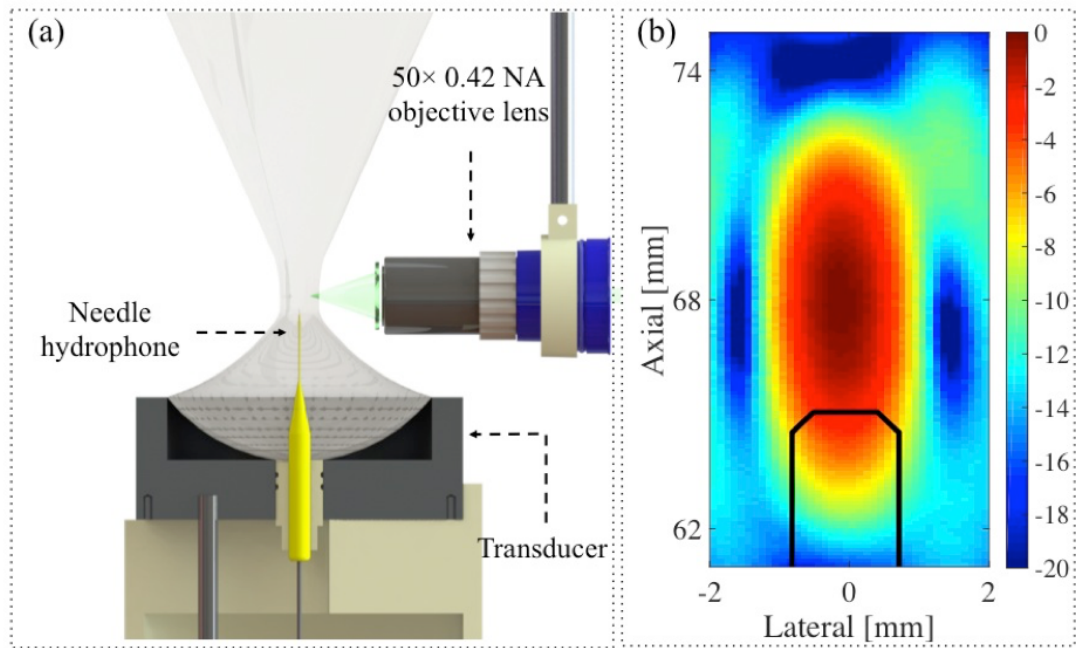


Figure 4.3: Illustrates the specific configuration used to validate the spectral analysis model described: (a) cross-sectional side view, and (b) an axial scan of the HIFU focal region, with representations of the needle hydrophone outlined for 'emission collection' position (solid black).

focus, the laser-nucleation technique discussed in §2.3 (the second bubble regime), is used. A single 1.2 ± 0.1 mJ (instrument error according to manufacturer) laser pulse, discussed in §2.2, is passed through a long working distance microscope objective lens ($50\times$ 0.42 NA Mitutoyo, Japan), submerged in a sealed unit, mounted on an xyz manipulator (Velmex Motor, Bloomfield, NY, USA), and pre-aligned to the HIFU focus, ~ 3 mm above the needle hydrophone tip *in-situ*. The laser pulse, triggered to be incident ~ 5 cycles into a 65-cycle burst of HIFU, generated the cavitation activity reported below.

High-speed shadowgraphic imaging of the resulting cavitation activity is undertaken orthogonally to the nucleating laser axis, through a Monozoom 7 lens system (Bausch & Lomb, USA), at 5×10^6 fps (HPV-X2, Shimadzu, Japan), described in §2.4.

The Q-switch of the laser, which is detected by the needle hydrophone, Fig. 3.3b, signifies laser pulse emission and cavitation nucleation, and is taken as $t = 0 \mu\text{s}$.

4.1.3 Assessment of HIFU field perturbation

To assess the effect of placing the needle hydrophone in the emission collection position a fibre-optic hydrophone (Precision Acoustics, UK) ⁴ is introduced with the tip aligned to the HIFU focus, Fig. 4.4a and 4.4b, and the point to which the cavitation nucleating laser pulse is focused. The fibre-optic hydrophone sensitivity below 1 MHz is non-flat (as referenced by [1], and also experimentally verified down to 1 MHz by [150]) similar to the needle hydrophone below 4 MHz, Fig. 3.2, however with a tip size of 125 μm and a fiber diameter of 10 μm (the effective active area), it does have the advantage of sampling the specific region of the field at which cavitation will be introduced. The fibre-optic hydrophone is calibrated for 692 kHz, via the substitution method with the needle hydrophone placed in an equivalent position, across a range of *PPA*'s.

Two *PPA* values were used to drive cavitation, for the results presented below as $f_0/2$ and $f_0/3$ regimes. The fibre-optic hydrophone measurements in free-field conditions (validated with the needle hydrophone) indicated $PPA = 1.94 \pm 0.13$ and 2.84 ± 0.15 MPa (average \pm standard deviation, over at least 20 measurements), respectively, for each of these regimes. With the needle hydrophone in the emission collection position, the fibre-optic hydrophone indicated the perturbation to the field reduced the *PPA* to 1.63 ± 0.12 and 2.42 ± 0.09 MPa, respectively, a reduction of $\sim 15\%$. The positioning of the fibre-optic hydrophone and the needle hydrophone for the HIFU field perturbation measurements is shown in Fig. 4.4a,b.

A further important consideration for any acoustic field driving cavitation activity, is the harmonic content at $n f_0$, established due to non-linear propagation. Fig. 4.4c represents the spectrum of the field, as an average of the fibre-optic hydrophone measurements taken with, and without, the needle hydrophone in the emission collection position. Under free-field conditions, a $2 f_0$ peak is apparent at ~ 30 dB less than f_0 , which is also within the fibre-optic hydrophone signal-to-noise ratio (SNR). With the needle hydrophone in the emission collection position, the peak appears to be somewhat suppressed, in line with a reduced *PPA*. The needle hydrophone measurements of the HIFU, with superior SNR, in the free-field conditions, confirm that low amplitude harmonics are established, at magnitudes < 30 dB that of f_0 .

The low f-number of 0.62 for the transducer used, ensures that sufficient HIFU will propagate

⁴Many thanks to Dr Helen Mulvana for use of the fibre-optic hydrophone.

to drive cavitation at the focus, with the needle hydrophone in the emission collection position. In any case, cavitation activity responding in the desired sub-harmonic regime is confirmed by high-speed imaging.

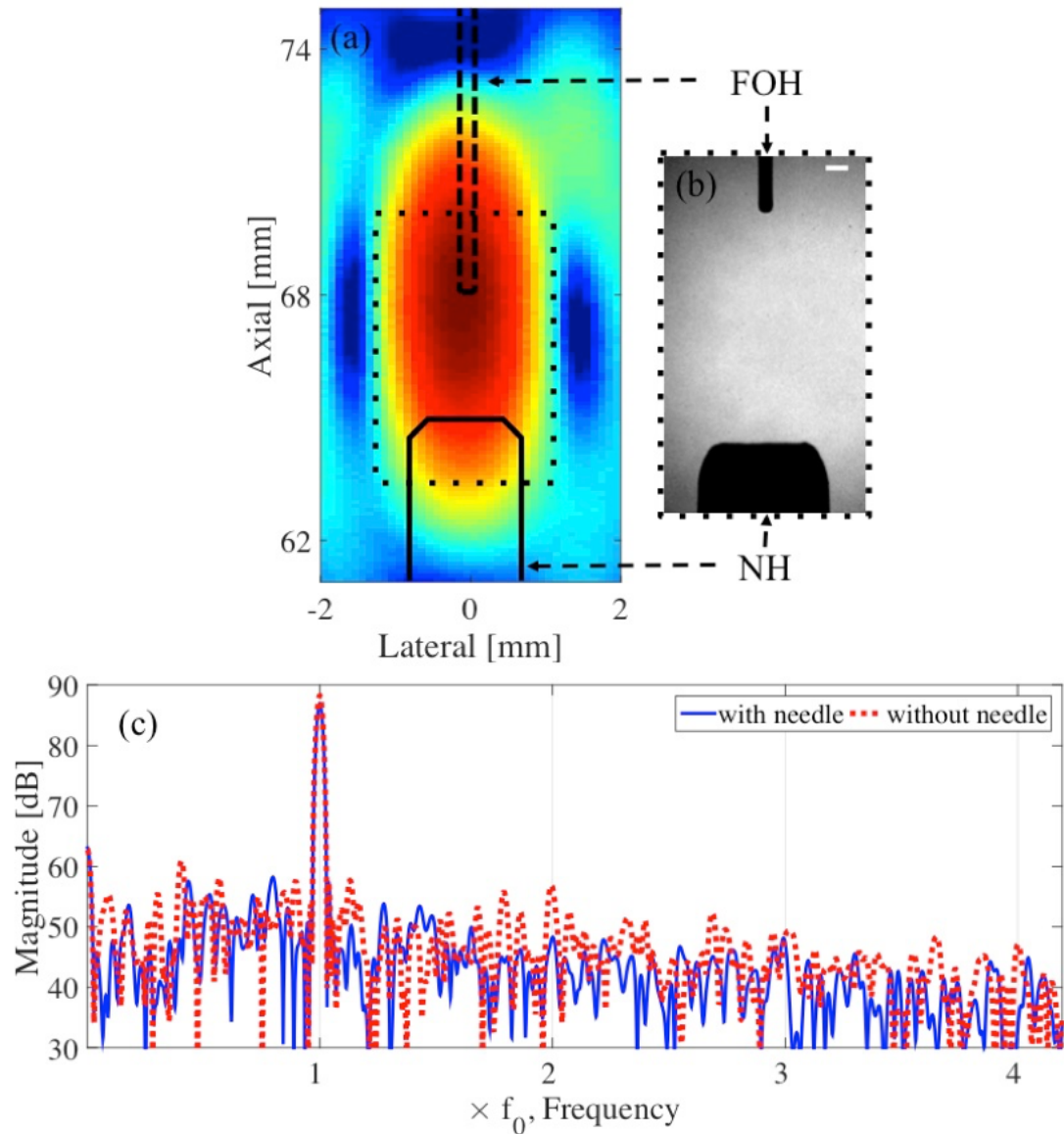


Figure 4.4: (a) Representation of the hydrophone configuration used to assess the field perturbation, introduced by the needle hydrophone in the emission collection position (b) Image depicting the needle hydrophone and fibre-optic hydrophone tips during the measurements taken. Scale bar represents 250 μm . (c) Frequency spectra of HIFU field used to drive cavitation in the $f_0/3$ regime, measured by the fibre-optic hydrophone both with and without the needle hydrophone in the emission collection position.

4.2 Results

4.2.1 High-speed imaging

$f_0/2$ regime

Figures 4.5 represent high-speed imaging data captured for cavitation driven by a $PPA = 1.63 \pm 0.12$ MPa. The activity appears to consist of a single bubble, undergoing pseudo-spherical oscillation, with alternating strong collapses coincident to shock wave emission at $f_0/2$, captured Fig. 4.5b at 8.25, 14.05, 17.05 μs and arrowed, Fig. 4.5c, and intervening partial deflations. It is known that for shadowgraphic imaging of acoustic transients, the focal plane for best resolution of the pressure fluctuations is slightly removed from the plane within which the emitting bubble is located [151]. For this reason, the bubble of Figs. 4.5a and 4.5b is slightly out of focus, and the bubble oscillation is not optimally resolved. Nonetheless, the data confirms the cavitation

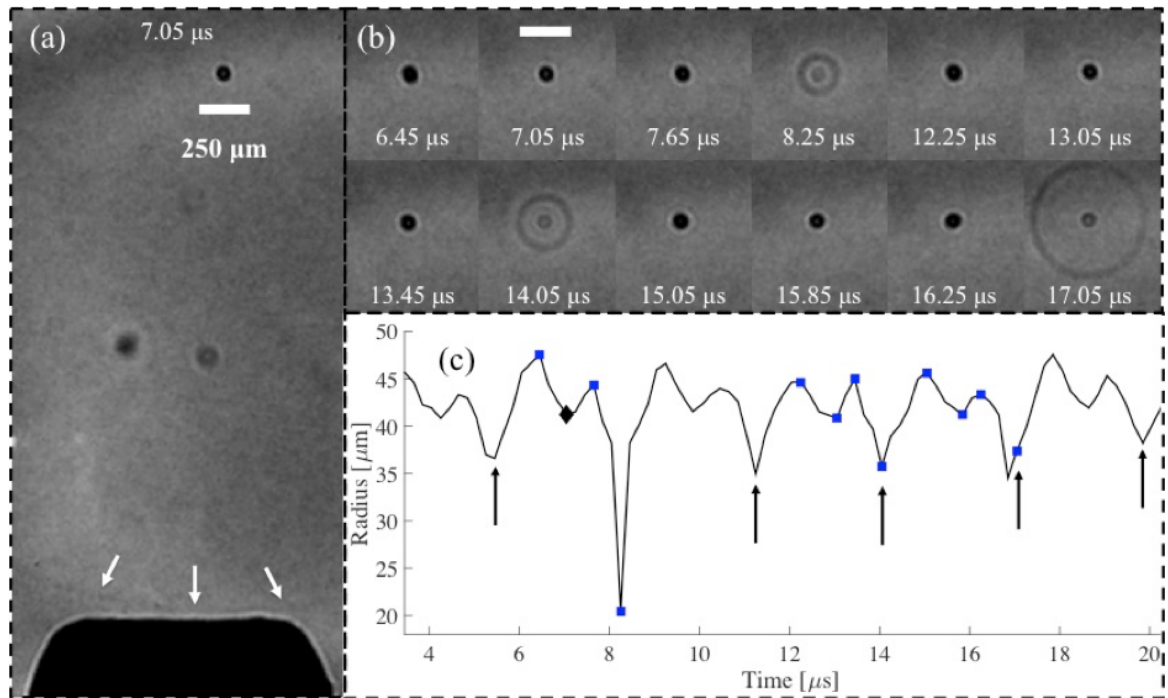


Figure 4.5: Images extracted from a high-speed sequence recorded at 5×10^6 fps, of cavitation activity in the $f_0/2$ regime. (a) The whole field of view, depicting the needle hydrophone tip position relative to the activity, with a shock wave (arrowed white) incident to it. (b) Selected images representing the cavitation oscillation dynamics, including three strong collapses, and coincident shock wave emission. (c) Radius-time curve based on a dark pixel counting algorithm, described in §2.4.1 and Matlab script in Appendix E.4, for the time interval under investigation. Diamond and squares indicate the specific images represented in (a) and (b), respectively. Scale bar represents 250 μm .

behaviour reported previously [9], for a HIFU-cloud system in the $f_0/2$ regime. Fig. 4.5c represents the bubble radius variation with time, graphically, determined from the entire image sequence captured for this experiment. To acquire the radius-time curve from the imaging data, a dark pixel counting algorithm was used, described in §2.4.1. Because the imaging configuration was adjusted to have a large field of view, such that both the cavitation bubble and the needle hydrophone could be captured in the same frame (displaying emission and detection of periodic shock waves), and combined with the effect of out of focus imaging, the dark pixel counting algorithm is incapable of analysing the actual radius during the collapse. As described in §2.4.1, during the image analysis, each frame is subject to thresholding and converted to a black and white image. Depending on the threshold value, the number of pixels counted inside the contour of the bubble may vary for different collapses. In the case of the image at $8.25 \mu\text{s}$, less pixels were counted inside the bubble compared to the image at $14.25 \mu\text{s}$, and neither one of the reported radii reflect the actual radius during the respective collapses. However, from the acoustic measurements presented in §4.2.2, Fig. 4.8b, it is observed that the $PPPA_{\text{sw}}$ of the second and third to last shock wave in the detected acoustic emissions, are of similar pressure amplitude. This indicates that the two collapses had a comparable minimum radius.

Compared to microbubbles, discussed in §1.5.3, which are encapsulated by a stabilising shell and therefore may be observed for estimation of equilibrium radius both before and (potentially) after an ultrasound exposure, the equilibrium radius to a laser-nucleated acoustic cavitation bubble is not directly assessable through the high-speed imaging data, as discussed in §2.3.1. This is because the cavitation bubble is being continuously driven by the ultrasound exposure during the imaging, and it is also worth noting that after the ultrasound exposure is completed, the cavitation bubble disappears from the image due to the gas dissolving back into the host medium. However, the equilibrium radius can be estimated by comparing observed radial dynamics to numerical simulations. This was done for the high-speed imaging observations in Chapter 4 in Appendix B. The equilibrium radius for this cavitation bubble was estimated using the Keller-Miksis equation, and resulted in $R_0 = 3 \mu\text{m}$, slightly below the resonance radius to the acoustic field ($4.4 \mu\text{m}$, $f_0 = 692 \text{ kHz}$).

$f_0/3$ regime

Increasing the pressure amplitude of the HIFU driving is known to elevate the non-linear response of the HIFU-cloud system, such that the cloud collapse at nf_0/m for increasing m . In the high-speed images presented below, the PPA is increased such that the cloud responds at $f_0/3$.

Figure 4.6 represents high-speed imaging data captured for a laser-nucleated cavitation cloud, driven by $PPA = 2.42 \pm 0.09$ MPa, according to the fibre-optic hydrophone, with the needle hydrophone in the emission collection position, Fig. 4.3 and Fig. 4.4.

In comparison to Fig. 4.5 for the $f_0/2$ regime, a larger cloud consisting of a number of component bubbles has formed, consistent with higher PPA causing higher levels of fragmentation. A direct consequence of a larger, non-spherical cloud, is multi-fronted shock waves emitted during the strong collapses, arrowed at $34.21 \mu\text{s}$ and $47.21 \mu\text{s}$, Fig. 4.6b. The cloud oscillation behaviour of, in this case, two partial deflations between each strong collapse, is better represented

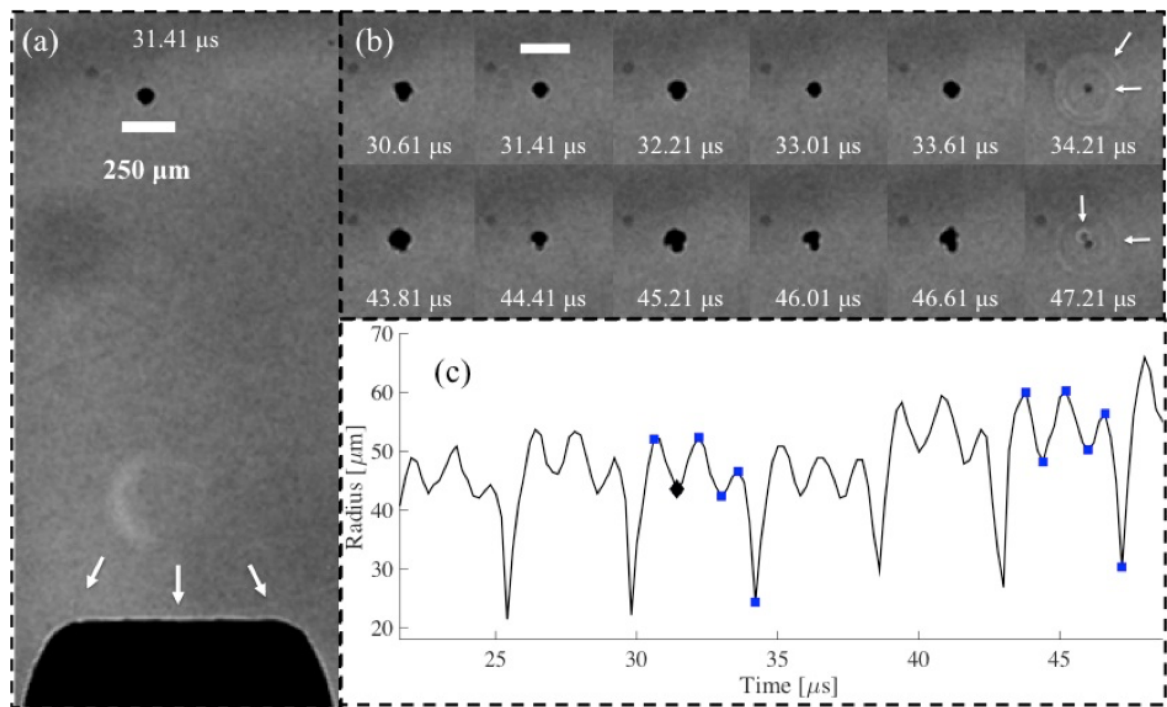


Figure 4.6: Images extracted from a high-speed sequence recorded at 5×10^6 fps, of cavitation activity in the $f_0/3$ regime. (a) The whole field of view, depicting the needle hydrophone tip position relative to the activity, with a shock wave (arrowed white) incident to it. (b) Selected images representing the cavitation oscillation dynamics, including the 3rd and 6th strong collapses, as presented in (c) radius-time curve based on a dark pixel count algorithm (§2.4.1), for the time interval under investigation. Diamond and squares indicate the specific images represented in (a) and (b), respectively. Scale bar represents $250 \mu\text{m}$.

by the cloud radius-time curve assessed via dark pixel counting, Fig. 4.6c, than for the $f_0/2$ imaging data, Fig. 4.5c.

As described for the $f_0/2$ imaging data, the equilibrium radius to the cloud consisting of a number of bubbles may be approximated by using the Keller-Miksis equation for a single bubble, as the cloud is closely packed. This is discussed in Appendix B, and the equilibrium radius is estimated to $R_0 = 6 \mu\text{m}$.

4.2.2 Needle hydrophone data

$f_0/2$ regime

Figure 4.7a is the raw voltage signal collected by the needle hydrophone in the emission collection position, with cavitation activity (blue solid) and a control experiment (red dot), for which the HIFU burst was generated, but no laser-pulse incident to nucleate cavitation, is also represented. Subtraction of the control, and needle hydrophone deconvolution (discussed in §3.2.5) within the calibration bandwidth via Eqs. (3.1) and (3.2) generates Fig. 4.7b, the cavitation emission signal, $\tilde{x}_{\text{cav}}^{\text{p}}(t)$, and Fig. 4.7c the cavitation emission spectrum, $\tilde{X}_{\text{cav}}^{\text{p}}(f)$.

The shock wave emitted by the cavitation bubble and imaged by the high-speed camera, Fig. 4.5, has a propagation time before detection at the needle hydrophone, Fig. 4.8, equal to $\sim 1.8 - 1.9 \mu\text{s}$, depending on the precise timing of bubble collapse and shock wave emission. The propagation distance can be measured from Fig. 4.5a as $\sim 2.7 \text{ mm}$, however neither the location of the sensing element within the shaft of the needle hydrophone, nor the properties of the intervening material, are known. An average propagation speed of $\sim 1520 \text{ ms}^{-1}$ in water can, however, be inferred from consecutive high-speed images of periodic shock wave propagation, and a short period of supersonic propagation may be assumed [128].

In Fig. 4.7b, acoustic emissions over more than $60 \mu\text{s}$ are shown, with detection of stable $f_0/2$ periodic shock waves from the second shock wave up to $\sim 50 \mu\text{s}$, where a f_0 collapse is detected, coincident with the decreasing driving amplitude, Fig. 4.7a. The spectrum of the acoustic emission in Fig. 4.7c features a clear $f_0/2$ peak, and over-harmonics up to $6f_0/2$, however, at higher multiples of the sub-harmonic, no peaks are apparent. This is in part caused

by the switching in shock emissions frequency of source bubble dynamics towards the end of the driving pulse, where the shock waves are not repeating sub-harmonically. Therefore, a section of the signal was chosen with high amplitude periodic shock waves and small variation in T_{PSW} to increase the bandwidth containing well defined spectral features, facilitating a better appreciation

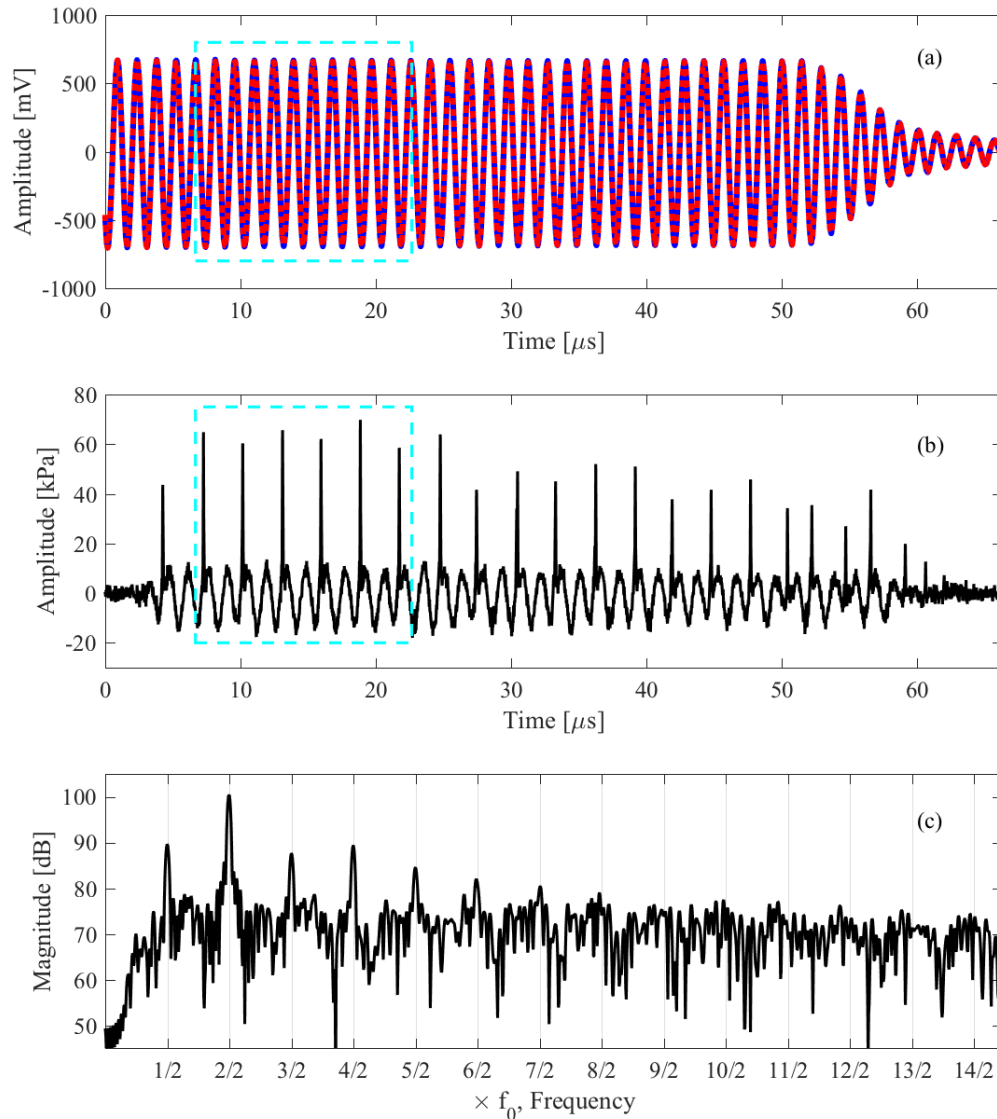
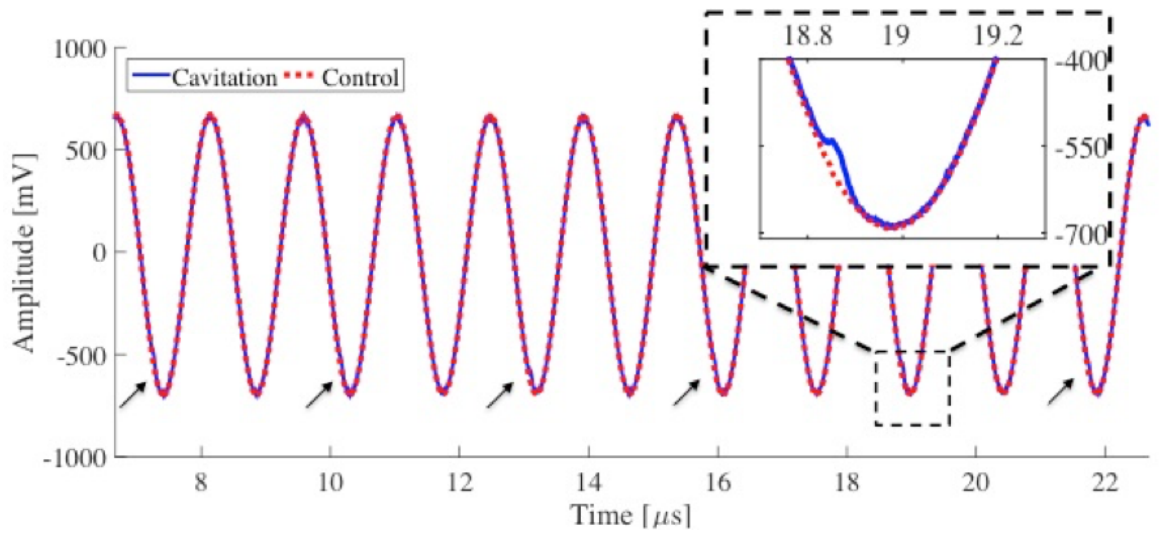
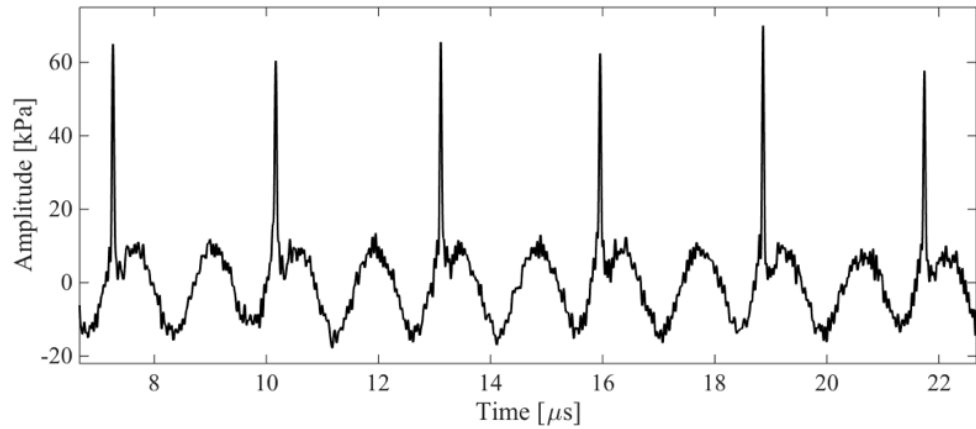


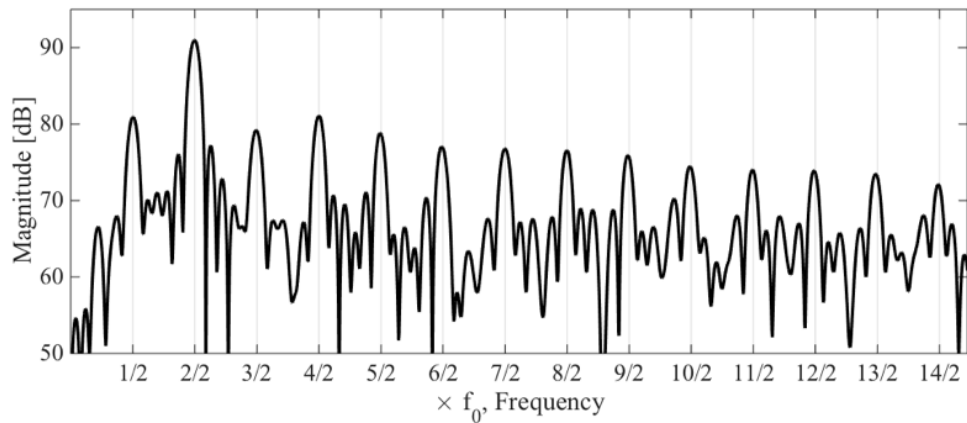
Figure 4.7: (a) Raw needle hydrophone data recorded during the cavitation activity (blue solid) of Fig. 4.5, and control exposure for an equivalent HIFU burst (red dot), without cavitation nucleation. It is worth noting how the two events are close to completely overlaid, as shown in Fig. 4.8a. (b) Control subtracted and needle hydrophone-deconvolved data, revealing the signal emitted by the cavitation, $\bar{x}_{cav}^p(t)$. (c) The cavitation spectrum $\bar{X}_{cav}^p(f)$, obtained via Fourier Transform of (b). Rectangular box (cyan) in (a,b) represent the section of the signal that is considered for further analysis.



(a)



(b)



(c)

Figure 4.8: (a) Section of raw needle hydrophone data recorded during the cavitation activity of Fig. 4.5, (blue solid) and control exposure for an equivalent HIFU burst (red dot), without cavitation nucleation. The inset zoom around $19.0 \mu\text{s}$, reveals a detected shock wave in the raw data, also arrowed for the rest of the trace. (b) Control subtracted and needle hydrophone-deconvolved data, revealing the signal emitted by the cavitation, $\tilde{x}_{\text{cav}}^{\text{p}}(t)$, captured in the high-speed imaging of Fig. 4.5c. (c) The cavitation spectrum $\tilde{X}_{\text{cav}}^{\text{p}}(f)$, obtained via Fourier Transform of (b).

of the role played by periodic shock waves. The acoustic emissions used in further analysis are contained within the dashed rectangle, Fig 4.7a,b, which encloses 6 periodic shock waves. This section of the signal is displayed in Fig. 4.8, for which the spectrum in Fig. 4.8c has spectral features with peaks up to $14f_0/2$.

Inspection of Fig. 4.8b indicates that the estimated cavitation emission signal, $\tilde{x}_{\text{cav}}^{\text{p}}(t)$, is comprised of an acoustic wave component, $\tilde{x}_{\text{AW}}^{\text{p}}(t)$, discussed in §4.2.4, and $x_{\text{PSW}}^{\text{p}}(t)$, manifested as $f_0/2$ periodic shock waves, of average period $T_{\text{PSW}} = 2.896 \pm 0.038 \mu\text{s}$ and $PPPA_{\text{SW}} = 63.5 \pm 4.29 \text{ kPa}$.

$f_0/3$ regime

Fig. 4.9 displays the entire acoustic emission emitted by the cavitation activity depicted in Fig. 4.6, with a $1.7 - 1.8 \mu\text{s}$ propagation delay time, as the cloud was located $\sim 2.5 \text{ mm}$ from the

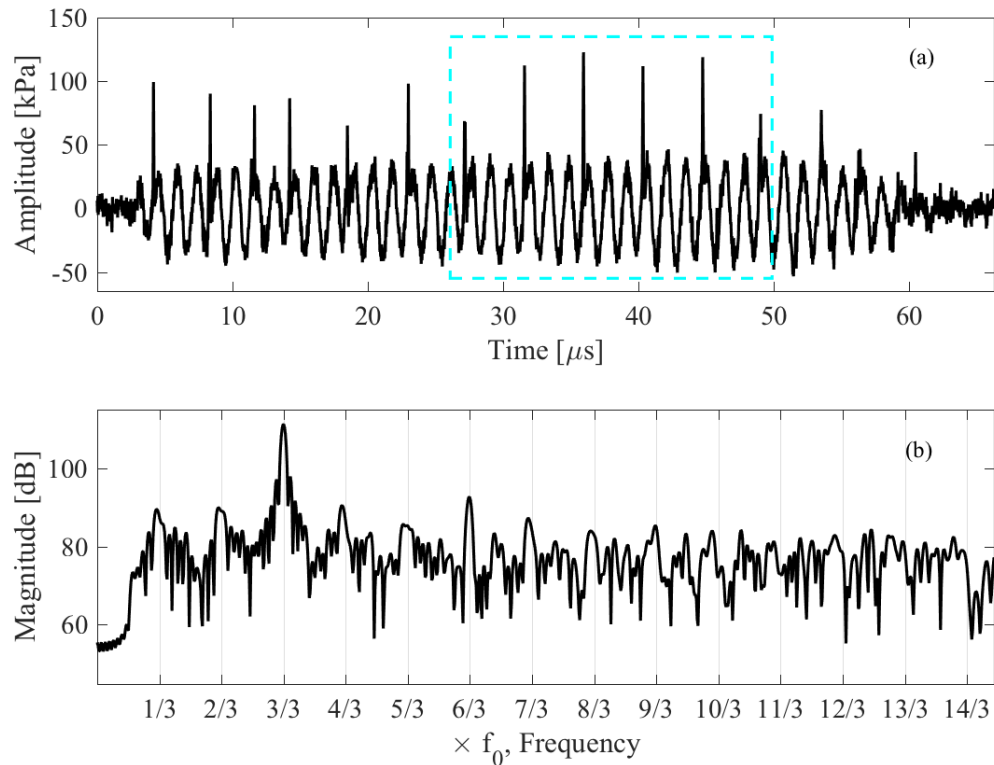


Figure 4.9: (a) Control subtracted and needle hydrophone-deconvolved data, revealing the signal emitted by the cavitation activity, $\tilde{x}_{\text{cav}}^{\text{p}}(t)$. (b) The cavitation spectrum $\tilde{X}_{\text{cav}}^{\text{p}}(f)$, obtained via Fourier Transform of (a). Rectangular box (cyan) in (a) represent the section of the signal that is considered for further analysis.

tip for this experiment. The spectrum has defined spectral features from $f_0/3$ up to $10f_0/3$. A section contained within the dashed rectangle in Fig. 4.9a, is considered for further analysis. This data is displayed in Fig. 4.10.

The acoustic emissions are characterised by an average shock wave period, $T_{PSW} = 4.36 \pm 0.08 \mu\text{s}$, with mean detection times used for multi-front emission. For single-fronted shock waves according to the needle hydrophone data the average $PPPA_{SW} = 108.09 \pm 11.86\text{kPa}$. The larger $PPPA_{SW}$ of the shock waves emitted in the $f_0/3$ regime, compared to those measured at $f_0/2$, can be attributed to the collapse of a larger cloud that has formed (which include higher fragmentation levels), under higher amplitude PPA .

For this bubble regime, the acoustic emissions considered for further analysis have spectral features detectable up to $14f_0/3$, however, with broader peaks compared to the $f_0/2$ data in Fig. 4.8c. This is in part explained by the multi-fronted shock waves, discussed below in §4.2.4.

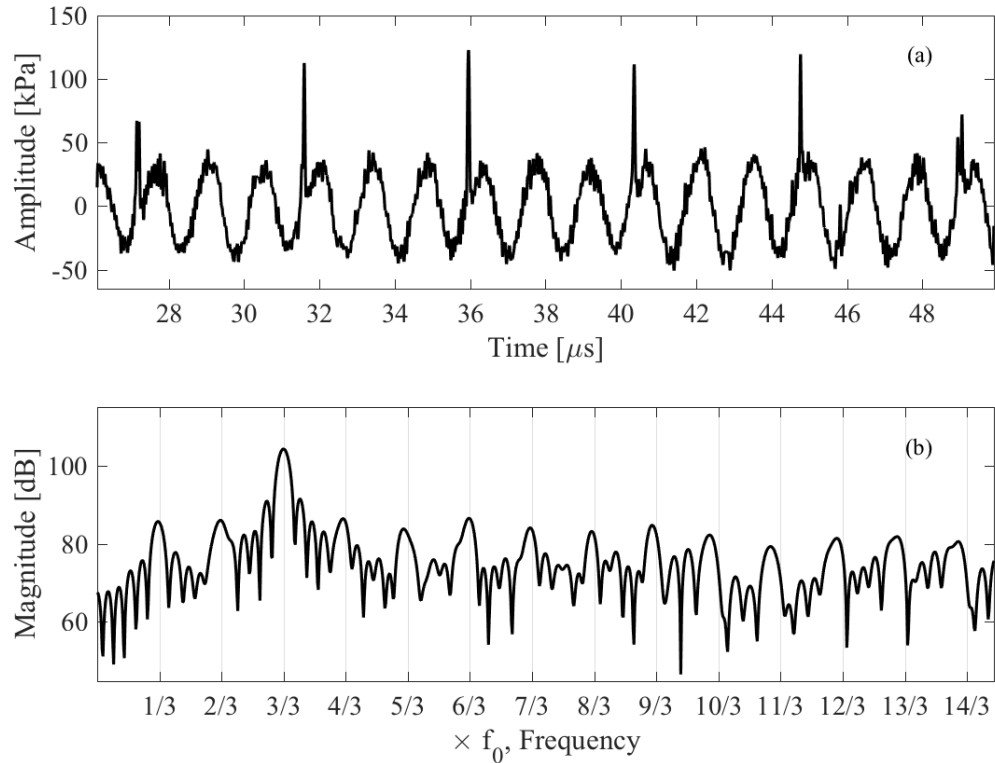


Figure 4.10: (a) Section of deconvolved needle hydrophone data used in analysis of the cavitation noise spectrum. (b) The cavitation spectrum $\tilde{X}_{cav}^p(f)$, obtained via Fourier Transform of (a).

4.2.3 Bubble collapse and shock wave generation

To generate a shock wave for the spectral analysis model in §4.1.1, a BCSW is computed using the methods presented in §3.2.6. Simulation parameters were informed by the the high-speed imaging observations of Fig. 4.5c, which indicates that a single bubble has a maximum radius $R_{\max} \sim 50 \mu\text{m}$, and the Minnaert resonance frequency, Eq. (1.3), was used to estimate the equilibrium radius $R_0 = 4.4 \mu\text{m}$ based on the driving frequency $f_0 = 692 \text{ kHz}$ ⁵. Figure 4.11 shows the solution to Eq. (3.3) for a freely collapsing bubble, and the acoustic emission computed by Eq. (3.14) at a distance of 3 mm from the centre of the cavity. The simulated BCSW in Fig. 4.11, is denoted $s_{\text{sim}}(t)$, and forms the basis of the synthetic spectra construction, described below.

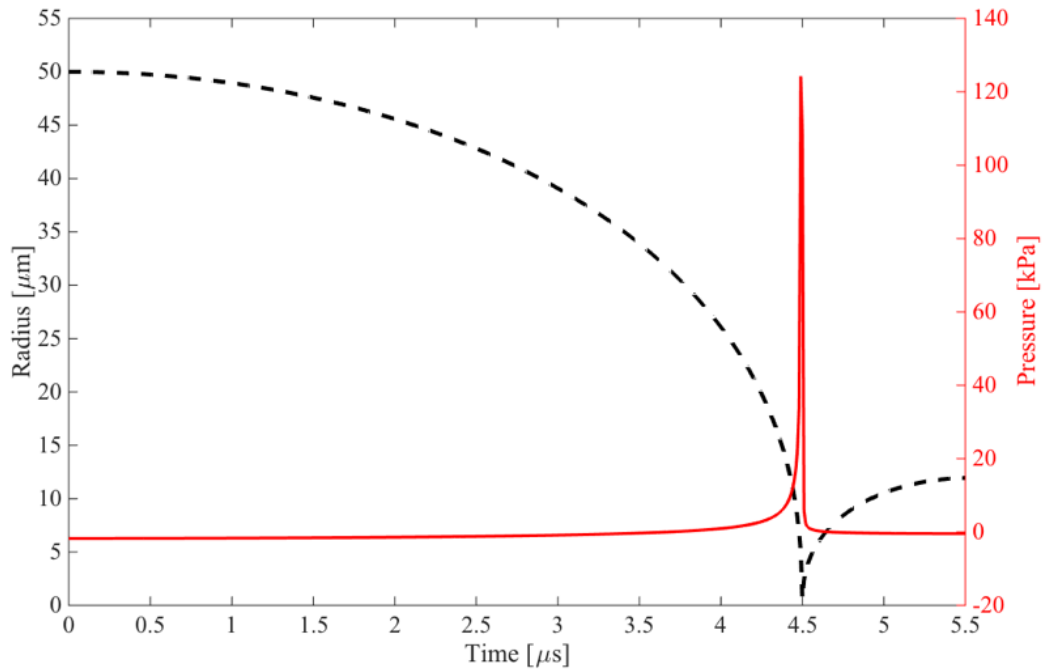


Figure 4.11: Simulated radius-time curve (black dash) and bubble collapse shock wave (solid red) for a free bubble with the parameters, $R_0 = 4.4 \mu\text{m}$, $\dot{R}(0) = 0 \text{ ms}^{-1}$, $R_{\max} = 50 \mu\text{m}$, $c_0 = 1484 \text{ ms}^{-1}$, $p_0 = 101 \text{ kPa}$, $\rho_0 = 998 \text{ kg m}^{-3}$, $m = 0$, $\sigma = 0.072 \text{ Nm}^{-1}$, $\eta = 0.001 \text{ Pa s}$, and $r = 3 \text{ mm}$.

⁵Matlab script is found in Appendix E.1

4.2.4 Synthetic cavitation signal and spectrum

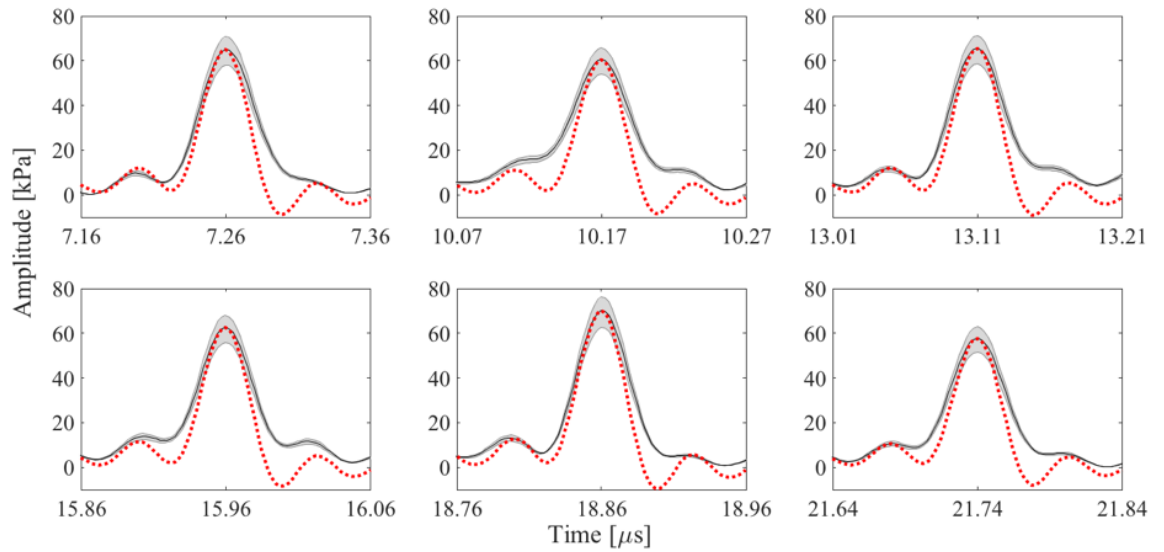
$f_0/2$ regime

In order to elucidate the contribution of component signals to the spectrum of the emitted signal, $\tilde{X}_{\text{cav}}^{\text{p}}(f)$ of Fig. 4.8c, a synthetic spectrum is constructed [152, 153], starting with simulated shock wave profiles. To meaningfully implement $s_{\text{sim}}(t)$ from §4.2.3, for direct comparison to $\tilde{x}_{\text{PSW}}^{\text{p}}(t)$, it is necessary to filter $s_{\text{sim}}(t)$ according to the calibration bandwidth of the needle hydrophone, as discussed in §3.3.2. This is achieved via application of $H_{\text{bpf}}(f)$, such that $S_{\text{sim}}^{\text{bpf}}(f) = S_{\text{sim}}(f) \times H_{\text{bpf}}$, which is retrieved to the time domain as $s_{\text{sim}}^{\text{bpf}}(t) = FT^{-1}S_{\text{sim}}^{\text{bpf}}(f)$.

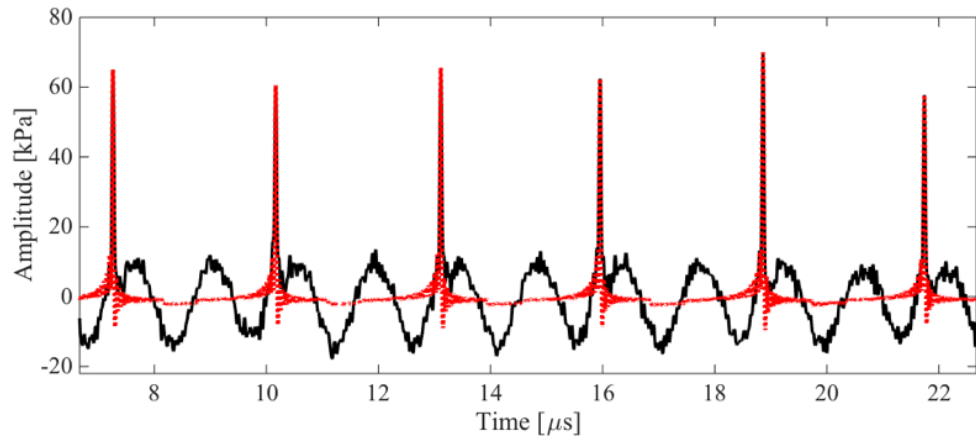
A synthetic periodic shock wave signal, comprising six $s_{\text{sim}}^{\text{bpf}}(t)$ waveform profiles, is constructed via positioning of a $s_{\text{sim}}^{\text{bpf}}(t)$ to coincide with each of the periodic shock waves detected experimentally, and normalised to fit the measured $PPPA_{\text{SW}}$ of that detected shock wave. This matching is illustrated in Fig. 4.12a, with the total synthetic periodic shock wave signal depicted in Fig. 4.12b. In accordance with the spectral analysis model developed in §4.1.1, the spectrum of the synthetic periodic shock waves, Fig. 4.12c, demonstrates peaks at all the frequency values of the experimental spectrum.

It is noted from Fig. 4.12a, that the FWHM of $s_{\text{sim}}^{\text{bpf}}(t)$ underestimates that of $\tilde{x}_{\text{PSW}}^{\text{p}}(t)$, for each of the periodic shock waves under consideration, which was also highlighted in §3.4 for BCSW from laser-plasma mediated vapour bubbles at greater propagation distances. As the spectral analysis model indicates that the periodic shock waves make significant contributions at $n f_0/2$, including $n f_0$, it is reasonable to expect some underestimation across all spectral peaks, for the synthetic periodic shock wave spectrum, Fig. 4.12c.

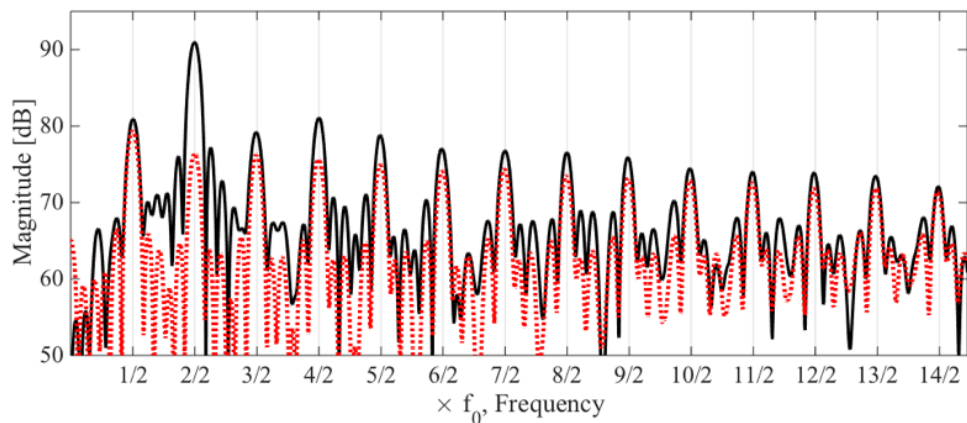
The magnitude of the peak at f_0 , however, is disproportionately underestimated, as is $2 f_0$ to a lesser extent. These deficits may be attributed to acoustic wave components. To estimate the acoustic wave component, $\tilde{x}_{\text{AW}}^{\text{p}}(t)$, the sections of experimentally detected signal between the shock waves are analysed, such as that highlighted by blue-dash, Fig. 4.13a. The signal section intervals are selected so that the data sampled starts 200 ns after the instant of $PPPA_{\text{SW}}$ of preceding shock wave, and ends 400 ns before the next. This provides as long a signal interval as possible for analysis, whilst reducing the influence of the shock waves, and the gradual rise, to



(a)



(b)



(c)

Figure 4.12: (a) The filtered simulated shock wave profiles, $s_{\text{sim}}^{\text{bpf}}(t)$, fitted to each of the shock waves detected experimentally, in the $f_0/2$ regime. The grey envelope represents the calibration uncertainty, incorporated via the deconvolution process. (b) the synthetic periodic shock wave signal (red dot), overlaid to the experimentally detected signal $\hat{x}_{\text{cav}}^{\text{p}}(t)$, (solid black). (c) The synthetic periodic shock wave spectrum overlaid to the experimentally measured cavitation emission spectrum, $X_{\text{cav}}^{\text{p}}(f)$.

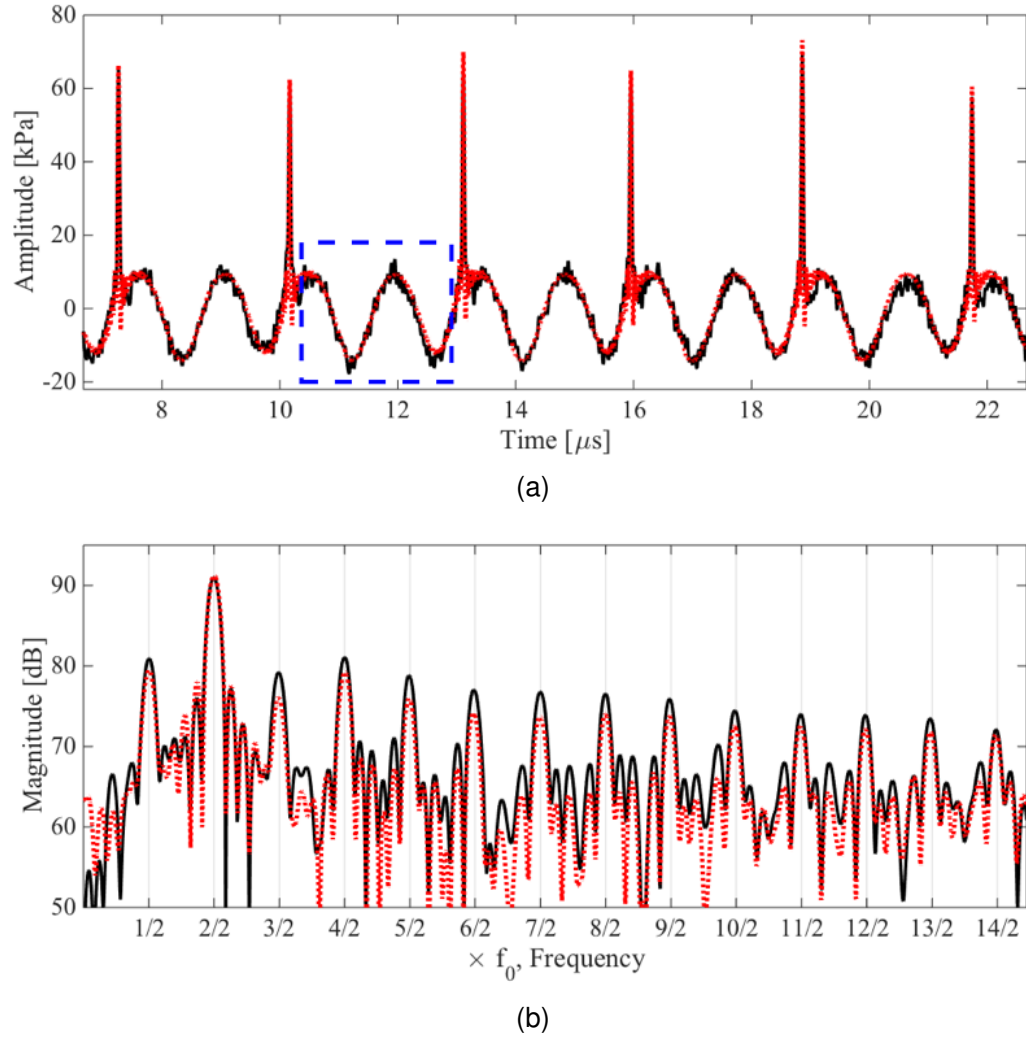


Figure 4.13: (a) The synthetic cavitation signal (red dot) composed of filtered simulated shock wave profiles, $s_{\text{sim}}^{\text{bpf}}(t)$, and synthetic acoustic wave of f_0 and $2f_0$, overlaid to the experimentally detected signal $\tilde{x}_{\text{cav}}^{\text{p}}(t)$, (solid black). (b) The synthetic cavitation spectrum, overlaid to the measured cavitation emission spectrum, $\tilde{X}_{\text{cav}}^{\text{p}}(f)$.

$PPPA_{\text{SW}}$ (characteristic for BCSWs)

An amplitude and phase for the f_0 component from each section is determined by the Fourier Transform of each signal section, giving a mean value of $A_{f_0} = 11.13 \pm 0.58$ kPa and $\theta_{f_0} = 57.68 \pm 4.22^\circ$, for the whole signal of Fig. 4.13a.

As Fig. 4.12c also indicates a deficit at $2f_0$, in comparison with the experimental cavitation spectrum $\tilde{X}_{\text{cav}}^{\text{p}}(f)$, again the signal sections are analysed, such as highlighted in Fig. 4.13a, for this component. The synthetic f_0 component, described previously, is subtracted from each section to minimize the side lobe of the f_0 peak, and an Fourier Transform of the remaining signal taken to give amplitude and phase values of $A_{2f_0} = 0.96 \pm 0.34$ kPa and $\theta_{2f_0} = -150.35 \pm 11.52^\circ$,

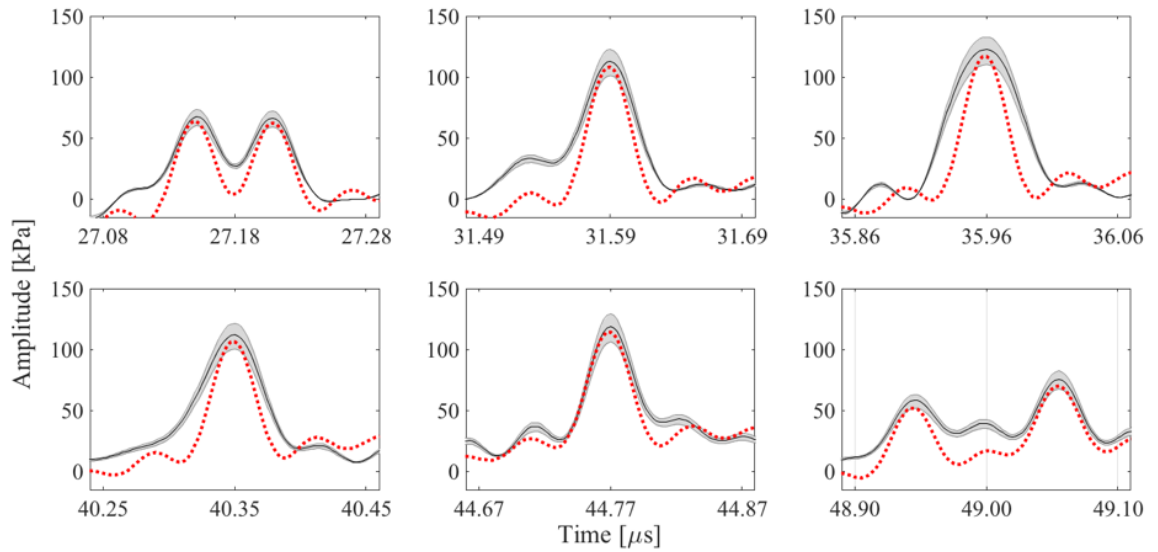
respectively. Addition of these synthetic acoustic wave components to the synthetic periodic shock wave signal generates the total synthetic cavitation emission signal, Fig. 4.13a, and its spectrum Fig. 4.13b. The cross-correlation coefficient between the experimentally detected, and needle hydrophone-deconvolved signal, and the synthetic signal is 0.97⁶.

$f_0/3$ regime

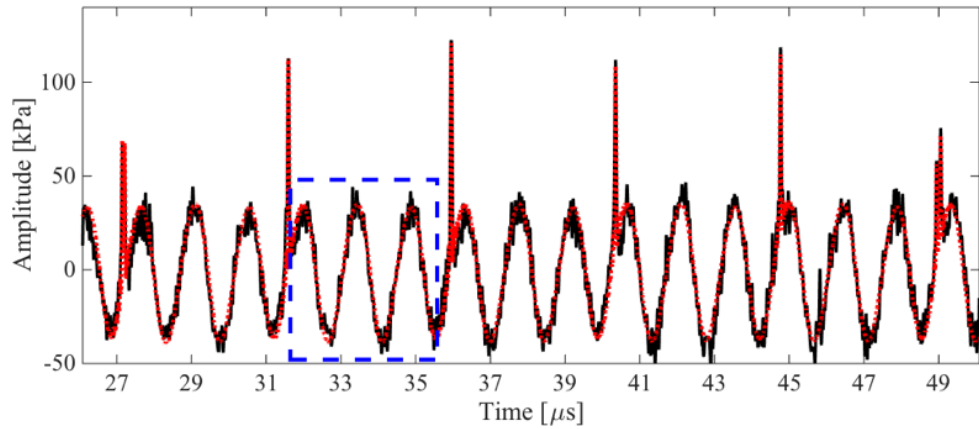
Fig. 4.14a are the needle hydrophone-deconvolved periodic shock waves, emitted by the strong collapses depicted in Fig. 4.6c. The first and sixth shock waves, emitted around 27.18 and 49.00 μs , are comprised of at least two separate fronts, which are resolved by the needle hydrophone. Closer inspection of the high-speed image at 34.21 μs , Fig. 4.6b indicates that this shock wave is also multi-fronted, although this is not resolved by the needle hydrophone, at $\sim 35.96 \mu\text{s}$, Fig. 4.14a. However, the underestimation the FWHM of the needle hydrophone-deconvolved shock wave, by $s_{\text{sim}}^{\text{bpf}}(t)$, is noticeably larger than for this shock wave, than for the others of Fig. 4.14a. This is compatible with the needle hydrophone registering more than one shock wave profile, but failing to resolve the component shock wave peaks.

Figure 4.14a depicts the fitting of the filtered simulated shock waves, $s_{\text{sim}}^{\text{bpf}}(t)$, to those detected experimentally, which are compiled to produce the synthetic periodic shock wave signal. The acoustic wave components at f_0 and $2f_0$ are estimated consistent with the approach adopted previously for the $f_0/2$ regime, as $A_{f_0} = 35.49 \pm 2.20 \text{ kPa}$, $\theta_{f_0} = 111.78 \pm 1.16^\circ$, $A_{2f_0} = 2.47 \pm 0.19 \text{ kPa}$ and $\theta_{2f_0} = 27.30 \pm 10.87^\circ$. The total synthetic signal and its spectrum are presented in Figs. 4.14b and 4.14c, with a cross-correlation coefficient of 0.97 to the experimentally detected, and needle hydrophone-deconvolved signal.

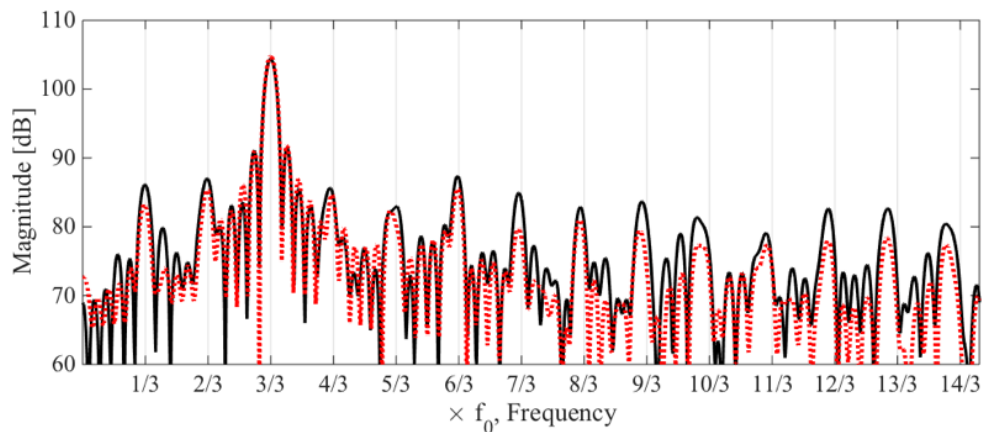
⁶In Appendix B the Keller-Miksis equation is solved for parameters relevant to the experimental configuration used in this Chapter. Both the computed radial dynamics and acoustic emissions, are compared to the high-speed imaging observations and needle hydrophone measurements for both sub-harmonic cavitation regimes, $f_0/2$ and $f_0/3$. This work featured as a conference proceeding: **K. Johansen, J. H. Song, and P. Prentice.** "Validity of the Keller-Miksis equation for "non-stable" cavitation and the acoustic emissions generated." *International Ultrasonics Symposium (IUS) IEEE, 2017.*



(a)



(b)



(c)

Figure 4.14: (a) The filtered simulated shock wave profiles, $s_{\text{sim}}^{\text{bpf}}(t)$, fitted to each of the shock waves detected experimentally, in the $f_0/3$ regime. The grey envelope represents the calibration uncertainty, incorporated via the deconvolution process. (b) the synthetic cavitation emission signal (dotted red), with acoustic emission components $\tilde{x}_{\text{AW}}^{\text{p}}(t)$ added, overlaid to the experimentally measured cavitation emission signal (solid black). (c) The synthetic periodic shock wave spectrum, overlaid to the experimentally measured cavitation emission spectrum, $\tilde{X}_{\text{cav}}^{\text{p}}(f)$.

4.2.5 Comparing cavitation noise spectra for $f_0/2$ and $f_0/3$

The cavitation noise spectra for the two regimes are compared in Fig. 4.15, and several noticeable features may be highlighted. For instance, the pressure amplitude of all spectral features exclusive to the $f_0/3$ regime are higher than those exclusive to the $f_0/2$ regime. This is because the periodic shock waves forming the spectral features are of higher $PPPA_{sw}$ for the $f_0/3$ regime, which is in agreement with the theory presented in §4.1.1. Furthermore, it is appreciated that the broadband noise is higher between spectral features above $3f_0$ for the $f_0/3$ regime. This is because the acoustic emissions collected (for the $f_0/3$ regime) are composed of 3 double fronted shock waves, and this causes the periodic shock waves not to repeat ‘perfectly’ at $f_{PSW} = f_0/3$. Consequently, spectral content is ‘leaked’ into the frequency range typically characterised as broadband noise.

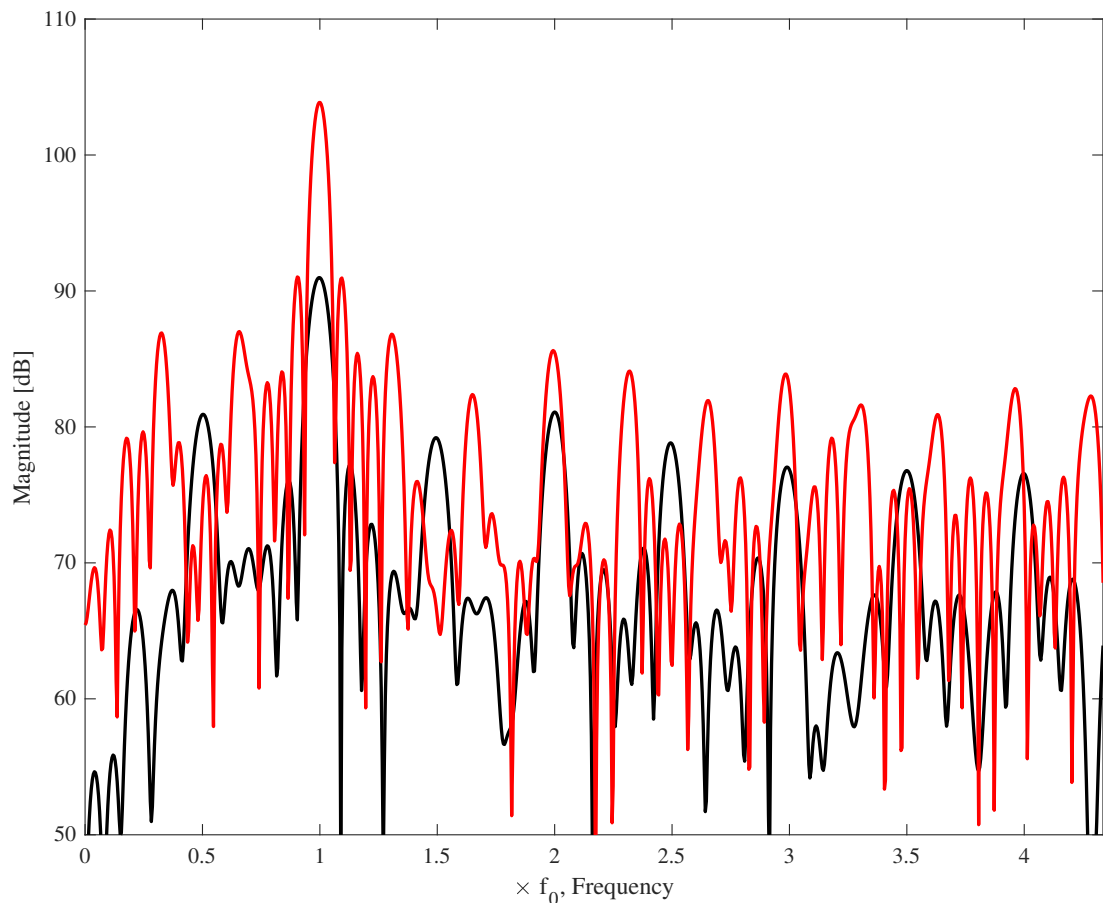


Figure 4.15: A comparison of the acoustic cavitation noise spectra from $f_0/2$ (black) and $f_0/3$ (red) data.

4.3 Discussion

The spectral analysis model presented in §4.1.1, is verified by the experimental evidence in §4.2.4. The results confirm that periodic shock waves have a significant contribution to the acoustic cavitation noise spectrum.

To compare the amplitudes of the emitted signal components $x_{\text{PSW}}(t)$ and $x_{\text{AW}}(t)$, the root mean square (RMS) amplitudes of the synthetic $f_0/2$ signal is calculated, Fig. 4.13a, as 6.58 and 7.90 kPa, respectively. This shows that the two components are of similar RMS amplitude. Moreover, the experimental cavitation spectra can be well approximated as a series of bubble-collapse shock waves and an acoustic f_0 component. Under this approximation, the non-linearity of the cavitation emission signal is concentrated within the shock wave content, or in terms of bubble oscillation, the collapse phases.

In §1.4.3 it was proposed that the non-linear acoustic emissions from stable-inertial cavitation are shock wave mediated, and the variation in the periodicity to the periodic shock waves is related to the stability of the cavitation activity. This is supported by the results shown in Fig. 4.15, where the cavitation spectrum for the $f_0/2$ regime is reasonably described as being generated by more ‘stable’ and less inertial source bubble dynamics than the $f_0/3$ regime, with both lower amplitude of broadband noise and more well defined spectral features at frequencies exclusive to the cavitation regime. It is worth noting that the comparison presented in Fig. 4.15 is in agreement with the binary classification of cavitation, discussed in §1.4.2, where a higher level of broadband noise is understood to be a result of inertial (or more inertial) cavitation.

It is also worth remarking that the results presented in Fig. 1.8 for a collection of microbubbles, generally are described by similar changes in over all characteristics, as discussed for Fig. 4.15. However, the change in broadband noise for frequencies below $3f_0$ is less pronounced in Fig. 4.15 for a higher driving amplitude. This is because the variation in periodicity ($T_{\text{PSW}} = 2.896 \pm 0.038 \mu\text{s}$ for $f_0/2$, and $T_{\text{PSW}} = 4.36 \pm 0.08 \mu\text{s}$ for $f_0/3$) is small compared to the frequencies ($f = 1/T$) forming the peaks in the spectra below $3f_0$. Moreover, the acoustic emissions selected for further analysis were specifically chosen because of the small variation in T_{PSW} , but when the spectra of the entire acoustic emission, Fig. 4.7c and Fig. 4.9b, are compared in terms of broadband noise

level, the $f_0/2$ and $f_0/3$ regime have ~ 70 dB and ~ 80 dB, respectively. This is in agreement with what would be expected from a more strongly driven cavitation activity.

All the results in Fig. 1.8 above 100 kPa contain a $3f_0/2$ ultra-harmonic spectral feature, and the amplitude was elevated for increasing driving amplitude. It is not possible to meaningfully compare the change in amplitude of ultra-harmonics to the cavitation data presented in Fig. 4.15, because it represents two different sub-harmonic regimes. Obviously, the comparison between the results in Fig. 1.8 and Fig 4.15 is limited by the fact that a collection of microbubbles distributed throughout the focus to the acoustic field (and therefore responding to different pressure amplitude driving, as discussed by the authors in §1.4.3), is not directly equivalent to a single cavitation bubble or a tightly packed cloud of bubbles.

For the purposes of constructing synthetic spectra, the cavitation emissions have been considered as separate components. It should be emphasised, however, that the cavitation signal is continuously emitted according to the source bubble dynamics, and should not generally be considered as individually emitted components. This point is particularly pertinent when considering the simulated BCSW profile of Fig. 4.11, and that detected from a laser-plasma mediated vapour bubble collapse in Fig. 3.5c (ii), particularly in contrast to the optical break down shock wave of Fig. 3.5c (i). BCSW profiles exhibit a characteristic gradual rise to $PPPA_{SW}$, appreciable from several tenths of a microsecond before the time of $PPPA_{SW}$, and distinct to the sharp rise typical of other shock wave profiles, including the optical break down shock wave. This gradual rise is generated by the bubble emitting as it deflates into the collapse, with the spike of the shock wave generated at the moment of minimum radius. For periodic shock waves emitted from driven clouds, the gradual rise will be irrevocably imposed over the acoustic emissions, or rather is integral to them. The influence of the gradual rise is also apparent in Fig. 4.13a, where the alternating troughs of the acoustic signal component, preceding the shock wave detections, are elevated relative to the other troughs, by 2.36 ± 0.71 kPa, for this data.

The synthetic f_0 , as the dominant component required to fit the synthetic spectra to those measured experimentally, may be attributed to scattering of the primary field, or linear bubble oscillation-generated emission. The underestimation of the $2f_0$ peak of the experimental spectra, by the synthetic periodic shock wave signal, could indicate some non-linearity of the bubble

oscillations between collapses. However, the gradual rise of the periodic shock waves will not have been fully removed by the selecting of the signal sections from 200 ns after, to 400 ns before, the $PPPA_{SW}$. The $2f_0$ component could originate from either of these sources, or some combination of both.

For both the $f_0/2$ and $f_0/3$ regimes, the synthetic periodic shock wave signal underestimated the magnitude of all spectral features within the respective cavitation spectra, detected experimentally. Inspection of the simulated shock waves, normalised to the pressure amplitude of the experimentally detected needle hydrophone-deconvolved shock waves, indicates that the FWHMs are also consistently underestimated, in the synthetic signal Figs. 4.12a and 4.14a. It is speculated that one source of this underestimation is a spreading effect, across the tip of the needle hydrophone, during shock wave detection. This effect can be appreciated from Figs. 4.5a and 4.6a, where direct observation of the shock wave confirms that the shock front is initially incident to the sensing surface at the point directly below the cavitation cloud position. As the shock wave spreads across the tip, the detected FWHM will become extended in duration. Considering the geometry of the experimental configuration, the effect of shock wave spreading is estimated to be several tens of ns of widening for the FWHM of the detected shock wave profile. This is estimated by considering the shock wave as a Dirac-function, and computing the difference in arrival time at the centre and the edge of the active area to the needle hydrophone⁷. A detector with a smaller active area, or placed further from the cavitation activity would reduce the radius of curvature of the shock wave on detection, leading to better matching between the experimental and simulated shock wave profiles, as in Chapter 3.

The key aspect behind the spectral analysis of periodic shock waves is the periodicity of the shock waves. A single shock wave, or many aperiodic shock waves may be expected to contribute via raising the noise floor of the spectrum, as discussed in §1.4.4. In contrast, periodic shock waves, emitted sub-harmonically at f_0/m , must provide spectral peaks at $n f_0/m$, for all values of n and m .

The focused acoustic field and frequency used for the cavitation measurements presented in this Chapter are typical for medical applications, as discussed in §1.5.1. Though, cavitation is

⁷The same method was used in Chapter 3 to estimate the spreading effects.

not limited to medical applications, and in sonochemistry lower frequencies are used, normally below 100 kHz [154]. For example, fundamental research on cavitation dynamics in aluminium melts is carried out at frequencies ~ 20 kHz with sonotrodes using magnetostrictive ultrasonic transducers [155]. At such frequencies the resonance radius is ~ 100 μm , which is ~ 20 times greater than the resonance radius at 692 kHz (4.4 μm). Even though bubbles in sonochemistry are typically larger than nucleated in this work, it is interesting to note that Rayleigh-Plesset-like equations, such as the Gilmore equation and the Keller-Miksis equation, suggest that periodic shock waves from sub-harmonically responding bubble should exist [15]. It is therefore reasonable to speculate that even larger bubbles than studied in this thesis, have sub-harmonic spectral features mediated via periodic shock waves. It is also worth noting that experimental verification, reconciling source bubble dynamics and acoustic emissions for large bubbles has yet to be achieved.

Another important feature of large bubbles ($R_0 \sim 100$ μm) is that they are inherently more unstable than competitively smaller bubbles ($R_0 \sim 5$ μm) [71]. This causes large bubbles to more easily fragment and coalesce during collapses. At resonance, surface wave may be established, and for intense driving conditions the amplitude may grow large, sometimes sufficient to throw off microbubbles from their crests. Additionally, jets may also occur within a cloud of bubbles after fragmentation [120]. This is expected to cause multi-fronted shock waves because the collapse is not symmetric, as seen in Fig. 4.6, which will contribute to a larger variation in the periodicity to the emitted acoustic emissions, and raise the broadband noise level as discussed for Fig. 4.7c and Fig. 4.9b.

From the broadband nature of the shock waves, detection of cavitation activity can be undertaken at any $m f_0/n$ peak, however the sub-harmonics and ultra-harmonics are exclusive to cavitation. Nevertheless, experimental constraints such as absorption of higher frequency content and detector characteristic should be taken into account when selecting a monitoring protocol, as discussed in §1.4.1.

4.4 Conclusion

In this Chapter, a simple spectral analysis model demonstrating a significant contribution to the cavitation spectrum from periodic shock waves, at $n f_0/m$ peaks for all values of n and m , with supporting experimental data for $m = 2$ and 3. It is concluded that simultaneous detection of the sub-harmonic signal at f_0/m , with ultra-harmonics at $n f_0/m$, is suggestive of a cavitating system that is generating periodic shock waves.

Chapter 5

Covert cavitation: Spectral peak suppression in the acoustic emissions from spatially configured nucleations

The previous chapter demonstrates the role of periodic shock waves in the cavitation noise spectrum – from a single cavitation bubble. In any application of acoustic cavitation, however, the occurrence of a single bubble in a medium exposed to intense ultrasound is highly improbable. The question then arises as to how the results of Chapter 4 translate to ‘real’ cavitation spectra, from multiple and distributed cavitation events. This chapter, resulting from a ‘thought experiment’ conceived during a group meeting goes some way to address this question, through the introduction of a second bubble ¹ to the experiment described in Chapter 4 ².

¹There are direct consequences when a ‘reflected cavitation signal’ is co-detected with ‘primary signal’. This is identified and assessed, with the model developed in this chapter, in Chapter 6.

²The results presented in this Chapter were first published in; *J. H. Song, K. Johansen, P. Prentice. "Covert cavitation: Spectral peak suppression in the acoustic emissions from spatially configured nucleations." The Journal of the Acoustical Society of America 141, no. 3, pp EL216-EL221, 2017.*

5.1 Materials and methods

The experimental arrangement is broadly similar to that described in detail in both Chapter 4 §4.1.2 and Song *et al.* [48], with two modifications distinguishing the current work.

Briefly, the HIFU transducer (§2.1), generates a 90-cycle burst of ultrasound at $f_0 = 692$ kHz and peak-positive pressure amplitude, $PPA = 1.63 \pm 0.12$ MPa, identified as driving cavitation at the focus in the $f_0/2$ regime, as described in §4.1.3. The NH is mounted within the central hole through the body of the HIFU transducer, such that it aligns to the propagation axis of the field generated, Fig. 5.1a and 5.1b. Cavitation is again introduced to the focus of the HIFU field via the laser-nucleation technique, however, to generate the results presented below, however, a 50:50 beam splitter (BS010, Thorlabs, Ely, UK) is introduced to the nucleating laser-pulse beam path. The component beams from the nucleation laser of energy 2.4 ± 0.2 mJ (instrument error according to manufacturer), are steered to the back apertures of two long-working distance microscope objective lenses ($50\times$ 0.42 NA Mitutoyo, Kawasaki, Japan), Fig. 5.1a, sealed in water-tight units and mounted on xyz manipulators³. This configuration permits simultaneous

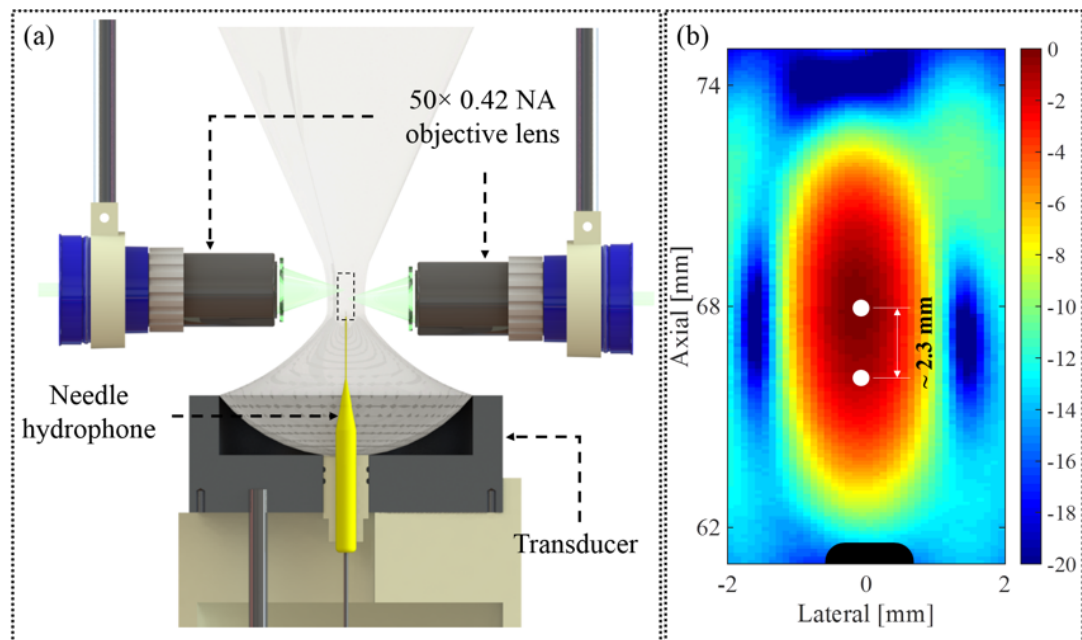


Figure 5.1: Illustration of experimental setup: (a) cross-sectional view of HIFU transducer-needle hydrophone configuration, and two long-working distance objective lenses facilitating dual-laser nucleation of cavitation bubbles. (b) An axial scan of the HIFU focal region, including the targeted laser-nucleation zones, to which the laser-nucleating foci were aligned.

³The modification of the experimental configuration used in Chapter 4 was performed by Dr Paul Prentice.

dual laser-nucleation of two, independently positioned, cavitation-bubbles, Fig. 5.2. Ultra-high speed shadowgraphic imaging is undertaken at 5×10^6 fps with a Shimadzu HPV-X2 camera (Shimadzu, Kyoto, Japan), as described in §2.4.

The second difference is a macro-objective lens (Zeiss 100 mm f2 Makro-Planar Milvus ZF.2, Oberkochen, Germany) issued for imaging, facilitating a larger field of view than that reported previously in §4.2.1, such that shock wave emission from both cavitating bubbles, can be visualised. This field of view also provides some appreciation of HIFU propagation, which is used for HIFU-detection purposes in Appendix C ⁴.

5.2 Results

5.2.1 High-speed imaging

Figure 5.2a displays a schematic of the dual-nucleated acoustic cavitation activity positioned relative to the needle hydrophone, and in Fig. 5.2b representative images extracted from a high-speed sequence, each comparable to the single bubble $f_0/2$ regime activity reported previously in §4.2.1, characterised by stable $f_0/2$ periodic shock wave emission ⁵. At the field of view delivered by the macro-objective, the bubble activity is barely resolved. However, the compressional and rarefactional phases of the propagating HIFU can be appreciated [156], as fringes slightly brighter and darker than the ambient background (labelled C and R, Fig. 5.2), respectively. The effect is better perceived from the video version of the data, where it can be seen that the bubbles collapse and emit shock waves in response to every other compressional phase, confirming the $f_0/2$ response regime ⁶. The salient features of this data are two cavitating bubbles (hereafter referred to as top^t and bottom^b bubbles), separated by 2.3 ± 0.1 mm, which compares to the

⁴In Appendix C shadowgraphic high-speed imaging is used to characterise aspects of the acoustic field for another transducer at a higher frequency ($f_0 = 1.1$ MHz) where it is easier to see the propagating field. This work originally featured as a proceeding; **K. Johansen, J. H. Song, P. Prentice.** "Characterising focused ultrasound via high speed shadowgraphic imaging at 10 million frames per second". In *IEEE Ultrasonics Symposium*, pp. 1-4. 2016. [156].

⁵Many thanks to Dr Jae Hee Song for the development of the spectral analysis model for dual bubbles, collection of experimental data, and preparation of figures. The author contributed with the Gilmore model for computation of a bubble collapse shock wave used in the construction of the synthetic signal, simulation of bubble-bubble interaction using the Keller-Miksis equation, including analysis and discussion of experimental results for publication.

⁶The video is found as supplementary material to the original publication [157]. The web address is: <https://asa.scitation.org/doi/full/10.1121/1.4977236>

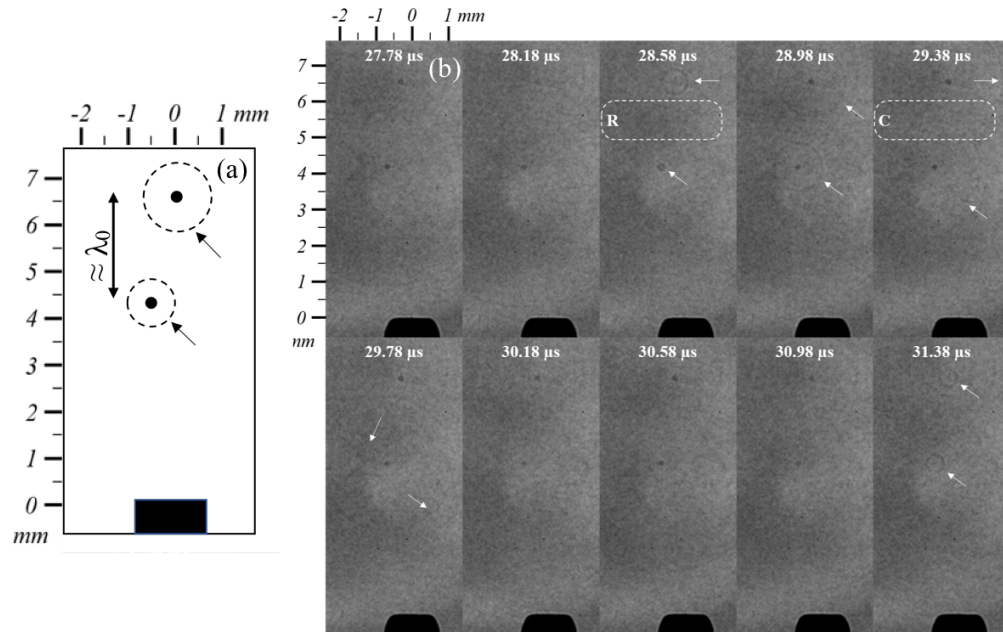


Figure 5.2: (a) Schematic of dual-nucleated cavitation bubbles emitting periodic shock waves (arrowed) displaced $\approx \lambda_0$ apart such that the $nf_0/2$ spectral content in the shock waves is detected 90° out of phase for the respective bubbles. The bubbles are positioned approximately in-line with the needle hydrophone. (b) Selected high-speed shadowgraphic images, recorded at 5×10^6 fps of two cavitation-bubbles, with an inter-bubble spacing $\approx \lambda_0$. Bright and dark regions, indicated by dash box C and R, represent compressional and rarefactional phases of the HIFU driving. Periodic shock wave emission, arrowed (white) at 28.58 μs and 31.38 μs (but not 30.18 μs , when an intervening compressive phase is incident) verifies that both bubbles are in the $f_0/2$ sub-harmonic regime.

HIFU wavelength, $\lambda_0 = 2.14$ mm, emitting $f_0/2$ periodic shock waves approximately in-phase. Intuitively, this leads to a combined effective shock wave detection frequency of f_0 , at the needle hydrophone tip, visible to the bottom of each image, Fig. 5.2. It is also worth noting that, since the bubbles are collapsing in-phase in the $f_0/2$ regime, with a $\sim T_0$ difference in arrival time for the top and bottom shock wave, all spectral content at $nf_0/2$ is detected by the needle hydrophone with a 90° phase difference, from the respective bubbles.

5.2.2 Hydrophone data

Figure 5.3a contains the raw data from the dual-nucleated cavitation bubbles (blue solid) and the control exposure (black dot) for an equivalent HIFU burst. Towards the end of the HIFU burst, the

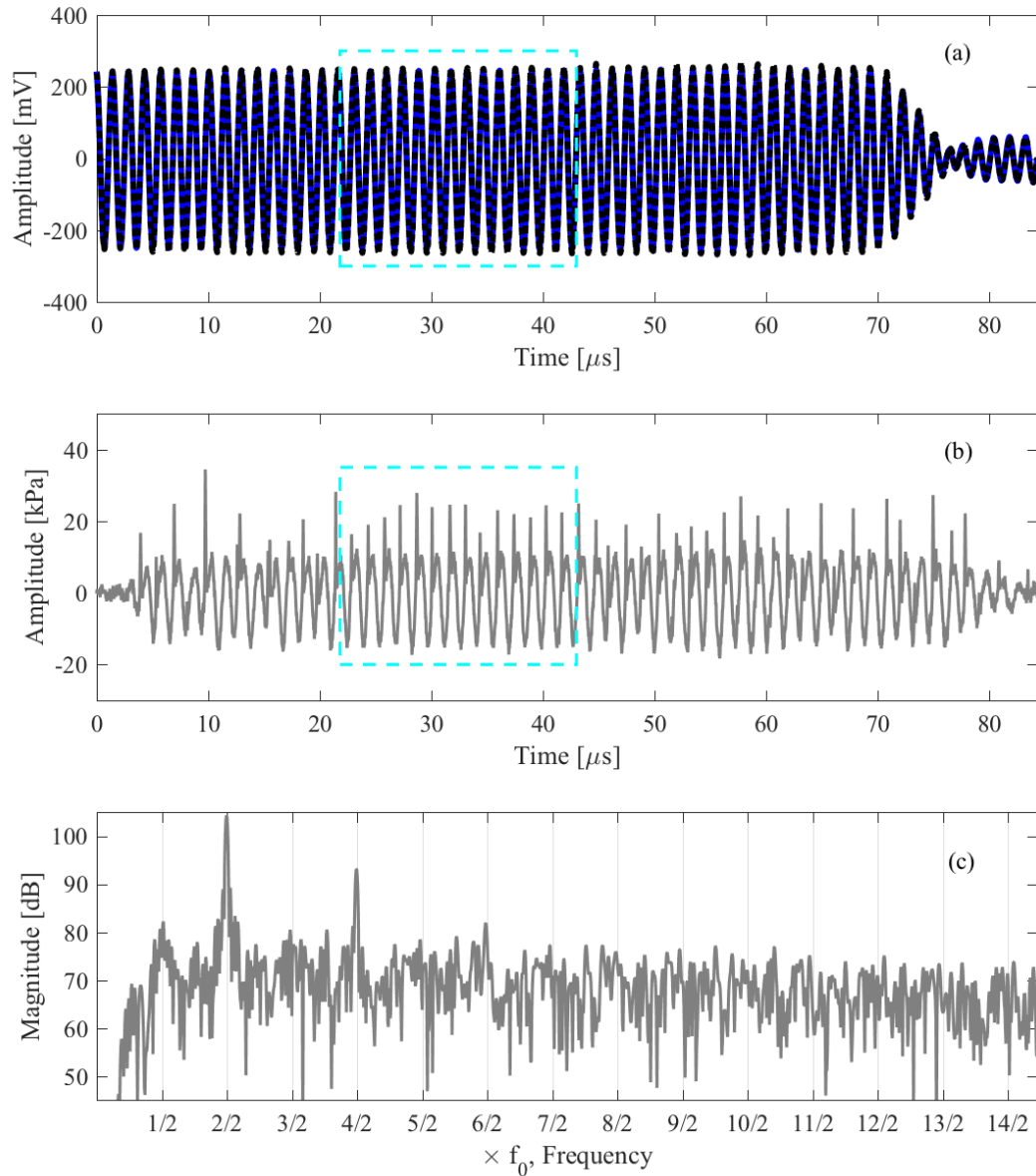


Figure 5.3: (a) Raw needle hydrophone data recorded during the cavitation activity captured in Fig. 5.2 (blue solid) and control exposure for an equivalent HIFU burst (black dot). (b) Pressure-time waveforms of control-subtracted and deconvolved needle hydrophone data (solid grey). (c) The acoustic emission spectrum (solid grey) for the combination system. Rectangular box (cyan) in (a,b) represent the section of the signal that is considered for further analysis.

amplitude of the detected signal reduces, however due to reflections from the water-air interface, the signal does not fall to zero at the end of the upwardly propagating HIFU burst. Figure 5.3b represent the control-subtracted needle hydrophone data (solid grey), deconvolved from the impulse response of the needle hydrophone with magnitude and phase calibration (§3.2.5). Figure 5.3c is the spectrum of the acoustic emissions in Fig. 5.3b, which is characterised by containing strong over-harmonics of the driving frequency, and a broad low amplitude peak at the $f_0/2$ spectral feature. To better appreciate how spatially configured cavitation bubbles can suppress spectral features exclusive to cavitation, a section of the acoustic emissions contained within the dashed rectangle in Fig. 5.3a,b, captured prior to the arrival of the reflections, with the combined periodic shock waves arrive at f_0 , is considered. This section of the acoustic emission

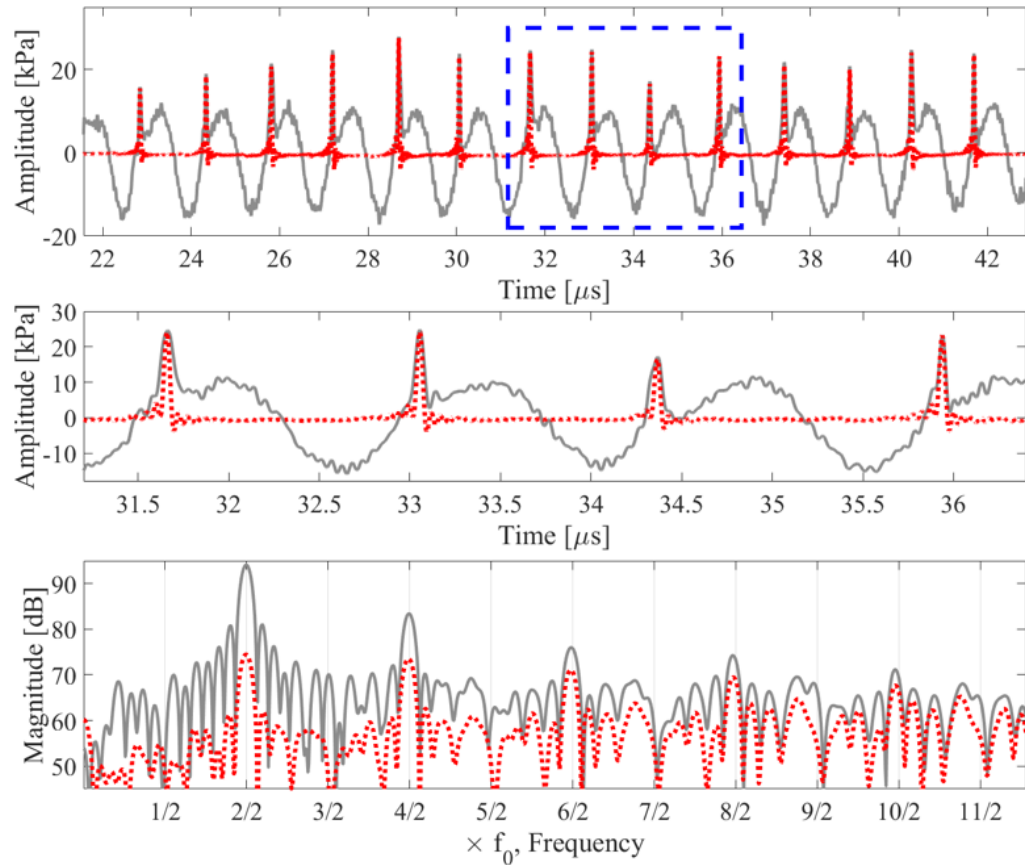


Figure 5.4: (a) Pressure-time waveforms of control-subtracted and deconvolved needle hydrophone data (solid grey) and synthetic periodic shock wave signal (red dot), with the blue-dash box reproduced in (b) corresponding directly to the selected images of Fig. 5.2. (c) The experimental needle hydrophone (solid grey) and periodic shock wave synthetic (red dot) spectra for the combination system, revealing no sub-harmonic content including at odd-numbered higher harmonics.

is displayed in Fig. 5.4a, with Fig. 5.4 corresponding to the emissions imaged during high-speed acquisition, Fig. 5.8b.

A synthetic periodic shock wave signal (red dot, Figs. 5.4a and 5.4b), is constructed from simulated shock wave profiles, derived from solving the Gilmore equation for a freely collapsing resonant bubble (§3.2.6 and §4.2.3), and fitting to the experimental data. Synthetic acoustic f_0 and $2f_0$ components, of amplitudes and phases 10.68 ± 0.62 kPa, $121.75^\circ \pm 5.31^\circ$ and 1.88 ± 0.52 kPa and $52.59^\circ \pm 21.96^\circ$, respectively, can be added for consistency with the full synthetic spectrum construction procedure described previously in §4.2.4. This yields a correlation coefficient of 0.96 between the full synthetic and experimental spectrum (solid grey, Fig. 5.4c), indicating the signal is well represented. However, for the purpose of developing the model below to derive a window function in the frequency domain, only the periodic shock wave spectra (red dot, Fig. 5.4c) of the synthetic periodic shock wave signal are considered, which presents peaks at all relevant frequency values.

Inspection of the periodic shock wave profiles of Fig. 5.4b, demonstrates that the shock waves from the top and bottom bubbles can be distinguished by their FWHM, with the wider shocks from the lower bubble, detected at $31.66 \mu\text{s}$ and $34.37 \mu\text{s}$, due to the more oblique incidence to the needle hydrophone tip, represented in Fig. 5.2a.

In Fig. 5.5a the acoustic emission is bandpass filtered from 1.5 to 20 MHz to remove f_0 and $2f_0$ components, revealing detected shock widths of $FWHM_{\text{PSW}}^{\text{t}} = 40.57 \pm 3.97$ and $FWHM_{\text{PSW}}^{\text{b}} = 65.00 \pm 7.62$ ns from the top and bottom bubbles, respectively. Analysis of Fig. 5.4a also reveals that the period of shock wave emission, $T_{\text{PSW}}^{\text{t}} = 2.893 \pm 0.068 \mu\text{s}$ and $T_{\text{PSW}}^{\text{b}} = 2.905 \pm 0.116 \mu\text{s}$, compared to $2T_0 = 2.890 \mu\text{s}$, for the HIFU field.

5.2.3 Simulation of bubble-bubble interaction

It is recognised that the scattered sound field from a cavitation bubble can substantially influence the radial dynamics of neighbouring bubbles during multi-bubble cavitation [158]. However, in this section, it is shown that approximating the top and bottom bubble in Fig. 5.2 as independent,

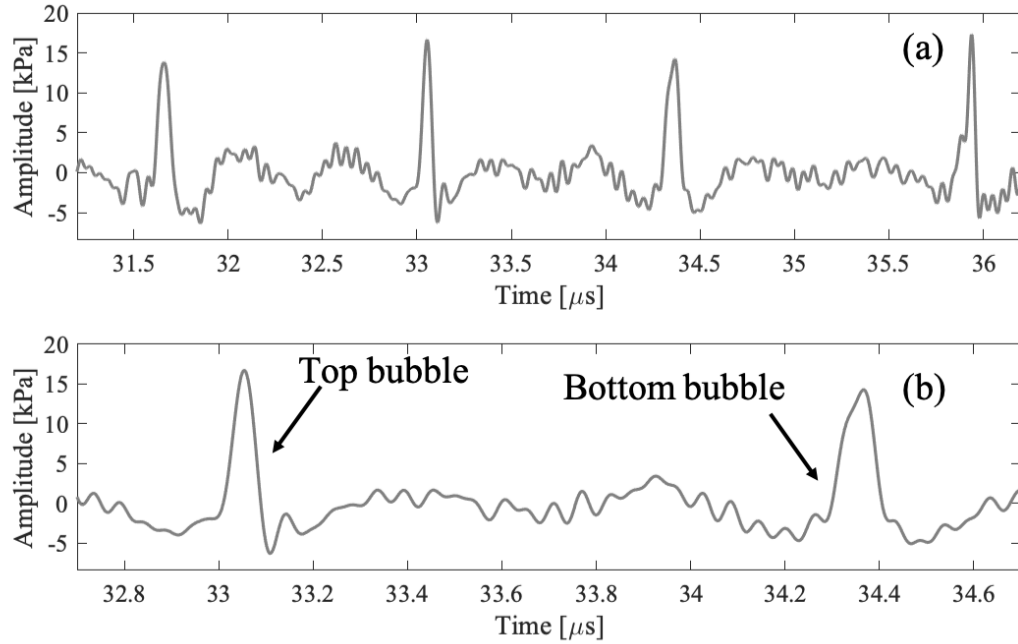


Figure 5.5: (a) Control-subtracted deconvolved needle hydrophone signal after bandpass filtering from 1.5 MHz to 20 MHz for the acoustic emissions in Fig. 5.4b. (b) 2nd and 3rd shock wave from Fig. 5.4b, which demonstrates the difference in FWHM from the top and bottom bubble (arrowed) caused by the positioning relative to the needle hydrophone, Fig. 5.2.

is reasonable⁷. This is done because it is one of the assumptions used in the development of the spectral analysis model, discussed below in §5.2.4.

In Fig. 5.2 it is observed that the distance between the two bubbles is much greater than the radius of the individual bubbles, which makes it reasonable to assume that both bubbles remain spherical during the HIFU burst, as reported in §4.2.1. This suggests that Rayleigh-Plesset-like equations, as discussed in §3.2.6, can be utilised for evaluation of the bubble dynamics under consideration. In this section, the Keller-Miksis equation for bubble-bubble interaction, which is an accepted model for interpreting multi-bubble dynamics [158–163], is used⁸.

$$\left(1 - \frac{\dot{R}_i}{c}\right) R_i \ddot{R}_i + \left(\frac{3}{2} - \frac{\dot{R}_i}{2c}\right) \dot{R}_i^2 = \frac{1}{\rho_0} \left(1 + \frac{\dot{R}_i}{c}\right) p_{i,w} + \frac{R_i}{\rho_0 c} \frac{dp_w}{dt} - \frac{R_j^2 \ddot{R}_j + 2R_j \dot{R}_j^2}{D_{i,j}}, \quad (5.1)$$

⁷This section was not a part of the original publication, however, it was an important component of the response to reviewers document, particularly with regards to the assumption of the top and bottom bubble being independent sources of periodic shock waves.

⁸A more comprehensive discussion of the validity to the Keller-Miksis equation for a single cavitation bubble in the same oscillation regime, is found in Appendix B.

where R_i is the instantaneous radius of bubble i , R_j is the instantaneous radius of bubble j , and the dots indicate time derivatives, $D_{i,j}$ is the centre to centre distance between bubble i and j , c is the speed of sound, and $p_{i,w}$ is the pressure at the wall of bubble i , which can be expressed as:

$$p_{i,w} = \left(p_0 + \frac{2\sigma}{R_{i0}} \right) \left(\frac{R_{i0}}{R_i} \right)^{3\gamma} - \frac{2\sigma}{R_i} - \frac{4\mu\dot{R}_i}{R_i} - p_0 - PPA \sin(\omega t), \quad (5.2)$$

where σ is the surface tension between the gas–water interface, R_{i0} is the equilibrium radius of bubble i , γ is the polytropic exponent, and $PPA \sin(\omega t)$ is the acoustic driving term⁹. The last term on the right-hand side is the coupling between the two bubbles, which has the same form as Eq. (3.14), excluding ρ_0 . Omitting the last term of Eq. (5.1) reduces it to a single bubble model, as discussed in Appendix B.

In closely spaced cavitation, and particularly for long HIFU exposures, radiation forces induced by the driving acoustic field, and the acoustic emissions generated by neighbouring

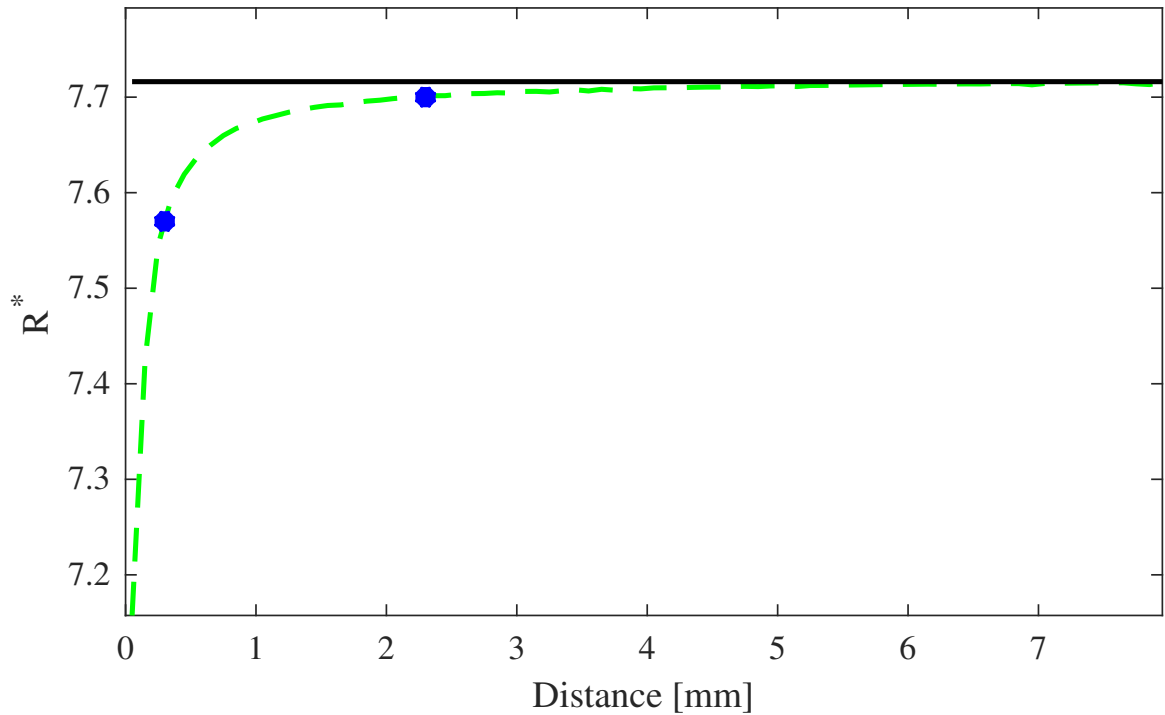


Figure 5.6: Normalised maximum radius defined as $R^* = (R_{\max} - R_0)/R_0$ for solutions of Keller-Miksis equation for single bubble (solid black) and bubble-pair (stapled green) as a function of separation distance. Computed radial dynamics and acoustic emissions for two separation distances (blue dots), are shown in Figs. 5.8 and 5.7. Parameters used are $\sigma = 0.072 \text{ N m}^{-1}$, $\mu = 0.001 \text{ Pa s}$, $p_0 = 101 \text{ kPa}$, $\rho = 998 \text{ kg m}^{-3}$, $\gamma = 4/3$, $R_0 = 3 \text{ }\mu\text{m}$, $f_0 = 692 \text{ kHz}$ and $PPA = 1.6 \text{ MPa}$. Where the initial conditions are $R(0) = R_0$ and $\dot{R}(0) = 0$.

⁹Matlab script is found in Appendix E.2.

oscillating bubbles, influence the spatio-temporal bubble dynamics under consideration. Commonly these two radiation forces are known as the *primary Bjerknes force* and the *secondary Bjerknes force* [71]. The primary Bjerknes force describes how the acoustic field exerts a force on a bubble, which for a propagating acoustic field is in the direction of propagation, and for a standing acoustic field is either in the direction of the closest node/antinode, depending on if the equilibrium radius is smaller or larger than the resonant radius (determined by the frequency of the ultrasound, as discussed in §1.2) [71]. The secondary Bjerknes force describes how the acoustic emissions from two (or more) bubbles acts as an attractive or repellent force between the bubbles [71, 159]. The equilibrium radius also determines whether the secondary Bjerknes force is repelling or attracting neighbouring bubbles. If all bubbles have an equilibrium radius smaller or larger than the resonant radius, they will oscillate approximately in-phase and be attracted to each other, in all other cases the secondary Bjerknes force is repellent.

However, in Eq. (5.1) the primary Bjerknes force has been excluded, and no translational motion due to secondary Bjerknes forces are included, which is justified by studying the high-speed images in Fig. 5.2 (and the complete video in supplementary materials to the original publication), for which it is seen that both bubbles remain approximately stationary during the HIFU exposure. Moreover, in the results presented below, it is assumed that both bubbles have the same equilibrium radius, and initial conditions. The simulation parameters are informed by the experimental conditions and the results presented in Appendix B, which investigates the validity of the Keller-Miksis equation for a single bubble in both the $f_0/2$ and $f_0/3$ regime.

Figure 5.6 presents the normalised maximum radius defined as $R^* = (R_{\max} - R_0)/R_0$ for a single bubble and a bubble-pair at different separation distances. For a single bubble (solid black) R^* is constant, and for a bubble-pair (stapled green) R^* decreases as the two bubbles move closer to each other, indicating stronger coupling. The blue dots corresponds to the separation distance observed in Fig. 5.2 (~ 2.3 mm, λ_0 for the HIFU) and 0.3 mm, for which radial dynamics and acoustic emissions, Fig. 5.8 and Fig. 5.7, are taken to represent the effect of bubble-bubble interaction. The simulated bubble-pair for a 2.3 mm separation is predicted to have $R^* \sim 0.1\%$ smaller compared to the single bubble, suggesting that the bubble-system is only weakly coupled. For a separation of 0.3 mm R^* is $\sim 2\%$ smaller for the bubble-pair compared to the single bubble,

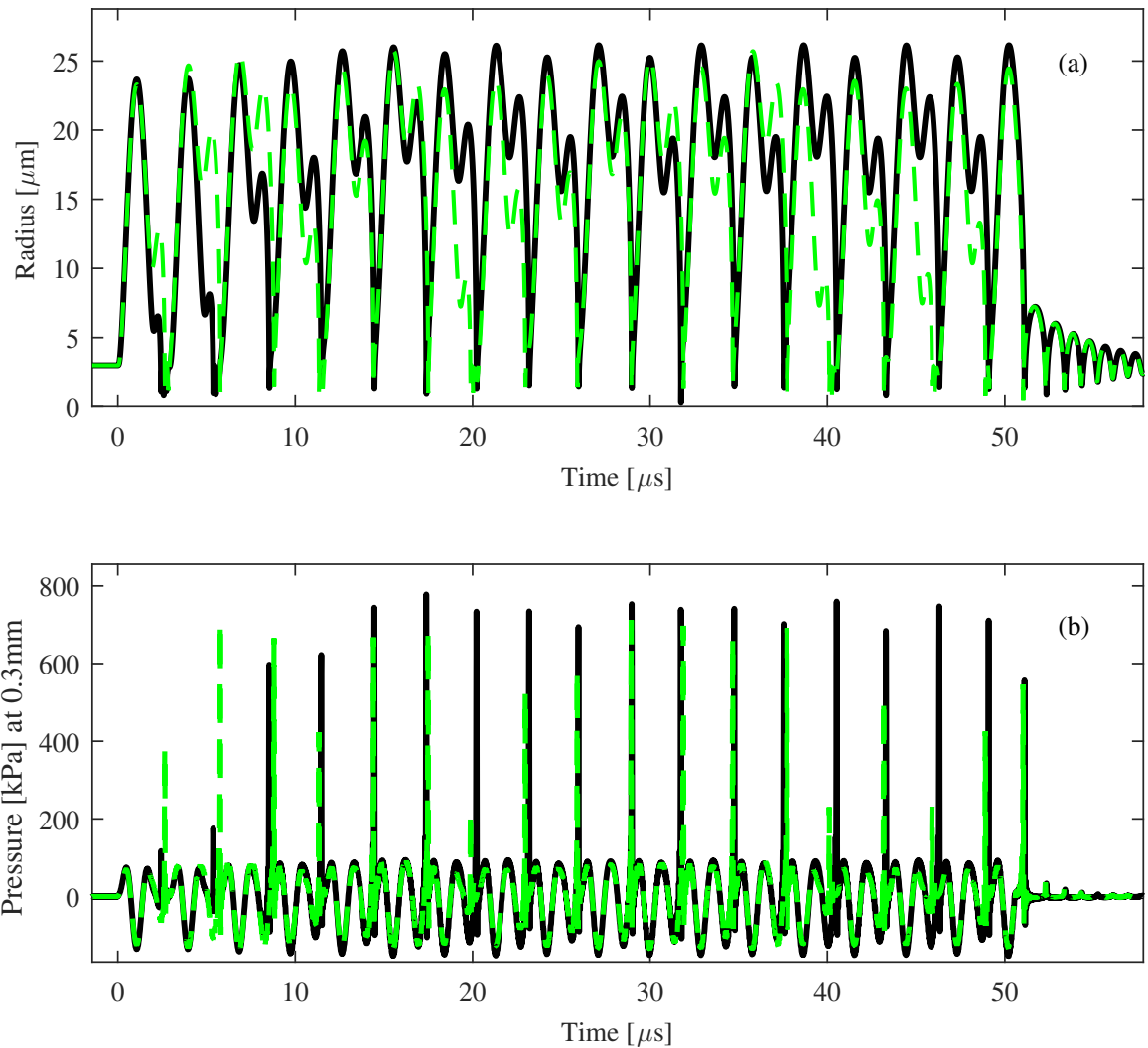


Figure 5.7: (a) Radius-time curves for single bubble (solid black) and bubble-pair (stapled green) for solutions of Keller-Miksis equation separation distances of 0.3 mm. (b) Predicted acoustic emissions affecting the neighbouring bubble. Parameters used are $\sigma = 0.072 \text{ N m}^{-1}$, $\mu = 0.001 \text{ Pa s}$, $p_0 = 101 \text{ kPa}$, $\rho = 998 \text{ kg m}^{-3}$, $\gamma = 4/3$, $c = 1500 \text{ m s}^{-1}$, $R_0 = 3 \text{ }\mu\text{m}$, $f_0 = 692 \text{ kHz}$ and $PPA = 1.6 \text{ MPa}$. Where the initial conditions are $R(0) = R_0$ and $\dot{R}(0) = 0$.

indicating that the coupling is stronger.

In another numerical study of bubble-bubble interaction, it was remarked that the initial separation between two bubbles determines whether it is likely that the bubbles will continue to exist on their own or coalesce. For an initial separation distances of 1 mm, bubbles coalesce rapidly within a few acoustic cycles, and for larger separation distances ($\sim 2 \text{ mm}$), bubbles with a resonance frequency equal to the driving frequency survive shorter, than bubbles with a resonance radius equal to sub-harmonic or ultra-harmonic frequencies [164].

Figures 5.7 a,b shows that if the experimental bubbles had been separated by a distance

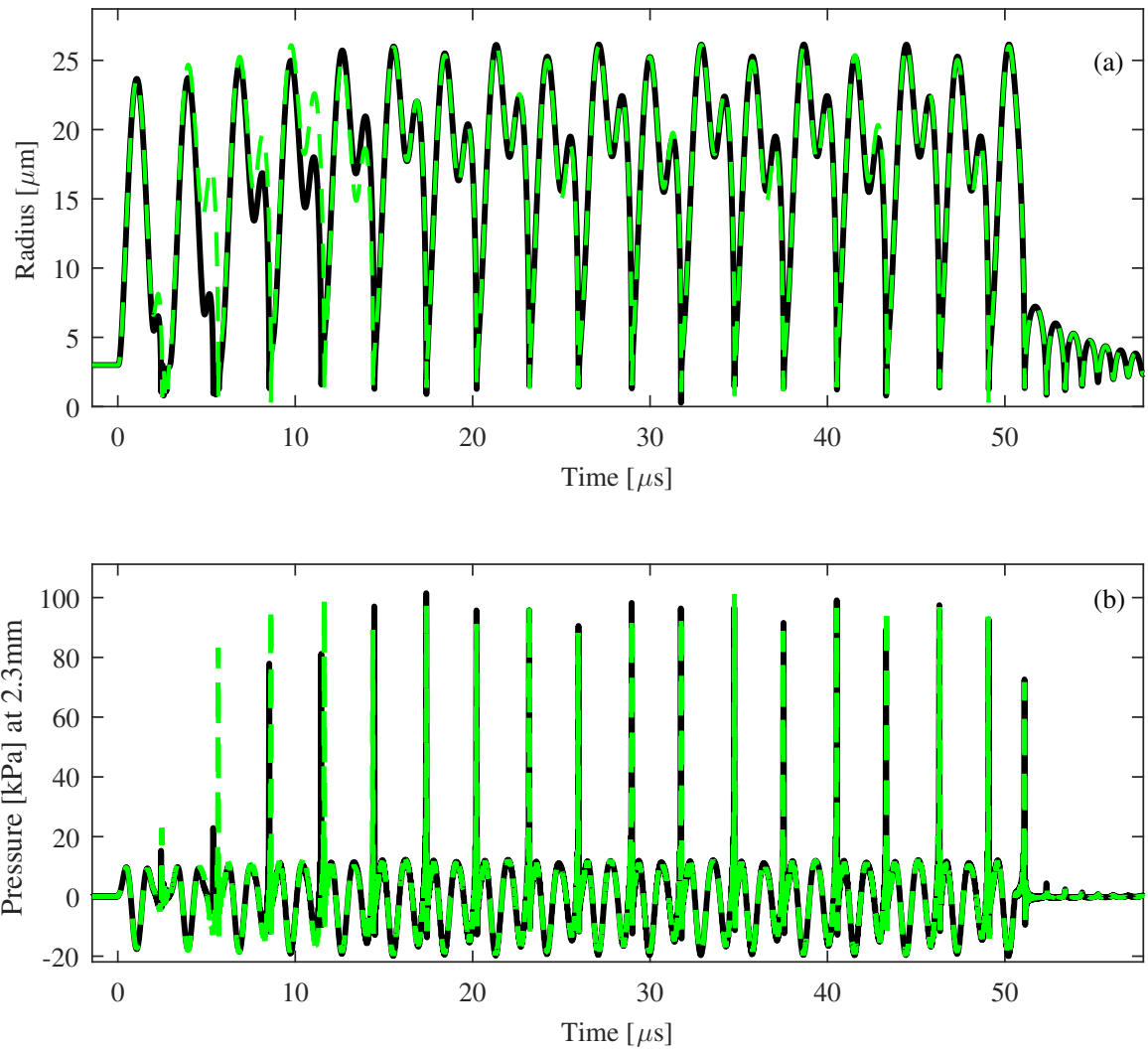


Figure 5.8: (a) Radius-time curves for single bubble (solid black) and bubble-pair (stapled green) for solutions of Keller-Miksis equation separation distances of 2.3 mm. (b) Predicted acoustic emissions affecting the neighbouring bubble. Parameters used are $\sigma = 0.072 \text{ N m}^{-1}$, $\mu = 0.001 \text{ Pa s}$, $p_0 = 101 \text{ kPa}$, $\rho = 998 \text{ kg m}^{-3}$, $\gamma = 4/3$, $c = 1500 \text{ m s}^{-1}$, $R_0 = 3 \text{ }\mu\text{m}$, $f_0 = 692 \text{ kHz}$ and $PPA = 1.6 \text{ MPa}$. Where the initial conditions are $R(0) = R_0$ and $\dot{R}(0) = 0$.

of 0.3 mm, the secondary sound field emitted by a bubble would affect the radial dynamics of the neighbouring bubble. At this separation distance the HIFU pressure amplitude is only 20 times higher than that of the secondary sound field, Fig. 5.7b. It is worth noting that the two first collapses of the simulated bubble-pair are different in terms of radial response compared to the single bubble. This difference also manifests in the emitted secondary sound field. The bubble-pair system is fundamentally different from a single bubble, and as both are non-linear systems which are sensitive to small variations in both driving and initial conditions (such as the presence of a secondary sound field), significant changes in the response before a steady-state

solution is reached, may be expected.

In contrast, Figs. 5.8 a,b indicate that the bubble-bubble interaction will have insignificant influence on the radial dynamics and acoustic emissions for a separation of 2.3 mm compared to a single bubble. Because the oscillations are only weakly damped by the neighbouring bubble, larger pressures are emitted locally by the secondary sound field. This is in agreement with previous numerical studies of bubble-bubble interaction [164]. Note that the HIFU pressure amplitude being ~ 160 times higher than that of the secondary shock waves emitted from one collapsing bubble and experience by the other. Thus, constructing a synthetic spectrum and investigating windowing effects from the dual cavitation bubble emissions in Fig. 5.4, under the assumption of the two cavitation bubbles acting as individual independent sources of periodic shock wave, is valid. The difference in radial response before the steady-state solution is reached, is also demonstrated by the bubble-pair separated by 2.3 mm, as discussed for Fig. 5.7.

5.2.4 Spectral analysis model for dual bubbles

To analyse the effect on the spectrum of the combined emissions from the dual cavitation-bubble system represented in Fig. 5.2, the synthetic periodic shock wave signal that would be detected by the needle hydrophone from both bubbles, $x_{\text{PSW}}^{\text{NH}}(t)$, the sum of the synthetic periodic shock wave signals from the top bubble, $x_{\text{PSW}}^{\text{t}}(t)$, and bottom bubble, $x_{\text{PSW}}^{\text{b}}(t)$, are considered as if emitted in isolation from the other. This is a reasonable approximation, as discussed in §5.2.3. $x_{\text{PSW}}^{\text{t}}(t)$ and $x_{\text{PSW}}^{\text{b}}(t)$ are deduced from the distinct shock wave profile FWHMs apparent from Fig. 5.4b, in combination with the high speed image sequence of the activity, such that each shock wave and its source bubble is individually identified. As both bubbles are responding to the HIFU in the same $f_0/2$ sub-harmonic regime, $x_{\text{PSW}}^{\text{t}}(t)$ can be approximated in terms of $x_{\text{PSW}}^{\text{b}}(t)$, as

$$x_{\text{PSW}}^{\text{t}}(t) \approx \xi x_{\text{PSW}}^{\text{b}}(t - \tau) \quad (5.3)$$

where ξ is the ratio of peak-positive pressure amplitudes $PPPA_{\text{SW}}^{\text{t}} : PPPA_{\text{SW}}^{\text{b}}$, of the periodic shock waves from the top and bottom bubbles, respectively, and τ is the propagation time difference from each bubble, to the needle hydrophone tip. The frequency spectrum of the

combined periodic shock wave signal detected by the needle hydrophone, $X_{\text{PSW}}^{\text{NH}}(f) = \text{FT}x_{\text{PSW}}^{\text{NH}}(t)$, can therefore be expressed in terms of the magnitude of the periodic shock wave spectrum from the bottom bubble, as

$$|X_{\text{PSW}}^{\text{NH}}(f)| \approx |1 + \xi \cos(2\pi f \tau)| |X_{\text{PSW}}^{\text{b}}(f)| \quad (5.4)$$

The $|1 + \xi \cos(2\pi f \tau)|$ term of Eq. (5.4) acts as a ‘periodic windowing’ function to the magnitude response of the periodic shock wave spectrum of the bottom bubble, to obtain magnitude of the needle hydrophone spectrum, $|X_{\text{PSW}}^{\text{NH}}(f)|$. τ thus determines the spacing of the window suppressions in the frequency domain, with ξ determining the degree of suppression. To apply the model to the dual-bubble cavitation system of Fig. 5.2, values are ascertained for the windowing parameters as $\tau = 1.444 \pm 0.074 \mu\text{s}$, and $\xi = 1.07 \pm 0.18$ (with $PPPA_{\text{SW}}^{\text{t}} = 22.92 \pm 2.20 \text{ kPa}$ and $PPPA_{\text{SW}}^{\text{b}} = 21.91 \pm 4.29 \text{ kPa}$). The resulting window function (solid blue, Fig. 5.9) imposed to the synthetic periodic shock wave spectrum, $X_{\text{PSW}}^{\text{b}}(f)$ (red dot), of the bottom bubble, generates the periodic shock wave spectrum as detected by the needle hydrophone from dual-bubble system, $X_{\text{PSW}}^{\text{NH}}(f)$ (solid red). Figure 5.9 also confirms that $X_{\text{PSW}}^{\text{b}}(f)$, in isolation, generates peaks at all values of $n f_0/2$, including the sub-harmonic and its higher harmonics, and f_0 and its higher harmonics, consistent with the observations of Chapter 4.

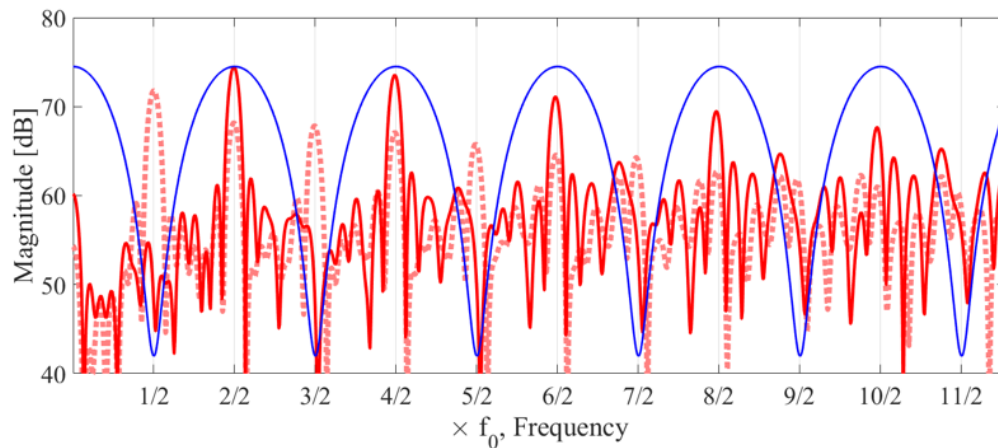


Figure 5.9: The magnitude of the synthetic $f_0/2$ periodic shock wave spectrum, $|X_{\text{PSW}}^{\text{b}}(f)|$, expected from the bottom bubble only (red dot), the windowing function (solid blue) for both bubbles with ξ and τ deduced from the experimental needle hydrophone data, and the resulting needle hydrophone periodic shock wave spectrum, $|X_{\text{PSW}}^{\text{NH}}(f)|$ (solid red), on application of the window.

In applying the window function of Eq. (5.4), to deduce the periodic shock wave spectrum from the dual-bubble system, however, all spectral content at $n f_0/2$ for odd-values of n , are suppressed, in line with the experimental spectrum of the dual-bubble emissions, collected by the needle hydrophone, (solid grey, Fig. 5.4c).

5.3 Discussion

With this experiment, it is definitively demonstrated that a medium can host cavitation activity, of a particular regime, and yet appear not to generate the acoustic signals specifically associated with that regime. In the particular example presented, the cavitation sub-harmonic at $f_0/2$, and its higher harmonics, which are signals widely used to infer the very existence of acoustic cavitation and a key emission for therapeutic applications, are completely suppressed for any detector aligned to the HIFU axis. A windowing function is analytically expressed to predict the frequency values at which peak suppressions will occur for the spectrum of the dual-bubble cavitation activity, in terms of the periodic shock wave spectrum from one of the component bubbles. This confirms suppression at $n f_0/2$, for odd values of n , as seen in the experimental results. Moreover, the resulting signal enhancement, at even values of n (harmonics of f_0), could easily be misinterpreted as due to nonlinear HIFU propagation (as discussed in *Overview of Thesis*), rather than cavitation activity.

The model easily allows other configurations of two $f_0/2$ bubbles to be considered. For example, an inter-bubble spacing of $\lambda_0/2$, along the HIFU propagation axis, will result in an effective shock wave detection frequency of $2 f_0$. This would halve the value of τ used above, doubling the frequency values at which suppression occurs, such that odd-order f_0 harmonics (f_0 , $3 f_0$, $5 f_0$, $7 f_0$...) are suppressed.

More than two bubbles responding in the same regime would result in additional ξ and τ values, and more complex periodic windowing functions, of variable frequency spacing and degrees of suppression. For multiple cavitation-bubbles responding to an insonation in different sub-harmonic or f_0 regimes, such as for a HIFU field with bubbles simultaneously within the focus and also outside of it, the windowing function cannot be analytically derived.

However, the presented model may be applicable for combinations of f_0/n and f_0/m (where $n \neq m$) bubbles within limited frequencies, if they have common spectral peaks at $kL f_0$ where $k \in \mathbb{N}$, and L is the smallest common multiple of $1/m$ and $1/n$. By taking the approximation that $X_{\text{PSW}}^b(f) \approx \xi' X_{\text{PSW}}^t(f)$ where $\xi' = \xi m/n$ and $f = kL f_0$, constructive and destructive interference at specific spectral peaks may be anticipated. The windowing effect which is demonstrated for spatially configured cavitation bubbles, has similarities to a phenomenon known as *shielding*, in which a screen of bubbles develops in the host medium, and prevents a hydrophone from detecting radiation emanating from stable sources [15, 164].

Evidently, the precision of laser-nucleation has allowed for spatially configuring bubble activity for maximum effect, to demonstrate spectral windowing and peak suppression. The alignment of the bubble-pair relative to the needle hydrophone was critical for achieving such a strong windowing effect. A second detector, aligned orthogonally to the one described here, would certainly be expected to detect sub-harmonic signal. This would indicate that multiple, spatially configured cavitation detectors would yield more reliable, and reproducible measurements for correlation of cavitation-mediated effects, particularly for systems where a low number of nucleations may be anticipated.

5.4 Conclusion

In this Chapter, two cavitation bubbles were configured to be nucleated $\sim \lambda_0$ apart in the HIFU focus close to the tip of the needle hydrophone. Collected acoustic emissions consisted of periodic shock waves at f_0 , for which no sub-harmonic or ultra-harmonic spectral features were detected in the cavitation noise spectrum, despite both cavitation bubble responded at $f_0/2$. A spectral analysis model was developed to describe how spatially configured cavitation bubble can suppress and enhance spectral features, for which experimentally verification was achieved. Simulation of the bubble-bubble interaction indicated that the coupling between the bubbles was weak, and considering the two cavitation bubbles as independent sources of periodic shock waves, was reasonable. Different spatial configurations, and implications for detection of cavitation, were discussed.

Chapter 6

Performance characterisation of a passive cavitation detector optimised for sub-harmonic periodic shock waves from acoustic cavitation in MHz and sub-MHz ultrasound

Chapters 4 and 5 involved measurement of shock waves emitted during acoustically driven periodic bubble collapses with a needle hydrophone device, the tip of which was located several mm from the source bubble. Hydrophone deconvolution revealed peak positive pressure amplitudes of the order of several 10's of kPa, at this short propagation distance. For detection of cavitation during various applications, the detector is generally located further from the bubble activity to protect sensitive components, and in the case of medical therapy, due to anatomical constraints.

Typically the most critical component of a PCD design is the active material. Two commonly used materials are PZT and PVdF. The choice of material for a particular design is influenced by the application the PCD is intended for. For instance, PZT is characterised by having a greater sensitivity around resonance compared to PVdF, which is defined by a superior bandwidth. In the case that a single spectral feature or harmonics of that feature are targeted for monitoring, a PCD design based on PZT may be favourable because of the greater sensitivity. Similarly, if a detector is sought for multiple experimental configurations, in which different bandwidths of spectral content are targeted for monitoring, PVdF is a desired material. Moreover, for certain applications in sonochemistry, the temperature of the host medium is

high (aluminium melts), and in such cases PZT is the superior active material [67] because of the higher Curie temperature ¹, which is ~ 300 °C [165]. PVdF has a relatively low Curie temperature, which is ~ 135 °C [166], making it unsuitable for high temperature applications.

In the following chapter the development of a PCD is described, with an overriding objective of detecting low amplitude shock waves with as high a sensitivity as possible. The design is guided by a finite element model of the device, and performance is described in terms of a 'working knowledge' of acoustics. The utility of targeting periodic shock wave detection, in accordance with the work described in previous chapters, is ultimately demonstrated against a comparable commercially available device, which retails at over US \$3000².

¹The Curie temperature is the temperature at which certain magnetic materials undergo a sharp change in their piezoelectric properties.

²The results presented in this chapter features in **K. Johansen, J. H. Song, P. Prentice, *Performance characterisation of a passive cavitation detector optimised for sub-harmonic periodic shock waves from acoustic cavitation in MHz and sub-MHz ultrasound, Ultrasonics Sonochemistry*, 43, 146-155, 2018.**

6.1 Design considerations for a PCD

The performance characteristics of a PCD device, and subsequently the suitability for monitor cavitation during an experiment, are determined by a wide range of options, such as active material, operational bandwidth, size of device, focused/unfocused, robustness, requirement for a pre-amplifier, to mention some. Alternatively, specialist suppliers, such as Sonic Concepts Inc., Precision Acoustics Ltd, and National Physical Laboratory (NPL) offer devices with a stated application as a PCD, supplied with an operating bandwidth, and perhaps the option of some sort of calibration data. Full technical construction details, however, including the active material of the element, are often proprietary [32, 44, 52–54, 58, 96, 167, 168]. Otherwise, commercially available generic hydrophones, particularly needle hydrophone [48, 49, 128, 157], and capsule devices [43, 45, 60] have also been used. Focused PZT bowl transducers, that could also be used for transmission, are commonly used in passive receive mode to monitor cavitation activity [41, 44, 59, 122, 169]. Bespoke PCDs, developed in-house, are also commonly reported. These are typically constructed from PZT-elements in the form of disks [4, 8, 9, 40, 67] , or PVdF [4, 31, 168, 170].

Another metric which is used to evaluate a PCD design is the spatial resolution to detect cavitation occurrences in a host medium. This can be measured by a technique developed at NPL, where the PCD is scanned around in a multi-frequency cavitation reference vessel [165]. This metric is particularly important for applications where cavitation activity is not limited to a small predetermined volume in the acoustic field. By understanding the spatial resolution of a PCD (*"the ability of a sensor to resolve the detail of cavitation within the volume under test"* [67]), a qualified evaluation of the possibility to scale-up cavitating systems, with a good understanding of effective treatment volumes, is achievable. By knowing the spatial resolution of a PCD in a cavitation reference vessel, the maximum resolvable frequency, f_{MaxRes} , can also be estimated. This is related to the maximum frequency of the acoustic emissions from a cavitation field, which a PCD can measure without effects of spatial averaging, and it is defined as:

$$f_{MaxRes} = \frac{\text{Speed of sound in host medium}}{\text{Spatial resolution of PCD}} \quad (6.1)$$

However, neither the spatial resolution nor the maximum resolvable frequency are typically provided for PCDs intended to measure cavitation activity in a predetermined volume of the acoustic field, which is often the case in medical applications and also in this thesis. Moreover, for all the literature on medical applications (and also the majority of sonochemistry publications) previously reviewed in this thesis, the PCDs used have not been characterised using these metrics. This is why the needle hydrophone (described in §3.2.2), the Y-107 (described in §6.2), and the swPCD (described in §6.2) have not undergone such characterisation.

In the case that the swPCD was purposefully designed to measure cavitation activity throughout a large volume of the host medium, a characterisation of the spatial resolution in a cavitation reference vessel would be warranted. However, in this Chapter the swPCD is compared to the Y-107 which is designed to be sensitive to cavitation activity within the focal region of the HIFU transducer driving the cavitation activity, Fig. 6.4. Therefore the spatial resolution was not considered, as all detectors were always pointed toward the cavitation activity.

6.2 Rationale for the swPCD and review of a bespoke PCD

Taken collectively, the results presented in Chapter 3-5 indicate that a swPCD designed for sensitivity to lower frequency components of periodic shock waves (and bubble collapse shock waves, generally), may be expected to offer superior detection of the features commonly reported for cavitation-mediated effects, particularly the sub-harmonics and their over-harmonics, but also significant contributions to the over-harmonics of f_0 .

However, the $PPPA_{SW}$ generated by the sub-harmonic collapses of acoustically driven cavitation clouds are somewhat variable, with clouds of more than a few component bubbles emitting multi-fronted shock waves, as discussed in §4.2.1. For the purposes of this report, objective testing of the swPCD³ is therefore undertaken relative to laser-plasma mediated bubble collapse shock waves, which have a $PPPA_{SW}$ proportional to the maximum radius the bubble attains following the expansion phase [22], through which $PPPA_{SW}$ reproducibility may be confirmed,

³Many thanks to Dr Keith Johnston for collaborating on the design and fabrication of the swPCD as well as assisting with experimental testing of the different swPCD designs. Preparation of manuscript for publication was carried out by the author which included the rationale for the swPCD, analysis of simulations and experimental data, evaluation of spectral peak suppression caused by reflections, and discussion of results.

as discussed in Chapter 3.

To demonstrate the utility of identifying the component of the cavitation signal to be detected, as guidance for the design, a comparison of the performance of the swPCD to a commercially available device, Y-107 from Sonic Concepts Inc (Bothell, WA, USA), Fig. 6.1. Y-107 is constructed to fit within a central 20 mm opening through the HIFU transducer (§2.1), which is used to drive the acoustic cavitation activity reported below. Y-107 has a 17.5 mm active diameter and is geometrically focused to 68 mm [171], such that it is confocal to the focus of the H-149 HIFU transducer, when *in-situ*, Fig. 6.4. It has a stated bandwidth of 10 kHz – 15 MHz, and its construction, provided by Sonic Concepts Inc on request, is described as a "0.2 mm thick piezo-polymer stack, with high acoustic impedance backing material > 4 MRayl and an EMI [electromagnetic interference] shielded plastic outer casing (20 mm OD × 40 mm length) to optimize the operating bandwidth and signal-to-noise ratios".

The swPCD was therefore designed to be interchangeable with Y-107, within the H-149



Figure 6.1: Picture of Y-107 PCD from Sonic Concepts with stated bandwidth of 10 kHz to 15 MHz, and geometrically focused to 68 mm.

HIFU transducer, such that the outer diameter of the 3D printed casing is ~ 20 mm. The casing holds the active material, an unfocused disk of diameter equal to 15 mm.

For the purpose of seeking to assess shock wave sensitivity directly (including against a the Y-107 PCD), PVdF was therefore chosen as the active material for the swPCD. The thickness of PVdF film was selected on the basis of the power spectrum of the bubble collapse shock wave, as described in Chapter 3. The bubble collapse shock wave power peaks at < 1 MHz, Fig. 3.9b, it is therefore desirable to select a PVdF-film sensitive to lower frequencies, which can be further tuned with backing and matching layers as outlined in §6.3.2 [172], to obtain the largest magnitude sub-harmonic features. As such, the swPCD is constructed from 110 μm PVdF, as the thickest commonly available film (9 – 110 μm being commonly available), with the lowest thickness mode resonance frequency of ~ 10 MHz.

Below a comparable bespoke PCD design from the literature is reviewed, which also uses 110 μm thick PVdF film as the active material, for microbubble cavitation detection during MRI - monitored trans-cranial blood brain barrier opening [4]. In Fig. 6.2 a schematic of the detector is seen, where the receiving element is constructed by stretching PVdF film across brass tubing of diameter 4.76 mm, which is inserted into another brass tube after applying a thin electrically insulating layer. Figure 6.2 shows how the two brass tubes form the electrode connections, with the external and internal brass tubing functioning as signal and ground connections, respectively. The receiving element has no matching layer, and is air backed⁴, with the benefit of being able to

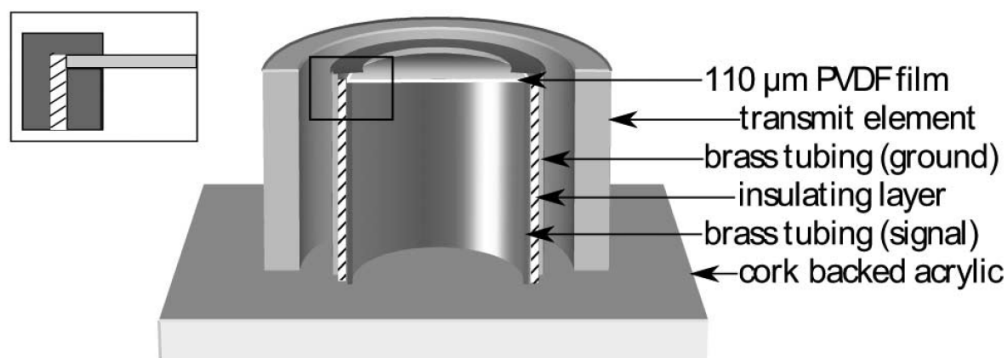


Figure 6.2: Cross-section of PCD described in O'Reilly *et al* using PVdF as active material where the film is clamped between two brass tubes that function as electrical connections to the electrodes. Taken from [4].

⁴The authors acknowledge that this sacrifices bandwidth of the device. For completeness purposes, finite element method results for air backing of the swPCD will also be presented.

fit a pre-amplifier inside the brass tubing. The pre-amplifier is necessary as the PCD is required to have long cables to reach outside the MRI machine. The PCD is mounted inside a PZT-4 cylinder (height = 6mm; internal diameter = 7mm; external diameter = 10 mm), which acts a transmitting element of length mode resonance frequency $f_0 = 306$ kHz.

In Fig. 6.3 acoustic emissions from microbubbles driven by a HIFU burst of fundamental frequency $f_0 = 548$ kHz, are used to compare the PVdF-based PCD to a ceramic based receiver with the same effective area. This is achieved by measuring the area under the Fourier Transform (FT) of the second harmonic, half-harmonic (first sub-harmonic at $f_0/2$) and broadband acoustic emissions for increasing driving pressure amplitudes. It is observed that for the second harmonic, Fig. 6.3 a,d, the performance of the PVdF based receiver is comparable to that of the ceramic receiver, however, for the first sub-harmonic and broadband emissions, the PVdF based design is superior. This is in part explained by the high sensitivity over a narrow bandwidth around the resonance frequency that ceramics are characterised by, compared to a lower sensitivity which is ‘flat’ over a greater bandwidth for PVdF. If target monitored spectral features, or the relevant frequency intervals, are not within the resonance frequency of a ceramic based PCD, even generic PVdF-based PCDs can be more sensitive when attempting to monitor cavitation activity.

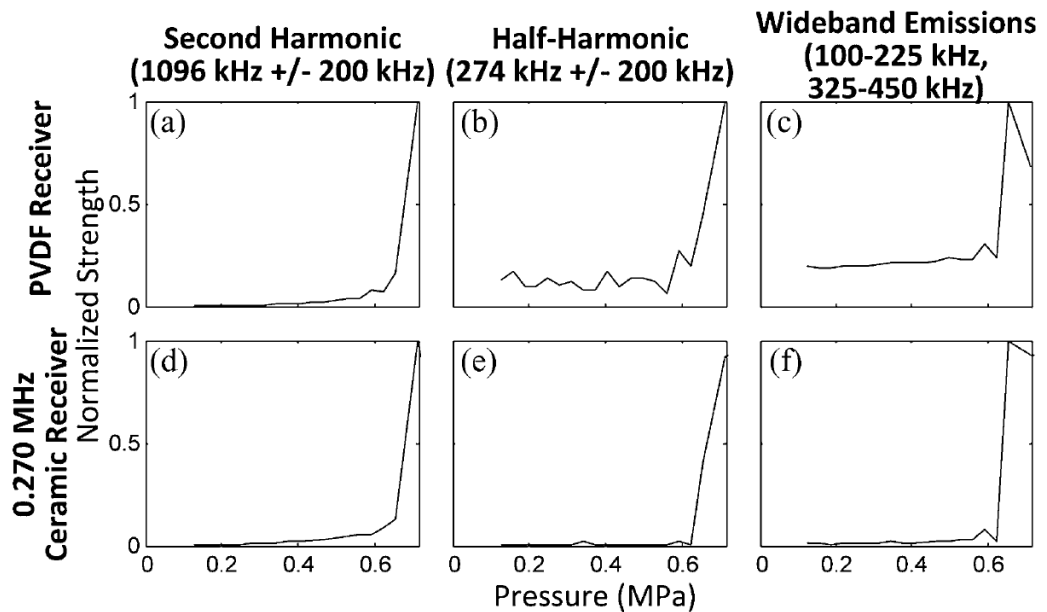


Figure 6.3: Area under Fourier Transform of acoustic emissions from microbubbles detected by PVdF receiver and ceramic receiver for increasing driving pressure amplitudes. Second harmonic (a,d), first sub-harmonic (b,e) and broadband emissions (c,f) are monitored. Taken from [4].

6.3 Materials and Methods

6.3.1 Experimental setup

The experimental arrangement within which all swPCD testing was undertaken, has been described in detail in Chapter 3, for laser-plasma mediated vapour bubbles, and Chapter 4 for laser-nucleated acoustic cavitation. For this Chapter, however, the latter bubble regime is captured with the HIFU transducer operating at the fundamental frequency of $f_0 = 220$ kHz.

The Y-107 PCD is geometrically focused to 68 mm, and designed for insertion within the hole through the transducer, Fig. 6.4. As mentioned previously, the dimensions of the swPCD were primarily chosen for direct comparison of cavitation measurements recorded with Y-107,

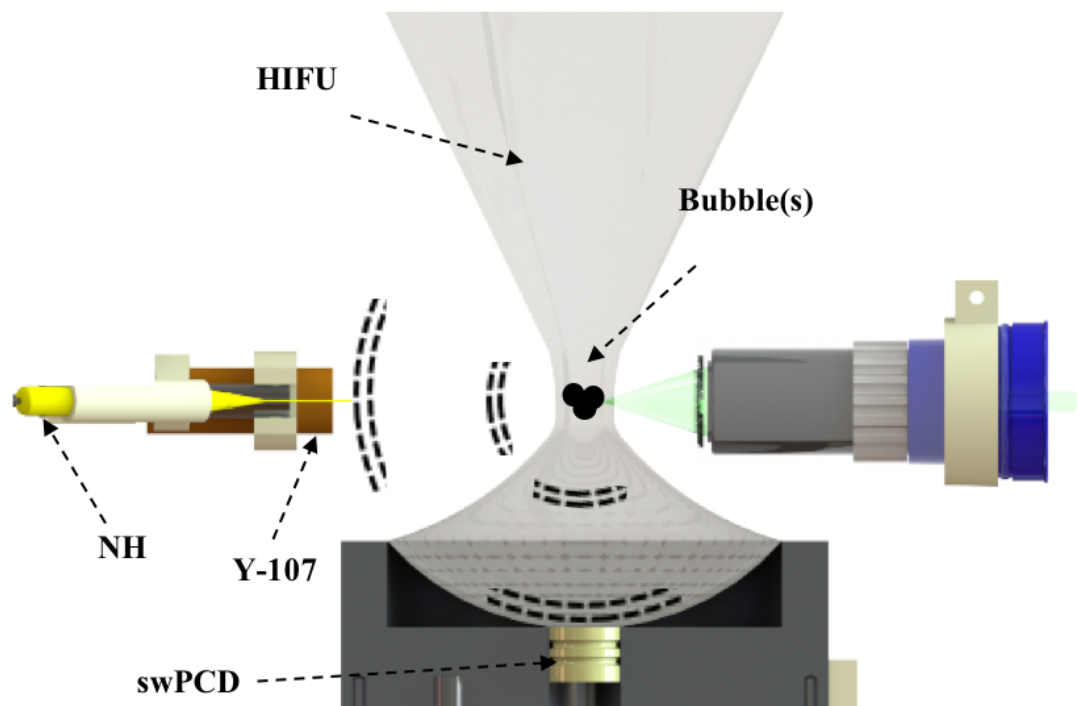


Figure 6.4: Experimental setup used for detection of laser plasma-mediated bubble collapse shock waves (no HIFU), and laser-nucleated acoustic cavitation (with HIFU). Three sensors are depicted, the needle hydrophone, swPCD, and Y-107. The needle hydrophone is used for determining the characteristics of the input function used in the finite element method simulation. Needle hydrophone and Y-107 are positioned with an xyz-manipulator. A nucleating laser pulse is focused through the microscope objective lens. swPCD is placed through a hole in a transducer with an O-ring retainer. All sensors are placed at a distance of 68 ± 1 mm from the nucleation site, equal to the geometric focus of the Y-107.

and as such the swPCD is also mountable within the transducer. For the various testing described below, the swPCD occupied the hole through the transducer, with Y-107 and the calibrated needle hydrophone arranged orthogonally to the axis of HIFU propagation, mounted on an xyz–manipulator and positioned 68 ± 1 mm from the bubble activity, Fig. 6.4.

High-speed imaging is undertaken at 1×10^6 fps with the bubble activity resolved using the Monozoom 7 lens system.

6.3.2 Finite element method model of swPCD

Fig. 6.5a is a photograph of the final stage swPCD, with Fig. 6.5b depicting a schematic cross–section, with the components including the PVdF–film, backing and matching layers labelled. Fig. 6.5c is a representation of the finite element method model of the swPCD, used to verify the effect on the shock wave detection of the device with various matching and backing layer materials. PZFlex (Weidlinger Associates Inc., Glasgow, UK)⁵, a commercially available finite element method package, used to simulate the acoustic field and propagation effects from a prototyped transducer, was used.

The simulated pressure–time waveform of Fig. 6.6b forms the user-defined input, and planar propagation to the swPCD is modelled. Simulations reported below were undertaken at a meshing frequency of 40 MHz, with convergence confirmed for 50 and 60 MHz, with 16 elements per

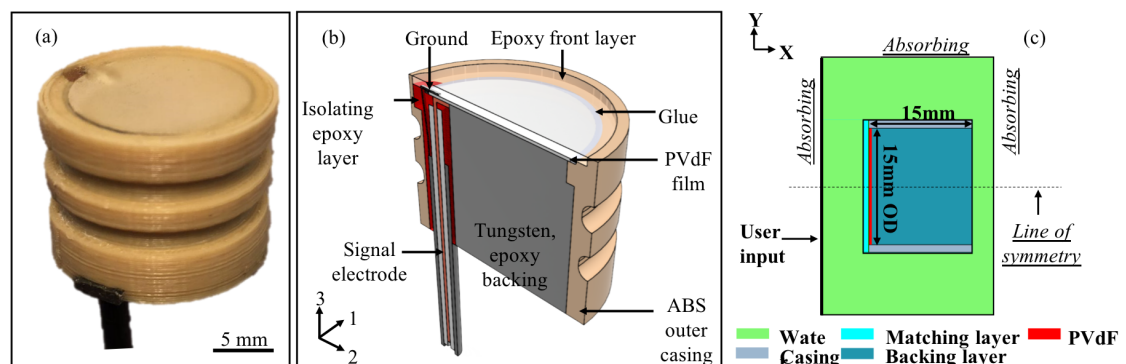


Figure 6.5: (a) Photograph of final stage swPCD, (b) schematic cross-section of the swPCD, and (c) schematic of finite element method geometry used in the guidance of swPCD construction.

⁵Many thanks to to PZFlex for significant input to the validation models, and Dr Andrew Tweedie in particular.

wavelength. Rotational symmetry around the axis, Fig. 6.5c, reduces computational load and mimics 3-dimensional effects.

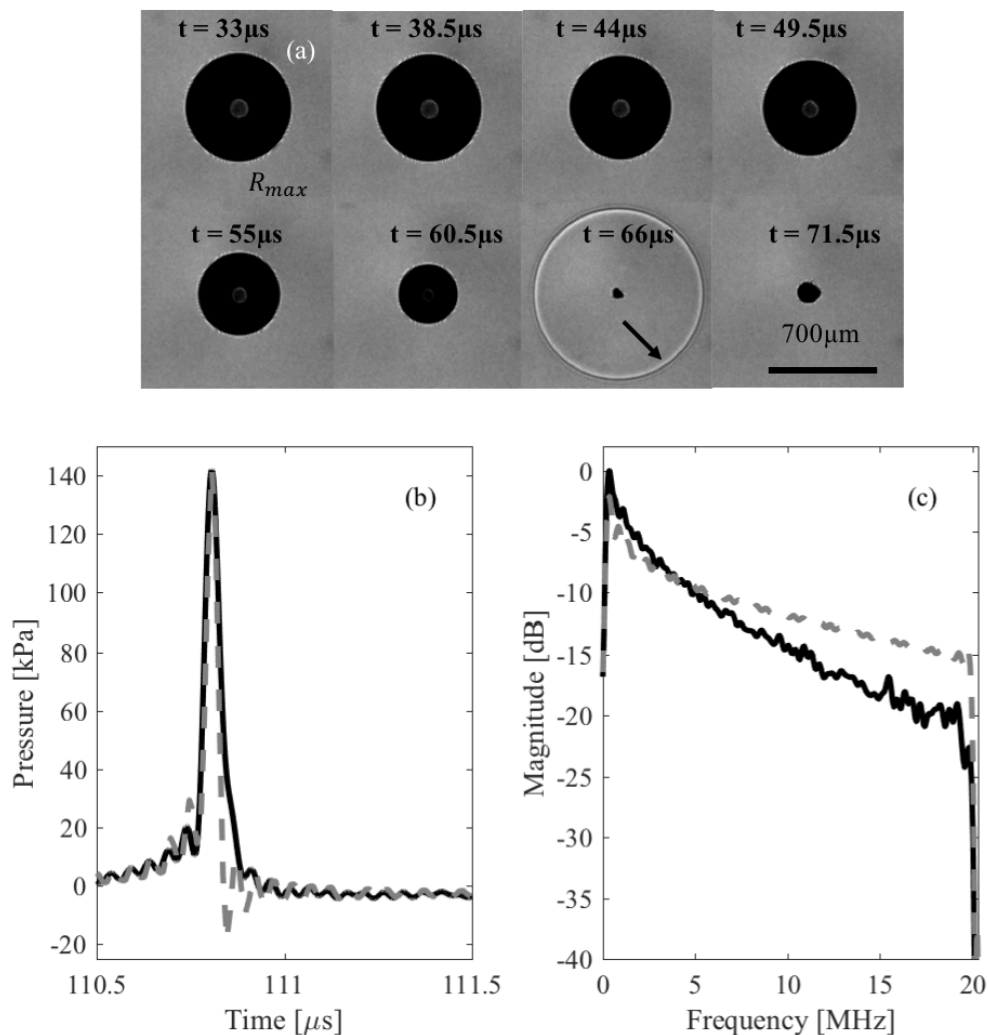


Figure 6.6: (a) High-speed shadowgraphic images of a laser plasma-mediated bubble, including maximum radius, $t = 33\mu\text{s}$, and collapse with coincident emission of a bubble collapse shock wave at $t = 66\mu\text{s}$, imaged at 1×10^6 fps. The $PPPA_{\text{SW}}$ of the bubble collapse shock wave is intrinsically related to R_{max} (b) Full waveform deconvolved bubble collapse shock wave (solid black) measured by needle hydrophone from laser plasma-mediated bubble at a distance of 68 mm, and computed bubble collapse shock wave (stapled grey) bandpass filtered at 125 kHz – 20 MHz. (c) Spectra of experimentally detected and computed bubble collapse shock wave, where the computed bubble collapse shock wave spectra is normalised to the maximum of the experimentally detected bubble collapse shock wave.

Backing layer

Backing materials are used to ‘tune’ the characteristics of a piezoelectric material, promoting narrow-band or broadband features [173–175]. Backing with a material of acoustic impedance lower than the active material further narrows the response bandwidth, such as with air encapsulating hollow glass beads, with greater absolute sensitivity over that bandwidth. This is typically done for PZT-based focused bowl transducers, promoting the resonant nature for both transmission and reception [173]. It is less typical for PVdF-based transducers to be air-backed, as it decreases the advantageous broadband response inherent to PVdF. In contrast, heavy backing, such as epoxy loaded with tungsten powder, is used to promote broadband characteristics. Moreover, if the backing is of acoustic impedance higher than the active material, then $\lambda/4$ resonance behaviour can be expected [176].

Representative results from the finite element method investigation of backing layers for the swPCD are shown in Fig. 6.7, with both Fig. 6.7a the time waveform representation of the detection of a bubble collapse shock wave, and Fig. 6.7b the relative sensitivity deconvolved from

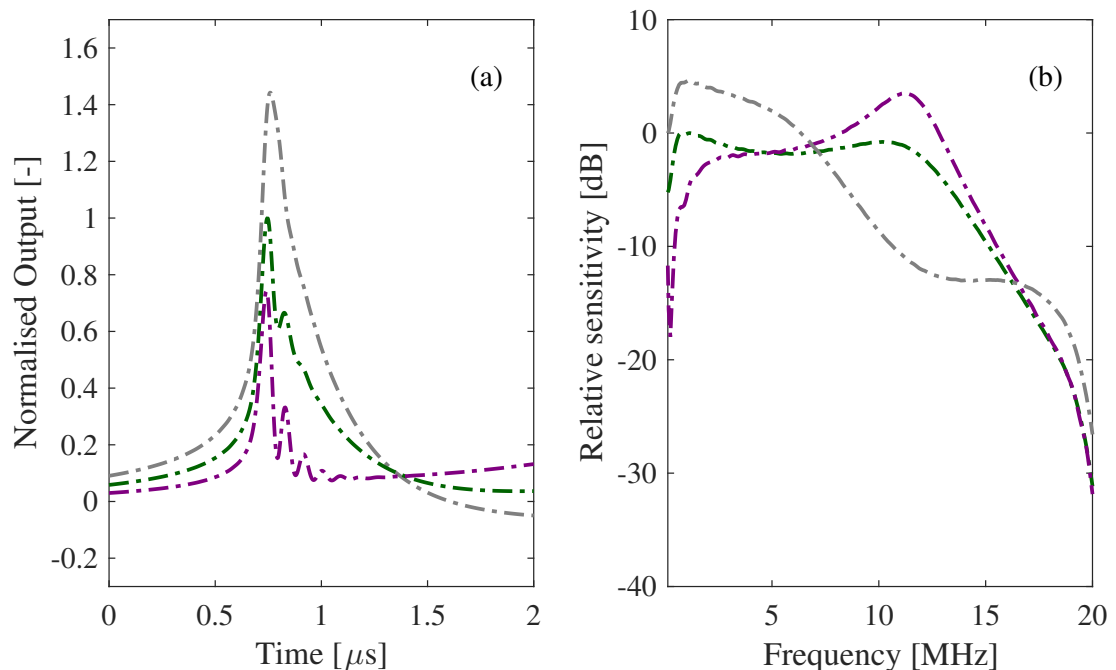


Figure 6.7: (a) Finite element method simulation of bubble collapse shock wave detection using air backing (violet) and 25% Tungsten–Epoxy (grey) backing layers, as representatives of low and high acoustic impedance respectively. Results are normalised to PVdF–only (green) as no backing (or water backing). (b) Relative sensitivity for the backing configurations investigated in (a).

the bubble collapse shock wave spectrum over the needle hydrophone calibration bandwidth. The pertinent properties for the backing materials presented are given in Table 6.1.

In order to suppress reflected shock wave detection within the swPCD, a 15 mm thick backing layer, at attenuation 3.43 dB/(cm × MHz), was deemed sufficient.

Finite element method simulation allows for assessment of air and 25% volume fraction (VF) Tungsten–Epoxy as indicative of the effects for low and high acoustic impedance backing respectively, relative to unbacked (or water backed) PVdF–film. Fig. 6.7b confirms that the unbacked PVdF–film has a $\lambda/2$ thickness resonance around ~ 10 MHz. This feature is enhanced by air backing, which also decreased sensitivity for frequencies below 2 MHz. In contrast, 25% VF Tungsten–Epoxy promotes $\lambda/4$ thickness resonance. Specifically, there is a ~ 4 dB increased relative sensitivity for frequencies below 6 MHz. As discussed in §3.4, and represented in Fig. 6.6c, this is the bandwidth of the bubble collapse shock wave containing the highest pressure amplitudes.

The results discussed for Fig. 6.7b manifest the following way in the time–domain, Fig. 6.7a. For air backing, the peak–normalised output is decreased by 27%, and both the rise time and the FWHM are decreased, compared to the unbacked swPCD. Conversely, for the 25% VF Tungsten–Epoxy, the peak–normalised output is increased by 44%, and both the rise time and the FWHM are increased. The non-smooth response seen for both the unbacked and air backed swPCD, are due to reflections between the PVdF and backing layer, which would manifest in the impulse response of the swPCD. These reflections are also representative examples of detector convolution artefacts, which can all be removed by deconvolving the detected signal with the complex impulse response to the detector, as discussed in Chapter 3.

Table 6.1: Material properties of backing layer investigated using finite element method. Attenuation and longitudinal speed of sound are measured at 1 MHz, taken from the PZFlex database.

Material	Density [kg m ⁻³]	Longitudinal. velocity [ms ⁻¹]	Impedance [MRayl]	Attenuation [dB cm ⁻¹ MHz ⁻¹]
Air	1.24	343	0.000425	1.64
Water	1000	1500	1.50	0.0022
25% VF tungsten/epoxy	5710	1750	9.99	3.43

Matching layer

Matching layers are designed to increase the transmission coefficient around resonance [174]. This is ultimately making the transducer more broadband, with a higher absolute sensitivity within the operation bandwidth. If a single matching layer is to be used, quarter-wavelength thickness of the centre frequency is ideal [172, 177]. Moreover, multiple matching layers of different thicknesses and acoustic impedances may be used in the construction of more advanced transducers, such as for harmonic imaging [178]. PVdF-based transducers, including PCDs, are generally not matched, as it is counter-productive to match a material for a single centre frequency, considering this active material is generally selected on account of its broadband properties.

For this work the following equation was used to approximate the optimal acoustic impedance of a single matching layer, Z_{ml} [172].

$$Z_{ml} = \sqrt{Z_W Z_{PVdF}} \quad (6.2)$$

where Z_W , and Z_{PVdF} are the acoustic impedance of water and PVdF, respectively.

The finite element method investigation of matching layers for the swPCD are shown in Fig. 6.8, with both Fig. 6.8a the time-domain representation of the detection of a bubble collapse shock wave, and Fig. 6.8b the relative sensitivity. The pertinent properties for the materials presented, are given in Table 6.2.

Two representative results from the investigation of matching layers materials are presented, in addition to unmatched (PVdF-film backed by 25% VF Tungsten-Epoxy); both of which are close to the optimal acoustic impedance computed from Eq. 6.2, of ~ 2.62 MRayl. The inset of Fig. 6.8b, indicates that the swPCD matched with both materials, at a layer thickness of 1mm, have a higher relative sensitivity from $\sim 100 - 900$ kHz, compared to the unmatched swPCD design. Furthermore, at higher frequencies (> 4 MHz) the presence of a matching layer decreases the relative sensitivity of the high frequency content.

The results discussed for Fig. 6.8b manifest the following way in the time-domain, Fig. 6.8a. The two different matching materials suggest that a 8 – 13% gain in peak-normalised output

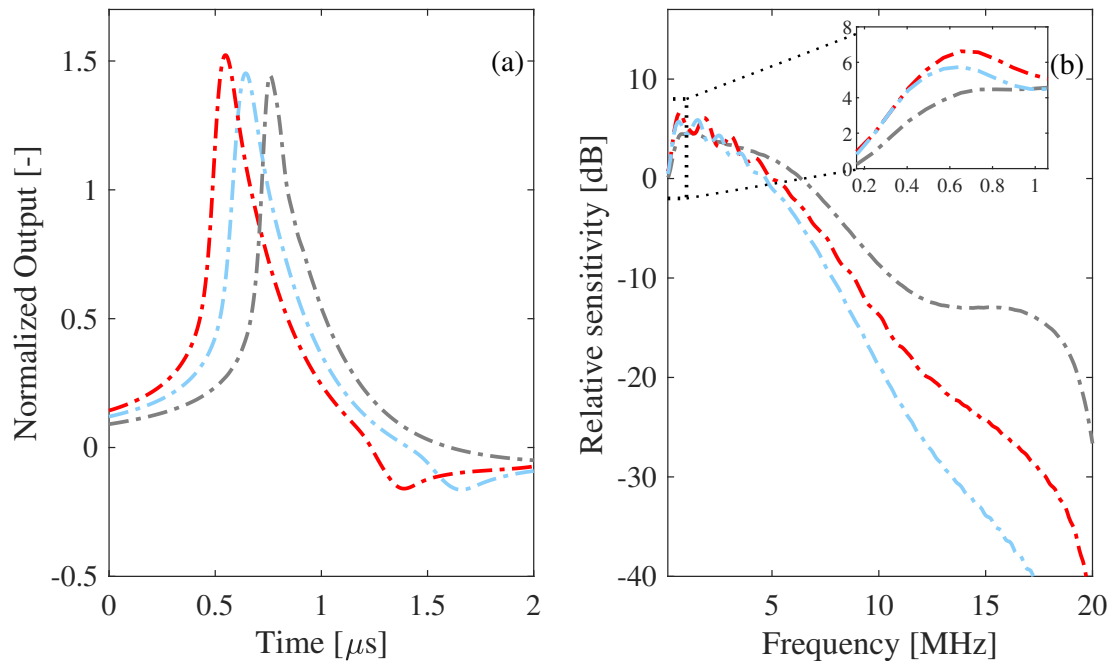


Figure 6.8: (a) Finite element method simulation of bubble collapse shock wave detection using epoxy materials Vantico HY956EN/CY208 (light blue) and Vantico HY956EN/CY221 (red) as matching layers, representatives of close to desired acoustic impedance respectively. All results have a backing layer of 25% Tungsten–Epoxy (red) and normalised to PVdF–only (water backing), 6.7. (b) Relative sensitivity for the matching configurations investigated in (a).

can be achieved by tuning the performance of the swPCD with a matching layer, in which an identical argument as presented for the heavy backing, holds true for this increase. Moreover, as the speed of sound is higher in the matching layers, compared to water, the bubble collapse shock wave arrives earlier at the PVdF–film, combined with a reflection of the bubble collapse shock wave within the swPCD, which displays as a negative phase in the normalised output, 6.8a. Equivalently, as for the results presented in Fig. 6.7a, these reflections are representative examples of detector convolution artefacts, which can be removed by deconvolving the detected

Table 6.2: Material properties of matching layer investigated using finite element method. Attenuation and longitudinal speed of sound are measured at 1 MHz, taken from the PZFlex database.

Material	Density [kg m ⁻³]	Longitudinal velocity [ms ⁻¹]	Impedance [MRayl]	Attenuation [dB cm ⁻¹ MHz ⁻¹]
Water	1000	1500	1.50	0.0022
Vantico HY956EN/CY208	1165	1989	2.31	16.33
Vantico HY956EN/CY221	1134	2452	2.78	8.95

signal with the complex impulse response to the detector, as discussed in Chapter 3.

A summary of all the component materials selected for the swPCD, with material properties is seen in Table 6.3.

Table 6.3: Material properties of final swPCD taken from PZFlex database

Material	Density [kg m ⁻³]	Longitudinal velocity [ms ⁻¹]	Impedance [MRayl]
Water	1000	1500	1.50
HY956EN/CY221	1134	2452	2.78
110 μm PVdF	1780	2560	4.56
25% VF tungsten/epoxy	5710	1750	9.99

6.4 Results

The results sections below are divided up as follows; §6.4.1 demonstrates qualitative agreement for bubble collapse shock wave detection between the finite element method and experimental testing, for each stage of swPCD construction, specifically the addition of backing and matching layers to the PVdF-film. §6.4.1 presents simultaneous detection of bubble collapse shock waves for the final stage swPCD, and the Y-107 PCD, along with a description of the detectors' relative sensitivities. §6.4.2 validates the design and testing of the swPCD, through the detection of a single laser-nucleated acoustic cavitation cloud, resolved by high-speed shadowgraphic imaging, and emitting low pressure amplitude periodic shock waves [48]. These results are presented in parallel with simultaneous measurements taken with the Y-107 PCD, from the same cavitation cloud, and a comparison between both PCD performances is made.

6.4.1 Detection of a single laser plasma mediated bubble collapse shock wave

For each swPCD construction stage

Fig. 6.9 presents the raw data from measurements taken of laser plasma-mediated vapour bubbles of comparable maximum diameter, which is verified via high speed imaging⁶ and also appreciated from the optical break down shock wave and bubble collapse shock wave (arrowed) arriving approximately at the same time, for each stage of swPCD construction at a distance of $\sim 68 \pm 1$ mm from the plasma position. For all construction stages, significant oscillations in the time waveform are observed between the optical break down shock wave and the arrival of the bubble collapse shock wave. These are convolution artefacts, which can be removed by full waveform deconvolution, as discussed in Chapter 3. For further analysis of the change in response to the different construction stages, only the bubble collapse shock wave is considered

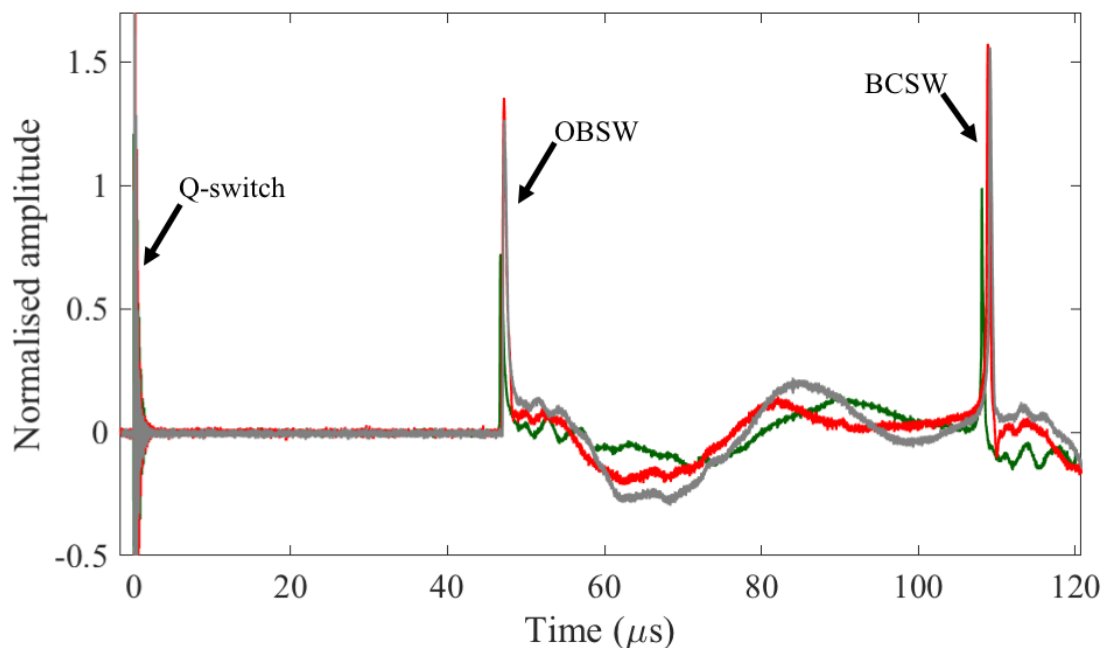


Figure 6.9: Raw data from experimentally detected acoustic emissions from laser-plasma mediated vapour bubbles for different construction stages of the swPCD. For PVdF-only (green), backed PVdF (grey), matched and backed (red). All measurements are performed at $\sim 68 \pm 1$ mm from nucleation site, where all laser plasma-mediated bubbles had a maximum radius of 365 ± 4 μm . All data is normalised to the bubble collapse shock wave detected by PVdF-only. See Fig. 6.10 for zoomed in bubble collapse shock wave profiles.

⁶Examples of such high-speed images are seen in Fig. 6.6a.

as it is similar to the shock waves emitted by acoustic cavitation. In Fig. 6.10a the experimentally detected bubble collapse shock waves and finite element method simulations from the different construction stages, are displayed. The measurements confirm that the finite element method predictions of §6.3.2 translate to the performance of the physical swPCD, in terms of peak-voltage output, rise time and FWHM [172]. The discrepancies between the experimental measurements and the finite element method simulations can in part be explained by the assumption of a plane wave in the simulation, whereas experimentally, some spatial-averaging would be expected from a spherically diverging bubble collapse shock wave. In addition, the input bubble collapse shock wave has a slight overestimation of the high frequency content, Fig. 6.6c, which combined with the plane wave assumption contributes to the shorter rise time and FWHM, Table 6.4. Fig. 6.10 (b) depicts the spectra for the experimental measurements, again confirming the effect on the sensitivity of the backing and matching layers. The noise floor for each swPCD construction stage, assessed from the voltage output prior to bubble collapse shock wave detection, is also

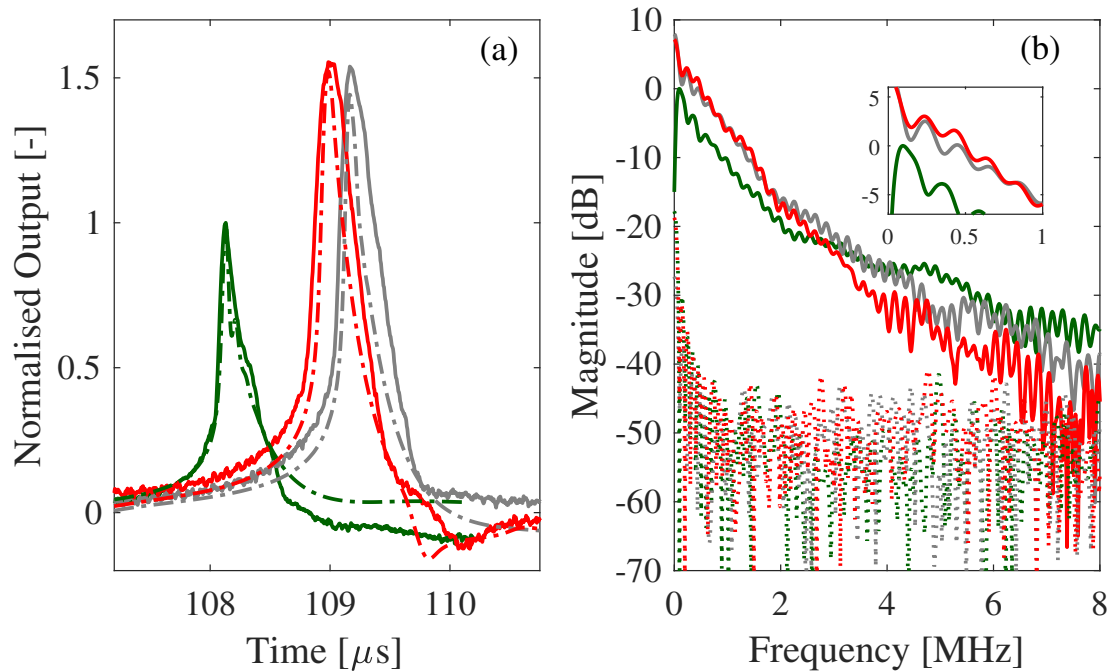


Figure 6.10: Comparison of experimentally detected (solid) and simulated bubble collapse shock wave (dashed) response for different construction stages of swPCD. For PVdF-only (green), backed PVdF (grey), matched and backed (red). All measurements are performed at $\sim 68 \pm 1$ mm from nucleation site, where all laser plasma-mediated bubbles had a maximum radius of 365 ± 4 μm . (b) Spectra of shock waves detected by different build stages. Same color coding as in (a), with dotted spectra representing the noise floor for the different stages. All experimental and simulated results are normalised to PVdF-only.

Table 6.4: Summary of normalised amplitude, rise time (RT) and FWHM for both experimental and computational results for all build stages of the swPCD. All results are normalised to PVdF–film only

swPCD	Norm. Amp.	RT [ns]	FWHM [ns]
	Exp./Sim.	Exp./Sim.	Exp./Sim.
PVdF-film only	1/1	375/408	265/185
With backing	1.53/1.44	620/447	390/228
With matching and backing	1.56/1.52	635/483	415/268

presented. The salient features of Fig. 6.10b are the $\sim 4 - 5$ dB increase in sensitivity < 2 MHz on the addition of the Tungsten-Epoxy backing layer, and the ~ 1 dB increase on the addition of the CY221 matching layer for between 0.1 and 0.6 MHz. Conversely, for the higher frequency components, the backed and matched swPCD converges with the noise floor at ~ 7.0 MHz.

The swPCD versus the Y-107 PCD

Fig. 6.11 displays raw data of the acoustic emissions detected by the final stage swPCD and the commercial Y-107 PCD from a laser-plasma mediated vapour bubble with both devices at 68 ± 1 mm (geometric focus to Y-107) from the plasma location in the configuration of Fig. 6.4.

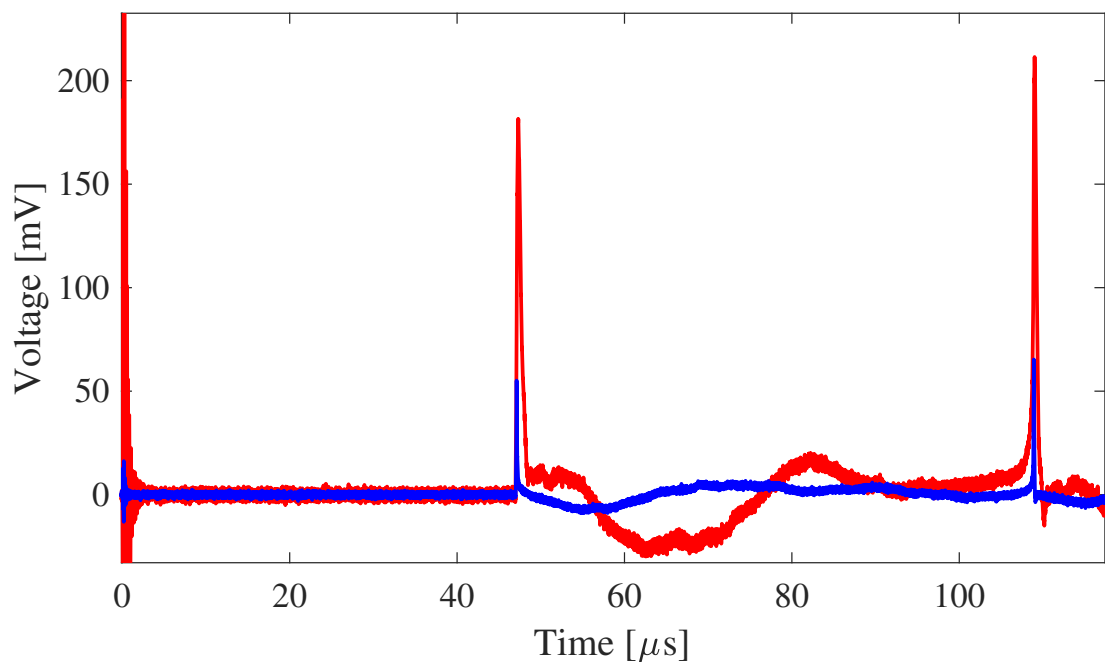


Figure 6.11: Raw voltage-trace comparing final stage swPCD (solid red) and Y-107 (solid blue) for detection of a acoustic emissions from laser-plasma mediated vapour bubble.

It is evident that the final stage swPCD has recorded a higher amplitude signal compared to the Y-107 PCD. As mentioned in the previous section, the further analysis is concerned with the bubble collapse shock wave, which is displayed in Fig. 6.12, with Fig. 6.12a the time-domain and Fig. 6.12b the frequency-domain (with noise floors for each, as described previously). Fig. 6.12a indicates that the peak-voltage output from the swPCD is $\sim 4\times$ that of Y-107, with a RT and FWHM $\sim 6\times$ longer. Fig. 6.12b reveals that these features are readily explained by an ~ 20 dB greater magnitude response at ~ 1 MHz, and an -10 dB at 7 MHz difference in the magnitude response of the PCDs. In terms of SNR, the swPCD exhibits 40 – 60 dB across the frequencies < 2 MHz, compared to the Y-107 20 – 30 dB.

6.4.2 swPCD and Y-107 detection of acoustic cavitation

The previous results sections dealt with testing and characterisation of the swPCD (and Y-107 PCD) against laser-plasma mediated bubble collapse shock waves, as a verifiable and reproducible shock wave source. In this section, the energy of the laser pulse is reduced to below the breakdown threshold for the host medium and laser focusing arrangement, and a burst of HIFU generated to be incident simultaneously to the combined laser-HIFU foci. This serves to generate a single acoustic cavitation cloud at a predetermined position and instant, such that the PCDs can be

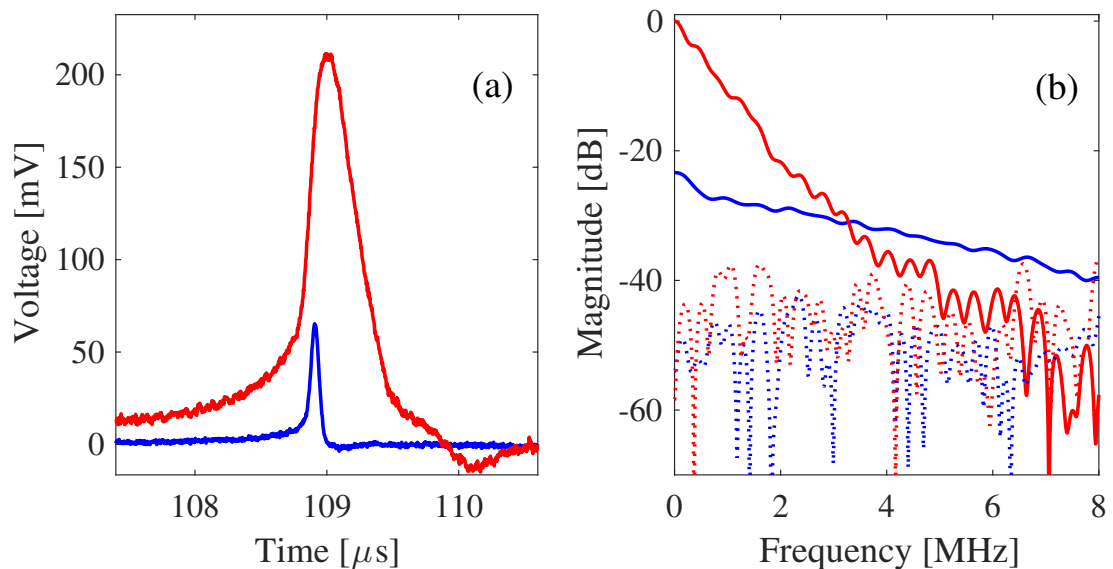


Figure 6.12: (a) Voltage-trace comparing final stage swPCD (solid red) and Y-107 (solid blue) for detection of a bubble collapse shock wave. (b) Spectra of shock waves in (a), where stapled data represents the noise floor. Spectra are normalised to final stage swPCD.

configured to detect the activity and the detections meaningfully compared, and the bubble activity itself resolved with high-speed shadowgraphic imaging.

Fig. 6.13 is the raw voltage data from the acoustic emissions collected by the final stage swPCD and the commercial Y-107 PCD, 68 ± 1 mm from a single cavitation cloud driven by

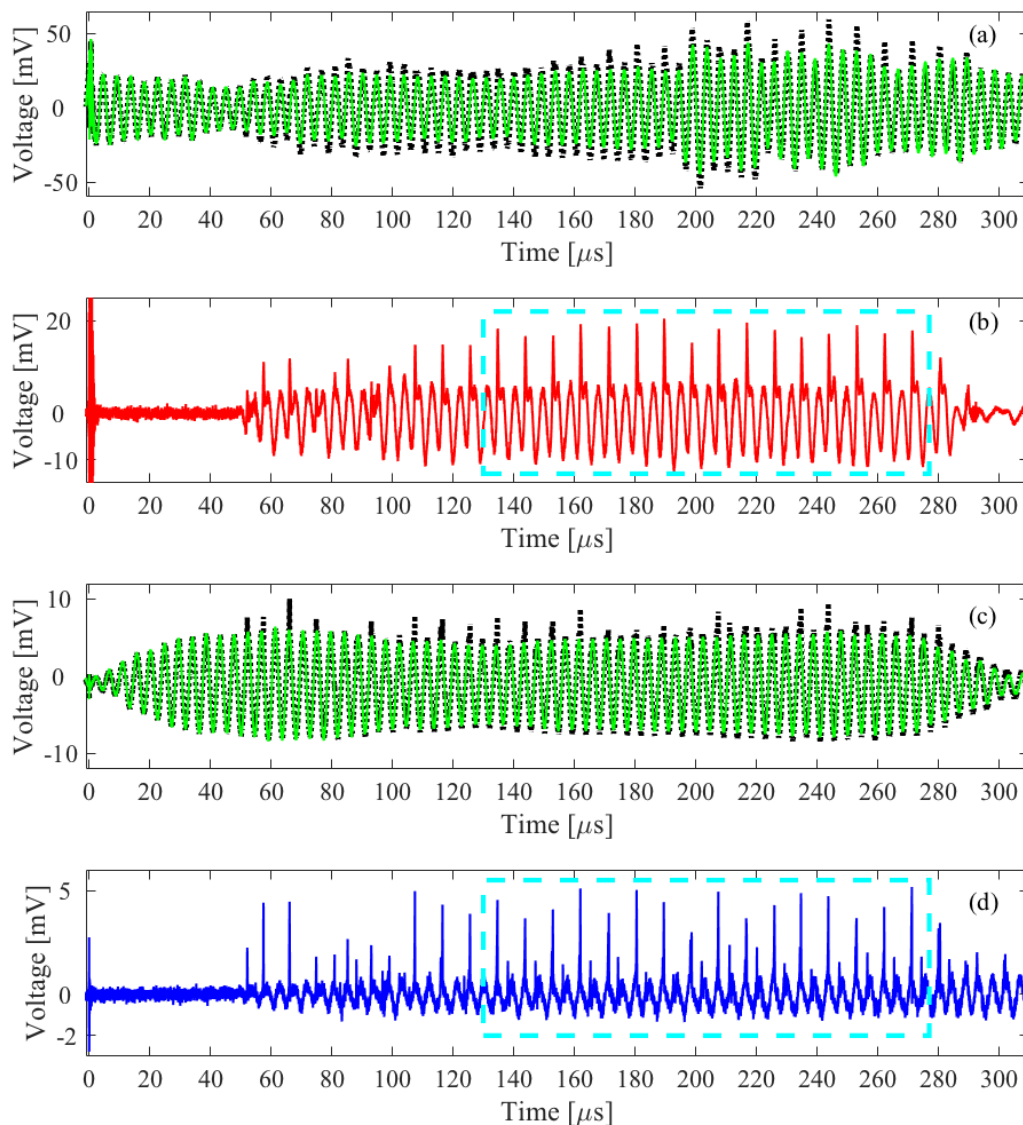


Figure 6.13: (a) Raw voltage data from swPCD for cavitation event (black dots) and control exposure (green solid). (b) Control subtracted cavitation emission data for the swPCD. (c) Raw voltage data from Y-107 for cavitation event (black dots) and control exposure (green solid). (d) Control subtracted cavitation emission data for the Y-107. Rectangle in (b,d) contains the cavitation emissions which are considered for further analysis.

HIFU at $f_0 = 220$ kHz with $PPA = 682.9 \pm 62.0$ kPa, with the Q-switch of the laser taken as $t = 0$ μ s. Fig. 6.13 a,c are the cavitation event (black dots) and control exposure (green solid) for the swPCD and Y-107 PCD, respectively. For both of these figures, periodic shock waves are visible in raw data without subtracting a control experiment (note different voltage scales). This is because both devices are positioned such that they are not facing in direction of the propagating HIFU, as seen in Fig. 6.4. However, after ~ 190 μ s reflections from the water-air interface arrive at the swPCD. The reflections are of low amplitude compared to the driving HIFU, and they are disregarded for further analysis. Fig. 6.13b is the control subtracted acoustic cavitation emissions detected by the swPCD. It is observed that in the beginning of the acoustic emissions, the cavitation cloud is not responding purely sub-harmonically, however, from $\sim 130 - 247$ μ s the acoustic emissions are exclusively generated by sub-harmonics collapses. For the further analysis, the interval of the acoustic emissions generated by the stable sub-harmonics behaviour, contained within a dashed rectangles of Fig. 6.13 b,d, are considered. This data is displayed in Fig. 6.14, with corresponding high-speed images confirming the cloud undergoes strong collapses and periodic shock wave emission at $f_0/2$, with periodic shock waves arrowed at 106 μ s, 124 μ s and 179 μ s.

Fig. 6.14 b,d is the time waveform and frequency spectra for the swPCD and Fig. 6.14 c,e is the time waveform and the frequency spectra for the Y-107. The periodic shock waves arrowed in the imaging data are similarly arrowed (angled) in the acoustic data for Y-107.

It is further worth noting that the acoustic emissions detected by the Y-107 PCD are affected by reflected acoustic emissions from the lens holder in Fig. 6.4. In Fig. 6.14c, the reflected periodic shock waves arrowed (vertical) are arriving approximately midway between two consecutive collapses at the Y-107 PCD, such that periodic shock waves are detected with an overall frequency close to f_0 . The swPCD is not affected by such reflections, as it is placed in the opening through the HIFU transducer, Fig. 6.14b. The effect of the reflected periodic shock waves on the acoustic cavitation noise spectrum detected by the Y-107 PCD, is discussed in §6.4.3.

Inspection of the time-domain data from each PCD indicates that the periodic shock waves within the emission signal detected by the swPCD are $\sim 4\times$ the voltage-output of those detected by Y-107 (note different voltage scales), consistent with the plasma-mediated bubble collapse

shock wave detection result of §6.4.1. Accordingly, from the spectra of the emission signal detected by each PCD, the magnitude of the $f_0/2$ sub-harmonic peak is ~ 20 dB higher for the swPCD than for the Y-107. Moreover the swPCD has an SNR of ~ 50 dB, compared to Y-107 of ~ 20 dB, at this frequency value.

As described previously, in *Overview of Thesis*, larger cavitation clouds that have developed in higher PPA and lower frequencies HIFU exposures, collapse non-uniformly, such that periodic shock waves are often multi-fronted with up to 10's of ns between the component fronts. An example of such an emission from the cavitation cloud of Fig 6.14, is highlighted in Fig. 6.15,

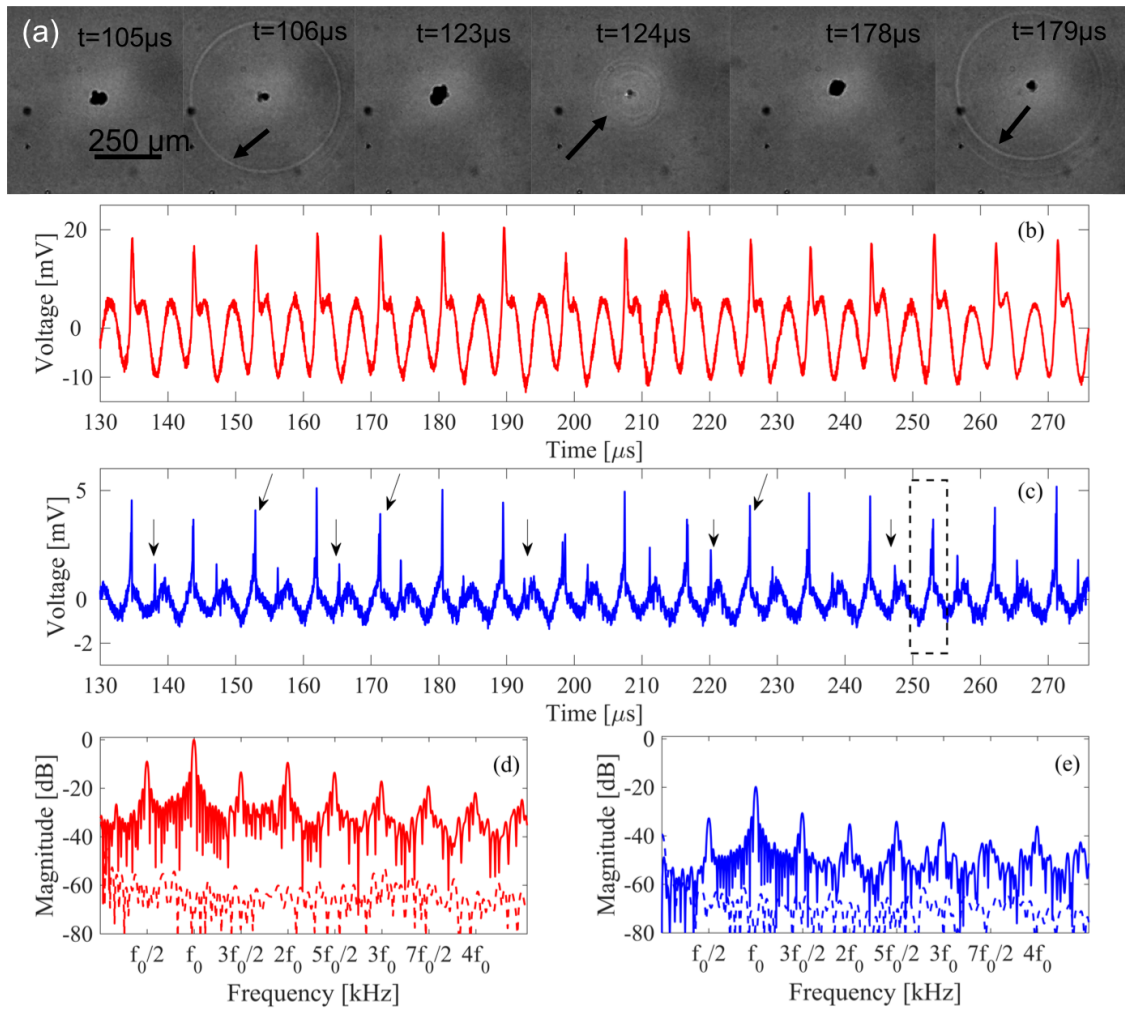


Figure 6.14: (a) High-speed shadowgraphic images of sub-harmonically collapsing cavitation cloud imaged at 1×10^6 fps. (b,c) Control subtracted cavitation emission data in the time-domain detected by (b) swPCD and (c) Y-107. (d,e) Spectra of data in (b,c), where swPCD (solid red) with noise-floor (stapled red), and Y-107 (solid blue) with noise-floor (stapled blue). All spectra are normalised to the maximum of swPCD, with $f_0 = 220\text{kHz}$.

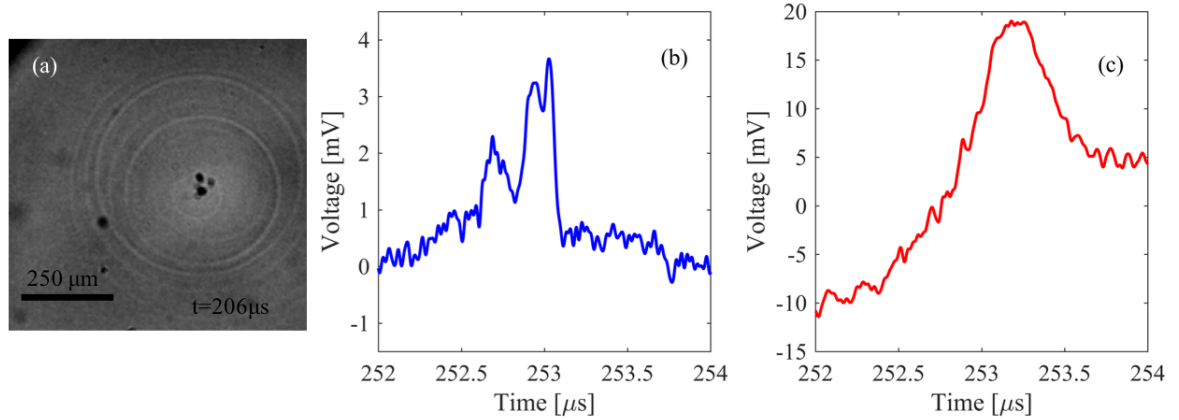


Figure 6.15: (a) High-speed image of multi-fronted periodic shock waves from asymmetric cavitation cloud collapse imaged at 1×10^6 fps. Cavitation emission data subtracted control during detection of multi-fronted periodic shock waves, detected by (b) Y-107 and (c) swPCD

along with the voltage–time domain data collected with each PCD device. Fig. 6.15b demonstrates that Y-107 distinguished the component periodic shock wave fronts, whereas the swPCD, Fig. 6.15c, did not. Whilst Y-107 is geometrically focused, such that the spherically radiating shock-fronts will have better planar incidence on the detecting surface, the inferior sensitivity at higher frequencies of the swPCD, identified in Fig. 6.10b also limits the temporal resolution.

6.4.3 Spectral peak suppression from reflections

The periodic shock waves from the acoustic cavitation activity detected by Y-107, are detected in combination with the periodic shock wave reflections from the laser-focusing lens casing (arrowed Fig. 6.14c). The combination of directly detected and reflected detected periodic shock waves should therefore be expected to introduce some windowing effect to the spectrum of Fig. 6.16, which will have enhanced or suppressed the various spectral features, following the same principle for detection of two bubbles sources, discussed in Chapter 5.

For objective comparison of the relative performances of Y-107 and the swPCD at $f_0/2$, the spectral suppression must therefore be assessed. The spectral windowing function adopted from Eq. (5.3) applies to the spectrum of a series of directly detected periodic shock waves, $x_{\text{Dir}}(t)$, by the concurrent detection of a series of reflected periodic shock waves, $x_{\text{Ref}}(t)$, may be

approximated by:

$$x_{\text{Ref}}(t) \approx \xi x_{\text{Dir}}(t - \tau) , \quad (6.3)$$

Where ξ is the ratio of the average $PPPA_{\text{SW}}$ of the reflected periodic shock waves to those detected directly, and τ the difference in detection time. The window function that may be expected to be imposed over the spectrum of the combined directly detected and reflected periodic shock waves, as detected by Y-107, may be further approximated by

$$|X_{Y-107}(f)| \approx |1 + \xi \cos(2\pi f \tau)| |X_{\text{Dir}}(f)| , \quad (6.4)$$

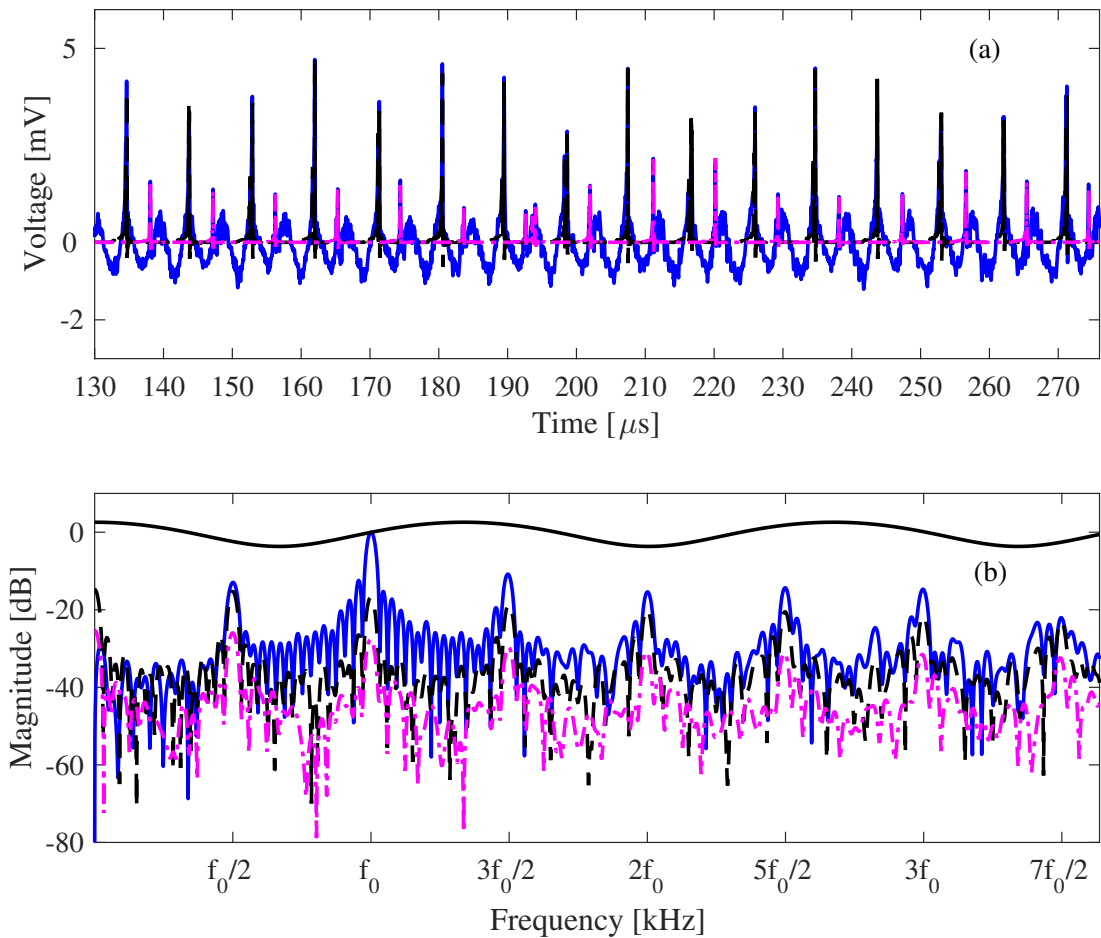


Figure 6.16: (a) Voltage-trace of Y-107 (blue), synthetically reconstructed direct acoustic emission (stapled black), and synthetically reconstructed reflected acoustic emission (dotted magenta). (b) Spectra of all time domain signals in (a), and spectral window (solid black) imposed on the voltage-trace spectrum (blue) from the reflections (dotted magenta). For the spectral window the parameters are $\xi = 0.34$ and $\tau = 3.4\mu\text{s}$

Values for ξ of $\sim 34\%$, and $\tau \approx 3.4 \mu\text{s}$, can be deduced from Fig. 6.14c, and the resulting spectral window is depicted in Fig. 6.16b. A suppression of $\sim 2.4 \text{ dB}$ can therefore be inferred for the $f_0/2$ peak of the spectrum detected by Y-107, due to the reflected periodic shock waves.

6.5 Discussion

This Chapter provides a comprehensive performance evaluation for a simple, inexpensive and easy-to-fabricate PCD design. Identification of a specific component within the cavitation emission signal – periodic shock waves – allowed optimisation of the swPCD for detection of low frequency components within the individual bubble collapse shock waves, where the majority of the power resides. This was primarily realised through the rudimentary use of a high acoustic impedance Tungsten–Epoxy ($> 10 \text{ MRayl}$) backing layer to adjust the resonance of $110 \mu\text{m}$ PVdF film ($\sim 4.56 \text{ MRayl}$), toward sensitivity for the target bandwidth ($< 5 \text{ MHz}$).

The utility of identification of the target signal component, and subsequent design of the swPCD, is demonstrated via coincident detection of controlled and resolved cavitation activity relative to a commercially available PCD device, with the dimensions of the swPCD selected to permit the comparison. The swPCD exhibited a $\sim 30 \text{ dB}$ higher SNR than the commercial device at $f_0/2$ ($f_0 = 220 \text{ kHz}$), and superior sensitivity up to $\sim 3 \text{ MHz}$. This bandwidth covers many commonly reported cavitation emission frequencies, including for higher values of f_0 driving. It is further noted that the swPCD design effectively sacrifices temporal resolution for magnitude sensitivity, although a geometrically focused swPCD may be expected to improve the temporal resolution, and indeed further improve sensitivity via a closer approximation to planar incidence. Moreover, the large active area of the device will endow the swPCD with poor directivity, which was necessary for the comparison to Y-107. Thus, tailoring swPCD dimensions to the experimental requirements within which it is to be deployed, is suggested.

More generally, improved characterisation of PCDs in the literature is required, to facilitate better comparison of reports on cavitation mediated effects, with a minimum requirement for magnitude calibration at the stated frequencies. For cavitation emission signals within which shock wave content plays a significant role, however, an assessment of impulse response is also

highly desirable. This would typically require expensive and often time-consuming calibration procedure at a national institute with accredited and standardised instrumentation.

In the work described here, however, the use of laser plasma mediated bubble collapse shock waves is introduced, as a reproducible and broadband signal, for rapid and general characterisation of a PCD. Moreover coincident detection of the bubble collapse shock wave with a needle hydrophone pre-calibrated over a representative bandwidth, allows the absolute sensitivity of the PCD to be assessed via the substitution technique, as a rapid ‘one-shot’ procedure. This process, was applied to each construction stage of the swPCD and Y-107 PCD, with preliminary results described fully in Appendix D.

Although appropriate characterisation is a prerequisite to good cavitation reporting, it is further worth recognising that there are other obstacles to fully and transparently communicating single element PCD detection of cavitation, such as the reflection-induced spectral windowing identified and described in §6.4.3. Reflected periodic shock waves had a marginal influence of ~ 2.4 dB on the comparison of the swPCD to the Y-107 performance, two or more ‘apparent’ cavitation sources (either actual sources, or reflecting objects) can corrupt any reporting that assesses emissions based on the magnitudes of spectral features, and potentially significantly suppress those features such that they become obscured from the spectrum. An assessment of reflection-effects around the expected cavitation location, and the location of the PCD within a given experimental configuration, is recommended.

6.6 Conclusion

A bespoke PCD design is described, targeting periodic shock wave content with in acoustic cavitation emissions. It is demonstrated that rapid-prototyping of the swPCD in a finite element method package can be used for guidance on optimal backing and matching layers. Experimental characterisation was conducted using laser-plasma mediate bubbles, which provided reproducible bubble collapse shock waves for testing of each construction stage. The final stage swPCD outperforms a comparable commercial PCD by ~ 20 dB at the $f_0/2$ sub-harmonic. Appropriate characterisation, at stated detection frequencies, and an assessment of impulse response, is

required for PCD reporting and quantification of bubble activity. The role of reflections, and spectral peak suppression are also discussed with regards to cavitation reporting.

Chapter 7

Conclusions and Future Work

The following points summarise the key results from the research presented in this thesis. This is followed by a brief discussion, linking the experimental results to both the literature reviewed in Chapter 1 and potential future work.

- For the needle hydrophone used throughout this thesis, bubble collapse shock waves (and periodic shock waves) are detected with an apparent negative phase. This is a convolution artefact caused by the impulse response to the needle hydrophone. Full waveform deconvolution provides the best match between the experimentally measured and filtered simulation data, removing the non-flat detector response within the calibration bandwidth; most notably the apparent negative phase. After full waveform deconvolution, the simulated shock wave profiles may be used to reconcile detected acoustic emissions and source bubble dynamics from acoustic cavitation bubbles.
- A single cavitation bubble, undergoing stable-inertial cavitation, was nucleated only a few mm away from a calibrated needle hydrophone using a laser nucleation technique. The cavitation activity was resolved using high-speed shadowgraphic imaging, such that source bubble dynamics and acoustic emissions could be studied in unprecedented detail. A simple spectral analysis model demonstrated a significant contribution to the cavitation spectrum from periodic shock waves, for all spectral features, with supporting experimental data for two sub-harmonic cavitation regimes. It was concluded that simultaneous detection of the sub-harmonic signal at f_0/m , with ultra-harmonics at $n f_0/m$, is suggestive of a cavitating

system that is generating periodic shock waves. This is considered the most significant result in this thesis.

- To investigate how multiple and distributed cavitation events are detected by a single needle hydrophone, the experimental setup in Chapter 4 was expanded to facilitate the nucleation of two cavitation bubbles. Collected acoustic emissions from both cavitation bubbles placed approximately λ_0 apart, consisted of periodic shock waves detection at f_0 , for which no sub-harmonic or ultra-harmonic spectral features were detected. However, both cavitation bubbles were confirmed via high-speed imaging to be collapsing every second acoustic cycle. A spectral analysis model was developed to describe how spatially configured cavitation bubbles can suppress and enhance spectral features.
- Building on the increased understanding of acoustic emissions achieved in Chapter 3-5, a bespoke PCD design was described, which targeted periodic shock wave content within acoustic cavitation emissions. Rapid-prototyping of the swPCD, was achieved using finite element method, and experimental characterisation was undertaken with laser-plasma mediated bubbles. The swPCD outperforms a comparable commercial PCD by ~ 20 dB at the $f_0/2$ sub-harmonic. The role of reflections, and spectral peak suppression was also discussed with regards to cavitation reporting.

In Chapter 1 several papers detecting cavitation were reviewed, and it was demonstrated that equivalent spectral features, such as the sub-harmonic, was used to indicate both stable and inertial cavitation. An example of this is Cornu *et al.* [72] which correlates the sub-harmonic to stable cavitation, and Schoellhammer *et al.* [43] to inertial cavitation. Furthermore, both ultra-harmonics and over-harmonics are commonly used to indicate stable cavitation, however, no distinction is made in terms of source bubble dynamics, or why one spectral feature should be preferred over the other. Generally, a better understanding of classification of cavitation may only be achieved if source bubble dynamics is reconciled with detected acoustic emissions. This would potentially allow spectral features to be understood in terms of source bubble dynamics, and be related to cavitation-mediated effects with greater certainty. However, to achieve this deconvolution of the detector impulse response is required as described in Chapter 3, otherwise

misinterpretations of collected acoustic emissions, as suggested by Church *et al.* in §1.4.3, may become prevalent. Another examples of potential misinterpretation due to convolution artefacts is seen in §1.4.4, where Lauterborn notes that ultra-harmonic bubble oscillations, could be the the source of the sub-harmonic signal, as they had previously detected $5f_0/2$ and $3f_0/2$ before the $f_0/2$ spectral feature appeared. It is unknown what detector was used for this study, however, it is not unlikely that the interpretation of the data would have been in agreement with the results presented in this thesis, if the detector was characterised.

The literature reviewed in §1.4.4, proposed that shock waves could be responsible for certain spectral features, however, no experimental evidence unequivocally confirmed these assertions. However, one of the previously proposed mechanisms stand out as describing aspects of the collected experimental data: *Incomplete bubble oscillations due to the inertia of the surrounding liquid, such that the bubble does not have time to collapse before the end of an acoustic cycle, and collapses on subsequent cycles, potentially with the emission of shock waves.* There are recognisable similarities between the experimental high-speed imaging data, Fig. 4.5 and Fig. 4.6, and computed radial dynamics in Fig. 1.13a. The notion presented by Neppiras, suggesting that the linear acoustic emission and the non-linear acoustic emissions should be of comparable amplitude, is supported by the RMS amplitude of the experimental data presented in Chapter 4. This hypothesis was proposed to explain the sub-harmonic spectral features from inertial cavitation, however, the results presented in this thesis demonstrate that all spectral features can largely be mediated via periodic shock waves, for certain cavitation regimes.

In terms of the cavitation activity itself, the observations in Chapter 4 align with speculation from recent literature discussed in §1.4.3 that the conventional, binary classification of cavitation as stable or unstable/inertial is inadequate, and that an intermediate ‘stable-inertial’ category is required. The cavitation from the $f_0/2$ regime of Fig. 4.5 is, in every sense other than the collapse-mediated shock wave generation, activity that would be described as stable. The oscillations are periodic and of regular amplitude in terms of the bubble radius, and there is no indication of fragmentation events during the collapses. Nonetheless, shock waves, which are synonymous with inertial cavitation, form a significant component of the emitted signal. The $f_0/3$ activity at higher HIFU driving of Fig. 4.6, may be interpreted as exhibiting stronger inertial

characteristics, particularly the fragmentation that has led to the formation of a bubble cloud. The cloud is of irregular morphology for each oscillation, with bubbles or small sub-clusters of bubbles within the cloud, collapsing individually to generate multi-fronted shock waves. The effect of multi-fronted shock waves on the cavitation spectrum is the formation of broadened and misshaped peaks, which are reproduced by the spectral analysis model when simulated shock waves of variable $PPPA_{SW}$ and emission times are used. These observations indicate that a spectrum of cavitation activity exists between the extremes of the classic linear-stable and chaotic-inertial categories [40]. Applying the categorisation suggested by Leighton in Fig. 1.5, the observed cavitation activity may be classified as "High-energy stable cavitation". Periodic shock wave emission and generation of the sub-harmonic signal at $f_0/2$ could mark the first departure from classically stable cavitation, into stable-inertial or high-energy stable cavitation, with increasing of the driving amplitude.

Reconciliation of acoustic emissions and source bubble dynamics, is beneficial for future development of rapid control feedback loop systems, discussed in §1.5.2. The increased understanding of how to categorise different regimes of cavitation activity, and relate the activity to cavitation-mediated effects, is determining how future controller algorithms are being designed. Certainly it would be expected that this could influence parameters such as driving frequency, pulse duration, pressure amplitude, and more importantly how these variables are dynamically adjusted to limit or promote cavitation activity at a specific location. Furthermore, it is reasonable to propose that accepted bubble theory, such as the Gilmore equation and the Keller-Miksis equation, can be used to guide the design of future controller algorithms. This is a computationally inexpensive process, which is much faster than the current (assumed) *ad hoc* approach adopted today, albeit for more complex cavitation systems. It is reasonable to speculate that computational insights from simpler systems, such as those studied experimentally in this thesis, could be helpful for the design of clinically viable rapid control feedback loop systems.

Moreover, the results presented in this thesis demonstrate that spatial configured cavitation clouds can lead to stable-inertial cavitation being classified as stable cavitation (§1.4.2), even though all detected spectral features are predominantly shock wave mediated. In principle, spectral windowing effects could manifest in rapid control feedback loop systems (§1.5.2), for

instance during interrogations of how the concentration of microbubbles affect the safety and efficiency of blood-brain barrier disruption [107], however, in all likelihood to a lesser extent than demonstrated here. Yet, as discussed in §1.4.1 where a paper by Wu *et al.* is reviewed, which suggests that blood-brain barrier opening is achieved by surpassing a detection limit by 1 dB, it is tempting to speculate that spectral windowing effects can have consequences in ‘real world’ applications. Similarly, in §1.4.3 a paper by Petit *et al.* discussing the role of stable and inertial cavitation in sonothrombolysis, is reviewed. In this paper it is concluded that stable and inertial cavitation are distributed throughout the focal region of the driving HIFU field. For such experimental configurations, it is reasonable to speculate that some (less significant) arbitrary spectral windowing of the collected acoustic emissions are established. For an analysis which attempts to distinguish cavitation-mediated effects from stable and inertial cavitation (§1.4.2), spectral windowing may add another layer of complexity, as discussed in Chapter 6.

In this thesis, cavitation activity is observed over only a few hundred μs , and a natural next step is to extend the length of the observations to multiple ms using pulsed sonication. This would allow for increased understanding of how a single cavitation bubble develops in to a cloud of bubbles distributed over a larger volume. For certain experimental configurations, multiple cavitation bubbles are going to be closely spaced during the excitation, and in such cases it would be of interest to investigate how the shock waves emitted by the bubbles are effecting the overall dynamics of the cavitation field, particularly with regards to development of medical applications using rapid control feedback loops. To facilitate the cavitation activity to be sufficiently resolved with high-speed imaging over an extended period of time, without the bubbles moving out of the field of view, a reflector of the same curvature as the HIFU source, may be used to counteract the primary radiation force from the initial HIFU exposure.

Laser-plasma mediated bubble collapse shock waves are used to characterise different construction stages of the swPCD, and some preliminary work on absolute characterisation using bubble collapse shock waves is presented in Appendix D. Potential future work would be to develop this characterisation process further, and compare it to established techniques. However, the preliminary results suggests that different array designs could be characterised over a significant bandwidth with a single-shot experiment. This would be beneficial for future rapid-prototyping

of both single element and arrays of PCDs.

Microbubble dynamics and acoustic emissions thereof (§1.5.3) should be investigated with a similar setup to that used in this thesis. This would establish whether the reconciliation achieved, manifests for contrast agent microbubbles. To optically resolve the microbubble dynamics with high-speed imaging, a stronger objective lens with a small field of view placed in close proximity to the bubble activity, is required. The necessary changes to the experimental setup implies that it would be difficult to observe microbubbles in a propagating well defined acoustic field, as discussed in §1.2.

In *Overview of Thesis*, Minnaert is quoted for his insight regarding the importance of studying simple systems, if any progress is to be made in advancing our understanding of cavitation. In this thesis, simple cavitation systems have been studied, with incremental improvements in knowledge of the relationship between acoustic emissions and source bubble dynamics. This has an impact on the discussion related to categorisation of cavitation activity, which again may impact the design of future rapid control feedback loop systems, and the design of PCDs used for monitoring. Cavitation remains a complex phenomenon, however, using the results presented in this thesis and future research efforts, enhanced harnessing of cavitation is realistic.

Appendix A

Blind deconvolution of a hydrophone with a bubble collapse shock wave

As described in Chapter 3, to deconvolve a measurement using knowledge of the magnitude response, or magnitude and phase response, the hydrophone requires characterisation, or calibration from an accredited laboratory using standardised techniques. This is an expensive and time consuming operation, no matter if it is done in-house or at a dedicated facility. In this Appendix a novel technique for characterising hydrophones by using bubble collapse shock waves, is presented. This is achieved by computing a bubble collapse shock wave which is used to deconvolve the hydrophone to obtain the absolute sensitivity ¹.

Generally, bubble observations are achieved by high-speed imaging, however, the proposed technique permits you to blindly estimate the physical bubble collapse shock wave that is measured by a hydrophone, making it possible to perform a single-shot characterisation of one or multiple hydrophones, simultaneously. This is something that is particularly desired during prototyping of new hydrophone designs. Results are presented for two propagation distances for a pre-calibrated needle hydrophone, to evaluate the rigidity of the method, in which strengths and weaknesses are discussed.

¹The results and methods presented in this Appendix featured as a conference proceeding; **K. Johansen, J. H. Song, P. Prentice. Blind deconvolution of a hydrophone with a bubble-collapse shock wave. International Ultrasonics Symposium (IUS) IEEE, pp. 1-4, 2017**

A.1 Materials and methods

From the voltage-trace, the collapse time, T_c (discussed in §1.1) to a bubble, is found. The collapse time is used to estimate the initial conditions for simulation of the radial dynamics, and subsequent computation of a bubble collapse shock wave, which is used to blindly deconvolve the needle hydrophone. The collapse time T_c is defined in Eq. (1.1). For these measurements both laser-plasma mediated vapour bubbles have a collapse time of $T_c = 32.8 \mu\text{s}$, Fig. A.1. The calculated maximum radius is used as an initial condition when solving a Rayleigh–Plesset–like equation, that approximates the radial dynamics of the inertial collapse.

For this work, the Keller–Miksis equation was used, as it is specifically derived for inertial bubble dynamics ²:

$$\left(1 - \frac{\dot{R}}{c}\right)R\ddot{R} + \left(\frac{3}{2} - \frac{\dot{R}}{2c}\right)\dot{R}^2 = \frac{1}{\rho_0}\left(1 + \frac{\dot{R}}{c}\right)p_w + \frac{R}{\rho_0 c} \frac{dp_w}{dt}, \quad (\text{A.1})$$

where R is the instantaneous radius, and the dots indicate time derivatives, c is the speed of sound, and p_w is the pressure at the bubble wall, which can be expressed as:

$$p_w = \left(p_0 + \frac{2\sigma}{R_0}\right)\left(\frac{R_0}{R}\right)^{3\gamma} - \frac{2\sigma}{R} - \frac{4\mu\dot{R}}{R} - p_0 - PPA \sin(\omega t), \quad (\text{A.2})$$

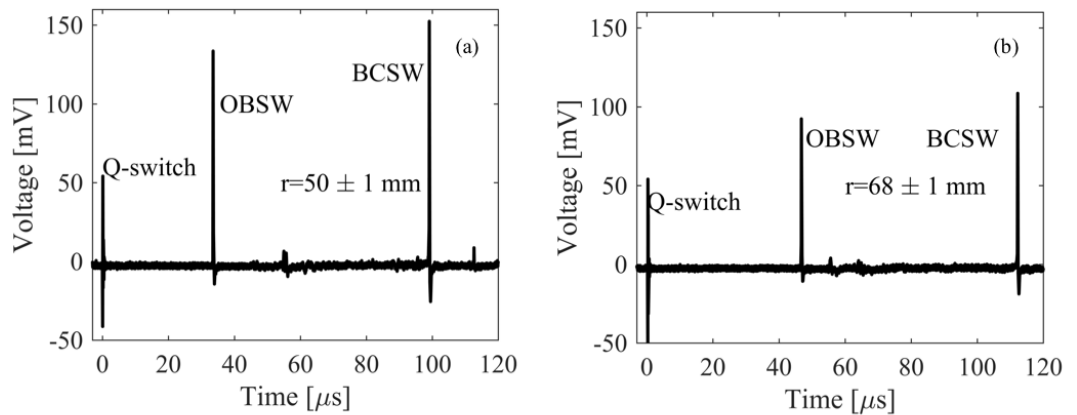


Figure A.1: (a,b) A full hydrophone voltage-trace, recorded at $50 \pm 1 \text{ mm}$ and $68 \pm 1 \text{ mm}$, respectively, with key features described in the text. Both laser-plasma mediated vapour bubbles have a collapse time $T_c = 32.8 \mu\text{s}$, equalling an estimated maximum radius of $R_{\text{max}} = 358 \mu\text{m}$.

²Matlab script found in Appendix E.2.

where σ is the surface tension between the gas–water interface, R_0 is the equilibrium radius, γ is the polytropic exponent, and $PPA \sin(\omega t)$ is the acoustic driving term, which is used in Appendix B to study the validity of the Keller-Miksis equation for the stable-inertial cavitation observations in Chapter 4. The acoustic emissions are computed using Eq. (3.14).

The computed bubble collapse shock wave is used to deconvolve the physically detected bubble collapse shock wave from the needle hydrophone voltage-trace, making the transfer function to the needle hydrophone accessible, over a wide bandwidth, via a single–shot experiment. In the frequency domain, the magnitude of the transfer function, or the absolute sensitivity $|H_{\text{NH}}|$, can be expressed as:

$$|H_{\text{NH}}| = \frac{|U_{\text{NH}}|}{|P_{\text{rad}}||H_{\text{bpf}}|}, \quad (\text{A.3})$$

where $|U_{\text{NH}}|$ is the magnitude of the voltage–trace, and $|H_{\text{bpf}}|$ is the magnitude of the brick wall band pass filter used, equal to that seen in §3.2.2, Fig. 3.6a. This limits the blind deconvolution to the calibrated bandwidth of the needle hydrophone, such that a direct comparison can be made.

A.2 Results

Acoustic detection with the needle hydrophone, of an optical break down shock wave and a bubble collapse shock wave, are shown at two distances in Fig. A.1, with (a) at $r = 50 \pm 1$ mm, and in (b) at $r = 68 \pm 1$ mm. The collapse time for both these laser-plasma mediated vapour bubbles are $T_c = 32.8 \mu\text{s}$, equivalent to a maximum radius $R_{\text{max}} \approx 358 \mu\text{m}$. This is used as one of two initial conditions in the solution of Eq. (A.1), where the second initial condition is $\dot{R}(0) = 0 \text{ ms}^{-1}$. As both laser-plasma mediated vapour bubbles are of same size, the accuracy of blind deconvolution of the absolute sensitivity at different propagation distances, can be evaluated.

It is evident that there are observable differences between the temporal profile of the computed bubble collapse shock wave and the convolved voltage-trace. The most notable difference is the apparent negative phase in the electrical signal. This is a typical example of a convolution artefact from the non-smooth transfer function, H_{NH} to the needle hydrophone used, as discussed in Chapter 3.

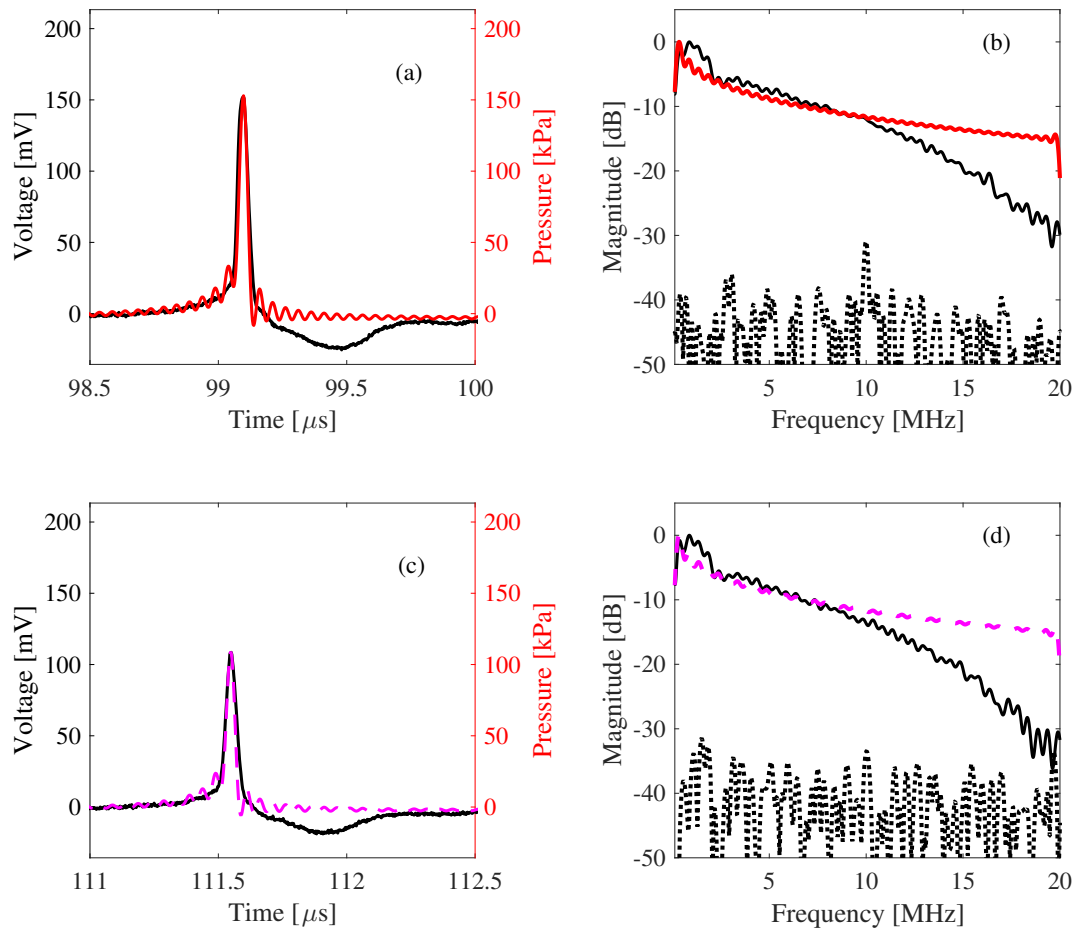


Figure A.2: (a) Convolved voltage-trace (black) and computed bubble collapse shock wave (red) at 50 ± 1 mm, (b) spectra of bubble collapse shock waves in (a), (c) convolved voltage-trace (black) and computed bubble collapse shock wave (stapled magenta) at 68 ± 1 mm, (d) spectra of bubble collapse shock waves in (c). The noise floor (dotted black) from the needle hydrophone is shown in both (b,d). Computed bubble collapse shock waves are bandpass filtered at 125 kHz – 20 MHz. Parameters used solving Eq. (A.1); $R_0 = 75 \mu\text{m}$, $\rho = 998 \text{ kg m}^{-3}$, $\mu = 0.001 \text{ Pa s}$, $\sigma = 0.072 \text{ N m}^{-1}$ $c = 1484 \text{ m s}^{-1}$, $P_0 = 101 \text{ kPa}$, $R(0) = 358 \mu\text{m}$, and $\dot{R}(0) = 0 \text{ m s}^{-1}$

Fig. A.2 b,d show the spectra of the bubble collapse shock waves in Fig. A.2 a,c. The computed bubble collapse shock waves in b and d are equal, in terms of relative frequency content. In contrast, the experimentally measured bubble collapse shock waves are different in terms of relative (high) frequency content. Potentially indicating that the bubble collapse shock waves are significantly affected by propagating through the host medium.

Fig. A.3 show the result from deconvolving the voltage-traces in Fig. A.2 a,c, with the computed bubble collapse shock waves, in accordance with Eq. (A.3), which gives the absolute sensitivity to the needle hydrophone. The blindly deconvolved absolute sensitivity, for both distances, agrees with the general trends associated with the NPL calibrated sensitivity, Fig. 3.2.

For instance, all three characterisations suggests that the highest sensitivity is found up to 10 MHz, and for higher frequencies the sensitivity drops off. However, both blind characterisations overestimate the sensitivity at low frequencies, and under estimates the sensitivity a high frequencies. Yet for all frequencies, the blind characterisations are within 6 dB of the NPL calibration. The most distant characterisation, more severely underestimates the sensitivity compared to the NPL calibration at high frequencies. This could be related to the poorer SNR displayed in Fig. A.2d, and the fact that Eq. (3.14) does not account for attenuation.

Both the over- and underestimation observed in the blind characterisations may be explained by the fact that the computed bubble collapse shock waves are insufficient representations of the physical bubble collapse shock waves that were emitted from the collapsing laser-plasma mediated vapour bubbles. A similar result was also observed in Chapter 3, where the low

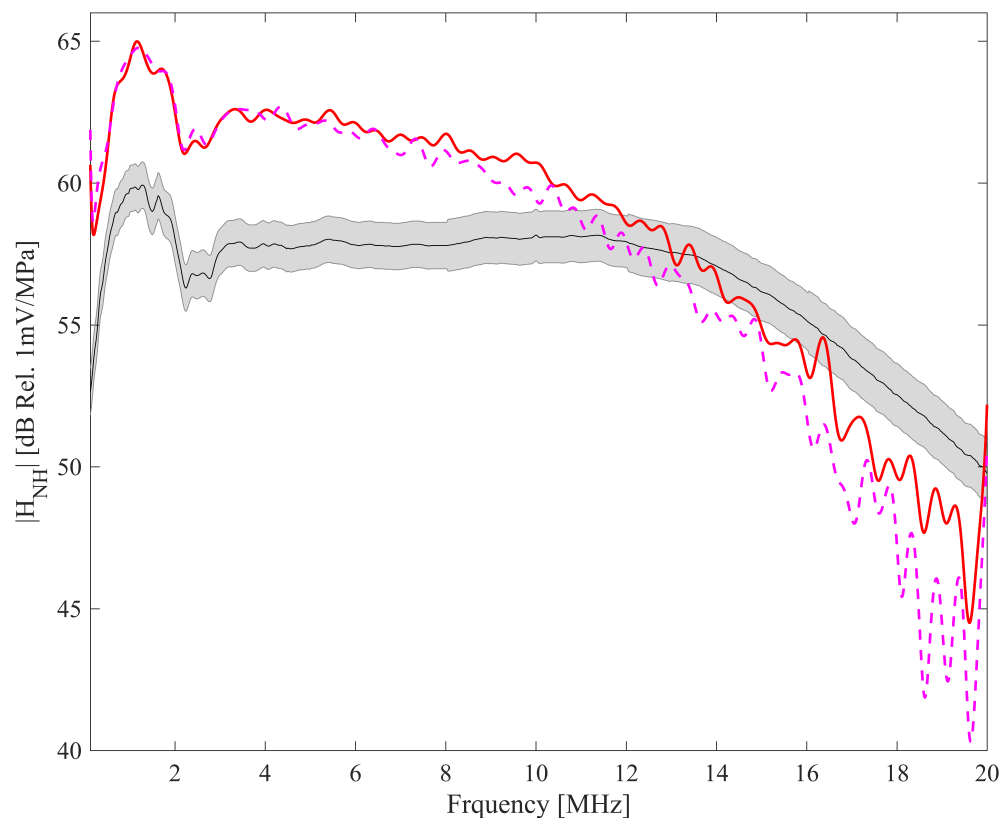


Figure A.3: Calibrated magnitude response (black) of the needle hydrophone over a bandwidth of 125 kHz to 20 MHz in 25 kHz increments. The shadow represent the uncertainty of the calibration. Blindly deconvolved magnitude response at 50 ± 1 mm (solid red) and at 68 ± 1 mm (stapled magenta).

frequency content of the bubble collapse shock wave was underestimated, and the high frequency content was overestimated by the computed bubble collapse shock wave. There are at least two potential culprits for this discrepancy; the Keller-Miksis equation is not realistically simulating the collapse dynamics, and secondly, the linear first order approximation used to compute and extrapolate the acoustic emissions to the detection site, are insufficiently accurate. Potentially, describing the bubble collapse shock wave using the Kirkwood-Bethe hypothesis [19], and a more refined method for propagating it to the detection site, would facilitate improved blind deconvolution.

A.3 Conclusion

Preliminary evidence, indicating that blind deconvolution of hydrophones are currently not able to replicate standardised calibration techniques, however, it does provide insights into the general features of the magnitude response, and it estimates the order of magnitude to the absolute sensitivity.

Appendix B

Validity of the Keller–Miksis equation for 'non-stable' cavitation and the emissions generated

Cavitation clouds are commonly described by complex theoretical considerations [179–183], which are computationally demanding. The requirement for more advanced modelling approaches is recognised for multiple cavitation phenomena, including large cavitation clouds where component bubbles are weakly coupled to the overall dynamics of the cloud behaviour, and large bubble structures such as filaments [5, 184]. However, in the case that component bubbles are closely packed, influenced by the frequency and focusing of the acoustic field, the cavitation cloud behaviour may be considered to approximate that of a single bubble. Moreover, recent theoretical endeavours, based on single bubble theory suggest that the physical insight to the sub-harmonic cavitation response, specifically the bifurcations at higher driving amplitudes, may be found in non-linear oscillator theory [185, 186].

In Chapter 4 the individual periodic shock waves are fitted manually, achieving a high similarity between the synthetic signal and its spectrum when compared to the experimental measurements. However, this is a time consuming and labour intensive process. For that reason, the validity of the Keller-Miksis equation and computed acoustic emissions, is investigated in this Appendix to simplify the generation of a synthetic signal. This is achieved by comparing the numerical solutions to the high-speed imaging observations and acoustic measurements in §4.2.1 and §4.2.2. The Keller-Miksis equation is presented in Appendix A ¹. The results in this Appendix demonstrates that a cavitation cloud with corresponding acoustic emissions, can be approximated by equations which were derived to describe the behaviour of a single-bubble, for

¹Matlab script is found in Appendix E.2.

several cycles of stable-inertial cavitation ².

²The work presented in this Appendix featured as a conference proceeding; **K. Johansen, J. H. Song, P. Prentice**, 2017, September. *Validity of the Keller-Miksis equation for “non-stable” cavitation and the acoustic emissions generated. International Ultrasonics Symposium (IUS) IEEE, pp. 1-4, 2017*

B.1 $f_0/2$ regime

Figures B.1 shows high-speed images from the cavitation observations in §4.2.1. The reader is referred back to this section for a description of the high-speed imaging data.

As previously mentioned, to enhance the shadowgraphic performance of the setup, the optical focus is placed slightly off from the plane of the bubble, causing the bubble to be sub-optimally resolved [151]. In part for this reason, the dark-pixel data is presented in normalised form, Fig. B.2a. This facilitates the comparison between relative temporal evolution measured experimentally and numerically computed radial dynamics. The simulated radius-time curve in Fig. B.2a, shows that the solution of Eq. (A.1) is to a large extent, in agreement with the temporal profile of the dark-pixel count. Features such as the collapse times and the oscillations between collapses, are well replicated. However, Eq. (A.1) is solved with a driving pressure of 1.31 MPa, which is lower than the pressure amplitude, $PPA = 1.63 \pm 0.12$ MPa, measured with the fibre-optic hydrophone, §4.1.3. Simulating the radial dynamics and acoustic emissions at a pressure of 1.6 MPa achieves a less satisfactory comparison to the experimental data.³ This difference may be explained by the fibre-optic hydrophone having been positioned slightly off from the plane where the bubble was oscillating. Alternatively, the discrepancy may be linked

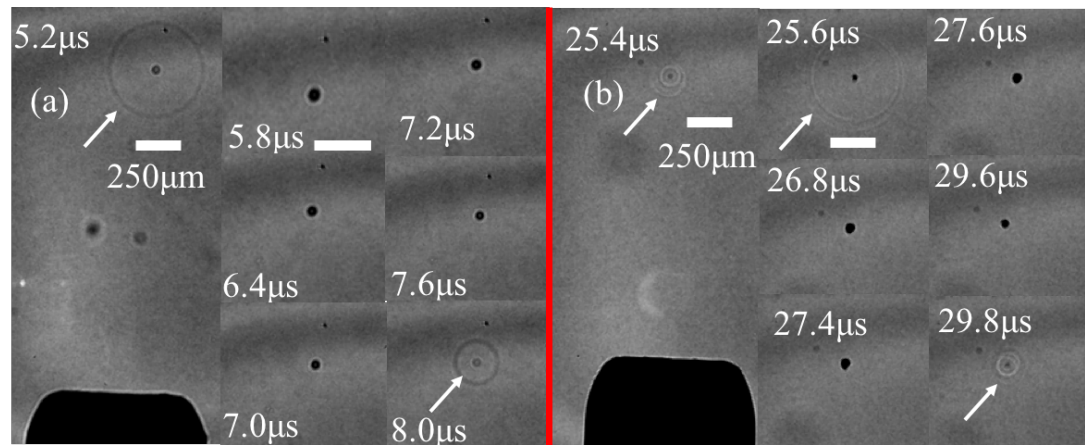


Figure B.1: (a) High-speed images of a single $f_0/2$ cavitation event, 2.7 mm from needle hydrophone tip. (b) High-speed images of a single $f_0/3$ cavitation event, 2.5 mm from needle hydrophone tip.

³Fig. 5.6 shows the solution of Eq. A.1 for a driving pressure of 1.6 MPa with acoustic emissions computed at a distance of 2.3 mm from the bubble. It is observed that the oscillations between collapses are of greater amplitude, and since the driving amplitude is higher, the overestimation of $PPPA_{SW}$ is even higher than in Fig. B.2.

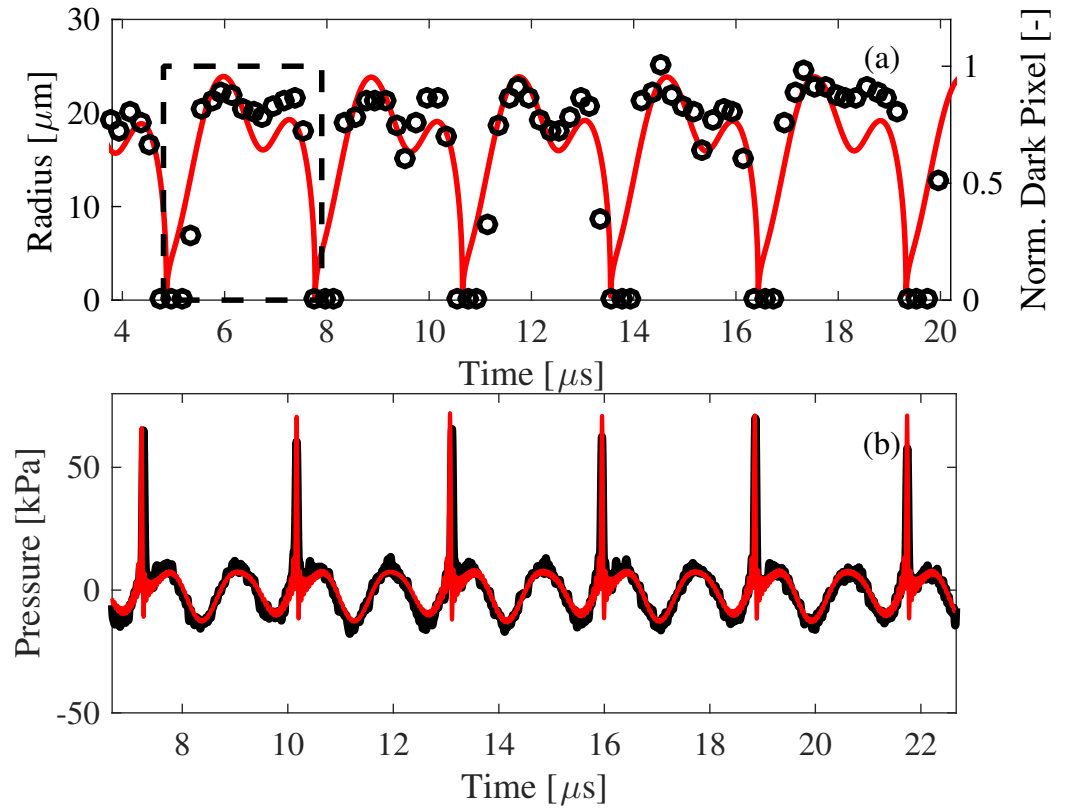


Figure B.2: (a)(left) Simulated radius-time curve from Keller-Miksis equation (red), with dashed rectangle representing the sub-harmonic oscillation imaged, and (right) normalised dark-pixel count (black scatter) from images in Fig. B.1(a). (b) Acoustic emissions from the driven bubble, measured by the needle hydrophone (black) and simulated (red), with periodic shock wave features arrowed from collapses in (b). The Keller-Miksis equation is solved with the following parameters: $R_0 = 3 \mu\text{m}$, $\rho = 998 \text{ kg m}^{-3}$, $\mu = 0.001 \text{ Pa s}$, $\sigma = 0.072 \text{ N m}^{-1}$, $c = 1484 \text{ m s}^{-1}$, $P_0 = 101 \text{ kPa}$, $PPA = 1.31 \text{ MPa}$, $R(0) = 3 \mu\text{m}$, and $\dot{R}(0) = 0 \text{ m s}^{-1}$

to the Keller-Miksis equation not accurately describing the radial dynamics at the measured driving pressure. Another unknown parameter is the equilibrium radius, and for this fit it is $R_0 = 3 \mu\text{m}$, which is slightly smaller than the resonance size of $4.4 \mu\text{m}$ predicted by Eq. (1.3) for a fundamental driving frequency of $f_0 = 692 \text{ kHz}$. The equilibrium size of the bubble in the numerical simulation indicate that the Keller-Miksis equation does not support the large bubble theory, discussed in §1.4.4, for this cavitation observation.

Figure B.2b is the deconvolved acoustic emissions collected by the needle hydrophone. The acoustic emissions consists of 6 periodic shock wave of average peak positive pressure amplitude $PPA_{\text{SW}} = 63.5 \pm 4.3 \text{ kPa}$, emitted during the respective collapses of the cavitation cloud, 2.7 mm away from the needle hydrophone, as described in §4.2.1. The oscillation between collapses in Fig. B.2a is acoustically manifested by emissions, primarily consisting of the fundamental

frequency. This is to be expected as the oscillations between collapses are of small amplitude compared to the difference between maximum and minimum radius, and therefore may be considered linear. The acoustic emissions computed from Eq. (3.14) are also shown in Fig. B.2b, in which the temporal evolution is generally in agreement with the experimental data. However, the $PPPA_{SW}$ is somewhat higher, $PPPA_{SW} = 70.1 \pm 2.5 \text{ kPa}$, and the fundamental frequency emission emitted between collapses is slightly lower, achieving a cross-correlation coefficient of 0.83 compared to 0.97 in §4.2.4.

Figure B.3 shows the spectra of the experimentally measured acoustic emissions and the simulated emission in Fig. B.2c. As discussed in Chapter 4, all spectral features except parts of the fundamental come from periodic shock waves. However, solving the Keller-Miksis equation to simulate a series of shock waves, and replicating the spectral features, is achieved with less satisfaction compared to fitting individual bubble collapse shock waves manually, as was done in §4.2.4. Nevertheless, it is recognised that the crude simulation of the stable-inertially collapsing cavitation cloud is reproducing all spectral features within 3 dB, up to $11 f_0/2$. Thus, it is reasonable to suggest that the Keller-Miksis equation and computed acoustic emissions are approximating the experimentally measured response of the cavitation cloud, for this data.

B.2 $f_0/3$ regime

When the pressure amplitude of the HIFU field is increased to $PPA = 2.40 \pm 0.09 \text{ MPa}$, the cavitation cloud starts to collapse every third cycle. In Fig B.1b it is observed that the cavitation cloud is larger, compared to Fig. B.1a. The images are also demonstrating that the cloud of bubbles is non-spherical, consisting of a set of closely packed component bubbles. This observable characteristic suggests a weakening of the underlying assumption for the application of the Keller-Miksis equation. This concern is further supported by the double-fronted shock waves, at $25.4 \mu\text{s}$ and $25.6 \mu\text{s}$, which is showing that the component bubbles are not collapsing in-phase. This is a typical feature of cavitation clouds, that a single-bubble model does not support.

Figure B.4a represents the normalised dark-pixel count and the Keller-Miksis equation

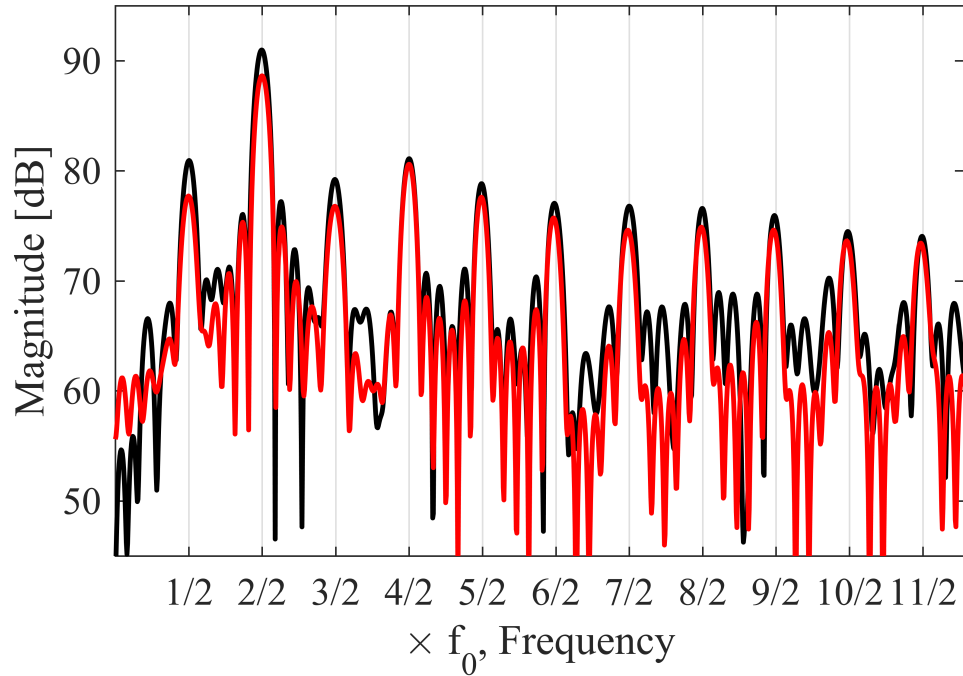


Figure B.3: Spectra of acoustic emissions in Fig B.2 (b), where measured by needle hydrophone (black) and simulated (red).

simulation of the radial dynamics. The simulation and the experimental data mimics the same trends, such as collapse times and oscillations between collapses. However, it is also worth to note that, compared to the $f_0/2$ results in Fig. B.2a, the agreement is less satisfying. The dark-pixel data indicates that the cavitation cloud is slightly growing over this small time period. An explanation for the growth of the cavitation cloud would be that the component bubbles are less closely packed after a certain number inertial collapses, making the cavitation cloud more non-spherical and appear larger. In any case, this is not something the current Keller-Miksis equation model can replicate. However, coupling the Keller-Miksis equation to an equation that describe mass diffusion, might promote a better fit.

Similarly, for the acoustic emissions there are much larger discrepancies, compared to the results presented in Fig. B.2b. The experimental data has periodic shock waves with average amplitude $PPPA_{SW} = 108.1 \pm 11.9$ kPa, and the simulation has $PPPA_{SW} = 172.5 \pm 20.5$ kPa, showing that the simulation is again consistently overestimating the periodic shock wave pressure amplitude. This resulted in a cross-correlation coefficient of 0.73 compared to 0.97 for §4.2.4. The results illustrate that the Keller-Miksis equation is less satisfactorily describing the temporal

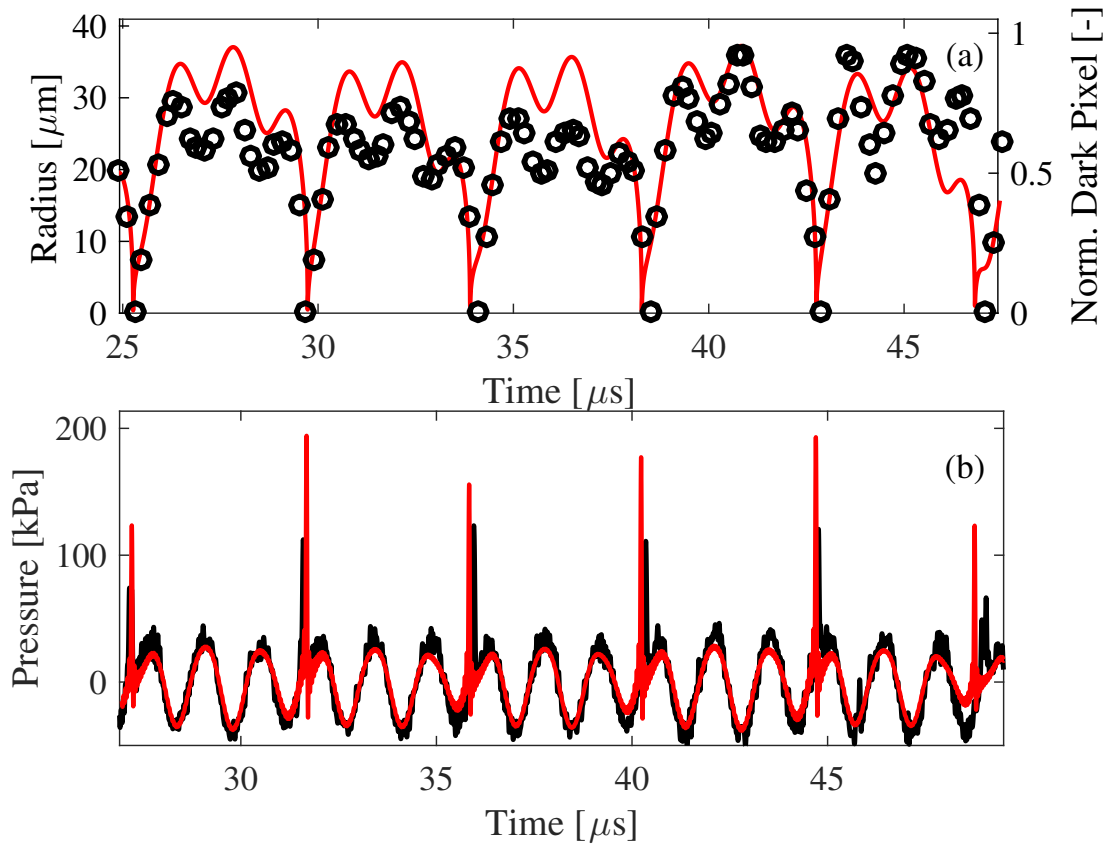


Figure B.4: (a) (left) Simulated radius-time curve from Keller-Miksis equation, with dashed rectangle representing the sub-harmonic oscillation imaged, and (right) normalised dark-pixel count (black scatter) from images in Fig. B.1 (b). (b) Acoustic emissions from the driven bubble, measured by the needle hydrophone (grey) and simulated (red), with periodic shock wave features arrowed from collapses in (b). The Keller-Miksis equation is solved with the following parameters: $R_0 = 6 \mu\text{m}$, $\rho = 998 \text{ kg m}^{-3}$, $\mu = 0.001 \text{ Pa s}$, $\sigma = 0.072 \text{ N m}^{-1}$, $c = 1484 \text{ ms}^{-1}$, $P_0 = 101 \text{ kPa}$, $PPA = 2.40 \text{ MPa}$, $R(0) = 6 \mu\text{m}$, and $\dot{R}(0) = 0 \text{ ms}^{-1}$

evolution of this cavitation cloud. Potentially, this could be related to the cavitation cloud collapsing harder, and more non-linearly, evidenced by the stronger acoustic emissions, for which the Keller-Miksis equation is not able to capture the totality of the dynamics adequately.

Figure B.5 contains the spectra of the emissions in Fig. B.4b. The agreement between the simulated acoustic emissions and experimentally measured is reasonable up to the second harmonic of the fundamental driving frequency. For higher frequency content, as should be expected, the agreement between the two spectra is significantly worse, compared to Fig. B.3. This is because the timings between respective shocks are not well replicated, and therefore high frequency content is not adding at the correct phases in the simulated acoustic emissions [48, 157].

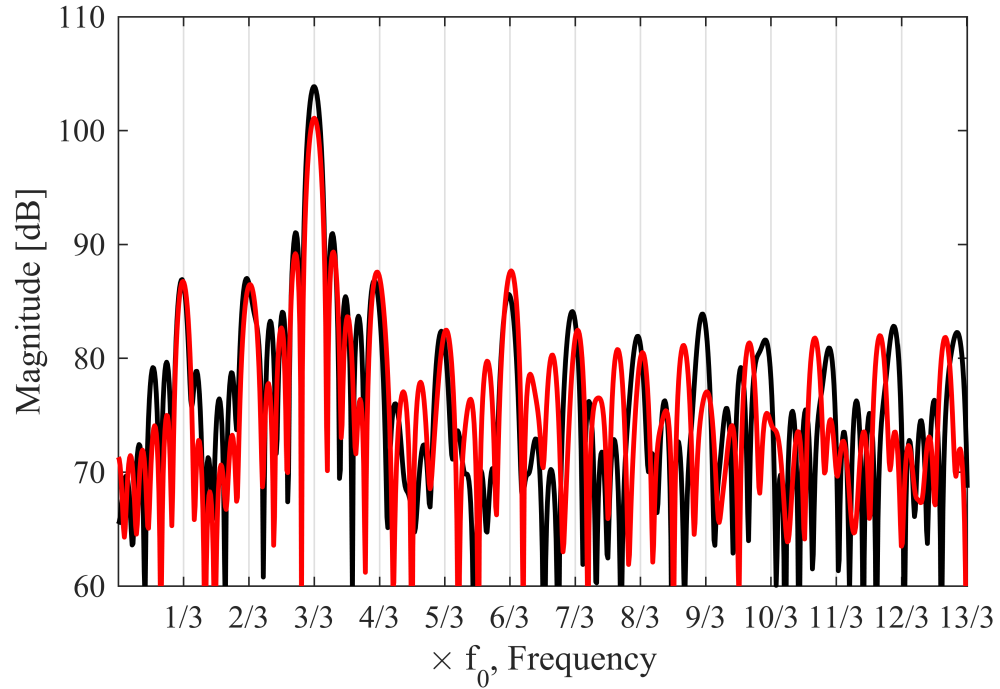


Figure B.5: Spectra of acoustic emissions in Fig B.4 (b), where measured by needle hydrophone (black) and simulated (red).

B.3 Conclusion

For $f_0/2$ sub-harmonic cavitation cloud behaviour, the Keller-Miksis equation and Eq. (3.14) are performing reasonably over a wide bandwidth, however, there are discrepancies. For higher HIFU driving pressures, where the cavitation cloud is collapsing at $f_0/3$, the behaviour is less satisfactorily described, as the cavitation cloud is failing to satisfy the single-bubble assumption. However, even at $f_0/3$ oscillations, acoustic emissions up to the second harmonic of the fundamental are well replicated with the suggested theory.

Appendix C

Characterising focused ultrasound via high-speed shadowgraphic imaging at 10 million fps

Intuitively, the introduction of a hydrophone, or any other in-situ measurement device such as a thermocouple, to an acoustic field for calibration or characterisation purposes, will also act to perturb the field itself [187]. It is, however, difficult to make any direct assessment of the perturbations that may occur, and therefore anticipate how they may affect any given experiment. In this Appendix, ultra-high speed shadowgraphic imaging at 10 million frames per second (Mfps) is utilised, to directly observe the interaction of a focused ultrasound field and the sensing tip of a typical needle hydrophone device. This technique has only recently become commercially available, where a 10ns synchronised laser pulse is used for imaging illumination. The short duration of the illumination pulse enables the imaging system to capture changes in the refractive index, as a result of the propagating acoustic field [9, 119]. Each imaging sequence is 256 frames, which allows for extended observations of how the field evolves over time. Current literature has already suggested that imaging systems which possess a shadowgraphic capability can be used for acoustic field characterisation [151]. However, in this Appendix, it is demonstrated how unprecedented ultra-high speed shadowgraphic imaging has a greater application range than previously demonstrated¹.

¹The work presented in this Appendix featured as a conference proceeding; **K. Johansen, J.H. Song, P. Prentice.** "Characterising focused ultrasound via high speed shadowgraphic imaging at 10 million frames per second." In *IEEE Ultrasonics Symposium*, pp. 1-4. 2016.

C.1 Methods

The experimental arrangement depicted in Fig. C.1 is used to study hydrophone–acoustic field interaction in detail, both optically and acoustically². HIFU is generated via a single element piezoceramic transducer (H-198, Sonic Concepts, USA), connected to a power amplifier (2100L, Electronic and Innovation, USA) and a waveform generator (DG4102, Rigol Technologies, China). The transducer has an outer diameter of 90 mm and is geometrically focused to 77 mm from the front face. The HIFU transducer has a natural fundamental resonance frequency at 1.1 MHz, and the 3rd harmonic at 3.3 MHz, through impedance matching networks. The needle hydrophone (§3.2.2) is mounted on an xyz manipulator (Velmex Motor, Bloomfield, NY, USA).

For acoustic field interaction at the third harmonic, it is placed closer to the acoustic focus, Fig. C.2a and b, and for phase characterisation of the needle hydrophone and speed of sound estimation in the propagation medium, the needle hydrophone is placed vertically above the acoustic focus, Fig. C.1 and Fig. C.3. The needle hydrophone is connected to an oscilloscope (MS07104A, Agilent Technologies, USA), and data collected at 4 GSs^{-1} . The experimental configuration is contained within the chamber described in §2.2, filled with degassed, deionised water. Two of the walls of the chamber are recessed, to allow the placement of imaging optics,

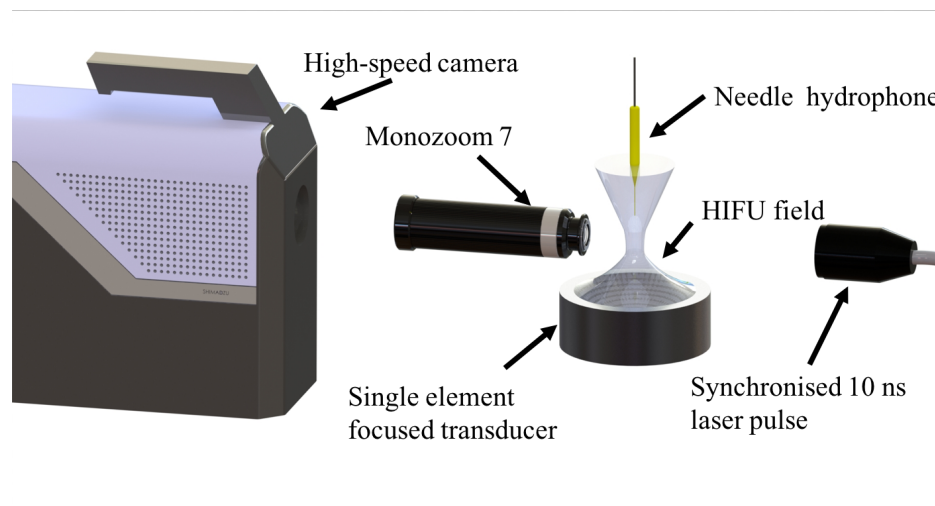


Figure C.1: Schematic of experimental setup, including high-speed camera, synchronised 10 ns laser pulses, Monozoom 7 lens, HIFU transducer, and needle hydrophone.

²Many thanks to Dr Jae Hee Song for collaborating on the collection of experimental data, and technical assistance on the analysis of the results. The author performed the analysis of the data, prepared figures, discussed results and prepared manuscript for publication.

facilitating a spatial resolution of $\sim 25 \mu\text{m}/\text{pixel}$ and $\sim 29 \mu\text{m}/\text{pixel}$, for the two respective lens configurations. High-speed shadowgraphic imaging of the propagating acoustic field is undertaken, at the fundamental driving frequency of the HIFU transducer through a makro-lens (Zeiss 100mm f2 Makro-Planar Milvus ZF.2 Lens, Germany), and at the third harmonic through a Monozoom 7 lens system (Bausch & Lomb, USA), at 10×10^6 fps as described in §2.4. A delay generator (DG535, Stanford Research Systems, USA) provides electronic triggering to synchronise each of the instruments.

C.2 Needle hydrophone–acoustic field interaction

Figure C.2 shows optical and acoustic measurements of a 3.4 MHz ultrasound field. In Fig. C.2a and b, changes in the refractive index of the medium, and consequently the grey scale in the images, are a manifestation of the propagating acoustic field. Both constructive and destructive interference was observed in the coloured rectangles, respectively. This is further demonstrated by Fig. C.2c, where the variation in grey scale value, along the z-axis centred at the needle hydrophone, shows the effect of interference from reflections of the needle hydrophone. Examining the acoustic measurement from the needle hydrophone in Fig. C.2c (stapled blue), it is not possible to discern how the needle is perturbing the free–field conditions. As the shadowgraphic imaging quality is highest in the acoustic focal region, these results suggest that if optical measurements of the field are to be correlated to the acoustic measurements, the needle hydrophone needs to be moved further away from the acoustic focal region. In addition, the images also clearly demonstrate how diffraction correction or spatial averaging is required, as the wave-fronts incident to the needle hydrophone are not plane waves, Fig C.2a. Both of the two last remarks have been taken into account when attempting phase characterisation of the needle hydrophone at the fundamental frequency of the driving transducer.

In Fig. C.3 high–speed shadowgraphic imaging and acoustic measurement of a 1.1 MHz ultrasound field is seen. The position of the needle hydrophone is further away from the acoustic focus, relative to Fig. C.2a,b, ensuring less interference from reflections from the needle hydrophone, and planer wave-fronts being incident to the needle hydrophone. These are both critical aspects of

the experimental setup when correlating optical and acoustic measurements. Along the solid red line, centred at the needle hydrophone, going through the acoustic focus, optical measurements of the acoustic field are undertaken. From these measurements, both phase characterisation of the needle hydrophone, and speed of sound measurements in the liquid are achieved, §C.3 and §C.4. The green asterisks indicate the region where the best results are obtained, Fig. C.4 - C.6.

C.3 Speed of sound estimation

Speed of sound is traditionally measured using a pulse/receive system, *i.e.*, two coaxially aligned identical transducers [188]. In this Appendix, it is demonstrated that it is feasible to estimate the

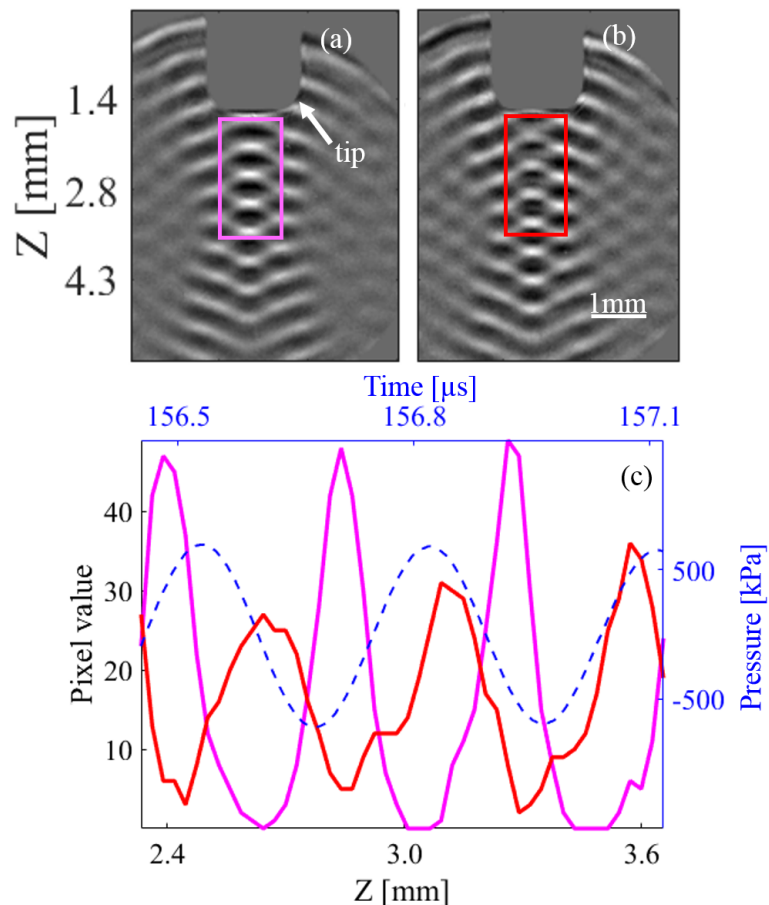


Figure C.2: Optical and acoustic measurement of 3.4 MHz ultrasound field. In (a) and (b), shadowgraphic imaging of ultrasound field, where the two frames are separated by 100 ns. Rectangular boxes (magenta and red) indicate the region of interest for constructive and destructive interference. In (c), needle hydrophone measurement (blue), and pixel values obtained along line centred at needle hydrophone for (a) and (b), respectively (magenta) and (red).

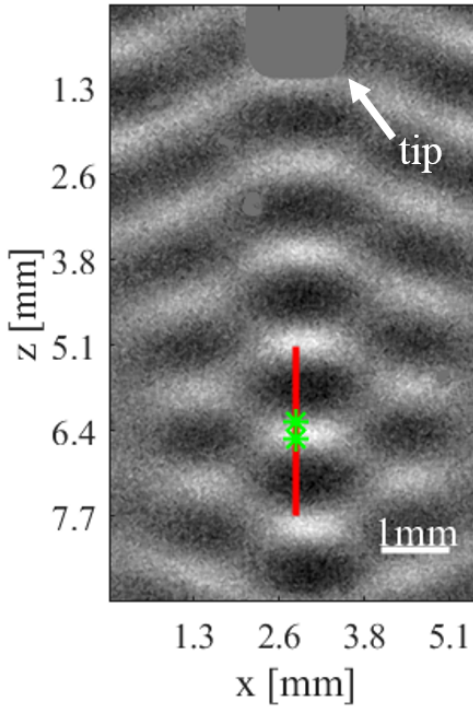


Figure C.3: In (a), high-speed shadowgraphic imaging of a 1.1 MHz ultrasound field at 10×10^6 fps, and acoustic measurement with needle hydrophone. Red line indicates pixels are sampled for speed of sound estimation and phase characterisation of needle hydrophone.

speed of sound in the propagation medium using the high-speed images. The technique presented extends to both nonlinear waves and shock waves. Sampling pixels along the solid red line in Fig. C.3a, speed of sound in the liquid was estimated by cross-correlation, finding the propagation time between pixels, using the following definition:

$$(g \star p)(\tau) = \int_{-\infty}^{\infty} g^*(t)p(t + \tau)dt \quad (\text{C.1})$$

where g and p represents waveforms at the two different pixel positions, g^* is the complex conjugate, and τ is the propagation time delay between two pixels. It was observed that more reasonable results were obtained when the two pixels were displaced by half a wave length, $\lambda/2$. Figure C.4 shows in solid red the estimated speed of sound along the red line in Fig. C.3 using this technique, where the shading represent the standard deviation. The average estimated speed of sound is $1496 \pm 9 \text{ ms}^{-1}$, and the theoretical prediction at $25 \text{ }^\circ\text{C}$ is $\sim 1497 \text{ ms}^{-1}$ [189]. However, the author would like to remark that this technique is highly sensitive to spatial calibration.

C.4 Phase characterisation of needle hydrophone

The phase response of a needle hydrophone will cause lead or lag of the incident pressure wave. This is of importance when measuring high precision transit times in fiscal measurements [190], and when deconvolving highly nonlinear pressure waves, *i.e.*, shock waves in the time domain [48, 191]. Calibrating the phase response of a hydrophone has only recently become available [192], as it is difficult to perform with adequate precision. Typical techniques include substitution calibration with a reference hydrophone, or primary calibration using optical interferometry and secondary calibration using time–delay spectrometry [193]. In this Appendix it is demonstrated how the optical measurement of the acoustic field allows to perform phase characterisation of the needle hydrophone. Assuming a linear propagating wave is observed both in the high speed images as a temporal variation of the grey scale, at a pixel along the red line in Fig. 3 (a), and at the needle hydrophone. The optically measured wave has a phase delay equal to

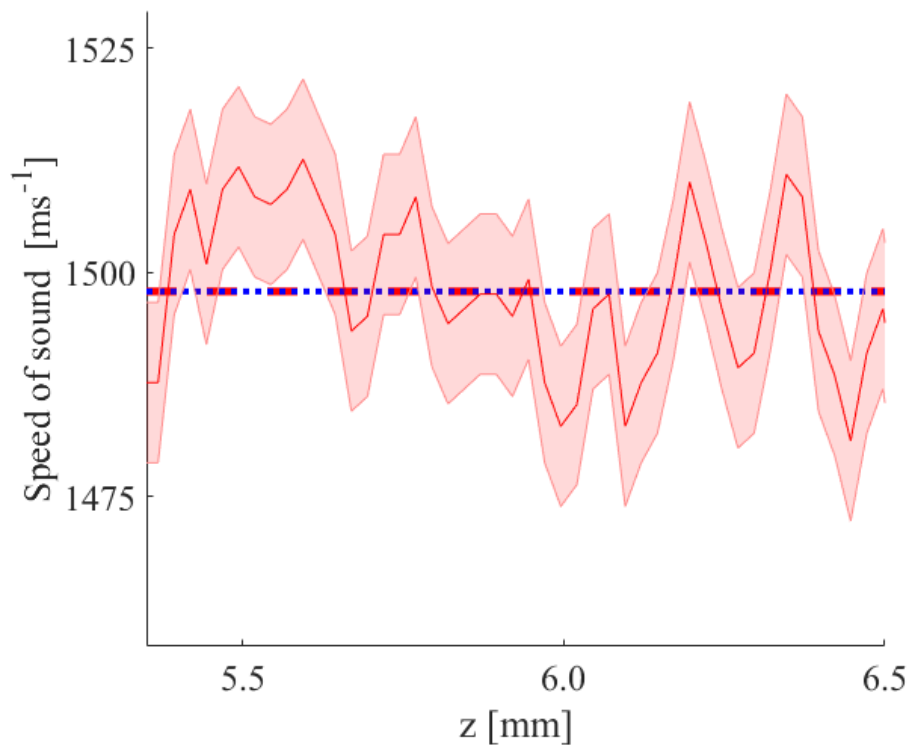


Figure C.4: In red (solid) speed of sound estimate along the red line in Fig. C.3 from cross correlation of pixels that are separated by $\lambda/2$, where stapled red line is the average estimated speed of sound, and dotted blue is the theoretical prediction. The shaded region represent the standard deviation of the measurement.

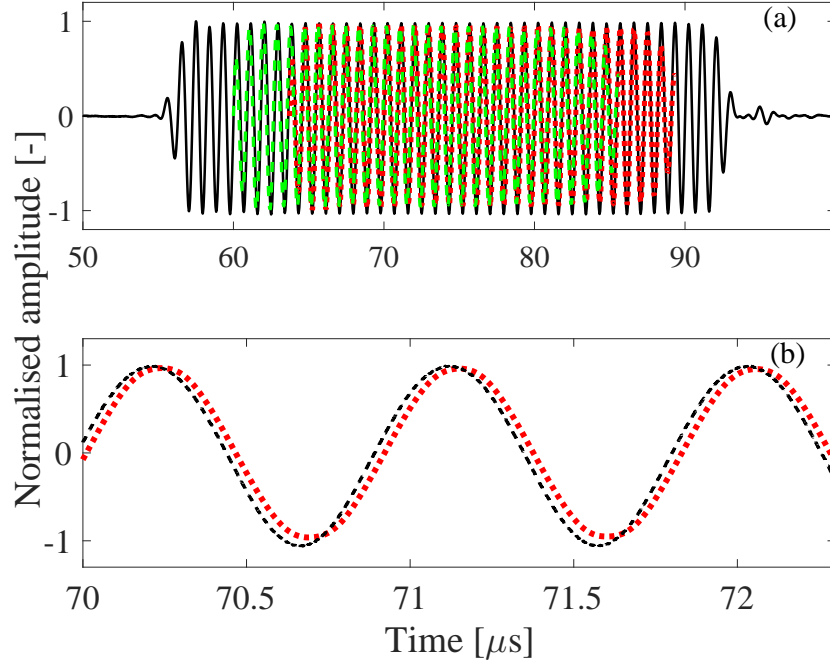


Figure C.5: Acoustical and optical measurement of ultrasonic field at 1.1 MHz. In (a), deconvolved needle hydrophone measurement (solid black), pixel sampled at midpoint (stapled green) of red line in Fig. C.3, and propagation time delayed pixel data (dotted red) relative to deconvolved needle. In (b), propagation time delayed (dotted red), and convolved needle hydrophone measurement (stapled black). All amplitudes are normalised to their respective maxima.

$\phi_{\text{tot}} = \phi_{\text{NH}} + \phi_{\text{prop}}$ in the convolved needle hydrophone data. Where ϕ_{NH} is equal to the phase of the needle hydrophone and ϕ_{prop} is the phase due to propagation. The optically measured wave can be represented as:

$$p = PPA \sin(\omega t + kz + \phi_{\text{tot}}) , \quad (\text{C.2})$$

where PPA is the normalised amplitude, ω is the angular frequency $2\pi f_c$, f_c is the centre frequency, k is the wave-number ω/c , c is the speed of sound, and z is the position along the propagating axis. Applying full-waveform deconvolution (§3.2.5) to the needle hydrophone measurement [192], with knowledge of both the magnitude and the phase, ϕ_{tot} becomes equal to ϕ_{prop} . As $\phi_{\text{prop}} = \omega\tau$ where τ is the propagation time delay due to propagation from optical detection at pixel sample position to acoustic detection at the needle hydrophone. The propagation time delay τ is estimated by a two step process, first the optically detected wave (stapled green) is temporally transformed, with a coarse time delay τ_1 estimated from the distance at pixel sample

position to the base of the needle hydrophone, assuming $c = 1497 \text{ ms}^{-1}$. Secondly, the temporally transformed wave is cross-correlated with the full-waveform deconvolved needle hydrophone measurement to find the fine delay τ_2 , following Eq. (C.1).

When temporally transforming the optical measurement (stapled green), Fig. C.5a, at pixel sample position by the propagation time delay τ , a wave which is in phase (dotted red) with the full-waveform deconvolved hydrophone (solid black) is realised, Fig. C.5a. Assuming the propagation time delay is constant for moderate changes in frequency, a delay equal to that found at the fundamental frequency can be applied to an optically measured wave at a different frequency, and cross-correlated with the convolved needle hydrophone data, Fig C.5b. The time delay between these two respective measurements is equal to the phase response of the needle hydrophone ϕ_{NH} at the frequency of interest. Phase characterisation is attempted from 0.7 MHz to 1 MHz and 1.2 MHz, using the propagation time delay estimated at 1.1 MHz. In Fig. C.6 the results of phase characterisation of the needle hydrophone is shown. The black-cross

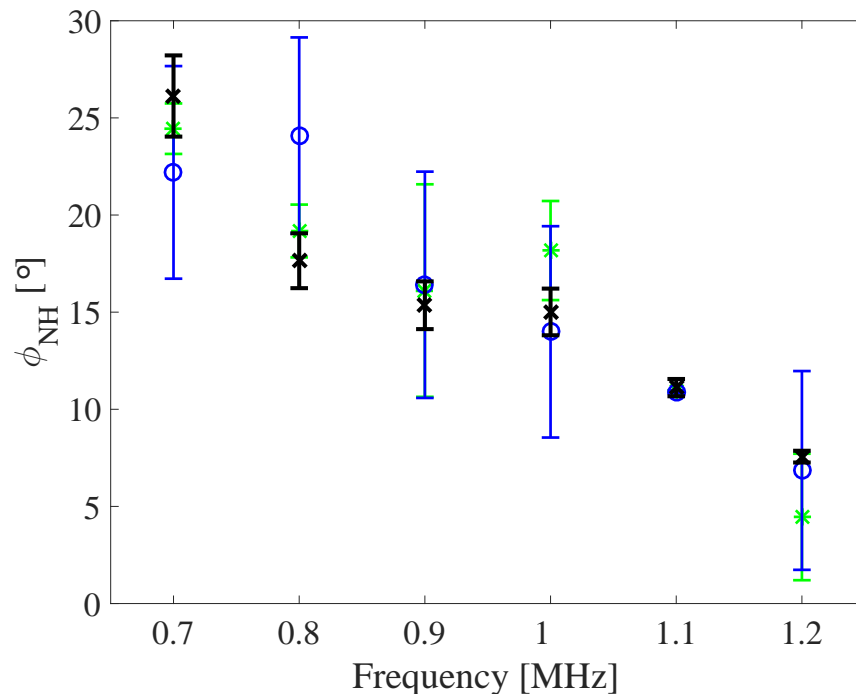


Figure C.6: Phase characterisation of needle hydrophone along red line in Fig. 2 (a) using high-speed shadowgraphic imaging, where black cross is NPL calibrated phase with uncertainties, blue circle is averaged estimated phase, and green asterisks is average estimated phase in acoustic focus, Fig. C.3. Uncertainties are represented by the standard deviation of estimated phase for respective regions.

scatter is the NPL calibration with its respective uncertainties, blue-circle is the average phase estimated for all pixel sample positions along the red line in Fig. C.3, and green-asterisks is a subsection of phase characterisation data, sampled in the acoustic focus, with lower standard deviation. For all frequencies the optically estimated phase is within the uncertainty of the NPL calibration, however, large variations in estimated phase are observed as depicted by respective error bars, particularly for the whole dataset. Sampling pixels close to the acoustic focus, where the shadowgraphic imaging is of highest quality gives estimates with significantly lower standard deviation, Fig. C.6.

C.5 Conclusion

In conclusion, the results in this Appendix show that ultra-high speed shadowgraphic imaging can be used to characterise the acoustic field pattern, estimating the speed of sound in the propagation medium, and phase characterisation of a needle hydrophone. Most reasonable results for speed of sound and phase characterisation of the needle hydrophone are obtained in the acoustic focus, where both measurements are in agreement with theory and NPL calibration, respectively.

Appendix D

Absolute sensitivity characterisation of all construction stages of swPCD

The substitution technique is commonly used to transfer the calibration of one device onto another, by measuring the same acoustic wave. As shown in Fig. 6.4 the calibrated needle hydrophone and the swPCD are equidistant from the laser focus. The spherical propagation of the bubble collapse shock wave allows the transfer of the needle hydrophone calibration to the swPCD at any construction stage (and Y-107 PCD), through a single-shot experiment.

We can express the sensitivity in the frequency domain to the swPCD, $|H_{\text{swPCD}}|$, the following way:

$$|H_{\text{swPCD}}| = \frac{|U_{\text{swPCD}}| \times |H_{\text{bpf}}| \times |H_{\text{NH}}|}{|U_{\text{NH}}|}, \quad (\text{D.1})$$

where $|U_{\text{NH}}|$ is the magnitude the voltage-output from the needle hydrophone, $|P_{\text{BCSW}}|$ is the magnitude to the bubble collapse shock wave, $|H_{\text{bpf}}|$ is the magnitude of the transfer function for a bandpass filter with the same bandwidth as the calibration of the needle hydrophone, $|H_{\text{NH}}|$ is the magnitude to the transfer function for the needle hydrophone, known from the calibration, and $|U_{\text{swPCD}}|$ is the magnitude to the voltage-output from the swPCD. All stages of the swPCD were characterised from 125 kHz to 8 MHz, as for frequencies above 8 MHz, the SNR for the

swPCD was insufficient at a distance of 68 ± 1 mm, and spatial averaging is not compensated for. Hence, the data presented below may only be considered as preliminary results.

Figure D.1 shows the sensitivity for all construction stages of the swPCD, Y-107, and the calibrated needle hydrophone. It demonstrates that the swPCD is tuned as expected from the design considerations, with the most notable change in sensitivity when the backing layer was added. This is in agreement with computational results from the FEM model, Fig. 6.7 and Fig. 6.8. Moreover, the results demonstrate that the in-house built swPCD is significantly more sensitive to low frequency content (< 3 MHz) than Y-107, reflecting the conclusions drawn from Fig. 6.10 and Fig. 6.12. Characterisation of all stages were achieved using 15 laser-plasma mediated bubbles of similar size, for each stage, to average out random noise. The uncertainty was computed from the standard deviation and the uncertainty of the needle hydrophone calibration.

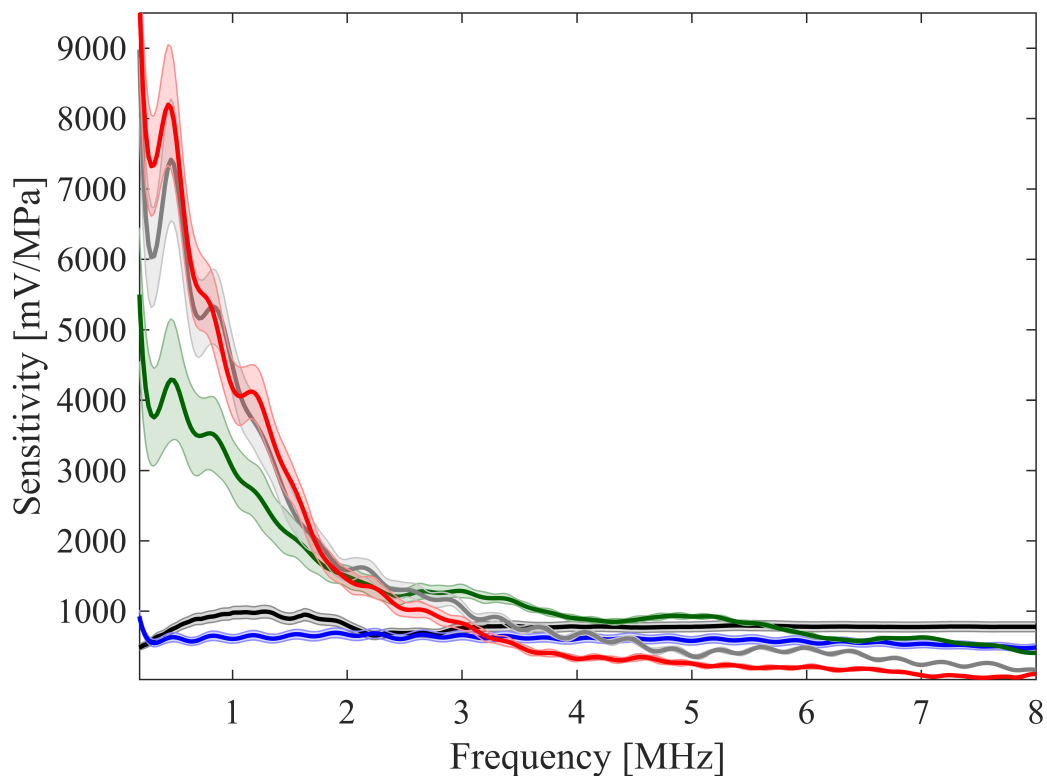


Figure D.1: Characterised sensitivity for all construction stages of the swPCD, Y-107, and needle hydrophone calibration. Where unbacked and unmatched (green), backed (grey), backed and matched (red), Y-107 (blue), and needle hydrophone (black). All uncertainties are represented by shading.

Appendix E

Selection of Matlab scripts

E.1 Gilmore equation and acoustic emissions

```
clear
close all;
clc;
global n amp R_0 p_v p_0 gamma c rho sigma mu omega f q ;

%% material input parameters
% initial bubble radius in m
R_0          = 4.4e-6;
% driving frequency in Hz
f            = 692e3;
% driving period in s
T            = 1./f;
% angular frequency in rad s(-1)
omega        = 2*pi*f;
% ambient pressure in Pa
p_0          = 1.013250e5;
% driving amplitude
```

```
amp          = 0e6;
% specific heat ratio (dimensionless)
gamma       = 4/3;
% viscosity of the liquid in Pa s
mu          = 1e-3;
% fluid density in kg m(-3)
rho        = 998;
% surface tension in N m(-1)
sigma      = 0.0728;
% speed of ultrasound in m s(-1)
c          = 1484.7;
% experimentally determined constant for water
q         = 6.5;
% vapor pressure in Pa
p_v      = 2.33e3;
% time step in S
tstep    = 1e-9;
% # cycles before ultrasound
m        = 0;
% # cycles with ultrasound
n        = 50;
% # cycles after ultrasound
o        = 0;
% time span in S
tspan    = m*T:tstep:(n+o)*T;
% relative tolerance
options  = odeset('RelTol',1e-12);
% Initial conditions [R(0) in m , dRdt(0) in m s(-1)]
y_0     = [ 50e-6  0 ];
```

```

% Runga-Kutta 4-5 solver
[t,y] = ode45('GilmoreEquation',tspan,y_0,options);

%%-----Acoustic emission-----
% distance from cavity
r = 3.0e-3;
% derivative of velocity potential
dphidt = gradient(-y(:,1).^2.*y(:,2),tstep);
% computed acoustic emissions
P_rad = -rho*dphidt/r;

function GilmoreEquation=f(t,y)

global R_0 p_0 gamma rho sigma mu c q ;

R = y(1);
dRdt = y(2);

%empirical constants
b = 1/(rho*c^2);
B = 1/(b*q) - p_0;
% van der Waals core
m = 0.00;
% pressure at bubble wall p_w in thesis
p = (p_0 + 2*sigma/R_0)*((R_0^3 -m*R_0^3)/(R^3 - m*
R_0^3))^gamma)...
- 2*sigma/R - 4*mu*dRdt/R;

```

```

% time derivative of p_w
dpdt_rest = -gamma * (p_0 + 2 * sigma / R_0)...
            * ((R_0^3 - m * R_0^3)/(R^3 - m * R_0^3))^(gamma-1)...
            * (3 * R^2 * dRdt * (R_0^3 - m * R_0^3)/(R^3 - m * R_0^3)
              ^2 )...
            + (2*sigma* dRdt/(R^2)) + (4 * mu * dRdt^2) / (R^2);

% enthalpy at bubble wall
H          = ((p_0 + B)^(1/q)/rho)*(q/(q-1))*((p + B)^((q-1)/
          q)...
            - (p_0 + p_ac(t) + B)^((q-1)/q));

% time derivative of enthaply at bubble wall
dHdt       = ((p_0 + B)^(1/q)/rho)*(dpdt_rest*(p + B)^(-1/q)
            ...
            - p_ac2(t)*(p_0 + p_ac(t) + B)^(-1/q));

% speed of sound at bubble wall
C          = sqrt(c^2 + (q-1)*H);

ddRdt      = ((-3*dRdt^2/2)*(1-dRdt/(3*C)) + (1 + dRdt/C)*H
            ...
            + (1 - dRdt/C)*(R/C)*dHdt) ...
            / (R*(1-dRdt/C)+(1 - dRdt/C)*((p_0 + B)^(1/q)
            )/rho)*(4*mu/C)*(p + B)^(-1/q));

GilmoreEquation = [dRdt ; ddRdt];

function y=p_ac(t)

```

```
global n amp omega;
```

```
% Heaviside step function
```

```
heav = (t>=0) & (t<=(2*pi*n/omega));
```

```
% acoustic driving
```

```
RF = -amp*sin(omega*t) .* heav;
```

```
y = RF;
```

```
function y=p_ac2(t)
```

```
global n amp omega;
```

```
% Heaviside step function
```

```
heav = (t>=0) & (t<=(2*pi*n/omega));
```

```
% derivative of driving function
```

```
RF = -amp*omega*cos(omega*t) .* heav;
```

```
y = RF;
```

E.2 Keller-Miksis for single bubble and bubble pair

```
close all;
```

```
clc;
```

```
close all hidden;
```

```
clear;
```

```
global n amp R_0 p_v p_0 gamma c rho sigma mu omega f q d;
```

```
% bubble diameter in m
```

```
diameter = 6.0e-6;
```

```
% initial bubble radius in m
R_0          = diameter/2;
% driving frequency vector
f            = 692e3;
% driving period in s
T            = 1./f;
% cycle frequency in rad s(-1)
omega        = 2*pi*f;
% ambient pressure in Pa
p_0          = 1.013250e5;
% peak positive pressure amplitude of driving function
amp          = 1.6e6;
% specific heat ratio (dimensionless)
gamma        = 4/3;
% viscosity of the liquid in Pa s
mu           = 1e-3;
% fluid density in kg m(-3)
rho          = 998;
% surface tension in N m(-1)
sigma        = 0.0728;
% speed of ultrasound in m s(-1)
c            = 1484.7;
% separation between the bubbles
d            = 2.3e-3;
% empirical constant
q            = 6.5;
% vapour pressure in Pa
p_v          = 2.33e3;
% time step
```

```

tstep          = 1e-9;
% # cycles before ultrasound
m              = 0;
% # cycles with ultrasound
n              = 65;
% # cycles after ultrasound
o              = 0;
% time span in S
tspan          = m*T:tstep:(n+o)*T;
% relative tolerance
options        = odeset('RelTol',1e-12);
% [R(0) in m , dRdt(0) in m s^(-1)]
y_0           = [ R_0  0 ];
% Runga-Kutta 4-5 solver
[t1,y1]= ode45('KellerMiksisBubblePair',tspan,y_0,options);
% Runga-Kutta 4-5 solver
[t2,y2]= ode45('KellerMiksisSingleBubble',tspan,y_0,options);

function KellerMiksisSingleBubble=f(t,y)

global R_0 p_0 gamma rho sigma mu c;

R              = y(1);
dRdt           = y(2);

m = 0.0;

```

```

p1          = (p_0 + 2*sigma/R_0)*((R_0^3 -m*R_0^3)/(R^3 - m*
R_0^3))^ (gamma) ...
            - 2*sigma/R - 4*mu*dRdt/R - p_0 - p_ac(t);

dp1dt_rest = -gamma * (p_0 + 2 * sigma / R_0)...
            * ((R_0^3 - m * R_0^3)/(R^3 - m * R_0^3))^ (gamma-1)...
            * (3 * R^2 * dRdt * (R_0^3 - m * R_0^3)/(R^3 - m * R_0^3)
            ^2 )...
            + (2*sigma* dRdt/(R^2)) + (4 * mu * dRdt^2) / (R^2) -
            p_ac2(t);

ddRdtt      = ( 1/rho * ( 1 + dRdt/c) * p1 + R*dp1dt_rest/(rho*
c) ...
            - ( 3/2 - dRdt/(2*c))*dRdt^2) ...
            / ( ( 1 - dRdt/c)*R + 4*mu/(rho*c) );

KellerMiksisSingleBubble = [dRdt ; ddRdtt];

function KellerMiksisBubblePair=f(t,y)

global R_0 p_0 gamma rho sigma mu c d;

R          = y(1);
dRdt       = y(2);

```

```

m = 0.0;

p1 = (p_0 + 2*sigma/R_0)*((R_0^3 - m*R_0^3)/(R^3 - m*
R_0^3))^(gamma)...
- 2*sigma/R - 4*mu*dRdt/R - p_0 - p_ac(t);

dp1dt_rest = -gamma * (p_0 + 2 * sigma / R_0)...
* ((R_0^3 - m * R_0^3)/(R^3 - m * R_0^3))^(gamma-1)...
* (3 * R^2 * dRdt * (R_0^3 - m * R_0^3)/(R^3 - m * R_0^3)
^2 )...
+ (2*sigma* dRdt/(R^2)) + (4 * mu * dRdt^2) / (R^2) -
p_ac2(t);

ddRdtt = ( 1/rho * ( 1 + dRdt/c) * p1 + R*dp1dt_rest/(rho*
c)...
- ( 3/2 - dRdt/(2*c))*dRdt^2 - 2*R*dRdt^2/d)...
/ ( ( 1 - dRdt/c)*R + 4*mu/(rho*c) + R^2/d);

KellerMiksisBubblePair = [dRdt ; ddRdtt];

```

E.3 Deconvolution of needle hydrophone

```
% Many thanks to Jae Hee Song for implementation.
```

```
function [DcvOut minDcvOut maxDcvOut rndDcvOut ImpRsp fx Mf Mp
] = func_PANeedle_DECONV_NPL_Error(sig_in, FS, sPhzOn)
```

```
FreqRes = 1;
```

```

CalFreq1 = 125;    % [kHz]
CalFreq2 = 20000; % [kHz]

%% load calibration data

fid      = fopen('Magnitude_NPL.txt');    % [mV/kPa]
NPLmag   = fscanf(fid, '%d');            fclose(fid);

fid      = fopen('Phase_NPL.txt');        % [rad]
NPLphz   = fscanf(fid, '%f');            fclose(fid);

freq     = linspace(CalFreq1, CalFreq2, length(NPLmag)); %
        calibration range: [125 kHz ~ 20 MHz]

%% Uncertainties - Magnitude

Muc1 = 9;    % [%],    0.125 MHz ~ 0.975 MHz
Muc2 = 9;    % [%],    1      MHz ~ 8 MHz
Muc3 = 10;   % [%],    8.05  MHz ~ 12 MHz
Muc4 = 11;   % [%],    12.05 MHz ~ 16 MHz
Muc5 = 12;   % [%],    16.05 MHz ~ 20 MHz

idx1 = find(freq == 125);
idx2 = find(freq == 975);

minNPLmag(idx1:idx2) = NPLmag(idx1:idx2) * (1-Muc1/100);
maxNPLmag(idx1:idx2) = NPLmag(idx1:idx2) * (1+Muc1/100);
rndNPLmag(idx1:idx2) = NPLmag(idx1:idx2) .* (1+(rand(idx2-
        idx1+1,1)-0.5)*Muc1*2/100);

idx1 = find(freq == 1000);

```

```
idx2 = find(freq == 8025);
minNPLmag(idx1:idx2) = NPLmag(idx1:idx2) * (1-Muc2/100);
maxNPLmag(idx1:idx2) = NPLmag(idx1:idx2) * (1+Muc2/100);
rndNPLmag(idx1:idx2) = NPLmag(idx1:idx2) .* (1+(rand(idx2-
    idx1+1,1)-0.5)*Muc2*2/100);

idx1 = find(freq == 8050);
idx2 = find(freq == 12025);
minNPLmag(idx1:idx2) = NPLmag(idx1:idx2) * (1-Muc3/100);
maxNPLmag(idx1:idx2) = NPLmag(idx1:idx2) * (1+Muc3/100);
rndNPLmag(idx1:idx2) = NPLmag(idx1:idx2) .* (1+(rand(idx2-
    idx1+1,1)-0.5)*Muc3*2/100);

idx1 = find(freq == 12050);
idx2 = find(freq == 16025);
minNPLmag(idx1:idx2) = NPLmag(idx1:idx2) * (1-Muc4/100);
maxNPLmag(idx1:idx2) = NPLmag(idx1:idx2) * (1+Muc4/100);
rndNPLmag(idx1:idx2) = NPLmag(idx1:idx2) .* (1+(rand(idx2-
    idx1+1,1)-0.5)*Muc4*2/100);

idx1 = find(freq == 16050);
idx2 = find(freq == 20000);
minNPLmag(idx1:idx2) = NPLmag(idx1:idx2) * (1-Muc5/100);
maxNPLmag(idx1:idx2) = NPLmag(idx1:idx2) * (1+Muc5/100);
rndNPLmag(idx1:idx2) = NPLmag(idx1:idx2) .* (1+(rand(idx2-
    idx1+1,1)-0.5)*Muc5*2/100);
```

```
%% Uncertainties - Phase
```

```

Puc1 = 8;      % [%],    0.125 MHz ~ 0.975 MHz
Puc2 = 8;      % [%],    1      MHz ~ 8 MHz
Puc3 = 4;      % [%],    8.05  MHz ~ 12 MHz
Puc4 = 4;      % [%],   12.05  MHz ~ 16 MHz
Puc5 = 8;      % [%],   16.05  MHz ~ 20 MHz

idx1 = find(freq == 125);
idx2 = find(freq == 975);
minNPLphz(idx1:idx2) = NPLphz(idx1:idx2) * (1-Puc1/100);
maxNPLphz(idx1:idx2) = NPLphz(idx1:idx2) * (1+Puc1/100);
rndNPLphz(idx1:idx2) = NPLphz(idx1:idx2) .* (1+(rand(idx2-
    idx1+1,1)-0.5)*Puc1*2/100);

idx1 = find(freq == 1000);
idx2 = find(freq == 8025);
minNPLphz(idx1:idx2) = NPLphz(idx1:idx2) * (1-Puc2/100);
maxNPLphz(idx1:idx2) = NPLphz(idx1:idx2) * (1+Puc2/100);
rndNPLphz(idx1:idx2) = NPLphz(idx1:idx2) .* (1+(rand(idx2-
    idx1+1,1)-0.5)*Puc2*2/100);

idx1 = find(freq == 8050);
idx2 = find(freq == 12025);
minNPLphz(idx1:idx2) = NPLphz(idx1:idx2) * (1-Puc3/100);
maxNPLphz(idx1:idx2) = NPLphz(idx1:idx2) * (1+Puc3/100);
rndNPLphz(idx1:idx2) = NPLphz(idx1:idx2) .* (1+(rand(idx2-
    idx1+1,1)-0.5)*Puc3*2/100);

idx1 = find(freq == 12050);
idx2 = find(freq == 16025);

```

```

minNPLphz (idx1:idx2) = NPLphz (idx1:idx2) * (1-Puc4/100);
maxNPLphz (idx1:idx2) = NPLphz (idx1:idx2) * (1+Puc4/100);
rndNPLphz (idx1:idx2) = NPLphz (idx1:idx2) .* (1+(rand(idx2-
    idx1+1,1)-0.5)*Puc4*2/100);

idx1 = find(freq == 16050);
idx2 = find(freq == 20000);

minNPLphz (idx1:idx2) = NPLphz (idx1:idx2) * (1-Puc5/100);
maxNPLphz (idx1:idx2) = NPLphz (idx1:idx2) * (1+Puc5/100);
rndNPLphz (idx1:idx2) = NPLphz (idx1:idx2) .* (1+(rand(idx2-
    idx1+1,1)-0.5)*Puc5*2/100);

```

%% Frequency response - Magnitude only

```

fx1      = [0:FreqRes:freq(1)];
ITPmf1   = ones(1, length(fx1)) * NPLmag(1);
minITPmf1 = ones(1, length(fx1)) * minNPLmag(1);
maxITPmf1 = ones(1, length(fx1)) * maxNPLmag(1);
rndITPmf1 = ones(1, length(fx1)) * rndNPLmag(1);

fx2      = [freq(1):FreqRes:freq(end)];
ITPmf2   = interp1(freq, NPLmag, fx2, 'pchip');
minITPmf2 = interp1(freq, minNPLmag, fx2, 'pchip');
maxITPmf2 = interp1(freq, maxNPLmag, fx2, 'pchip');
rndITPmf2 = interp1(freq, rndNPLmag, fx2, 'pchip');

fx3      = [freq(end):FreqRes:FS/2/1e3];
ITPmf3   = ones(1, length(fx3)) * NPLmag(end);
minITPmf3 = ones(1, length(fx3)) * minNPLmag(end);

```

```

maxITPmf3 = ones(1,length(fx3)) * maxNPLmag(end);
rndITPmf3 = ones(1,length(fx3)) * rndNPLmag(end);

fx_base    = [ fx1(1:end-1)      fx2      fx3(2:end)
              ];
Mf_base    = [ ITPmf1(1:end-1)  ITPmf2   ITPmf3(2:end)
              ];
minMf_base = [ minITPmf1(1:end-1) minITPmf2  minITPmf3(2:
end) ];
maxMf_base = [ maxITPmf1(1:end-1) maxITPmf2  maxITPmf3(2:
end) ];
rndMf_base = [ rndITPmf1(1:end-1) rndITPmf2  rndITPmf3(2:
end) ];

N = length(fx_base);

fx = [-fx_base(end:-1:2) fx_base];
Mf  = [   Mf_base(end:-1:2)   Mf_base]';
minMf = [ minMf_base(end:-1:2) minMf_base]';
maxMf = [ maxMf_base(end:-1:2) maxMf_base]';
rndMf = [ rndMf_base(end:-1:2) rndMf_base]';

%% Frequency response - Magnitude & Phase
ITPmp1 = zeros(1, length(fx1));
ITPmp2 = interp1(freq, NPLphz, fx2, 'pchip');
minITPmp2 = interp1(freq, minNPLphz, fx2, 'pchip');
maxITPmp2 = interp1(freq, maxNPLphz, fx2, 'pchip');
rndITPmp2 = interp1(freq, rndNPLphz, fx2, 'pchip');

```

```

ITPmp3 = zeros(1, length(fx3));

Mp_base = [ ITPmp1(1:end-1)    ITPmp2    ITPmp3(2:end) ];
minMp_base = [ ITPmp1(1:end-1) minITPmp2    ITPmp3(2:end) ];
maxMp_base = [ ITPmp1(1:end-1) maxITPmp2    ITPmp3(2:end) ];
rndMp_base = [ ITPmp1(1:end-1) rndITPmp2    ITPmp3(2:end) ];

Mp = [ -Mp_base(end:-1:2)    Mp_base]';
minMp = [-minMp_base(end:-1:2) minMp_base]';
maxMp = [-maxMp_base(end:-1:2) maxMp_base]';
rndMp = [-rndMp_base(end:-1:2) rndMp_base]';

Mreal = Mf ./ sqrt(1+tan(Mp).^2);
Mimag = Mreal .* tan(Mp);
M      = Mreal + j*Mimag;

minMreal = minMf ./ sqrt(1+tan(Mp).^2);
minMimag = minMreal .* tan(Mp);
minM      = minMreal + j*minMimag;

% minMreal = minMf ./ sqrt(1+tan(minMp).^2);
% minMimag = minMreal .* tan(minMp);
% minM      = minMreal + j*minMimag;

% minMreal = Mf ./ sqrt(1+tan(minMp).^2);
% minMimag = minMreal .* tan(minMp);
% minM      = minMreal + j*minMimag;

maxMreal = maxMf ./ sqrt(1+tan(Mp).^2);

```

```

maxMimag = maxMreal .* tan(Mp);
maxM      = maxMreal + j*maxMimag;

%   maxMreal = maxMf ./ sqrt(1+tan(maxMp).^2);
%   maxMimag = maxMreal .* tan(maxMp);
%   maxM      = maxMreal + j*maxMimag;

%   maxMreal = Mf ./ sqrt(1+tan(maxMp).^2);
%   maxMimag = maxMreal .* tan(maxMp);
%   maxM      = maxMreal + j*maxMimag;

rndMreal = rndMf ./ sqrt(1+tan(rndMp).^2);
rndMimag = rndMreal .* tan(rndMp);
rndM      = rndMreal + j*rndMimag;

%% generate post-filter
Mfilter_base = ones(1, length(fx_base));
Mfilter_base(1:CalFreq1) = 0;
Mfilter_base(CalFreq2+2:end) = 0;

Mfilter = [ Mfilter_base(end:-1:2) Mfilter_base]';

%% Impulse response
imp_base = ifft(iffshift(Mf));
imp0      = imp_base(end-length(sig_in)+1:end);
imp1      = imp_base(1:length(sig_in));

```

```

ImpRsp    = [imp0 ; imp1];

%% calculate Frequency-Domain De-convolution
SIG_FFT   = fftshift( fft(sig_in, 2*N-1) );

if sPhzOn == 1
    % Mag & Phz
        SIG_DCV   = SIG_FFT ./ M;
        minSIG_DCV = SIG_FFT ./ minM;
        maxSIG_DCV = SIG_FFT ./ maxM;
        rndSIG_DCV = SIG_FFT ./ rndM;
%         SIG_DCV   = SIG_FFT ./ 1000;
else
    % Mag only
        SIG_DCV   = SIG_FFT ./ Mf;
        minSIG_DCV = SIG_FFT ./ minMf;
        maxSIG_DCV = SIG_FFT ./ maxMf;
        rndSIG_DCV = SIG_FFT ./ abs(rndM);
end

SIG_OUT    = SIG_DCV .* Mfilter;
minSIG_OUT = minSIG_DCV .* Mfilter;
maxSIG_OUT = maxSIG_DCV .* Mfilter;
rndSIG_OUT = rndSIG_DCV .* Mfilter;

sig_ifft = ifft(iffshift(SIG_OUT)) * 1000; %
           convert to kPa
min_sig_ifft = ifft(iffshift(minSIG_OUT)) * 1000; %

```

```

    convert to kPa
max_sig_ifft = ifft(ifftshift(maxSIG_OUT)) * 1000;    %
    convert to kPa
rnd_sig_ifft = ifft(ifftshift(rndSIG_OUT)) * 1000;    %
    convert to kPa

    DcvOut      =      sig_ifft(1:length(sig_in));
    minDcvOut   = min_sig_ifft(1:length(sig_in));
    maxDcvOut   = max_sig_ifft(1:length(sig_in));
    rndDcvOut   = rnd_sig_ifft(1:length(sig_in));

% Many thanks to Jae Hee Song for implementation
% f1: lower cut-off freq [kHz]
% f2: upper cut-off freq [kHz]
function [sig_out,Mfilter_out] = func_BPF(sig_in, f1, f2, Fcut)

    FreqRes = 1;    % [kHz]
    fx_base = [0:FreqRes:Fcut];
    fx      = [-fx_base(end:-1:2) fx_base];

    N = length(fx_base);

%% generate filter response
Mfilter_base      = ones(1, length(fx_base));
Mfilter_base(1:f1) = 0;
Mfilter_base(f2+2:end) = 0;
Mfilter_out = Mfilter_base;

Mfilter      = [ Mfilter_base(end:-1:2) Mfilter_base]';

```

```

%      Mfilter_out = Mfilter;

      %% calculate Frequency-Domain filtering
SIG_FFT  = fftshift( fft(sig_in, 2*N-1) );
SIG_OUT  = SIG_FFT .* Mfilter;

sig_ifft = ifft(ifftshift(SIG_OUT));
sig_out  = sig_ifft(1:length(sig_in));

```

E.4 Dark pixel counting algorithm

```

function [PixCnt, PixCnt_max, PixCnt_min, t, dt, fname]=
    DarkPixelCountingAlgorithm(filt, fps, dname, fname1)

%-----load frames into matlab
-----

Pathname= [dname, '/', fname1];
cd(Pathname);

%-----selection of jpeg or tiff files

jpgfiles=dir('*.jpg');
tifffiles=dir('*.tiff');
if(~isempty(jpgfiles))
    for u=1:length(jpgfiles)
        Filename_sequence{u,1}=['/', jpgfiles(u).name];
    end
txtfile=dir('*.txt');

```

```
else
    for u = 1:length(tifffiles)
        Filename_sequence{u,1}=tifffiles(u).name;
    end
end

dt=1/fps; % works
    out the time between each frame
fr=1:length(Filename_sequence);
t=0:dt:(length(Filename_sequence)-1)*dt;

%-----image analysis
fname=[Filename_sequence{1}];
frame_now=imread([Pathname,Filename_sequence{1}]); % reads
    first frame image
frame_cal=imread([Pathname,Filename_sequence{50}]);
%% ( Ytop:Ybottom,X left, Xright)

% Display image with true aspect ratio
image(frame_cal); axis image

% Use ginput to select corner points of a rectangular
% region by pointing and clicking the mouse twice
p = ginput(2);
```

```
% Get the x and y corner coordinates as integers
sp(1) = min(floor(p(1)), floor(p(2))); %xmin
sp(2) = min(floor(p(3)), floor(p(4))); %ymin
sp(3) = max(ceil(p(1)), ceil(p(2))); %xmax
sp(4) = max(ceil(p(3)), ceil(p(4))); %ymax

% Index into the original image to create the new image
MM = frame_cal(sp(2):sp(4), sp(1): sp(3),:);
ytop = sp(2);
ybottom = sp(4);
xleft = sp(1);
xright = sp(3);

% Display the subsetting image with appropriate axis ratio
figure; image(MM); axis image
disp(['Push a button'])
k = waitforbuttonpress;
close all

frame_now=frame_now(sp(2):sp(4), sp(1): sp(3),:,1); %
    cropping    1
jj = 1;

for l=1:length(Filename_sequence);

    frame_n=imread([Pathname,Filename_sequence{l}]);

    frame_no=frame_n(ytop:ybottom,xleft:xright,1);
    frame=zeros(size(frame_no));
```

```
frame_now= imadjust(frame_no);

% threshold image
[~, threshold] = edge(frame_now, 'roberts');
fudgeFactor = 1.5;
BWs = edge(frame_now, 'roberts', threshold * fudgeFactor);

se90 = strel('line', 3, 90);
se0 = strel('line', 3, 0);

BWsdil = imdilate(BWs, [se90 se0]);
BWdfill = imfill(BWsdil, 'holes');
BWnobord = imclearborder(BWdfill, 4);

% count number of dark pixels
seD = strel('diamond', 1);
BWfinal = BWnobord;
PixCnt_max(1) = nnz(BWfinal);
BWfinal = imerode(BWnobord, seD);
PixCnt(1) = nnz(BWfinal);
BWfinal = imerode(BWfinal, seD);
PixCnt_min(1) = nnz(BWfinal);
jj=jj+1

BWcomplement = imcomplement(BWfinal);
images(:,:,1)=BWdfill(:,:,1);
images2(:,:,1)=frame_no(:,:,1); %cropping 3
imagefus(:,:,1)=[images(:,:,1),images2(:,:,1)];
```

end

% play movie of analysed data

implay(imagefus)

Bibliography

- [1] K. Johnston, *The cavitation subharmonic signal : mechanistic source and optimised detection*. Phd-thesis, University of Dundee, 2016.
- [2] G. F. Kinney and K. J. Graham, *Explosive shocks in air*. Springer Science & Business Media, 2013.
- [3] S. W. Ohl, E. Klaseboer, and B. C. Khoo, “Bubbles with shock waves and ultrasound: A review,” *Interface Focus*, vol. 5, no. 5, pp. 1–15, 2015.
- [4] M. A. O’Reilly and K. Hynynen, “A PVDF receiver for ultrasound monitoring of transcranial focused ultrasound therapy,” *IEEE Transactions on Biomedical Engineering*, vol. 57, no. 9, pp. 2286–2294, 2010.
- [5] W. Lauterborn and T. Kurz, “Physics of bubble oscillations,” *Reports on Progress in Physics*, vol. 73, p. 106501, 2010.
- [6] V. Belova, D. G. Shchukin, D. A. Gorin, A. Kopyshchev, and H. Möhwald, “A new approach to nucleation of cavitation bubbles at chemically modified surfaces,” *Physical Chemistry Chemical Physics*, vol. 13, no. 17, pp. 8015–8023, 2011.
- [7] D. Sette and F. Wanderlingh, “Nucleation by cosmic rays in ultrasonic cavitation,” *Physical Review*, vol. 125, no. 2, p. 409, 1962.
- [8] B. Gerold, S. Kotopoulis, C. McDougall, D. McGloin, M. Postema, and P. Prentice, “Laser-nucleated acoustic cavitation in focused ultrasound,” *Review of Scientific Instruments*, vol. 82, p. 044902, 2011.

-
- [9] K. Johnston, C. Tapia-Siles, B. Gerold, M. Postema, S. Cochran, A. Cuschieri, and P. Prentice, “Periodic shock-emission from acoustically driven cavitation clouds: a source of the subharmonic signal.,” *Ultrasonics*, vol. 54, no. 8, pp. 2151–2158, 2014.
- [10] J. M. Rosselló, D. Dellavale, and F. J. Bonetto, “Stable tridimensional bubble clusters in multi-bubble sonoluminescence (MBSL),” *Ultrasonics Sonochemistry*, vol. 22, pp. 59–69, 2015.
- [11] U. Parlitz, L. Junge, W. Lauterborn, and L. Kocarev, “Experimental observation of phase synchronization,” *Physical Review E*, vol. 54, no. 2, pp. 2115–2117, 1996.
- [12] J. T. Tervo, R. Mettin, and W. Lauterborn, “Bubble cluster dynamics in acoustic cavitation,” *Acta Acustica united with Acustica*, vol. 92, no. 1, pp. 178–180, 2006.
- [13] J.-B. Dumas, *Histoire de l’Académie royale des sciences, belles-lettres et arts de Lyon*, vol. 1. Giberton et Brun, 1839.
- [14] L. Rayleigh, “VIII. On the pressure developed in a liquid during the collapse of a spherical cavity,” *The London, Edinburgh, and Dublin Philosophical Magazine and Journal of Science*, vol. 34, no. 200, pp. 94–98, 1917.
- [15] E. Neppiras, “Acoustic cavitation,” *Physics Reports*, vol. 61, no. 3, pp. 159–251, 1980.
- [16] B. E. Noltingk and E. A. Neppiras, “Cavitation produced by ultrasonics,” *Proceedings of the Physical Society. Section B*, vol. 63, no. 9, pp. 674–685, 1950.
- [17] M. S. Plesset, “The Dynamics of Cavitation Bubbles,” *Journal of Applied Mechanics*, vol. 16, pp. 277–282, 1949.
- [18] R. Knapp and A. Hollander, “Laboratory Investigations of the Mechanism of Cavitation,” *Transaction of the ASME*, pp. 419–435, 1948.
- [19] F. R. Gilmore, “The Growth or Collapse of A Spherical Bubble in a Viscous Compressible Liquid,” *California Institute of Tech Engineering Report*, vol. 26, no. 4, pp. 1–40, 1952.

-
- [20] M. Minnaert, “On musical air-bubbles and the sounds of running water,” *The London, Edinburgh, and Dublin Philosophical Magazine and Journal of Science*, vol. 16, no. 104, pp. 235–248, 1933.
- [21] S. M. van der Meer, B. Dollet, M. M. Voormolen, C. T. Chin, A. Bouakaz, N. de Jong, M. Versluis, and D. Lohse, “Microbubble spectroscopy of ultrasound contrast agents,” *The Journal of the Acoustical Society of America*, vol. 121, no. 1, pp. 648–656, 2007.
- [22] A. Vogel, “Shock wave emission and cavitation bubble generation by picosecond and nanosecond optical breakdown in water,” *The Journal of the Acoustical Society of America*, vol. 100, no. 1, pp. 148–165, 1996.
- [23] C.-D. Ohl, T. Kurz, R. Geisler, O. Lindau, and W. Lauterborn, “Bubble dynamics, shock waves and sonoluminescence,” *Philosophical Transactions of the Royal Society A: Mathematical, Physical and Engineering Sciences*, vol. 357, no. 1751, pp. 269–294, 1999.
- [24] L. Crum, “Sonoluminescence, Sonochemistry, and Sonophysics,” *The Journal of the Acoustical Society of America*, vol. 95, no. 1, pp. 559–562, 1994.
- [25] G. Gimenez, “The simultaneous study of light emissions and shock waves produced by cavitation bubbles,” *The Journal of the Acoustical Society of America*, vol. 71, no. 4, pp. 839–846, 1982.
- [26] K. S. Suslick, “Sonochemistry,” *Science*, vol. 247, pp. 1439–1445, 1990.
- [27] W. Lauterborn and W. Hentschel, “Cavitation bubble dynamics studied by high speed photography and holography: part one,” *Ultrasonics*, vol. 23, no. 6, pp. 260–268, 1985.
- [28] H. G. Flynn, “Method of generating energy by acoustically induced cavitation fusion and reactor therefor,” June 8 1982. US Patent 4,333,796.
- [29] R. P. Taleyarkhan, C. West, J. Cho, R. Lahey, R. I. Nigmatulin, and R. Block, “Evidence for nuclear emissions during acoustic cavitation,” *Science*, vol. 295, no. 5561, pp. 1868–1873, 2002.

-
- [30] L. A. Crum, “Acoustically induced cavitation fusion,” *The Journal of the Acoustical Society of America*, vol. 103, no. 5, pp. 2275–2276, 1998.
- [31] M. A. O’Reilly and K. Hynnen, “Blood-Brain Barrier: Real-time Feedback-controlled Focused Ultrasound Disruption by Using an Acoustic Emissions-based Controller,” *Radiology*, vol. 263, no. 1, pp. 96–106, 2012.
- [32] B. Petit, Y. Bohren, E. Gaud, P. Bussat, M. Arditi, F. Yan, F. Tranquart, and E. Allémann, “Sonothrombolysis: The Contribution of Stable and Inertial Cavitation to Clot Lysis,” *Ultrasound in Medicine and Biology*, vol. 41, no. 5, pp. 1402–1410, 2015.
- [33] T. Sun, Y. Zhang, C. Power, P. M. Alexander, J. T. Sutton, M. Aryal, N. Vykhodtseva, E. L. Miller, and N. J. McDannold, “Closed-loop control of targeted ultrasound drug delivery across the blood-brain/tumor barriers in a rat glioma model,” *Proceedings of the National Academy of Sciences*, vol. 114, no. 48, pp. E10281–E10290, 2017.
- [34] W. G. Pitt, G. A. Hussein, and B. J. Staples, “Ultrasonic drug delivery—a general review,” *Expert Opinion on Drug Delivery*, vol. 1, no. 1, pp. 37–56, 2004.
- [35] M. W. Miller, D. L. Miller, and A. A. Brayman, “A review of in vitro bioeffects of inertial ultrasonic cavitation from a mechanistic perspective,” *Ultrasound in Medicine and Biology*, vol. 22, no. 9, pp. 1131–1154, 1996.
- [36] M. A. Santos, D. E. Goertz, and K. Hynnen, “Focused ultrasound hyperthermia mediated drug delivery using thermosensitive liposomes and visualized with in vivo two-photon microscopy,” *Theranostics*, vol. 7, no. 10, p. 2718, 2017.
- [37] Z. I. Kovacs, S. Kim, N. Jikaria, F. Qureshi, B. Milo, B. K. Lewis, M. Bresler, S. R. Burks, and J. A. Frank, “Disrupting the blood–brain barrier by focused ultrasound induces sterile inflammation,” *Proceedings of the National Academy of Sciences*, vol. 114, no. 1, pp. E75–E84, 2017.

-
- [38] E. A. Neppiras, “Subharmonic and Other Low-Frequency Emission from Bubbles in Sound-Irradiated Liquids,” *The Journal of the Acoustical Society of America*, vol. 46, no. 3B, pp. 587–601, 1969.
- [39] G. S. Lebon, I. Tzanakis, K. Pericleous, and D. Eskin, “Experimental and numerical investigation of acoustic pressures in different liquids,” *Ultrasonics Sonochemistry*, vol. 42, pp. 411–421, 2018.
- [40] W. Lauterborn and E. Cramer, “Subharmonic route to chaos observed in acoustics,” *Physical Review Letters*, vol. 47, no. 20, pp. 1445–1448, 1981.
- [41] J. Frohly, S. Labouret, C. Bruneel, I. Looten-Baquet, and R. Torguet, “Ultrasonic cavitation monitoring by acoustic noise power measurement,” *The Journal of the Acoustical Society of America*, vol. 108, no. 5, pp. 2012–2020, 2000.
- [42] R. E. Apfel and C. K. Holland, “Gauging the likelihood of cavitation from short-pulse, low-duty cycle diagnostic ultrasound,” *Ultrasound in Medicine and Biology*, vol. 17, no. 2, pp. 179–185, 1991.
- [43] C. M. Schoellhammer, A. Schroeder, R. Maa, G. Y. Lauwers, A. Swiston, M. Zervas, R. Barman, A. M. DiCiccio, W. R. Brugge, D. G. Anderson, D. Blankschtein, R. Langer, and G. Traverso, “Ultrasound-mediated gastrointestinal drug delivery,” *Science Translational Medicine*, vol. 7, no. 310, p. 310ra168, 2015.
- [44] E. Lyka, C. Coviello, R. Kozick, and C.-C. Coussios, “Sum-of-harmonics method for improved narrowband and broadband signal quantification during passive monitoring of ultrasound therapies,” *The Journal of the Acoustical Society of America*, vol. 140, no. 1, pp. 741–754, 2016.
- [45] Y. Son, M. Lim, J. Khim, and M. Ashokkumar, “Acoustic emission spectra and sonochemical activity in a 36 kHz sonoreactor,” *Ultrasonics Sonochemistry*, vol. 19, no. 1, pp. 16–21, 2012.

-
- [46] M. Ashokkumar, M. Hodnett, B. Zeqiri, F. Grieser, and G. J. Price, “Acoustic emission spectra from 515 kHz cavitation in aqueous solutions containing surface-active solutes,” *Journal of the American Chemical Society*, vol. 129, no. 8, pp. 2250–2258, 2007.
- [47] A. Lauterborn, Werner, Koch, “Holographic observation of period-doubled and chaotic bubble oscillations in acoustic cavitation,” *Physical Review A*, vol. 35, no. 4, pp. 1974–1977, 1987.
- [48] J. H. Song, K. Johansen, and P. Prentice, “An analysis of the acoustic cavitation noise spectrum : The role of periodic shock waves,” *The Journal of the Acoustical Society of America*, vol. 140, no. 4, pp. 2494 – 2505, 2016.
- [49] J. R. McLaughlan, S. Harput, R. H. Abou-Saleh, S. A. Peyman, S. Evans, and S. Freear, “Characterisation of Liposome-Loaded Microbubble Populations for Subharmonic Imaging,” *Ultrasound in Medicine and Biology*, vol. 43, no. 1, pp. 346–356, 2016.
- [50] J. McLaughlan, I. Rivens, T. Leighton, and G. ter Haar, “A study of bubble activity generated in ex vivo tissue by high intensity focused ultrasound,” *Ultrasound in Medicine and Biology*, vol. 36, no. 8, pp. 1327–1344, 2010.
- [51] K. V. Jenderka and C. Koch, “Investigation of spatial distribution of sound field parameters in ultrasound cleaning baths under the influence of cavitation,” *Ultrasonics*, vol. 44, pp. 401–406, 2006.
- [52] S. Y. Wu, M. Downs, C. S. Sanchez, T. Teichert, A. Buch, G. Samiotaki, F. Marquet, Y. S. Tung, C. Chen, V. Ferrera, and E. Konofagou, “Monitoring of focused ultrasound-induced blood-brain barrier opening in non-human primates using transcranial cavitation detection in vivo and the primate skull effect,” *IEEE International Ultrasonics Symposium, IUS*, pp. 1201–1204, 2013.
- [53] S. Y. Wu, Y. S. Tung, F. Marquet, M. Downs, C. Sanchez, C. Chen, V. Ferrera, and E. Konofagou, “Transcranial cavitation detection in primates during blood-brain barrier opening—a performance assessment study,” *IEEE Transactions on Ultrasonics, Ferroelectrics, and Frequency Control*, vol. 61, pp. 966–978, 2014.

-
- [54] S.-Y. Wu, C. S. Sanchez, G. Samiotaki, A. Buch, V. P. Ferrera, and E. E. Konofagou, “Characterizing Focused-Ultrasound Mediated Drug Delivery to the Heterogeneous Primate Brain In Vivo with Acoustic Monitoring,” *Scientific Reports*, vol. 6, p. 37094, 2016.
- [55] E. C. Everbach, I. R. S. Makin, M. Azadniv, and R. S. Meltzer, “Correlation of ultrasound-induced hemolysis with cavitation detector output in vitro,” *Ultrasound in Medicine and Biology*, vol. 23, no. 4, pp. 619–624, 1997.
- [56] M. W. Miller, E. C. Everbach, C. Cox, R. R. Knapp, A. A. Brayman, and T. A. Sherman, “A comparison of the hemolytic potential of Optison and Alburnex in whole human blood in vitro: Acoustic pressure, ultrasound frequency, donor and passive cavitation detection considerations,” *Ultrasound in Medicine and Biology*, vol. 27, no. 5, pp. 709–721, 2001.
- [57] K. Hynynen, “The threshold for thermally significant cavitation in dog’s thigh muscle in vivo,” *Ultrasound in Medicine and Biology*, vol. 17, no. 2, pp. 157–169, 1991.
- [58] D. M. Hallow, A. D. Mahajan, T. E. McCutchen, and M. R. Prausnitz, “Measurement and correlation of acoustic cavitation with cellular bioeffects,” *Ultrasound in Medicine and Biology*, vol. 32, pp. 1111–1122, 2006.
- [59] J. Lee, S. Kentish, T. J. Matula, and M. Ashokkumar, “Effect of surfactants on inertial cavitation activity in a pulsed acoustic field,” *Journal of Physical Chemistry B*, vol. 109, no. 35, pp. 16860–16865, 2005.
- [60] C. Desjoux, A. Poizat, B. Gilles, C. Insera, and J.-C. Bera, “Control of inertial acoustic cavitation in pulsed sonication using a real-time feedback loop system,” *The Journal of the Acoustical Society of America*, vol. 134, no. 2, pp. 1640–1646, 2013.
- [61] F. G. Blake Jr, *Onset of Cavitation in Liquids*. PhD thesis, Harvard University, 1949.
- [62] G. W. Willard, “Ultrasonically Induced Cavitation in Water: A Step-by-Step Process,” *The Journal of the Acoustical Society of America*, vol. 25, no. 4, pp. 669–686, 1953.
- [63] H. Flynn, “Physics of acoustic cavitation in liquids,” *Physical Acoustics*, vol. 1, no. Part B, pp. 57–172, 1964.

-
- [64] D. F. Gaitan, L. A. Crum, C. C. Church, and R. A. Roy, "Sonoluminescence and bubble dynamics for a single, stable, cavitation bubble," *The Journal of the Acoustical Society of America*, vol. 91, no. 6, pp. 3166–3183, 1992.
- [65] H. G. Flynn, "Cavitation dynamics: II. Free pulsations and models for cavitation bubbles," *The Journal of the Acoustical Society of America*, vol. 58, no. 6, pp. 1160–1170, 1975.
- [66] E. A. Neppiras, "Acoustic cavitation thresholds and cyclic processes," *Ultrasonics*, vol. 18, no. 5, pp. 201–209, 1980.
- [67] I. Tzanakis, M. Hodnett, G. S. B. Lebon, N. Dezhkunov, and D. G. Eskin, "Calibration and performance assessment of an innovative high-temperature cavitometer," *Sensors and Actuators, A: Physical*, vol. 240, pp. 57–69, 2016.
- [68] G. I. Eskin, "Cavitation mechanism of ultrasonic melt degassing," *Ultrasonics - Sonochemistry*, vol. 2, no. 2, pp. 137–141, 1995.
- [69] W. B. McNamara, Y. T. Didenko, and K. S. Suslick, "Sonoluminescence temperatures during multi-bubble cavitation," *Nature*, vol. 401, no. 6755, pp. 772–775, 1999.
- [70] L. K. Tompson, L. H., Doraiswamy, "Sonochemistry: Science and Engineering," *Industrial & Engineering Chemistry Research*, vol. 38, pp. 1215 – 1249, 1999.
- [71] T. G. Leighton, *The Acoustic Bubble*. London: Academic Press, 1994.
- [72] C. Cornu, M. Guédra, J. C. Béra, H. L. Liu, W. S. Chen, and C. Inserra, "Ultrafast monitoring and control of subharmonic emissions of an unseeded bubble cloud during pulsed sonication," *Ultrasonics Sonochemistry*, vol. 42, pp. 697–703, 2018.
- [73] C. C. Church and E. L. Carstensen, "'Stable' inertial cavitation," *Ultrasound in Medicine and Biology*, vol. 27, no. 10, pp. 1435–1437, 2001.
- [74] M. Ashokkumar, "The characterization of acoustic cavitation bubbles - an overview," *Ultrasonics Sonochemistry*, vol. 18, no. 4, pp. 864–872, 2011.

-
- [75] W. T. Shi, F. Forsberg, A. Tornes, J. Østensen, and B. B. Goldberg, “Destruction of contrast microbubbles and the association with inertial cavitation,” *Ultrasound in Medicine and Biology*, vol. 26, no. 6, pp. 1009–1019, 2000.
- [76] V. Akulichev and L. Rozenberg, “High intensity ultrasonic fields,” ed LD Rozenberg, *Plenum, New York*, pp. 239–259, 1971.
- [77] M. Versluis, D. E. Goertz, P. Palanchon, I. L. Heitman, S. M. Van Der Meer, B. Dollet, N. De Jong, and D. Lohse, “Microbubble shape oscillations excited through ultrasonic parametric driving,” *Physical Review E*, vol. 82, no. 2, pp. 2–7, 2010.
- [78] T. B. Benjamin and F. Ursell, “The stability of the plane free surface of a liquid in vertical periodic motion,” *Proceedings of the Royal Society of London. Series A, Mathematical and Physical Sciences*, vol. 225, no. 1163, pp. 505–515, 1954.
- [79] T. Benjamin, *Cavitation in Real Liquids*. New York: Elsevier, 1964.
- [80] E. Neppiras and J. Parrott, “Noise measurements relating to the threshold and intensity of cavitation,” *Proceeding 5th International Congress of Acoustics, Liege*, 1965.
- [81] W. Lauterborn, “Numerical investigation of nonlinear oscillations of gas bubbles in liquids,” *The Journal of the Acoustical Society of America*, vol. 59, no. 2, pp. 283–293, 1976.
- [82] W. Güth, “Nichtlineare schwingungen von luftblasen in wasser,” *Acta Acustica united with Acustica*, vol. 6, no. 6, pp. 532–538, 1956.
- [83] C. M. C. Tempany, E. A. Stewart, N. McDannold, B. J. Quade, F. A. Jolesz, and K. Hynynen, “MR Imaging-guided Focused Ultrasound Surgery of Uterine Leiomyomas: A Feasibility Study,” *Radiology*, vol. 226, no. 3, pp. 897–905, 2003.
- [84] J. Kennedy, G. Ter Haar, and D. Cranston, “High intensity focused ultrasound: surgery of the future?,” *The British Journal of Radiology*, vol. 76, no. 909, pp. 590–599, 2003.
- [85] S. Mitragotri, “Healing sound: the use of ultrasound in drug delivery and other therapeutic applications,” *Nature Reviews Drug Discovery*, vol. 4, no. 3, p. 255, 2005.

-
- [86] F. A. Jolesz, "MRI-guided focused ultrasound surgery," *Annual Review of Medicine*, vol. 60, pp. 417–430, 2009.
- [87] H. E. Cline, J. Schenek, K. Hynynen, and R. D. Watkins, "MR-guided focused ultrasound surgery," *Journal of Computer Assisted Tomography*, vol. 16, pp. 956–956, 1992.
- [88] K. J. Parker, R. M. Lerner, and R. C. Waag, "Attenuation of ultrasound: magnitude and frequency dependence for tissue characterization.," *Radiology*, vol. 153, no. 3, pp. 785–788, 1984.
- [89] S. Goss, L. Frizzell, and F. Dunn, "Ultrasonic absorption and attenuation in mammalian tissues," *Ultrasound in Medicine and Biology*, vol. 5, no. 2, pp. 181–186, 1979.
- [90] G. ter Haar, "High intensity ultrasound," in *Seminars in laparoscopic surgery*, pp. 77–89, Sage Publications Sage CA: Thousand Oaks, CA, 2001.
- [91] W. J. Elias, D. Huss, T. Voss, J. Loomba, M. Khaled, E. Zadicario, R. C. Frysjinger, S. A. Sperling, S. Wylie, S. J. Monteith, *et al.*, "A pilot study of focused ultrasound thalamotomy for essential tremor," *New England Journal of Medicine*, vol. 369, no. 7, pp. 640–648, 2013.
- [92] G. ter Haar, "Safety and bio-effects of ultrasound contrast agents," *Medical and Biological Engineering and Computing*, vol. 47, no. 8, pp. 893–900, 2009.
- [93] A. J. Healey, P. C. Sontum, S. Kvåle, M. Eriksen, R. Bendiksen, A. Tornes, and J. Østensen, "Acoustic cluster therapy: in vitro and ex vivo measurement of activated bubble size distribution and temporal dynamics," *Ultrasound in Medicine and Biology*, vol. 42, no. 5, pp. 1145–1166, 2016.
- [94] A. van Wamel, A. Healey, P. C. Sontum, S. Kvåle, N. Bush, J. Bamber, and C. de Lange Davies, "Acoustic cluster therapy (ACT)- pre-clinical proof of principle for local drug delivery and enhanced uptake," *Journal of Controlled Release*, vol. 224, pp. 158–164, 2016.

-
- [95] N. McDannold, N. Vykhodtseva, and K. Hynynen, "Targeted disruption of the blood–brain barrier with focused ultrasound: association with cavitation activity," *Physics in Medicine and Biology*, vol. 51, no. 4, p. 793, 2006.
- [96] M. E. Downs, A. Buch, M. E. Karakatsani, E. E. Konofagou, and V. P. Ferrera, "Blood-Brain Barrier Opening in Behaving Non-Human Primates via Focused Ultrasound with Systemically Administered Microbubbles," *Scientific Reports*, vol. 5, p. 15076, 2015.
- [97] H. L. Weiss, P. Selvaraj, K. Okita, Y. Matsumoto, A. Voie, T. Hoelscher, and A. J. Szeri, "Mechanical clot damage from cavitation during sonothrombolysis," *The Journal of the Acoustical Society of America*, vol. 133, no. 5, pp. 3159–3175, 2013.
- [98] X. Chen, P. Novák, D. G. Benson, J. S. Webber, L. Hennings, G. Shafirstein, P. M. Corry, R. J. Griffin, and E. G. Moros, "An alternating focused ultrasound system for thermal therapy studies in small animals," *Medical Physics*, vol. 38, no. 4, pp. 1877–1887, 2011.
- [99] K. Kooiman, H. J. Vos, M. Versluis, and N. De Jong, "Acoustic behavior of microbubbles and implications for drug delivery," *Advanced Drug Delivery Reviews*, vol. 72, pp. 28–48, 2014.
- [100] M. Emmer, A. van Wamel, D. E. Goertz, and N. de Jong, "The Onset of Microbubble Vibration," *Ultrasound in Medicine and Biology*, vol. 33, no. 6, pp. 941–949, 2007.
- [101] N. de Jong, R. Cornet, and C. T. Lancée, "Higher harmonics of vibrating gas-filled microspheres. Part two: measurements," *Ultrasonics*, vol. 32, no. 6, pp. 455–459, 1994.
- [102] J. Sijl, B. Dollet, M. Overvelde, V. Garbin, T. Rozendal, N. de Jong, D. Lohse, and M. Versluis, "Subharmonic behavior of phospholipid-coated ultrasound contrast agent microbubbles," *The Journal of the Acoustical Society of America*, vol. 128, no. 5, pp. 3239–3252, 2010.
- [103] N. de Jong, M. Emmer, C. T. Chin, A. Bouakaz, F. Mastik, D. Lohse, and M. Versluis, "'Compression-Only' Behavior of Phospholipid-Coated Contrast Bubbles," *Ultrasound in Medicine and Biology*, vol. 33, no. 4, pp. 653–656, 2007.

-
- [104] P. Marmottant, S. van der Meer, M. Emmer, M. Versluis, N. de Jong, S. Hilgenfeldt, and D. Lohse, “A model for large amplitude oscillations of coated bubbles accounting for buckling and rupture,” *The Journal of the Acoustical Society of America*, vol. 118, no. 6, pp. 3499–3505, 2005.
- [105] B. Dollet, S. M. van der Meer, V. Garbin, N. de Jong, D. Lohse, and M. Versluis, “Nonspherical Oscillations of Ultrasound Contrast Agent Microbubbles,” *Ultrasound in Medicine and Biology*, vol. 34, no. 9, pp. 1465–1473, 2008.
- [106] S. W. Fong, E. Klaseboer, C. K. Turangan, B. C. Khoo, and K. C. Hung, “Numerical analysis of a gas bubble near bio-materials in an ultrasound field,” *Ultrasound in Medicine and Biology*, vol. 32, no. 6, pp. 925–942, 2006.
- [107] D. McMahon and K. Hynynen, “Acute inflammatory response following increased blood-brain barrier permeability induced by focused ultrasound is dependent on microbubble dose,” *Theranostics*, vol. 7, no. 16, pp. 3989–4000, 2017.
- [108] H. J. Vos, B. Dollet, M. Versluis, and N. De Jong, “Nonspherical Shape Oscillations of Coated Microbubbles in Contact With a Wall,” *Ultrasound in Medicine and Biology*, vol. 37, no. 6, pp. 935–948, 2011.
- [109] G. Lajoinie, Y. Luan, E. Gelderblom, B. Dollet, F. Mastik, H. Dewitte, I. Lentacker, N. de Jong, and M. Versluis, “Non-spherical oscillations drive the ultrasound-mediated release from targeted microbubbles,” *Communications Physics*, vol. 1, no. 1, p. 22, 2018.
- [110] C. K. Holland, C. X. Deng, R. E. Apfel, J. L. Alderman, L. A. Fernandez, and K. J. Taylor, “Direct evidence of cavitation in vivo from diagnostic ultrasound,” *Ultrasound in Medicine and Biology*, vol. 22, no. 7, pp. 917–925, 1996.
- [111] C. E. Brennen, *Cavitation and bubble dynamics*. Cambridge University Press, 2013.
- [112] C. C. Coussios and R. A. Roy, “Applications of Acoustics and Cavitation to Noninvasive Therapy and Drug Delivery,” *Annual Review of Fluid Mechanics*, vol. 40, no. 1, pp. 395–420, 2008.

-
- [113] B. A. Rabkin, V. Zderic, L. A. Crum, and S. Vaezy, “Biological and physical mechanisms of HIFU-induced hyperecho in ultrasound images,” *Ultrasound in Medicine and Biology*, vol. 32, no. 11, pp. 1721–1729, 2006.
- [114] A. D. Maxwell, T.-Y. Wang, C. A. Cain, J. B. Fowlkes, O. A. Sapozhnikov, M. R. Bailey, and Z. Xu, “Cavitation clouds created by shock scattering from bubbles during histotripsy,” *The Journal of the Acoustical Society of America*, vol. 130, no. 4, pp. 1888–1898, 2011.
- [115] A. D. Maxwell, C. A. Cain, A. P. Duryea, L. Yuan, H. S. Gurm, and Z. Xu, “Noninvasive thrombolysis using pulsed ultrasound cavitation therapy–histotripsy,” *Ultrasound in Medicine and Biology*, vol. 35, no. 12, pp. 1982–1994, 2009.
- [116] J. A. Jensen, “Linear description of ultrasound imaging systems,” tech. rep., Technical University of Denmark, 2001.
- [117] K. Johansen, J. H. Song, K. Johnston, and P. Prentice, “Deconvolution of acoustically detected bubble-collapse shock waves,” *Ultrasonics*, vol. 73, pp. 144–153, 2017.
- [118] J. B. Keller, “Bubble oscillations of large amplitude,” *The Journal of the Acoustical Society of America*, vol. 68, no. 2, pp. 628–633, 1980.
- [119] I. Thormählen, J. Straub, and U. Grigull, “Refractive Index of Water and Its Dependence on Wavelength, Temperature, and Density,” *Journal of Physical and Chemical Reference Data*, vol. 14, no. 4, pp. 933–945, 1985.
- [120] B. Gerold, *Cavitation in focused ultrasound Cavitation in focused ultrasound*. Phd-thesis, University of Dundee, 2013.
- [121] S. D. Rigby, Sam E., Tyas, Andrew, Bennett, Terry, Clarke, Sam D. , Fay, “International Journal of Protective Structures,” *International Journal of Protective Structures*, vol. 5, no. 1, pp. 1–20, 2014.
- [122] Y. Zhou, “Reduction of bubble cavitation by modifying the diffraction wave from a lithotripter aperture,” *Journal of Endourology*, vol. 26, no. 8, pp. 1075–1084, 2012.

-
- [123] T. G. Leighton and R. O. Cleveland, “Lithotripsy,” *Proceedings of the Institution of Mechanical Engineers, Part H: Journal of Engineering in Medicine*, vol. 224, no. 2, pp. 317–342, 2010.
- [124] E. Brujan and A. Vogel, “Stress wave emission and cavitation bubble dynamics by nanosecond optical breakdown in a tissue phantom,” *Journal of Fluid Mechanics*, vol. 558, no. 2006, pp. 281–308, 2006.
- [125] E. A. Brujan, “Shock wave emission from laser-induced cavitation bubbles in polymer solutions,” *Ultrasonics*, vol. 48, no. 5, pp. 423–426, 2008.
- [126] S. W. Karng and Y. P. Lee, “Implosion Mechanism for a Sonoluminescing Gas Bubble,” *Journal of the Korean Physical Society*, vol. 43, no. 1, pp. 135–144, 2003.
- [127] T. Asase and Y. Watanabe, “Observation of Shock Wave Propagation by a Sonoluminescing Bubble,” *Japanese Journal of Applied Physics*, vol. 43, no. 1, pp. 403–404, 2004.
- [128] E. A. Brujan, T. Ikeda, and Y. Matsumoto, “Shock wave emission from a cloud of bubbles,” *Soft Matter*, vol. 8, no. 21, p. 5777, 2012.
- [129] Y. Brelet, A. Jarnac, J. Carbonnel, Y.-B. André, A. Mysyrowicz, A. Houard, D. Fattaccioli, R. Guillermin, and J.-P. Sessarego, “Underwater acoustic signals induced by intense ultrashort laser pulse,” *The Journal of the Acoustical Society of America*, vol. 137, no. 4, pp. EL288–EL292, 2015.
- [130] K. R. Weninger, B. P. Barber, and S. J. Putterman, “Pulsed Mie Scattering Measurements of the Collapse of a Sonoluminescing Bubble,” *Physical Review Letters*, vol. 78, no. 9, pp. 1799–1802, 1997.
- [131] C. E. Brennen, “Cavitation in medicine,” *Interface Focus*, vol. 5, no. 5, p. 20150022, 2015.
- [132] S. L. Ceccio and C. E. Brennen, “Observations of the dynamics and acoustics of travelling bubble cavitation,” *Journal of Fluid Mechanics*, vol. 233, pp. 633–660, 1991.

-
- [133] D. Kröniger, K. Köhler, T. Kurz, and W. Lauterborn, “Particle tracking velocimetry of the flow field around a collapsing cavitation bubble,” *Experiments in Fluids*, vol. 48, no. 3, pp. 395–408, 2010.
- [134] H. G. Flynn, “Cavitation dynamics. I. A mathematical formulation,” *The Journal of the Acoustical Society of America*, vol. 57, no. 6, pp. 1379–1396, 1975.
- [135] W. Kreider, L. A. Crum, M. R. Bailey, and O. A. Sapozhnikov, “A reduced-order, single-bubble cavitation model with applications to therapeutic ultrasound,” *The Journal of the Acoustical Society of America*, vol. 130, no. 5, pp. 3511–3530, 2011.
- [136] C. C. Church, “A theoretical study of cavitation generated by an extracorporeal shock wave lithotripter,” *The Journal of the Acoustical Society of America*, vol. 86, no. 1, pp. 215–227, 1989.
- [137] A. Prosperetti and A. Lezzi, “Bubble dynamics in a compressible liquid. Part 1. First-order theory,” *Journal of Fluid Mechanics*, vol. 168, pp. 457–478, 1986.
- [138] L. Trilling, “The collapse and rebound of a gas bubble,” *Journal of Applied Physics*, vol. 23, no. 1, pp. 14–17, 1952.
- [139] J. R. Macdonald, “Some Simple Isothermal Equations of State,” *Reviews of Modern Physics*, vol. 38, no. 4, pp. 666–679, 1966.
- [140] H. Lin, B. D. Storey, and A. J. Szeri, “Inertially driven inhomogeneities in violently collapsing bubbles: the validity of the Rayleigh-Plesset equation,” *Journal of Fluid Mechanics*, vol. 452, pp. 145–162, 2002.
- [141] M. Koch, C. Lechner, F. Reuter, K. Köhler, R. Mettin, and W. Lauterborn, “Numerical modeling of laser generated cavitation bubbles with the finite volume and volume of fluid method, using OpenFOAM,” *Computers and Fluids*, vol. 126, pp. 71–90, 2016.
- [142] K. Ando, T. Colonius, and C. E. Brennen, *Bubble Dynamics and Shock Waves*. 2013.

-
- [143] V. Wilkens, S. Sonntag, and O. Georg, “Robust spot-poled membrane hydrophones for measurement of large amplitude pressure waveforms generated by high intensity therapeutic ultrasonic transducers,” *The Journal of the Acoustical Society of America*, vol. 139, no. 3, pp. 1319–1332, 2016.
- [144] R. M. Jones, M. A. O’Reilly, and K. Hynynen, “Transcranial passive acoustic mapping with hemispherical sparse arrays using CT-based skull-specific aberration corrections: a simulation study,” *Physics in Medicine and Biology*, vol. 58, no. 14, pp. 4981–5005, 2013.
- [145] S. E. Rigby, A. Tyas, T. Bennett, S. D. Clarke, and S. D. Fay, “The negative phase of the blast load,” *International Journal of Protective Structures*, vol. 5, no. 1, pp. 1–19, 2014.
- [146] A. M. Zhang, S. Li, and J. Cui, “Study on splitting of a toroidal bubble near a rigid boundary,” *Physics of Fluids*, vol. 27, p. 062102, 2015.
- [147] E. A. Brujan, G. S. Keen, A. Vogel, and J. R. Blake, “The final stage of the collapse of a cavitation bubble close to a rigid boundary,” *Physics of Fluids*, vol. 14, no. 1, pp. 85–92, 2002.
- [148] S. Shaw and P. Spelt, “Shock emission from collapsing gas bubbles,” *Journal of Fluid Mechanics*, vol. 646, pp. 363–373, 2010.
- [149] G. R. Harris, “The impact of piezoelectric PVDF on medical ultrasound exposure measurements, standards, and regulations 1,” *IEEE Transactions on Ultrasonics, Ferroelectrics, and Frequency Control*, vol. 47, no. 6, pp. 1321–1335, 2000.
- [150] P. C. Beard, A. M. Hurrell, and T. N. Mills, “Characterization of a polymer film optical fiber hydrophone for use in the range 1 to 20 MHz: A comparison with PVDF needle and membrane hydrophones,” *IEEE Transactions on Ultrasonics, Ferroelectrics, and Frequency Control*, vol. 47, no. 1, pp. 256–264, 2000.
- [151] N. Kudo, “A Simple Technique for Visualizing Ultrasound Fields Without Schlieren Optics,” *Ultrasound in Medicine and Biology*, vol. 41, no. 7, pp. 2071–2081, 2015.

-
- [152] J. Eisener and R. Mettin, “Synthetic acoustic spectra of ultrasonic cavitation emissions,” *Fortschritte der Akustik-DAGA*, pp. 435–436, 2012.
- [153] E. Cramer and W. Lauterborn, “Acoustic cavitation noise spectra,” *Applied Scientific Research*, vol. 38, no. 1, pp. 209–214, 1982.
- [154] K. S. Suslick, “Sonochemistry,” *Science*, vol. 247, pp. 1439 – 1445, 1990.
- [155] I. Tzanakis, G. S. Lebon, D. G. Eskin, and K. A. Pericleous, “Characterizing the cavitation development and acoustic spectrum in various liquids,” *Ultrasonics Sonochemistry*, vol. 34, pp. 651–662, 2017.
- [156] K. Johansen, J. H. Song, and P. Prentice, “Characterising Focused Ultrasound via High Speed Shadowgraphic Imaging at 10 Million Frames Per Second,” in *IEEE International Ultrasonics Symposium, IUS*, pp. 8–11, 2016.
- [157] J. H. Song, K. Johansen, and P. Prentice, “Covert cavitation : Spectral peak suppression in the acoustic emissions from spatially configured nucleations,” *The Journal of the Acoustical Society of America*, vol. 141, no. 3, pp. EL216–EL221, 2017.
- [158] L. Jiang, F. Liu, H. Chen, J. Wang, and D. Chen, “Frequency spectrum of the noise emitted by two interacting cavitation bubbles in strong acoustic fields,” *Physical Review E*, vol. 85, no. 3, pp. 1–7, 2012.
- [159] A. Doinikov, “Translational motion of two interacting bubbles in a strong acoustic field,” *Physical Review E*, vol. 64, no. 2, p. 026301, 2001.
- [160] R. Mettin, I. Akhatov, U. Parlitz, C. Ohl, and W. Lauterborn, “Bjerknes forces between small cavitation bubbles in a strong acoustic field,” *Physical Review E*, vol. 56, no. 3, pp. 2924–2931, 1997.
- [161] K. Yasui, T. Tuziuti, J. Lee, T. Kozuka, A. Towata, and Y. Iida, “Numerical simulations of acoustic cavitation noise with the temporal fluctuation in the number of bubbles,” *Ultrasonics Sonochemistry*, vol. 17, no. 2, pp. 460–472, 2010.

-
- [162] R. Sadighi-Bonabi, N. Rezaee, H. Ebrahimi, and M. Mirheydari, "Interaction of two oscillating sonoluminescence bubbles in sulfuric acid," *Physical Review E*, vol. 82, no. 1, p. 016316, 2010.
- [163] G. S. Lebon, K. Pericleous, I. Tzanakis, and D. G. Eskin, "Dynamics of two interacting hydrogen bubbles in liquid aluminum under the influence of a strong acoustic field," *Physical Review E*, vol. 92, no. 4, p. 043004, 2015.
- [164] G. S. B. Lebon, K. Pericleous, I. Tzanakis, and D. G. Eskin, "Dynamics of two interacting hydrogen bubbles in liquid aluminum under the influence of a strong acoustic field," *Physical Review E - Statistical, Nonlinear, and Soft Matter Physics*, vol. 92, no. 4, 2015.
- [165] L. Wang, G. Memoli, I. Butterworth, M. Hodnett, and B. Zeqiri, "Characterisation of a multi-frequency cavitation vessel," *IOP Conference Series: Materials Science and Engineering*, vol. 42, no. 1, 2012.
- [166] H. Li, Z. D. Deng, and T. J. Carlson, "Piezoelectric materials used in underwater acoustic transducers," *Sensor Letters*, vol. 10, no. 3-4, pp. 679–697, 2012.
- [167] F. Marquet, T. Teichert, S. Y. Wu, Y. S. Tung, M. Downs, S. Wang, C. Chen, V. Ferrera, and E. E. Konofagou, "Real-time, transcranial monitoring of safe blood-brain barrier opening in non-human primates," *PLoS ONE*, vol. 9, no. 2, pp. 1–11, 2014.
- [168] B. Zeqiri, M. Hodnett, and A. J. Carroll, "Studies of a novel sensor for assessing the spatial distribution of cavitation activity within ultrasonic cleaning vessels," *Ultrasonics*, vol. 44, no. 1, pp. 73–82, 2006.
- [169] C. C. Coussios, C. H. Farny, G. Ter Haar, and R. A. Roy, "Role of acoustic cavitation in the delivery and monitoring of cancer treatment by high-intensity focused ultrasound (HIFU)," *Int. J. Hyperthermia*, vol. 23, no. 2, pp. 105–120, 2007.
- [170] A. Sabraoui, C. Inserra, B. Gilles, J.-C. Béra, and J.-L. Mestas, "Feedback loop process to control acoustic cavitation.," *Ultrasonics sonochemistry*, vol. 18, no. 2, pp. 589–594, 2011.
- [171] Datasheet Y-107 and Y-102 Hydrophones, *Sonic Concepts, Bothell, WA, USA*.

-
- [172] T. L. Szabo, *Diagnostic ultrasound imaging: inside out*. Academic Press, 2004.
- [173] G. Kossoff, “The Effects of Backing and Matching on the Performance of Piezoelectric Ceramic Transducers,” *IEEE Transactions on Sonics and Ultrasonics*, vol. 13, no. 1, pp. 20–30, 1966.
- [174] C. S. Desilets, J. D. Fraser, and G. S. Kino, “The Design of Efficient Broad-Band Piezoelectric Transducers,” *IEEE Transactions on Sonics and Ultrasonics*, vol. 25, no. 3, pp. 115–125, 1978.
- [175] T. M. Reeder and D. K. Winslow, “Characteristics of Microwave Acoustic Transducers for Volume Wave Excitation,” *IEEE Transactions on Microwave Theory and Techniques*, no. 11, pp. 927 – 940, 1969.
- [176] B. Fay, G. Ludwig, C. Lankjaer, and P. A. Lewin, “Frequency response of PVDF needle-type hydrophones,” *Ultrasound in Medicine and Biology*, vol. 20, no. 4, pp. 361–366, 1994.
- [177] L. E. Kinsler, A. R. Frey, A. B. Coppens, and J. V. Sanders, *Fundamentals of acoustics*. Wiley-VCH, 1999.
- [178] P. N. Wells, “Ultrasound imaging,” *Physics in medicine and biology*, vol. 51, no. 13, p. R83, 2006.
- [179] Y.-C. Wang and C. E. Brennen, “Numerical Computation of Shock Waves in a Spherical Cloud of Cavitation Bubbles,” *Journal of Fluids Engineering*, vol. 121, no. 4, p. 872, 1999.
- [180] U. Rasthofer, F. Wermelinger, P. Hadijdoukas, and P. Koumoutsakos, “Large Scale Simulation of Cloud Cavitation Collapse,” in *International Conference on Computational Science*, (Zurich), pp. 1764–1772, Elsevier, 2017.
- [181] J. Ma, C. T. Hsiao, and G. L. Chahine, “Numerical study of acoustically driven bubble cloud dynamics near a rigid wall,” *Ultrasonics Sonochemistry*, vol. 40, pp. 944–954, 2018.

-
- [182] D. Y. Tan, J. Keller, R. L. Miorini, and J. Katz, “Numerical Study of Collapse of a Cavitating Cloud of Bubbles,” *International Symposium on Cavitation*, pp. 227–239, 2012.
- [183] E. S. Nasibullaeva and I. S. Akhatov, “Bubble cluster dynamics in an acoustic field,” in *Proceedings of the 8th International Symposium on Cavitation*, pp. 1–6, 2013.
- [184] I. Akhatov, U. Parlitz, and W. Lauterborn, “Towards a theory of self-organization phenomena in bubble-liquid mixtures,” *Physical Review E*, vol. 54, no. 5, pp. 4990–5003, 1996.
- [185] C. Scheffczyk, U. Parlitz, T. Kurz, W. Knop, and W. Lauterborn, “Comparison of bifurcation structures of driven dissipative nonlinear oscillators,” *Physical Review A*, vol. 43, no. 12, p. 6495, 1991.
- [186] V. Englisch, U. Parlitz, and W. Lauterborn, “Comparison of winding-number sequences for symmetric and asymmetric oscillatory systems,” *Physical Review E*, vol. 92, no. 2, pp. 1–18, 2015.
- [187] D. R. Bacon, “Characteristics of a pvdF Membrane Hydrophone for Use in the Range 1-100 MHz,” *IEEE Transactions on Sonics and Ultrasonics*, vol. 29, no. 1, pp. 18–25, 1982.
- [188] K. A. Wear, “The effects of frequency-dependent attenuation and dispersion on sound speed measurements: applications in human trabecular bone,” *IEEE Transactions on Ultrasonics, Ferroelectrics, and Frequency Control*, vol. 47, no. 1, pp. 265–273, 2000.
- [189] H. Medwin, “Speed of sound in water: A simple equation for realistic parameters,” *The Journal of the Acoustical Society of America*, vol. 58, no. 6, pp. 1318–1319, 1975.
- [190] K. K. Andersen, P. Lunde, and J. Kocbach, “Magnitude and phase reciprocity calibration of ultrasonic piezoelectric disk in air,” in *Proceedings of the 39th Scandinavian Symposium on Physical Acoustics*, pp. 1–21, 2016.

-
- [191] K. Johansen and M. Postema, “Lagrangian formalism for computing oscillations of spherically symmetric encapsulated acoustic antibubbles,” *Hydroacoustics*, vol. 19, no. 4, pp. 197–208, 2016.
- [192] A. Hurrell, “Voltage to pressure conversion: are you getting ‘phased’ by the problem?” *Journal of Physics: Conference Series*, vol. 1, pp. 57–62, 2004.
- [193] V. Wilkens and C. Koch, “Amplitude and phase calibration of hydrophones up to 70 MHz using broadband pulse excitation and an optical reference hydrophone,” *The Journal of the Acoustical Society of America*, vol. 115, no. 6, pp. 2892 – 2903, 2004.